

**Aerodynamics of Propellers in Interaction Dominated Flowfields
An Application to Novel Aerospace Vehicles**

Stokkermans, T.C.A.

DOI

[10.4233/uuid:46178824-bb80-4247-83f1-dc8a9ca7d8e3](https://doi.org/10.4233/uuid:46178824-bb80-4247-83f1-dc8a9ca7d8e3)

Publication date

2020

Document Version

Final published version

Citation (APA)

Stokkermans, T. C. A. (2020). *Aerodynamics of Propellers in Interaction Dominated Flowfields: An Application to Novel Aerospace Vehicles*. [Dissertation (TU Delft), Delft University of Technology]. <https://doi.org/10.4233/uuid:46178824-bb80-4247-83f1-dc8a9ca7d8e3>

Important note

To cite this publication, please use the final published version (if applicable).
Please check the document version above.

Copyright

Other than for strictly personal use, it is not permitted to download, forward or distribute the text or part of it, without the consent of the author(s) and/or copyright holder(s), unless the work is under an open content license such as Creative Commons.

Takedown policy

Please contact us and provide details if you believe this document breaches copyrights.
We will remove access to the work immediately and investigate your claim.

**AERODYNAMICS OF PROPELLERS IN
INTERACTION DOMINATED FLOWFIELDS**
AN APPLICATION TO NOVEL AEROSPACE VEHICLES

**AERODYNAMICS OF PROPELLERS IN
INTERACTION DOMINATED FLOWFIELDS**
AN APPLICATION TO NOVEL AEROSPACE VEHICLES

Dissertation

for the purpose of obtaining the degree of doctor
at Delft University of Technology,
by the authority of the Rector Magnificus prof. dr. ir. T.H.J.J. van der Hagen,
chair of the Board for Doctorates,
to be defended publicly on
Wednesday 18 November 2020 at 10:00 o'clock

by

Tom Caton Arnaud STOKKERMANS

Master of Science in Aerospace Engineering,
Delft University of Technology, the Netherlands
born in Heerlen, the Netherlands

This dissertation has been approved by the promotor.

Composition of the doctoral committee:

Rector Magnificus,	chairman
Prof. dr. ir. L. L. M. Veldhuis	Delft University of Technology, <i>promotor</i>
Prof. dr. ir. M. Voskuil	Nederlandse Defensie Academie, <i>copromotor</i>

Independent members:

Prof. dr. ir. C. J. Simão Ferreira	Delft University of Technology
Prof. Dr.-Ing. C. Breitsamter	Technical University of Munich, Germany
Dr. M. Keßler	University of Stuttgart, Germany
Dr. B. Ortun	ONERA, France
R. Fukari MSc.	Airbus Helicopters, France
Prof. Dr.-Ing. G. Eitelberg	Delft University of Technology, <i>reserve member</i>



This research was partially funded by the Clean Sky 2 Joint Undertaking under the European Union's Horizon 2020 research and innovation programme under grant agreement No 685569 — PROPTER — H2020-CS2-CFP01-2014-01.

Keywords: Propeller, aerodynamics, performance, interaction, propulsion integration, compound helicopter, tip-mounted propeller, eVTOL, swirl-recovery-vanes, computational fluid dynamics, wind-tunnel testing

Printed by: Ipskamp Printing

Copyright © 2020 by T. C. A. Stokkermnas

ISBN 978-94-6366-332-8

An electronic version of this dissertation is available at
<http://repository.tudelft.nl/>.

SUMMARY

This research is on the aerodynamics of propellers in interaction. As a propeller is dependent on the flowfield it encounters, any disturbance in that inflow results in changes in loading on the propeller. This can result in propulsive efficiency changes and affect stability through generation of in-plane forces and out-of-plane moments. The loading changes can also impact noise through loading fluctuations and cause vibrations in the structure leading to fatigue. The objective of the research in this dissertation is to get a fundamental understanding of the role of aerodynamic interaction on the loading and performance of primarily the propeller and secondarily the interacting object(s) in typical configurations where interaction dominates the flowfield. For the propeller this refers to situations where the inflow is disturbed by such an amount that the disturbance is a dominating factor in the propeller loading.

Five different configurations were studied: A wingtip-mounted propeller in tractor and pusher configuration, propeller interaction with swirl-recovery-vanes (SRVs), interaction between propellers in configurations applicable to eVTOL vehicles and propellers on a compound helicopter. The investigated compound helicopter was the Airbus RACER, studied in the Clean Sky 2 PROPTER project in which the author took part to investigate the aerodynamic interactions and their consequence on the performance of the propellers. On these configurations a variety of propeller interactions occurred. Investigated phenomena for the propeller include decreased and increased dynamic pressure from momentum sources and sinks, potential effects resulting in dynamic pressure and angle of attack changes, rotational flowfields and impinging vortices.

A combination of numerical and experimental results were obtained. RANS CFD simulations were performed by resolving the propeller and by modelling its effect in terms of momentum and energy by means of an actuator-disk and actuator-line representation developed as part of this work. Furthermore, lower-order propeller methods based on blade element momentum and lifting line theory were used for quick analysis and design. For all propellers, except for those on the compound helicopter, experimental datasets were created or available for validation of the numerical results and for quick parametric study of interaction effects. This includes two datasets where propeller performance was investigated in static condition (zero freestream airspeed) and with non-zero freestream airspeed at angles of attack up to 95 deg in terms of thrust, power, in-plane forces and out-of-plane moments.

The capability of the actuator-disk and actuator-line RANS propeller modelling methods was investigated for the simulation of a wingtip-mounted tractor-propeller, in order to reduce the cost of such simulations. This was done in the most accurate form, by applying propeller blade loading results extracted from simulations in which the blades

were fully resolved. The numerical results were validated by comparison with measurement data from wind-tunnel experiments. It was concluded that the aerodynamic interactions for the wingtip-mounted propeller in tractor configuration can be predicted by RANS CFD with a simple one-equation turbulence model (Spalart–Allmaras), provided that uncertainty due to numerical diffusion is accounted for by a grid dependency study or reduced by local grid refinement. The actuator-line model reduced the computational time by 17% without introducing errors into the time-accurate and time-averaged wing loading. The actuator-disk model reduced the computational cost by 85% by removing time dependency, with a small penalty in the accuracy of the time-averaged flowfield and a 3.9% overprediction of the wing lift.

With the validated actuator-disk model, the effects of windmilling, used for energy harvesting, were investigated for this configuration. While for positive thrust for inboard-up propeller rotation an increase in wing lift was found and also the lift-to-drag ratio increased by about 25% compared to the propeller-off case, in energy-harvesting mode a reduction of lift-to-drag ratio of about 25% was observed. The decrease in lift-to-drag ratio was reflected in the slipstream by an increase in average swirl from upstream of the wing to downstream, opposite to the observation with positive thrust.

The second investigated configuration consisted of a small-scale wingtip-mounted propeller in pusher configuration typical of a distributed propulsion setup. The consequences of propeller design, size and thrust target were investigated. A wingtip flowfield was extracted from a RANS CFD simulation of an isolated wing, circumferentially averaged and provided to a lower order propeller analysis and optimisation routine based on lifting line theory. Possible propulsive efficiency gains for the propeller due to installation were found to be significant, up to 16% increase at low thrust levels, decreasing to approximately 7.5% at the highest thrust level, for a range of thrust from 5% up to 100% of the wing drag. These gains were found to be independent of propeller radius for thrust levels larger than 30% of the wing drag. Effectively, the propeller geometry was optimised for the required thrust and to a lesser degree for the non-uniformity in the flowfield. Propeller blade optimisation and installation resulted in higher profile efficiency in the blade root sections and a more inboard thrust distribution.

The third configuration was used to study the aerodynamic impact of the installation of swirl-recovery-vanes downstream of a propeller. SRVs enhance propulsive efficiency by converting the rotational kinetic energy in a propeller slipstream into additional thrust and axial kinetic energy. RANS simulations were performed for a configuration where validating experimental data was present. Favourable comparisons between the experimental and numerical slipstream data validated the simulations, which predicted a maximum propulsive efficiency increase of 0.7% with the current design of the SRVs. The upstream effect of the SRVs on the time-averaged propeller performance was almost negligible. Yet, small but systematic unsteady propeller loads were measured with a peak-to-peak amplitude of at most 2% of the time-averaged loading, occurring at a frequency corresponding to the five SRV passages during one revolution. The downstream interaction was one order of magnitude stronger, with unsteady loading on the SRVs with a peak-to-peak amplitude of about 20% of the time-averaged load.

For the fourth configuration, two propeller interaction types were studied that may occur on many eVTOL concepts. Side-by-side and one-after-another propeller interaction were investigated in terms of effects on thrust, power, in-plane forces and out-of-plane moments, and how those performance effects depend on axial and lateral propeller spacing. A wind tunnel experiment was performed with two propeller units, one instrumented with a force/torque sensor for performance measurements, and the other introducing the aerodynamic interaction. Total pressure and planar PIV measurements were taken to investigate the slipstream characteristics. A strong dependency of interaction effects on the geometric layout was found. For side-by-side interaction characteristic of vertical take-off and transition, interaction effects varied from weak at small angles of attack to strong at larger angles. A drop in rear propeller thrust of up to 30% was found. Thrust compensation resulted in power penalties up to 13% for the two propellers combined. For one-after-another interaction characteristic of cruise, a maximum loss in thrust of up to 80% was observed. Thrust compensation led to power penalties up to 30% for the rear propeller alone. A blade element momentum model captured most interaction effects with sufficient accuracy.

For the last configuration, RANS simulations were performed to capture the various aerodynamic interactions which are occurring for the compound helicopter configuration, featuring a box-wing design for auxiliary lift in cruise and wingtip-mounted propellers (lateral rotors) in pusher configuration for auxiliary thrust in cruise and counter-torque in hover. Although the study was limited to a specific geometry, the effects and phenomena are expected to be to some extent applicable in general for compound helicopters and wingtip-mounted rotors in pusher configuration. A quantitative indication of the aerodynamic interaction effects could be established by leaving away different airframe components in the simulations. The downwash of the main rotor was found to cause a negative angle of attack in cruise and impinged directly on the propellers in hover, resulting in moderate to very significant sinusoidally varying blade loading. The wing increased propeller propulsive efficiency in cruise through its wingtip rotational flowfield and to a lesser extent through its wake. An upstream effect of the propellers on the wing loading was also found. The wing caused disturbances to the inflow of the left propeller in hover, resulting in a net thrust increase. A small thrust decrease for the right propeller was found due to the wing disturbing its slipstream. In general, very significant aerodynamic interaction effects can be expected when a main rotor, propellers and wing are in proximity to each other.

Furthermore, aerodynamic interaction with an upstream wing was tested experimentally with the propeller and wing normal to the flow, to represent the interaction occurring with a time-averaged main rotor slipstream on the compound helicopter. From an accompanying numerical investigation it was concluded that the results are thought to be qualitatively representative of this interaction. The experimental data showed that addition of the wing results in a net reduction of all propeller performance quantities, with thrust reducing up to 20%. A thrust decreasing and thrust increasing mechanism were found numerically. For most tested operating conditions, the wing resulted in a small decrease of propeller thrust-over-power ratio. Decrease of advance ratio, increase of wing distance to the propeller, and increase of flap deflection generally decreased the effect of the wing on thrust and power, however the influence of flap deflection was

found to be very small.

The presented results provide insight in the possible effects of aerodynamic interaction on the propeller loading through study of different configurations. However, it is also shown that every specific layout comes with its own peculiarities which may change the balance of performance increasing and decreasing effects that occur in a rotation. The provided experimental data can be used to the readers advantage as a validated starting point for more specific analysis with for instance the presented methods.

SAMENVATTING

Dit onderzoek gaat over de aerodynamica van propellers in interactie. Gezien een propeller afhankelijk is van de aanstroming die hij ondervindt, zorgt enige verstoring van die aanstroming in veranderingen in belasting op de propeller. Dit kan resulteren in veranderingen van voortstuwingsrendement en kan de vliegstabiliteit beïnvloeden door het ontstaan van krachten in het propeller vlak en momenten uit het vlak. De veranderingen in belasting kunnen ook invloed hebben op het geluid door fluctuaties in de belasting en deze kunnen ook vibraties in de structuur veroorzaken die kunnen leiden tot vermoeiing. Het doel van het onderzoek in deze dissertatie is het verkrijgen van een fundamenteel begrip van de rol van aerodynamische interactie op de belasting en prestaties van primair de propeller en secundair het/de object(en) in interactie in typische configuraties waar interactie het stromingsveld domineert. Ten aanzien van de propeller refereert dit naar situaties waar de aanstroming dusdanig verstoord is dat de verstoring een dominante factor in de propeller belasting is.

Vijf verschillende configuraties zijn bestudeerd: Een aan de vleugeltip geïnstalleerde propeller in trek- en duwconfiguratie, propeller interactie met 'swirl-recovery-vanes' (SRVs), interactie tussen propellers in configuraties toepasbaar op 'eVTOL' vliegtuigen en de propellers op een 'compound' helikopter. De onderzochte compound helikopter was de Airbus RACER, bestudeerd in het Clean Sky 2 PROPTER project waarin de auteur heeft deelgenomen om de aerodynamische interacties en hun consequenties op de prestaties van de propellers te onderzoeken. Op deze configuraties hebben zich verscheidene interacties plaatsgevonden. De onderzochte fenomenen voor de propeller omvatten verhoogde en verlaagde dynamische druk van impuls bronnen en sinks, potentiaaleffecten resulterende in dynamische druk en invalshoek veranderingen, roterende stroomvelden en wervels die de propeller treffen.

Een combinatie van numerieke en experimentele resultaten zijn verkregen. Er zijn RANS CFD simulaties uitgevoerd door het simuleren van de propeller bladen en door het modelleren van het effect wat betreft impuls en energie door middel van een trekkende schijf en trekkende lijn representatie, ontwikkeld als onderdeel van dit werk. Verder zijn er lagere orde propeller methodes gebruikt op basis van blad element impuls theorie en lijndraagkrachts theorie voor snelle analyse en ontwerp. Voor alle propellers, behalve die op de compound helikopter, zijn er experimentele datasets gecreëerd of waren deze al aanwezig voor de validatie van de numerieke resultaten en voor snelle parametrische studie van interactie effecten. Dit is inclusief twee datasets waar de propeller prestaties onderzocht zijn in statische conditie (geen vrije stroming) en met vrije stroming op invalshoeken tot en met 95 deg, aangaande de trekkracht, het vermogen, de krachten in het vlak en de momenten uit het vlak.

De geschiktheid van de trekkende schijf en trekkende lijn RANS propeller modellerings methodes was onderzocht voor de simulatie van de aan de vleugeltip gemon-

teerde propeller in trekconfiguratie, om de rekenkosten van zulke simulaties te reduceren. Dit was gedaan in de meest accurate vorm, door het toepassen van de propellerblad belastingsresultaten geëxtraheerd uit simulaties waarin de bladen volledig gesimuleerd zijn. De numerieke resultaten zijn gevalideerd door vergelijk met meetdata van windtunnel experimenten. De conclusie is dat de aerodynamische interacties van de aan de vleugeltip gemonteerde propeller in trekconfiguratie kunnen worden voorspeld door RANS CFD berekeningen met een eenvoudig één-vergelijking turbulentiemodel (Spalart–Allmaras), zolang de onzekerheid door numerieke diffusie door een gridsafhankelijkheidsstudie in acht wordt genomen of door lokale gridverfijning wordt verminderd. Het trekkende lijn model reduceerde de rekentijd met 17% zonder introductie van fouten in de tijdsafhankelijke en tijdsgemiddelde vleugelbelasting. Het trekkende schijf model reduceerde de rekentijd met 85% door het verwijderen van tijdsafhankelijkheid, met een kleine fout in het tijdsgemiddelde stromingsveld en een 3.9% over predictie van de vleugeldraagkracht.

Met dit gevalideerde trekkende schijf model zijn voor deze configuratie de effecten onderzocht van het gebruik van de propeller als turbine, voor het opwekken van energie. Voor positieve trekkracht met propeller rotatie aan de binnenkant omhoog, is er een toename van vleugeldraagkracht gevonden en ook een toename van de draagkrachtweerstandverhouding van ongeveer 25% vergeleken met de situatie zonder propeller, maar voor de situatie waar energie werd opgewekt was er een reductie van de draagkrachtsweerstandverhouding van ongeveer 25%. De afname van draagkrachtsweerstandverhouding was ook zichtbaar in de slipstroom door een toename van de gemiddelde werveling van stroomopwaarts van de vleugel naar stroomafwaarts, tegengesteld aan de observatie voor positieve trekkracht.

De tweede onderzochte configuratie betrof een kleine aan de vleugeltip gemonteerde propeller in duwconfiguratie typisch voor een gedistribueerde voortstuwingsopstelling. De consequentie van propeller ontwerp, formaat en trekkracht zijn onderzocht. Een stromingsveld rond de vleugeltip was geëxtraheerd uit een RANS CFD simulatie van een geïsoleerde vleugel, circumferentieel gemiddeld en voorgeschreven aan een lagere orde propeller analyse en optimalisatie routine gebaseerd op dragende vleugel theorie. Er zijn significante voortstuwingsrendementstoenames door installatie van de propeller gevonden, van een 16% toename bij lage trekkracht, afnemend naar ongeveer 7.5% voor de hoogste trekkracht, voor een trekkrachtsbereik van 5% tot en met 100% van de vleugelweerstand. Deze toenames zijn onafhankelijk van de propeller radius voor trekkrachtniveaus hoger dan 30% van de vleugelweerstand. De propeller geometrie is voornamelijk voor de benodigde trekkracht geoptimaliseerd en in mindere mate voor de niet-uniformiteit in het stromingsveld. Propellerblad optimalisatie en installatie zorgde voor een hoger profielrendement bij de profielen aan de wortel van het blad en ook voor een meer naar de wortel liggende trekkrachtsverdeling.

De derde configuratie is gebruikt voor het bestuderen van de aerodynamische impact van de installatie van 'swirl-recovery-vanes' stroomafwaarts van een propeller. SRVs zorgen voor een verhoging van het voortstuwingsrendement door het converteren van rotationele kinetische energie in de propeller slipstroom naar additionele trekkracht en axiale kinetische energie. Er zijn RANS simulaties uitgevoerd voor een configuratie waar

validerende experimentele data voor beschikbaar was. De simulaties zijn gevalideerd door een goede overeenkomst van de experimentele en numerieke slipstroom, en deze voorspelde een maximale voortstuwingsrendementsverhoging van 0.7% voor het huidige ontwerp van de SRVs. De stroomopwaartse effecten van de SRVs op de tijdsgemiddelde propeller prestaties waren bijna verwaarloosbaar. Toch is er een klein maar systematische tijdsafhankelijke propeller belasting gemeten met een piek-tot-piek amplitude van bijna 2% van de tijdsgemiddelde belasting, die plaatsvond met een frequentie corresponderende met de vijf SRV passages gedurende een rotatie. De stroomafwaartse interactie was een ordegrrootte sterker, met tijdsafhankelijke belasting op de SRVs met een piek-tot-piek amplitude van ongeveer 20% van de tijdsgemiddelde belasting.

Voor de vierde configuratie zijn er twee propeller interactie types onderzocht die kunnen plaatsvinden op vele eVTOL concepten. Propeller interactie in zij-aan-zij en achter-elkaar configuratie zijn onderzocht op de effecten op de trekkracht, vermogen, krachten in het vlak en momenten uit het vlak, en ook is onderzocht hoe deze prestatie effecten afhangen van axiale en laterale afstand. Een windtunnel experiment is uitgevoerd met twee propeller modellen, waarvan één geïnstrumenteerd was met een kracht/moment opnemer voor prestatiemetingen, en de ander ingezet was om de interactie te introduceren. Er zijn totale druk metingen en PIV metingen in een vlak genomen om de slipstroom karakteristieken te onderzoeken. Er is een sterke afhankelijkheid van de interactie effecten op de geometrische layout gevonden. Voor de zij-aan-zij interactie typisch voor het vertikaal opstijgen en transitie varieerde de interactie effecten van zwak bij kleine invalshoeken tot sterk bij grote invalshoeken. Er is een vermindering van de trekkracht van de achterste propeller van maximaal 30% gevonden. Compensatie van de trekkracht resulteerde in een verhoogde vraag naar vermogen van maximaal 13% voor de twee propellers gecombineerd. Voor de achter-elkaar configuratie interactie typisch voor kruisvlucht is er een maximaal verlies in trekkracht van 80% gemeten. Trekkraftcompensatie zorgde voor een verhoogde vraag naar vermogen van maximaal 30% voor de achterste propeller. Een blad element impuls model vatte de meeste interactie effecten met voldoende nauwkeurigheid.

Voor de laatste configuratie zijn er RANS simulaties uitgevoerd om de verschillende aerodynamische interacties vast te leggen die plaatsvinden voor de compound helikopter configuratie, die een box-vleugel ontwerp heeft voor extra lift in kruisvlucht en aan de vleugeltip geïnstalleerde propellers in duwconfiguratie heeft voor extra stuwkracht in kruisvlucht en tegenmoment in hover. Hoewel de studie beperkt was tot een specifieke geometrie, wordt verwacht dat de effecten en fenomenen tot op zekere hoogte in het algemeen toepasbaar zullen zijn voor compound helikopters en aan de vleugeltip geïnstalleerde propellers in duwconfiguratie. Het was mogelijk om een kwantitatieve indicatie van de aerodynamische interactie effecten vast te stellen door verschillende vliegtuig onderdelen weg te laten uit de simulaties. De neerstroming van de hoofdrotor bleek een negatieve invalshoek tijdens de kruisvlucht te veroorzaken en stroomde direct tegen de propellers in hover, resulterend in matige tot zeer significante sinusoidaal variërende bladbelasting. De vleugel verhoogde het propeller voortstuwingsrendement in de kruisvlucht door het roterende stromingsveld rond de vleugeltip en in mindere mate

door het zog. Er is ook een stroomopwaarts effect van de propellers op de vleugelbelasting gevonden. In de hover conditie veroorzaakte de vleugel verstoringen in de aanstroming van de linker propeller, resulterende in een netto stuwkrachtstoename. Een kleine stuwkrachtsafname is er gevonden voor de rechter propeller, doordat de vleugel zijn slipstroom verstoort. Over het algemeen kunnen zeer significante aerodynamische interactie-effecten worden verwacht wanneer een hoofdrotor, propellers en vleugel zich dicht bij elkaar bevinden.

Vervolgens is de aerodynamische interactie met een stroomopwaartse vleugel experimenteel getest met de propeller en vleugel loodrecht op de stroming, om de interactie na te bootsen die optreedt bij de compound helikopter met een tijdgemiddelde hoofdrotor slipstroom. Uit een bijbehorend numeriek onderzoek is geconcludeerd dat de resultaten kwalitatief representatief worden geacht voor deze interactie. De experimentele gegevens toonden aan dat toevoeging van de vleugel resulteert in een netto reductie van de propellerprestatie variabelen, waarbij de stuwkracht tot 20% afnam. Er is een stuwkrachtsverlagend en stuwkrachtsverhogend mechanisme gevonden. Voor de meeste geteste bedrijfsomstandigheden resulteerde de vleugel in een kleine afname van de ratio van stuwkracht en vermogen van de propeller. Daling van de voortgangscoefficiënt, toename van de vleugelafstand tot de propeller en toename van de klepuitslag verminderde in het algemeen het effect van de vleugel op stuwkracht en vermogen, maar de invloed van de klepuitslag bleek zeer klein te zijn.

De gepresenteerde resultaten geven inzicht in de mogelijke effecten van aerodynamische interactie op de propeller belasting door onderzoek van verschillende configuraties. Er is echter ook aangetoond dat elke specifieke lay-out zijn eigen kenmerken heeft die de balans tussen prestatieverhogende en verlagende effecten die in een rotatie optreden, kunnen veranderen. De gepresenteerde experimentele data kan door de lezers worden gebruikt als een gevalideerd startpunt voor meer specifieke analyse met bijvoorbeeld de gepresenteerde methodes.

CONTENTS

Summary	v
Samenvatting	ix
Nomenclature	xvii
1 Introduction	1
1.1 Dissertation objective	10
1.2 Dissertation scope and methods	11
1.3 Dissertation outline	12
2 Interaction dominated flowfields	15
2.1 Isolated propeller system	17
2.2 Interaction with nacelle or fuselage	20
2.2.1 Nacelle	20
2.2.2 Fuselage	21
2.3 Interaction with wing	23
2.3.1 Wingtip-mounted tractor-propeller	25
2.3.2 Wingtip-mounted pusher-propeller	26
2.4 Interaction with stator or rotor	27
2.4.1 Stator	27
2.4.2 Rotor	28
2.5 Combined interaction	32
3 Analysis methods and models	37
3.1 Experimental approach	37
3.1.1 Propellers	37
3.1.2 Wind-tunnel facilities	40
3.1.3 Models and measurement techniques	40
3.2 Numerical approach	52
3.2.1 Propeller modelling methods	52
3.2.2 RANS CFD solver setup	57
3.2.3 Geometries, domains and boundary conditions	60
3.2.4 Grids and grid dependency studies	70
4 Aerodynamics of the isolated propellers	73
4.1 Characteristics at zero angle of attack	73
4.1.1 XPROP propeller	74
4.1.2 F29 propeller	79
4.1.3 Beaver propeller	84
4.1.4 APIAN propeller	93

4.2	Angle of attack effects	97
4.2.1	XPROP propeller	97
4.2.2	F29 propeller	104
4.3	Conclusions.	106
5	Interaction with wingtip	109
5.1	Analysis and modelling of a wingtip-mounted tractor-propeller	110
5.1.1	Isolated wing configuration	111
5.1.2	Propeller-wing configuration	115
5.2	Effects of windmilling for a wingtip-mounted tractor-propeller	122
5.2.1	Wing loading.	123
5.2.2	Slipstream flowfield	124
5.3	Analysis and design of a small-scale wingtip-mounted pusher-propeller	127
5.3.1	Isolated wing analysis	127
5.3.2	Propeller design study	129
5.3.3	Propeller-wing analysis with actuator-disk	134
5.3.4	Blade resolving propeller-wing analysis	135
5.4	Conclusions.	138
6	Interaction with stator or propeller	141
6.1	An analysis of propeller-swirl-recovery-vane interaction	142
6.1.1	Grid convergence with installed SRVs	142
6.1.2	Slipstream flowfield	143
6.1.3	Propeller and SRV loading	145
6.2	Interaction with another propeller in typical eVTOL configurations.	149
6.2.1	Side-by-side (SBS) propeller configuration.	151
6.2.2	One-after-another (OAA) propeller configuration	158
6.3	Conclusions.	164
7	Combined interaction with main rotor and wingtip	167
7.1	Wingtip-mounted pusher-propellers on a compound helicopter in cruise	168
7.1.1	Temporal and grid convergence	169
7.1.2	Interaction effects on propeller loading and flowfield	170
7.1.3	Interaction effects on wing loading	176
7.1.4	Effect of wing lift on propeller loading	178
7.1.5	Effect of angle of attack and sideslip on propeller loading	180
7.2	Wingtip-mounted pusher-propellers on a compound helicopter in hover	181
7.2.1	Temporal and grid convergence	181
7.2.2	Interaction effects on propeller loading and flowfield	183
7.3	Propeller-wingtip interaction at large angle of attack	189
7.3.1	Propeller performance with wing	190
7.3.2	Effect of wing position and flap deflection	193
7.3.3	Effect of pylon and main rotor flow	194
7.4	Conclusions.	196

8	Conclusions and recommendations	199
8.1	Conclusions	199
8.1.1	Propeller modelling methods	200
8.1.2	Effects of interaction on propeller loading	202
8.1.3	Effects on studied objects in interaction with a propeller	206
8.2	Recommendations	208
	References	211
A	Simple wake ingestion model	231
A.1	Governing equations	231
A.2	Control volume analysis around body.	232
A.3	Control volume analysis around wake propeller	234
A.4	Observations	237
A.4.1	Constant properties over streamtube cross sections	237
A.4.2	Thrust–drag balance	237
A.4.3	Propeller power evaluation	238
	Acknowledgements	239
	Curriculum vitae	241
	List of publications	243

NOMENCLATURE

ABBREVIATIONS

AD	=	Actuator-disk
AL	=	Actuator-line
BEM	=	Blade element momentum
BLI	=	Boundary layer ingestion
CFD	=	Computational fluid dynamics
CG	=	Center of gravity
CROR	=	Contra-rotating open-rotor
eVTOL	=	Electrical vertical take-off and landing
FB	=	Full-blade
F/T	=	Force/torque
GCI	=	Grid convergence index
ISO	=	Isolated
LLF	=	Large low-speed facility
LTT	=	Low-turbulence tunnel
MRF	=	Multiple reference frames
NWFR	=	Nacelle-wing-fuselage-main rotor
OAA	=	One-after-another
OJF	=	Open jet facility
PIV	=	particle-image velocimetry
PN	=	Propeller-nacelle
PNP	=	Propeller-nacelle-pylon
PNR	=	Propeller-nacelle-main rotor
PNW	=	Propeller-nacelle-wing
PNWF	=	Propeller-nacelle-wing-fuselage
PNWFR	=	Propeller-nacelle-wing-fuselage-main rotor
PNWP	=	Propeller-nacelle-wing-pylon
PROPR	=	PRopeller analysis and OPTimisation Routine
RANS	=	Reynolds-averaged Navier-Stokes
SA	=	Spalart-Allmaras
SBP	=	Single blade passage
SBS	=	Side-by-side
SRV(s)	=	Swirl-recovery-vane(s)
UAM	=	Urban air mobility
UAV	=	Unmanned aerial vehicle

SYMBOLS

A	=	control surface, m^2
a	=	Speed of sound, ms^{-1}
B	=	Number of propeller blades
b	=	Span, m
C_D	=	Drag coefficient
C_{F_y}	=	$F_y / (\rho_\infty n^2 D_p^4)$ y-force coefficient
C_{F_z}	=	$F_z / (\rho_\infty n^2 D_p^4)$ z-force coefficient
C_f	=	τ_w / q_∞ skin-friction coefficient
C_L	=	Lift coefficient
C_{M_y}	=	$M_y / (\rho_\infty n^2 D_p^5)$ y-moment coefficient
C_{M_z}	=	$M_z / (\rho_\infty n^2 D_p^5)$ z-moment coefficient
C_P	=	$P / (\rho_\infty n^3 D_p^5)$ power coefficient
C_p	=	$(p - p_\infty) / q_\infty$ pressure coefficient ; heat capacity at constant pressure, $Jkg^{-1}K^{-1}$
$C_{p,r}$	=	$(p - p_\infty) / q_{\infty,r}$ pressure coefficient in rotating reference frame
C_{p_t}	=	$(p_t - p_\infty) / q_\infty$ total pressure coefficient
C_Q	=	$Q / (\rho_\infty n^2 D_p^5)$ torque coefficient
C_T	=	$T / (\rho_\infty n^2 D_p^4)$ thrust coefficient
C_{T_r}	=	$8/\pi^3 C_T$ helicopter rotor thrust coefficient
c	=	Chord, m
c_d	=	Section drag coefficient
$c_{F_y}(r)$	=	$(\frac{1}{2}BF'_y) / (\rho_\infty n^2 D_p^3)$ y-force coefficient distribution
$c_{F_z}(r)$	=	$(\frac{1}{2}BF'_z) / (\rho_\infty n^2 D_p^3)$ z-force coefficient distribution
c_l	=	Section lift coefficient
c'_n	=	$n' / (q_\infty c)$ unsteady section normal-force coefficient
$c_P(r)$	=	$(\frac{1}{2}BP') / (\rho_\infty n^3 D_p^4)$ power coefficient distribution
$c'_P(r)$	=	$P' / (\rho_\infty n^3 D_p^4)$ alternative power coefficient distribution
$c_T(r)$	=	$(\frac{1}{2}BT') / (\rho_\infty n^2 D_p^3)$ thrust coefficient distribution
$c'_T(r)$	=	$T' / (\rho_\infty n^2 D_p^3)$ alternative thrust coefficient distribution
$c_{T_{SRV}}(r)$	=	$T'_{SRV} / (\rho_\infty n^2 D_p^3)$ SRV thrust coefficient distribution
D	=	Diameter, m ; wing drag, N
d	=	Distance, m
d_x	=	Axial distance between propellers, m
d_y	=	Lateral distance between propellers, m
E_ϕ	=	Richardson extrapolation uncertainty
e	=	Internal energy per unit mass, Jkg^{-1}
\vec{F}	=	Momentum vector per unit of time and volume, $kgm^{-2}s^{-2}$
F	=	Force, N
F'	=	Force distribution, Nm^{-1}

f_i	= Force vector per unit mass in tensor notation, Nkg^{-1}
h	= Altitude, m
h_i	= Average cell size of grid i , m
J	= $V_\infty / (nD_p)$ advance ratio
k	= Turbulence kinetic energy, Jkg^{-1}
L	= Wing lift, N ; length, m
M	= Moment, Nm ; Mach number
M_{tip}	= Helical tip Mach number based on n and V_∞
M_w	= Molecular weight, kgkmol^{-1}
\dot{m}	= Mass flow, kgs^{-1}
\vec{n}	= Unit normal vector
n	= Propeller rotational speed, s^{-1}
n'	= Unsteady sectional normal force, Nm^{-1}
n_i	= Unit vector in tensor notation
P	= Shaft power, W
P'	= Power distribution, Wm^{-1}
P_C	= $P / (\rho_\infty V_\infty^3 D_p^2)$ power coefficient based on V_∞
p	= Static pressure, Pa ; observed order of accuracy
p_t	= Total pressure, Pa
Q	= Torque, Nm
\vec{Q}	= Torque vector, Nm
Q'	= Torque distribution, Nm m^{-1}
\dot{Q}	= Heat loss rate due to friction, W
q	= Dynamic pressure, Pa ; rate of heat addition per unit mass, $\text{Js}^{-1}\text{kg}^{-1}$
q_r	= $\frac{1}{2}\rho((2\pi nr)^2 + V^2)$ dynamic pressure in rotating reference frame, Pa
R	= Radius, m ; universal gas constant, $\text{Jkmol}^{-1}\text{K}^{-1}$
Re	= Reynolds number
r	= Radial coordinate, m
S	= Energy per unit of time and volume, $\text{Jm}^{-3}\text{s}^{-1}$; Sutherland temperature, K ; area, m^2
s	= Semi-span, m
T	= Thrust, N ; static temperature K
\vec{T}	= Thrust vector, N
T'	= Thrust distribution, Nm^{-1}
T_C	= $T / (\rho_\infty V_\infty^2 D_p^2)$ thrust coefficient based on V_∞
T_t	= Total temperature K
t	= Thickness, m
U_s	= Standard deviation of a fit based on observed order of convergence
U_ϕ	= Estimated discretization uncertainty
u	= x -velocity component, ms^{-1}
u_i	= Velocity vector in tensor notation, ms^{-1}
V	= Velocity, ms^{-1} ; control volume, m^3
\vec{V}	= Velocity vector, ms^{-1}
V_d	= $\sqrt{2T_{\text{mr}} / (\rho_\infty \pi R_{\text{mr}}^2)}$ downwash farfield velocity, ms^{-1}
v	= y -velocity component, ms^{-1}

\dot{W}	=	Work per unit of time, W
w	=	z -velocity component, ms^{-1}
x	=	Axial coordinate, m
x'	=	Coordinate along chord of wing and flap, m
y	=	Lateral coordinate, m
y^+	=	Dimensionless wall distance
z	=	Vertical coordinate, m
α	=	Angle of attack, deg
β	=	Blade pitch angle, deg ; sideslip angle, deg
γ	=	Specific heat ratio
$\Delta \dot{E}_k$	=	Change in kinetic energy flow, W
Δ_M	=	Maximum difference between solutions on different grids
Δx_c	=	Average cell size, m
δ_f	=	Flap deflection, deg
δ_{RE}	=	Difference between estimated exact solution and solution on chosen grid
δ_w	=	Boundary correction factor
ϵ	=	Regularization constant
η	=	Regularization function
η_p	=	$(TV_\infty \cos \alpha_p \cos \beta_p) / P$ propeller propulsive efficiency where β is the sideslip angle
η_{eh}	=	$P / (1/2\rho_\infty\pi R_p^2 V_\infty^3)$ energy-harvesting efficiency
ε	=	Regularization function constant
θ	=	Azimuthal coordinate, deg ; swirl angle, deg
μ	=	Dynamic viscosity, $\text{kgm}^{-1}\text{s}^{-1}$; V_∞ / V_{tip} alternate advance ratio
ρ	=	Density, kgm^{-3}
τ_w	=	Wall shear stress, Pa
ϕ_i	=	Numerical solution obtained using grid i
φ	=	Blade phase angle, deg
ω	=	Vorticity, s^{-1} ; turbulence dissipation rate, $\text{Jkg}^{-1}\text{s}^{-1}$

SYMBOL SUBSCRIPTS

0	=	At static condition ($V_\infty = 0$ m/s) ; extrapolated
$0.7R_p$	=	At blade section $r/R_p = 0.7$
$0.75R_p$	=	At blade section $r/R_p = 0.75$
a	=	Axial
b	=	Blade ; body
bl	=	Boundary layer
c	=	Chord ; corrected
e	=	Effective
front	=	Front propeller
h	=	Hub ; horizontal
hover	=	Hover
ISO	=	Isolated configuration
int	=	Integrated
k	=	Kink

LE	=	Leading edge
max	=	Maximum
min	=	Minimum
mr	=	Main rotor
n	=	Normal
nac	=	Nacelle
OAA	=	One-after-another configuration
PN	=	Propeller-nacelle configuration
PNP	=	Propeller-nacelle-pylon configuration
PNWP	=	Propeller-nacelle-wing-pylon configuration
p	=	Propeller
r	=	Root
ref	=	Reference
rot	=	Rotational
SBS	=	Side-by-side configuration
SRV	=	Swirl-recovery-vanes
s	=	Slipstream
sel	=	Selected
t	=	Tangential
tip	=	Tip
tot	=	Total
ts	=	Test section
x	=	x -direction
y	=	y -direction
z	=	z -direction
w	=	Wing ; wake
θ	=	Azimuthal
∞	=	Freestream

SYMBOL SUPERSCRIPTS

$0.65R_p$	=	At blade section $r/R_p = 0.65$
dwns	=	Downstream
ups	=	Upstream
*	=	Based on theoretical order of convergence

1

INTRODUCTION

The title of this dissertation contains three distinctive elements: *aerodynamics*, *propellers* and *interaction dominated flowfields*. The main object of study are *propellers* and the focus is their *aerodynamics*. The purpose of a propeller is to deliver a force by imposing a change in the momentum of the air in the direction of the rotation axis. This is accomplished by increasing the velocity of the air. As a consequence, axial kinetic energy is left behind in the air. This is one of the sources of efficiency losses. A propeller achieves a change in momentum by rotating a set of blades at the correct rotational speed for a given blade pitch angle. However, this generally does not only result in a force in axial direction on each blade but also in a force against the rotation direction, requiring a torque on the propeller shaft. Therefore, also an angular momentum change is imposed on the air with its associated rotational kinetic energy. This is a second source of efficiency loss.

As the propeller is dependent on the flowfield it encounters, any disturbance in that inflow results in changes in loading on the propeller. This can result in propulsive efficiency changes and affect stability through generation of in-plane forces and out-of-plane moments. The loading changes can also impact noise through loading fluctuations and cause vibrations in the structure leading to fatigue.

The remaining part of the title, *interaction dominated flowfields*, refers to situations where the inflow is disturbed by such an amount that the disturbance is a dominating factor in the propeller loading. Take for example the airplane depicted in Fig. 1.1, the Douglas XB-42 Mixmaster. Developed and flight tested near the end of the Second World War, it used two contra-rotating propellers mounted at the aft fuselage in pusher configuration [1]. For the front propeller disturbances in its inflow can be expected from the fuselage, the roots of the wings and the tailplanes, changing the inflow to this propeller by such an amount that interaction dominates its loading. For the rear propeller an additional disturbance from the front propeller is present. A more modern variant of this layout can be found on the LearAvia Lear Fan 2100 in Fig 1.2, developed and flight tested in the 1970s and early 1980s as a response to the rising fuel prices [2]. Unfortunately, both airplanes never made it past the flight test phase, the former because of the emergence of the jet engine, and the latter among others because of issues with the gearbox

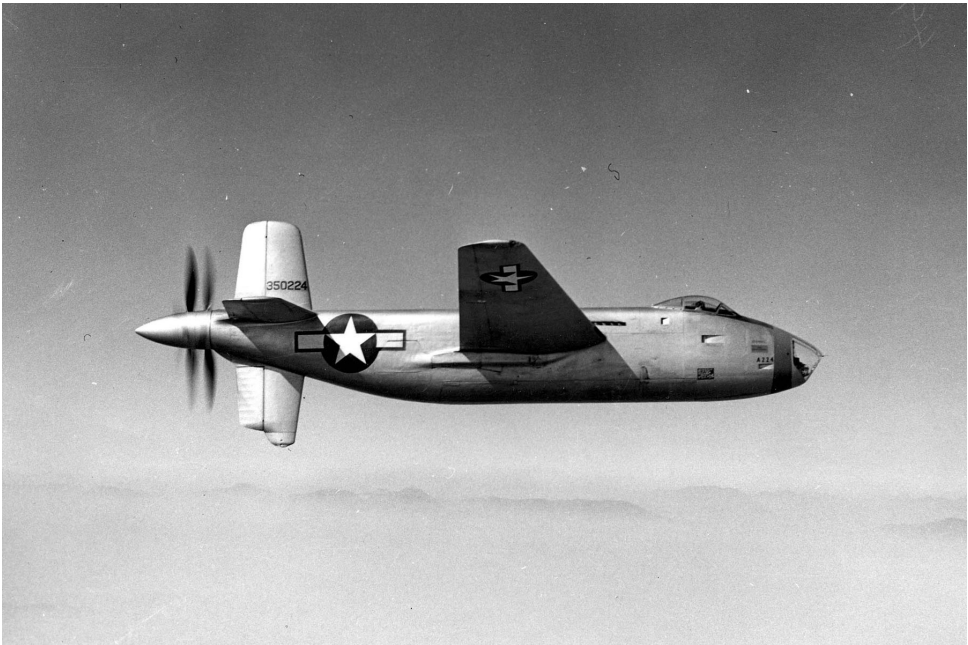


Figure 1.1: Douglas XB-42 Mixmaster, featuring two contra-rotating propellers in pusher configuration at the aft fuselage. Credits: U.S. Army.



Figure 1.2: LearAvia Lear Fan 2100, following the principle of the XB-42 with a single propeller at the aft fuselage. © 2019 The Museum of Flight Foundation. All rights reserved.

and related refusal of a Certificate of Airworthiness by the FAA. Bill Lear's idea was that new technology was required for the business aircraft industry to survive the oil crisis that was happening in the 1970s. This consisted not only of the use of light composite materials and a more laminar flow wing, but also of the novel propulsion layout. Also today's research on propellers is driven by their potential for reduced fuel consumption compared to turbofan propulsion. Not only the high propulsive efficiency of the propeller itself, but also its location on the airframe can enhance the overall efficiency of the aircraft. That was certainly true for the layout chosen for the Lear Fan, as it ingests among others the low momentum boundary layer of the fuselage. Such a boundary layer ingestion propeller is thought to increase propulsive efficiency [3–5], as it reduces the net axial kinetic energy left behind in the air by the propeller and airplane system.

Similar to the XB-42, another airplane featuring contra-rotating propellers in pusher configuration was the Northrop XB-35 [6] that is shown in Fig. 1.3. More parallels can be drawn with the XB-42, as it was also developed during the Second World War and had to give way to the jet engine. Following the principles of reducing wetted area to minimize parasitic drag and converting any drag producing surface into also lift producing, this flying wing was supposed to fly faster or farther than conventional layouts by 25% [7]. It also benefited from the use of contra-rotating propellers, as the rear propeller in such a layout can profit from the rotational kinetic energy left by the front propeller, resulting in gains in propulsive efficiency in the order of 8% [8]. However, governor and gearbox problems had the original counter-rotating propellers replaced by single-rotation propellers of larger diameter as a temporary measure [7]. An alternative to a second rotating propeller would have been a stationary row of vanes called swirl recovery vanes, which have shown lower gains in efficiency at reduced complexity [9]. Later, the propeller driven variants were converted into jet powered versions. These required additional vertical fins, as the propellers provided part of the directional stability [7].

An airplane that has similarities to the XB-35 is the Beech Starship. This airplane, depicted in Fig. 1.4, was one of the ideas born from the development of the Lear Fan [2] and the canard revolution initiated by Burt Rutan [10]. An 85% scale proof of concept was built with a carbon composite structure by Scaled Composites [11]. The propeller location was chosen to reduce cabin noise, and the tail cone was eliminated with the use of the canard to reduce wetted area to minimize parasitic drag [10]. The airplane did not become successful as it was too expensive and too slow compared to similar jets. Due to their pusher configuration, the propellers on the XB-42 and Starship operate in the downwash of the wing and ingest the wing wake. Furthermore, the exhaust jet impinges on the propellers. As a result of this flowfield, the propeller blades experience a sinusoidal variation in loading during their revolution, combined with sudden strong local increases and decreases in loading [12]. This also results in a noise penalty. Although noise is an important factor to consider for propellers in interaction dominated flowfields, only the aerodynamic aspects are treated in this dissertation.

While the main focus of this dissertation are propellers that operate in a flowfield dominated by interaction, the reverse situation is also treated. Since a propeller changes the flowfield by addition of momentum, it can dominate the loading on objects, especially if they are in its slipstream. One can utilize this fact, and for instance improve the



Figure 1.3: Northrop XB-35 flying wing, propelled by four wing-mounted contra-rotating propellers in pusher configuration. Credits: U.S. Air Force.



Figure 1.4: One of the few still flying Beech Starship, featuring two wing-mounted propellers in pusher configuration. © Chad Slattery. All Rights Reserved.



Figure 1.5: Vought V-173 in a wind-tunnel, a flying wing with wingtip-mounted tractor-propellers. Credits: NASA.



Figure 1.6: NASA X-57 Maxwell render, using wingtip-mounted tractor-propellers to improve cruise performance and distributed electric propulsion propellers to blow the wing during take-off and landing. Credits: NASA Langley/Advanced Concepts Lab, AMA, Inc.

propulsive efficiency of the system. A good example of this are propellers mounted at the wingtip in tractor configuration. One of the most peculiar airplanes that has ever flown is the Vought V-173, shown in Fig. 1.5 inside a wind-tunnel. Similar to the XB-42 and XB-35, it was developed during the Second World War and the project was cancelled due to the emergence of the jet engine [13]. This flying wing type aircraft, often called the flying pancake, used two counter-rotating propellers blowing the wing. This additional airspeed for the wing resulted in excellent take-off performance, or with a 25-knot headwind even in a zero-roll take-off [13], making it very suitable for operation from aircraft carriers. But not only that improved its performance: As the propellers also impose an angular momentum change and the rotation direction is such that it locally increases the angle of attack for the wing and rotates against the wingtip vortex, an induced drag reduction for the wing can be expected [14–16]. With this principle in mind, NASA is developing the X-57 Maxwell technology demonstrator with wingtip-mounted tractor-propellers, of which a render is shown in Fig. 1.6. These propellers are thought to reduce induced drag by 7.5% during cruise [17]. For this wing, a second interaction is present from an array of distributed electric propulsion propellers, blowing the wing only during take-off and landing. The idea is that wing area can be reduced significantly by this system, which improves cruise efficiency through an improved wing lift-over-drag ratio. Next to the X-57, there are many more recent airplane concepts that utilize (hybrid-) electric propulsion to distribute propellers and enhance aero-propulsive efficiency, e.g. Refs. [18–23]. The current and future development of these airplanes requires a thorough understanding of propellers in interaction.

Albeit from a different source, wingtip-mounted tractor-propellers can experience significant interaction effects. A picture of the Fairey Gyrodyne is shown in Fig. 1.7, featuring two wing halves mounted to the fuselage with no tail rotor and with one wingtip-mounted tractor-propeller on the starboard side [24]. This gyrodyne acted as a helicopter during take-off and hover and possibly as an autogyro in forward flight [25]. The propeller was used for forward propulsion and counter-torque. Compared to the counter-torque device of a conventional helicopter, the tail rotor, this propeller differed considerably in blade design: It incorporated blade twist, opposed to helicopter tail rotors which generally do not have twist [26]. The Fairey Gyrodyne was quite successful as it broke the World helicopter speed record at that time with an airspeed of 108 kts. Coming back to the topic of the dissertation, one can imagine that a significant interaction effect is present for the propeller from the main rotor slipstream, especially in hover, when the propeller is fully immersed in the accelerated air of the main rotor slipstream.

The gyrodyne is very similar to a compound helicopter. A compound helicopter is a helicopter where the function of the main rotor of providing lift and/or thrust is supported by different means. The goal is to expand the flight envelope, especially improve the high speed capability of the helicopter while maintaining a helicopters efficient hover advantage over fixed wing aircraft. There is a growing need for aircraft with vertical take-off and landing capability that can go fast and far [27]. While helicopters are excellent for vertical take-off and landing, they only have a limited maximum speed: The asymmetric flow condition of the main rotor at high speed causes compressibility effects on the advancing blade side and stall on the retreating blade side of the main rotor that limit its lifting and propulsive capability [28, 29]. A compound helicopter overcomes the



Figure 1.7: Fairey Gyrodyne, utilizing a single wingtip-mounted tractor-propeller to counter the main rotor torque and provide thrust. Credits: Ray Watkins Collection.



Figure 1.8: Render of the Airbus RACER compound helicopter, featuring a box-wing design for additional lift with two wingtip-mounted pusher-propellers or lateral rotors for thrust and counter torque. © Production Autrement Dit.

main rotor limitation at high speed by auxiliary lift and/or thrust devices [28, 30]. An example of such a compound helicopter concept is the Airbus RACER (Rapid And Cost-Effective Rotorcraft) [31, 32], optimized for a high cruise speed of 220 kts. A render of this helicopter is shown in Fig. 1.8. Supporting the main rotor, auxiliary lift in the cruise condition is provided by a box-wing, while wingtip-mounted lateral rotors in pusher configuration generate a major portion of the required thrust. Furthermore, these lateral rotors or propellers provide counter-torque in the hover condition to balance the main rotor torque, similar to the gyrodyne. Compared to a single wing design, the box-wing design reduces the overall surface affected by the downwash of the main rotor in hover, while delivering the required lift in cruise. It can also improve lift-over-drag ratio compared to a planar wing design [33]. As the propellers are located under the main rotor, a strong interaction effect can be expected from the main rotor slipstream in hover, like for the Fairey Gyrodyne. Furthermore, since the propellers are in pusher configuration at the wingtip, in cruise a swirling vortex inflow from the wing can be expected, improving the propeller efficiency as the propellers rotate against the wingtip vortex direction [15, 34–36]. Similar to the Fairey Gyrodyne, this helicopters predecessor, the Eurocopter X³, set an unofficial speed record at 255kts in level flight [37], which shows the promise of this technology if speed is the goal.

The promise of vertical flight and efficient forward flight has in recent years gained a lot of traction with the development of more unconventional aircraft. Urban air mobility (UAM) is an emerging market that is driven by recent developments of a range of startup companies, automotive companies, mobility providers, and aerospace industry giants [38–40]. Most UAM concepts rely on a fleet of (hybrid-)electric vertical take-off and landing (eVTOL) vehicles, operating as on demand taxis over a short range [41, 42]. These eVTOL vehicles are characterized by non-traditional vehicle layouts with distributed propellers or rotors with low disk loading. They mainly differ from traditional aircraft by their new propulsion architectures, which are driven by electrification of propulsion [38, 43, 44] and the requirement of vertical take-off and landing. According to Kasliwal et al. [45], distributed electric propulsion is the key enabler of efficiency enhancement for eVTOL vehicles because it gives the flexibility to gain benefit from aero-propulsive interaction compared to conventional layouts. These efficiency benefits are needed to reach the required range with the current or near future battery technology. Two prime examples of eVTOL aircraft are given in Figs 1.9 and 1.10. The Cora in Fig. 1.9 is a prototype aircraft designed for two passengers, using 12 propellers for lift during take-off and a pusher-propeller at the aft fuselage for thrust in forward flight [46]. One can expect that these propellers used for lift experience interaction effects not only with the wing, but in certain flight situations also with the other propellers: As this aircraft transitions from vertical flight to forward flight, the slipstream of the propellers mounted in front of the wings will move downstream towards the row of propellers behind the wing. Furthermore, the pusher-propeller experiences similar interactions as discussed for the XB-42 and Lear Fan.

The Airbus A³ Vahana in Fig. 1.10 is a prototype aircraft designed for one person, using tiltwings with 8 propellers for lift during vertical take-off and thrust in forward flight [47]. Apart from the clear interaction of the propeller slipstreams with the downstream wing and tailplane, in forward flight the slipstream of the front propellers may impinge



Figure 1.9: Test flight of the Cora eVTOL concept, equipped with 12 propellers for lift during vertical take-off and a pusher-propeller at the aft fuselage for thrust in forward flight. Photo courtesy of Cora Aero. © 2018 Richard Lord.



Figure 1.10: Front view of the Airbus A³ Vahana eVTOL vehicle, using tiltwings with 8 propellers for lift during vertical take-off and thrust in forward flight. © 2019 A³ by Airbus. All rights reserved.

in certain flight situations on the rear propellers too. Apart from these two concepts, many more eVTOL vehicles have been proposed, e.g. Refs. [42, 44, 48], of which most very likely experience some form of aerodynamic interaction between propellers. Propellers on such vehicles are clearly operating in a flowfield dominated by interaction, and therefore are a perfect example for the topic of this dissertation.

1.1. DISSERTATION OBJECTIVE

The dissertation topic was partially motivated by the Clean Sky 2 PROPTER project (Support to aerodynamic analysis and design of propellers of a compound helicopter), in which the author took part to investigate the aerodynamic interactions and their consequence on the performance of the propellers of the Airbus RACER as depicted in Fig. 1.8. In the review of lessons learned from the compound helicopter studies done by NASA and the US Army by Yeo [30], the need is stressed for high-fidelity computational fluid dynamics analyses to capture the various aerodynamic interactions which are occurring for compound helicopters. According to Yeo [30], these aerodynamic characteristics could then be used for calibration of lower order models, and layout and shape refinement. This need was addressed for this specific compound helicopter.

The second motivation for this work is that interaction of propellers should not only be regarded as a complicating factor, but can result in efficiency benefits. According to Kasliwal et al. [45], for eVTOL vehicles aero-propulsive interaction is the key enabler of efficiency enhancement compared to conventional layouts. However, Johnson et al. [42] stresses that performance issues with interaction between propellers is one of the important research areas for such vehicles. Although the future of urban air mobility and eVTOL vehicles may not be as bright as sketched by some, it is a key driver of technology development also required to improve efficiency of more conventional (hybrid-) electric airplanes. Within a world of depleting resources and global warming, such efficiency improvement is necessary to sustain aviation. Motivated by all of this, the following objective for the dissertation was established:

The dissertation objective is to get a fundamental understanding of the role of aerodynamic interaction on the loading and performance of primarily the propeller and secondarily the interacting object(s) in typical configurations where interaction dominates the flowfield.

In Chapter 2 the problem of propellers in interaction dominated flowfields is more thoroughly reviewed by means of a literature survey for the different categories of configurations that introduce an array of different interactions. Specific research questions addressed in this dissertation are presented in that chapter. The configurations that fall within the scope are introduced in the next section.

1.2. DISSERTATION SCOPE AND METHODS

The first factor determining the scope is the configuration. A number of typical configurations have been discussed in the introduction where interaction dominates the flowfield. Only a few fall within the scope of the dissertation. The focus of this work is on the following cases, which are more thoroughly introduced in Chapter 2:

- Wingtip-mounted propellers in tractor configuration (Section 2.3),
- wingtip-mounted propellers in pusher configuration (Section 2.3),
- propeller interaction with swirl-recovery-vanes (Section 2.4),
- propellers in configurations applicable to eVTOL vehicles (Section 2.4), and
- propellers on a compound helicopter (Section 2.5).

On these configurations a variety of propeller interactions occur. Investigated phenomena for the propeller include decreased and increased dynamic pressure from momentum sources and sinks, potential effects resulting in dynamic pressure and angle of attack changes, rotational flowfields and impinging vortices.

A variety of methods are used to arrive at results. A combined numerical and experimental approach was chosen. On the one hand, high-fidelity computational fluid dynamics (CFD) simulations allow investigation of the transient loading on and the complete flowfield around the complex geometries involved. Methods have been developed as part of the dissertation to reduce the cost of these CFD simulations but retain the interaction phenomena. This is especially useful for design or performance sweeps. On the other hand, experimental investigation in a wind tunnel allows validation of the taken numerical approaches. Furthermore, once a setup is established, experiments allow for very rapid parametric sweeps to gain improved insight in the dependency of the interaction results on the operating condition and geometric variables of the configuration. The methods are more thoroughly discussed in Chapter 3, along with the specifics of the numerical and experimental configurations.

In terms of scope, it also must be made clear what is meant with propeller in this dissertation. Different names are used in literature for very similar devices, e.g. propeller [49], rotor [50], airscrew [51], fan [46], proprotor [52] and propfan [53]. According to the Merriam Webster English dictionary a propeller or less commonly propellor is [54]:

a device that consists of a central hub with radiating blades placed and twisted so that each forms part of a helical surface and that is used to propel a vehicle (such as a ship or airplane).

The definition in the Oxford English dictionary is very similar but slightly less specific [55]:

a mechanical device for propelling a boat or aircraft, consisting of a revolving shaft with two or more broad, angled blades attached to it.

The seemingly more general term rotor is defined by Merriam Webster as [56]:

an assembly of rotating blades that supplies lift or stability for a rotorcraft.

And in the Oxford dictionary it is defined more specifically as [57]:

a hub with a number of radiating aerofoils that is rotated in an approximately horizontal plane to provide the lift for a helicopter or other rotary wing aircraft.

Airscrew is defined by both dictionaries as a synonym to propeller in predominantly British English [58, 59]. While the Oxford dictionary has no definition for fan applied to aircraft [60], Merriam Webster defines it as slang for an airplane propeller [61]. Proprotor is not defined in either dictionary. Propfan is only defined in the Oxford dictionary as an informal word meaning [62]:

an airscrew having broad blades swept back from a direction perpendicular to the rotation axis.

By Glauert [51] propeller was defined as an airscrew used for propulsion and as such not fully used as a synonym. According to Godston and Reynolds [53], the propfan is a high speed swept propeller, named by Hamilton Standard, in agreement with the Oxford dictionary definition. The propfan is lightly loaded compared to a turbofan and highly loaded compared to a propeller in terms of shaft power per disk area according to Strack et al. [8]. In line with the definition of either dictionary, rotor is often used in literature on rotorcraft or helicopters. This includes the tail rotor which does not provide lift and therefore does not follow the Oxford dictionary definition. The proprotor seems to be used when a clear distinction between an airplane and helicopter cannot be made and the propulsor is used for lift and thrust like in Droandi et al. [52] for tiltrotors.

The previous paragraphs haven't fully clarified the distinction between the different terms. Another distinction that can be made is whether or not articulation is present, which helicopter rotors generally have in some form and propellers on airplanes do not have. The freedom for a blade to move does result in differences in aerodynamic loading and dynamics of the system. Since clear distinctions in terms of function and use are lacking, in this dissertation the term propeller is exclusively used for non-articulated variants. The function of a propeller includes thrust, lift, the combination of thrust and lift or even, in an off-design condition, power generation. Rotor is then used as a more general term that includes articulated variants. When literature is referenced, the term used in the specific reference will be adopted.

1.3. DISSERTATION OUTLINE

The dissertation is divided in eight chapters. A flow diagram of the chapters is depicted in Fig. 1.11. After this introduction, in Chapter 2 interaction dominated flowfields are analysed and classified in terms of objects in interaction and flowfield phenomena. In that chapter, also the scope of the dissertation is specifically highlighted for each interaction type and specific research questions are posed.

In Chapter 3 the analysis methods are described including specification of the models. This is split in Section 3.1 on the experimental approach and Section 3.2 on the numerical approach.

Chapter 4 discusses the aerodynamics of isolated propellers. To understand propellers in interaction, it is vital to first establish their isolated aerodynamics. A key part of this are the effects of operating condition, in terms of rotational speed, freestream air-speed and angle of attack. Important for this topic is that the operating condition should cover the extremes, especially in terms of angle of attack. This data is used as reference data for the next chapters.

Chapters 5 through 7 cover the results on aerodynamic interaction, specified by object in interaction with the propeller. Interaction with the wingtip in tractor and pusher configuration is treated in Chapter 5 in the light of validation of numerical methods and investigation of interaction effects and propulsive efficiency benefits.

Experimental results on the interaction with another propeller relevant for eVTOL vehicles are presented in Chapter 6, as well as a numerical analysis and validation of propeller–stator interaction for propulsive efficiency enhancement.

A form of combined interaction with main rotor and wingtip found on compound helicopters is treated in Chapter 7, containing numerical work on the Airbus RACER layout in cruise and hover condition. In that chapter furthermore an experimental/numerical analysis of propeller–wingtip interaction is performed with inflow perpendicular to the wing planform to further investigate and validate the interaction effects on a compound helicopter in the hover condition.

The last Chapter 8 forms a synthesis of the interaction effects with a conclusion and presents some recommendations for future work.

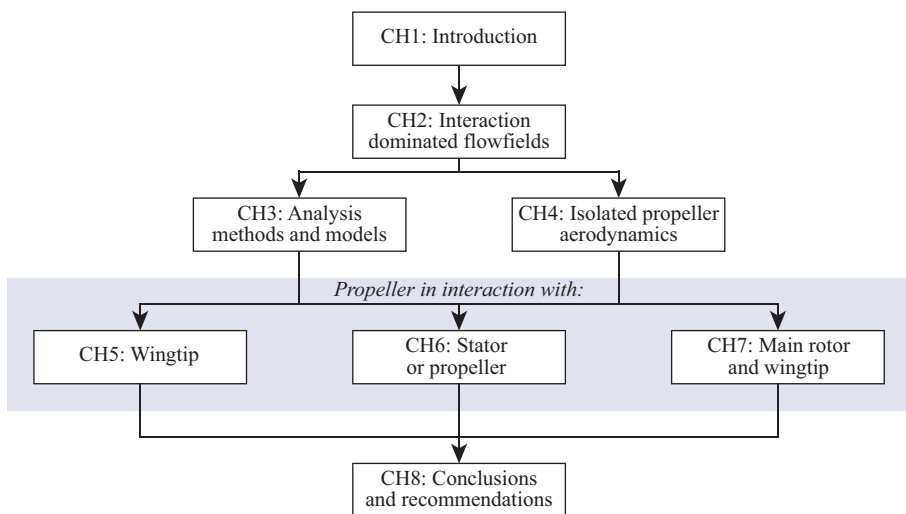


Figure 1.11: Flow diagram of dissertation.

2

INTERACTION DOMINATED FLOWFIELDS

This chapter discusses flowfields that a propeller and its surroundings experience. The focus is on flowfields which are dominated by aerodynamic interaction, in other words, where interaction plays an important role in the aerodynamic loading in comparison to the freestream flow. In order to treat propellers in interaction, first the propeller system without interaction is characterized in Section 2.1.

A way to classify interaction dominated flowfields is through the objects that are interacting. The list of objects that propellers can be in interaction with on aircraft include its nacelle, the fuselage, the wing, a pylon, tailplanes, stators and other rotors or a combination thereof. These interactions are not necessarily strong and so interaction is not necessarily dominating the flowfield. This depends very much on the geometric positioning of the objects with respect to the propeller and the aerodynamic loading on the propeller and objects. The interaction can be dominant for the propeller loading, for the loading on the object(s) that are in interaction with the propeller, or for both. While the focus in this dissertation is on situations where the interaction is dominating propeller loading, it is not limited to that, and also interactions dominating only the loading on the object(s) are discussed.

Another way to classify interaction dominated flowfields is through the flow phenomena that are dominant. Flowfield phenomena relevant for propellers and the object(s) in interaction include:

- A. decreased total pressure from momentum sinks like wakes or boundary layers,
- B. increased total pressure from momentum sources like slipstreams,
- C. changed dynamic pressure or angle of attack from potential effects,
- D. rotational flowfields like the swirl in a slipstream, and
- E. impinging vortices.

Parts of this chapter have been adapted from Refs. [63–71].

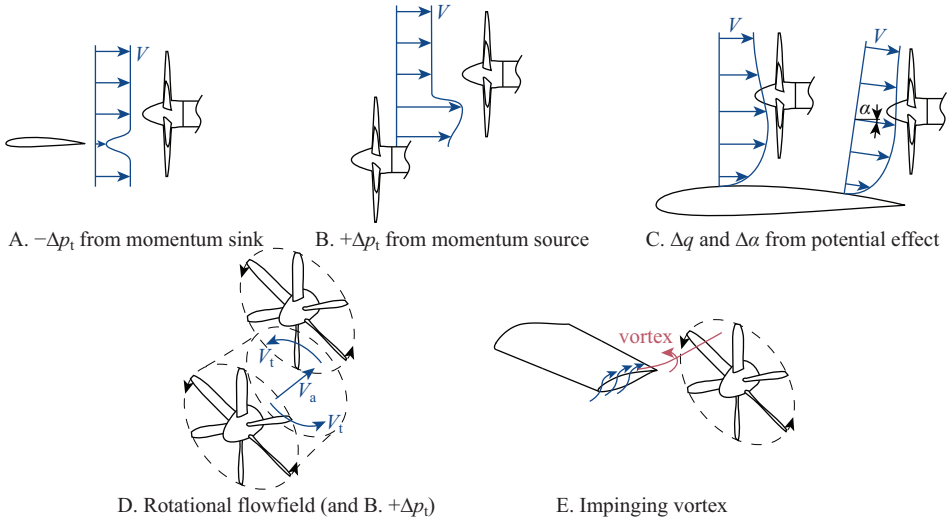


Figure 2.1: Example sketches of the relevant flowfield phenomena.

Examples of these flowfield phenomena are depicted in Fig. 2.1. These phenomena can have localized effects on the propeller blade loading, e.g. a sudden spike in thrust, and/or alter the time-averaged loading. In the next sections, tables are provided with estimates of the flowfield phenomena that play a role and by what amount they affect the averaged (avg) and local (loc) propeller loading. Therefore, an order of magnitude scale is devised as depicted in Table 2.1.

Table 2.1: Color scale depicting order of magnitude effect of flowfield phenomenon on local or averaged propeller loading.

effect on loading	color
< 1%	
1%	
10%	
100%	

A range of topics is covered in this dissertation for which it is thought that the interaction phenomena are dominating aerodynamic loading. The set of topics is of course limited and not complete, but do cover the identified flowfield phenomena. A general overview of propellers in interaction is given in the next sections, specified by the type of object the propeller is in interaction with. The topics of the dissertation are mainly discussed and are highlighted in each section. First, interaction with non-lifting bodies like a nacelle or fuselage is discussed in Section 2.2. In the following Section 2.3, lifting aerodynamic surfaces like wings are treated. Interaction with stators and other rotors are covered in Section 2.4. An example of combined interaction is introduced in Section 2.5 in the light of compound helicopters.

2.1. ISOLATED PROPELLER SYSTEM

To understand the effects of aerodynamic interaction on propeller loading, first the propeller system without interaction is introduced. In Fig. 2.2 a the streamtube and vortex system of a propeller is sketched. A propeller can be seen as a system, that receives a certain flowfield as input, which results in a loading on the propeller blades. As a result of the loading on the blades, a slipstream is formed as output. The slipstream consists of a vortex system with tip- and root-vortices for each blade that induce mainly an axial V_{a_i} and tangential V_{t_i} (or swirl) velocity component. As boundary layers are formed on the propeller blades due to friction, also wakes are present in the slipstream. The root vortices may roll up into a single hub vortex behind the nacelle or in case of a pusher-propeller directly behind the spinner. In Fig. 2.2 b the averaged axial development of the pressure and velocity terms is shown. In terms of pressure, a total pressure p_t rise and static pressure p_s rise is present at the propeller disk. Upstream of the propeller, the static pressure is reduced and downstream it is increased with respect to the freestream. The axial velocity is also already increased upstream of the propeller.

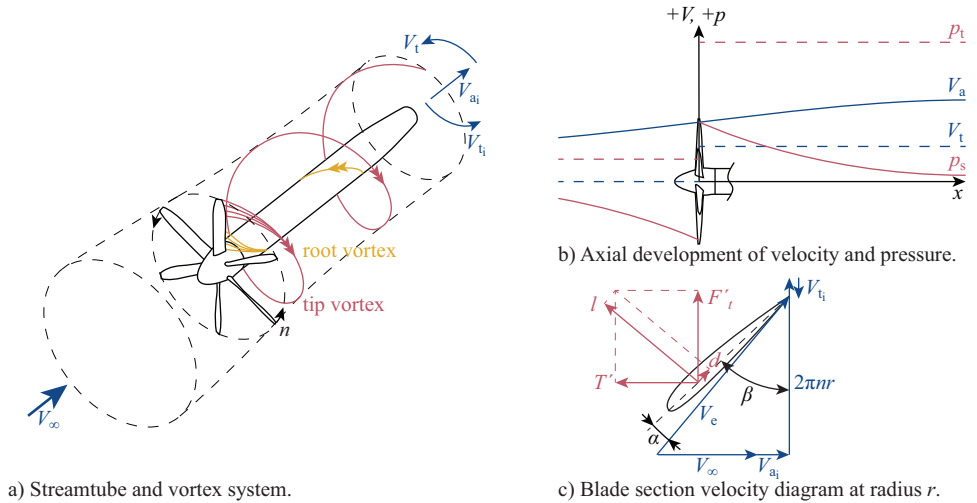


Figure 2.2: The propeller system is sketched, showing the streamtube and vortex system, the changes in axial V_a and tangential V_t velocity, static p_s and total p_t pressure, and the velocity triangle of a blade section.

By observing a single blade section at radius r , see Fig. 2.2 c, the relation between the velocities and the rotational speed becomes clear. Such a section at local blade pitch angle β sees an effective velocity V_e , composed of the freestream velocity V_∞ , the induced velocities and the section rotational speed $2\pi nr$. This results in a section lift l and drag d , which are composed of a section thrust T' and tangential force F'_t . Integrating the section thrust over the blade from the hub radius r_h to the tip or propeller radius R_p and summing the contribution of each blade b of a total of B blades, results in the propeller thrust T :

$$T = \sum_{b=1}^B \left(\int_{r_h}^{R_p} T'(r) dr \right) \quad (2.1)$$

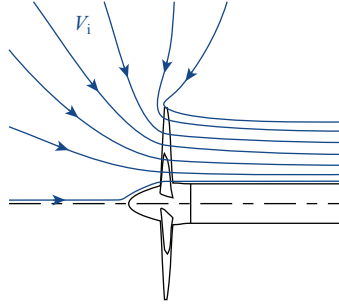


Figure 2.3: Sketch of the induced flowfield by a propeller in static condition.

A similar integration and summation for the section tangential force multiplied by section radius results in the torque Q required on the shaft:

$$Q = \sum_{b=1}^B \left(\int_{r_h}^{R_p} F'_t(r) r \, dr \right) \quad (2.2)$$

This torque corresponds to a required shaft power P of:

$$P = 2\pi nQ \quad (2.3)$$

Two distinctions can be made in terms of propeller operating conditions: Static (or hover if used for lift) and with freestream airspeed. In static condition, the propeller draws air from all of its surroundings, as sketched in Fig. 2.3. The variables determining the propeller performance are limited to blade pitch angle and rotational speed n (apart from density changes of the air). With a freestream airspeed, also upstream of the propeller a confined streamtube is formed as sketched in Fig 2.2 a. The freestream airspeed is a third performance variable, determining together with the rotational speed the propeller advance ratio:

$$J = \frac{V_\infty}{nD_p} \quad (2.4)$$

As density may fluctuate in experiments due to temperature and static pressure changes, the propeller performance results are made dimensionless. Two distinct coefficients are used, made dimensionless with the tip speed or with the freestream airspeed. For the thrust these coefficients are defined as:

$$C_T = \frac{T}{\rho_\infty n^2 D_p^4} \quad (2.5)$$

$$T_C = \frac{T}{\rho_\infty V_\infty^2 D_p^2} = \frac{C_T}{J^2} \quad (2.6)$$

For the shaft power these coefficients are:

$$C_P = \frac{P}{\rho_\infty n^3 D_p^5} \quad (2.7)$$

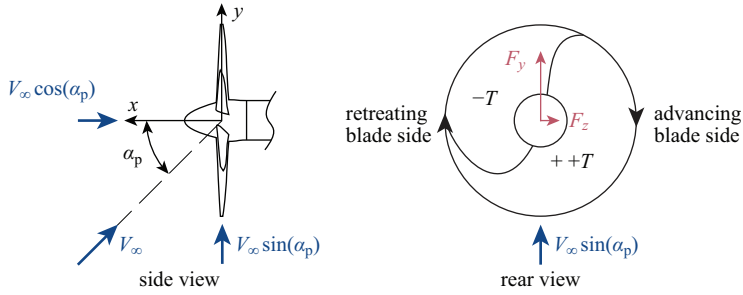


Figure 2.4: Sketch showing the effect of angle of attack on propeller forces, relative to the propeller at $\alpha_p = 0$ deg.

$$P_C = \frac{P}{\rho_\infty V_\infty^3 D_p^2} = \frac{C_P}{J^3} \quad (2.8)$$

These performance coefficients also allow scaling from the model scale to full-scale. However, Reynolds number effects play a role in the propeller performance and change the absolute values, although the performance characteristics remain similar. In this research, in general C_T and C_P are used to express propeller performance. To compare propeller performance at equal thrust when the rotational speed is different, T_C is used to find the equal thrust condition. The same holds for P_C .

The freestream airspeed may form an angle with respect to the propeller rotation axis, the propeller angle of attack α_p . This angle is the fourth variable determining propeller performance. In Fig. 2.4 a sketch is shown to illustrate the effects. The velocity component of the freestream in the propeller plane, $V_\infty \sin(\alpha_p)$, results in an asymmetric condition. Blade sections on the advancing blade side experience an increased angle of attack, increasing thrust. On the retreating blade side, the reverse occurs, reducing thrust. However, this is not exactly the opposite as the effective velocity experienced by the blade sections is reduced as well. With increasing α_p the axial component of the freestream, $V_\infty \cos(\alpha_p)$, reduces. This results in a uniform increase in blade section angle of attack over the propeller disk, increasing thrust. The net result is an increase in thrust with α_p , composed of a slightly reduced thrust on the retreating blade side ($-T$ in Fig. 2.4) and strongly increased thrust on the advancing blade side ($+ + T$ in Fig. 2.4). A discussion on these effects can also be found in Veldhuis [49] and Ortun et al. [72]. Specifically for large angles of attack some research has been done in e.g. Refs. [52, 73, 74].

While C_T and C_P are very relevant for vehicle performance, the in-plane forces and out-of-plane moments can be relevant for vehicle stability. The in-plane force component in the direction of the angle of attack, defined as the y-force by the axis system shown in Fig. 2.4, is zero at $\alpha_p = 0$ deg and increases with increasing α_p . The mechanism behind this is the asymmetry in thrust formed over the propeller disk as was shown in the sketch in Fig. 2.4. The asymmetry in thrust between the advancing and retreating blade side is accompanied by a similar asymmetry in tangential force, resulting in a net y-force F_y .

The in-plane z-force is much smaller than F_y . Due to a phase lag in the blade loading change, part of the retreating blade side experiences increased thrust and part of the

advancing blade side experiences decreased thrust. This is made visible in the sketch in Fig. 2.4 by the curvature in the dividing line between the -T and ++T region. The dominating mechanism behind this phase lag are variations in induced velocity across the propeller disc [72]. The tangential force components in these regions sum up to a net positive z-force. The asymmetry in loading on the propeller disk with angle of attack also results in non-zero out-of-plane moment coefficients M_y and M_z . M_y and M_z correlate to F_y and F_z respectively as they are caused by the same asymmetry in loading on the propeller disk, but resulting from the thrust component instead of tangential force component. For the in-plane forces, the same dimensionless coefficients can be made as for the thrust coefficient in Eq. (2.5). The out-of-plane moment coefficients are defined similarly with the power of the diameter increased by one.

In order to assess interaction effects, it is important to first establish the loading and other characteristics of the isolated propeller with changing operating conditions like freestream airspeed V_∞ , rotational speed n , and propeller angle of attack α_p . Often, interaction effects can be represented by such changes in operating condition. Therefore, Chapter 4 deals with the aerodynamics of the isolated propeller, focussing on performance effects as a function of operating condition. The following research question is addressed there:

Q1a: *What are the aerodynamic characteristics of the propellers used in this research as a function of advance ratio and angle of attack in terms of thrust, power, in-plane forces, out-of-plane moments and resulting slipstream?*

As an accurate prediction of the isolated propeller performance and flowfield is paramount for accurate prediction in interaction, RANS (Reynolds-averaged Navier-Stokes) CFD and lower order models used in this dissertation need to be validated against experimental results. Furthermore, appropriate grids need to be chosen based on uncertainty from grid dependency studies. Therefore, a second research question is posed:

Q1b: *How do the RANS CFD and lower order propeller models compare with experimental results in terms of isolated propeller performance and flowfield and what grid uncertainties are associated with the CFD results?*

2.2. INTERACTION WITH NACELLE OR FUSELAGE

2.2.1. NACELLE

A nacelle, the body to which a propeller is attached and often houses the engine or motor, is an almost essential part of the propeller system. Nacelles come in different shapes. For a tractor-propeller, the effect which a nacelle can have on the propeller system can be significant. As was found by Samuelsson [75], the distribution of velocities and pressure within the slipstream are influenced strongly by the nacelle shape. Rapid variations in its shape close to the propeller disk can also result in changes in inflow to the propeller. Depending on the circumferential non-uniformity, this could lead to time variations in blade forces and moments. These are mainly potential flow effects resulting at zero incidence angle in axial velocity differences. In Fig. 2.5 a such a situation is sketched where part of the propeller experiences reduced axial velocity. At larger angle of attack, the loading on the nacelle may induce a change in angle of attack for the propeller. That

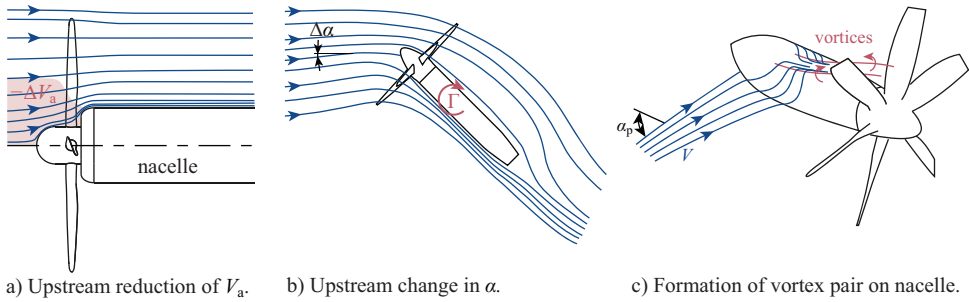


Figure 2.5: Sketch showing effects of nacelle on propeller inflow.

situation is sketched in Fig. 2.5 b. Since the nacelle is fully submerged in the slipstream, the propeller dominates the forces on the nacelle.

For a pusher-propeller, the nacelle can be of somewhat larger influence to the inflow of the propeller, not only through its potential flowfield but also through the boundary layer formed on the nacelle and ingested by the propeller. Only the root sections experience this low momentum flow, which are generally lightly loaded and thus this boundary layer effect is likely small. In a realistic application, exhausts are often present in the nacelle, from which high momentum flow may impinge on the propeller like in Yin et al. [12]. At very large angle of attack, a pair of vortices can form on the nacelle which are then ingested by the propeller as sketched in Fig. 2.5 c. As a nacelle is almost always present, its interaction effects are inherently present in the results of this dissertation. However, no detailed study of the nacelle effects is presented. The flowfield phenomena relevant for the propeller interacting with a nacelle are estimated in terms of importance in Table 2.2.

2.2.2. FUSELAGE

For small airplanes, propellers are often mounted at the front of the fuselage. This layout provides an almost undisturbed flowfield for the propeller, while the fuselage is fully submerged in the propeller slipstream. The forces on the fuselage, mainly drag, are heavily influenced by this interaction. Furthermore, the root of the wings and tailplanes see the accelerated flow in the slipstream. Considering the extensive presence of this layout on airplanes, this interaction type is supposedly well known. The experimental work on the influence of nacelle shapes from Samuelsson [75] may also be applicable for this interaction. The effects are likely very similar to the effects of the nacelle, but amplified as a fuselage is significantly larger than a nacelle. The flowfield phenomena relevant for the propeller interacting with a fuselage are also estimated in terms of importance in Table 2.2.

More interestingly from a propeller point of view is the reverse situation, where a propeller is mounted at the rear of the fuselage, ingesting the boundary layer of the fuselage as depicted in Fig. 2.7. Propeller boundary layer ingestion or more generally wake ingestion can result in a power benefit as has been shown theoretically [3, 76–79] and experimentally [4, 5, 80]. A simple analysis of the continuity, momentum and energy

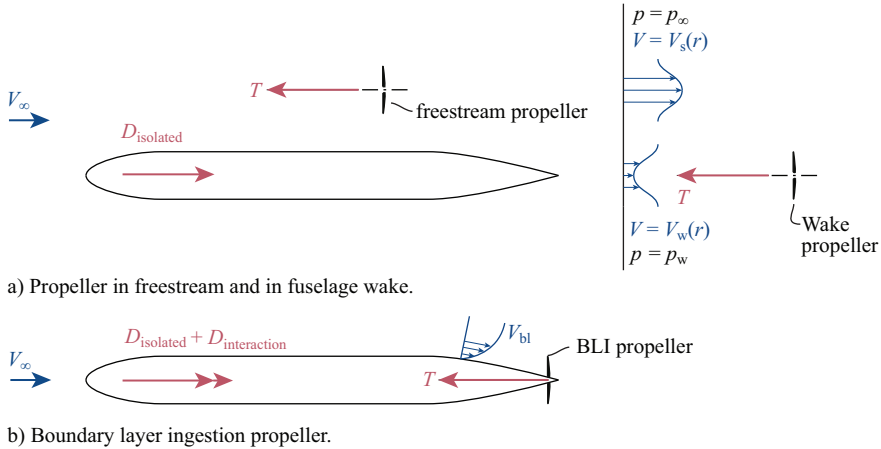


Figure 2.6: Sketch depicting wake ingestion and the additional complexity of boundary layer ingestion (BLI) because of the upstream interaction effect of such a propeller.

equations for frictionless non-stationary flow gives an idea of the interaction mechanism that results in a power reduction for a wake ingestion propeller compared to a propeller in the freestream. Such an analysis is performed in Appendix A, as an example of how aero-propulsive interaction can be beneficial. This analysis shows that the axial kinetic energy of the wake is utilised by the wake propeller and in an ideal situation no or in a realistic scenario less axial kinetic energy is left in the air. Similarly, the rotational kinetic energy left by the propeller in the air can be utilised as well by different means to reduce the power.

Of course, wake ingestion is not a realistic situation. A propeller mounted at the rear of the fuselage instead of behind, as sketched in Fig. 2.6 b, has an upstream effect, changing the drag of the fuselage. The question can also be raised whether a boundary layer ingestion (BLI) propeller can exactly balance the lost momentum, as this requires a specific thrust distribution on the propeller blades which may not be possible or efficient. Furthermore, a propeller mounted at the aft fuselage experiences a highly non-uniform inflow, in radial direction and in realistic applications with wings and tailplanes also in azimuthal direction. Although it is recognised that an adapted blade shape is beneficial for such a non-uniform inflow [5, 81–83], the merit of BLI is not always determined with propellers designed for non-uniform inflow [84].

To investigate the propeller design effect, in Ref. [63] a BLI propeller designed for a radially varying boundary layer inflow was compared with a propeller designed for uniform inflow. The BLI propeller was mounted at the aft of an axisymmetric fuselage geometry. From this analysis a 7% reduction in power was found for the BLI propeller compared to propeller in uniform inflow. The propeller was characterized with increased loading towards the root, where also the highest values of section thrust-to-power ratios were found.

While a BLI propeller clearly operates in a flowfield dominated by aerodynamic in-

Table 2.2: Flowfield phenomena relevant for a pusher or tractor propeller interacting with a nacelle or fuselage. Darker means stronger effect on average (avg) or local (loc) propeller loading as defined in Table 2.1.

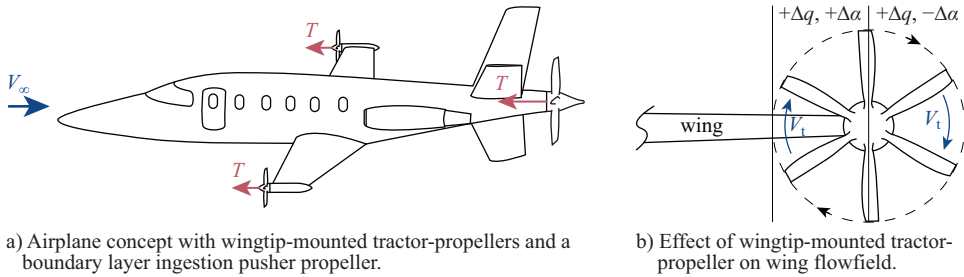
		Nacelle		Fuselage	
		tractor	pusher	tractor	pusher
$-\Delta p_t$ from momentum sink	avg				
	loc				
$+\Delta p_t$ from momentum source	avg				
	loc				
Δq or $\Delta \alpha$ from potential effect	avg				
	loc				
Rotational flowfield	avg				
	loc				
Impinging vortices	avg				
	loc				

teraction with the fuselage, this configuration is not further analysed in this dissertation. The initial assessment in Ref. [63] has also revealed the complexity involved in this configuration, warranting a lot of research, not suitable next to the other configurations studied. Research into boundary layer ingestion is ongoing in e.g. the Horizon 2020 Centreline project [80].

2.3. INTERACTION WITH WING

Currently, wing-mounted tractor-propellers are the conventional layout for regional turboprop aircraft. For this reason, a considerable amount of research has been performed on the interaction of the propeller with the downstream wing by for instance Veldhuis [49] and Refs. [85, 86]. The propeller sees a relatively freestream flow, disturbed by the upwash and pressure field from the wing. The wing locally experiences an increased dynamic pressure from the axial velocity increase in the slipstream and a positive and negative angle of attack change from the tangential velocity. A much stronger interaction effect for the propeller is present when it is mounted in pusher configuration, as for instance studied by Yin et al. [12]. The propeller not only operates in the downwash of the wing, but also the impinging wing wake and the engine exhausts result in a non-uniform velocity inflow to the propeller. A summary of these flowfield phenomena relevant for the propeller interacting with a wing is given in Table 2.3.

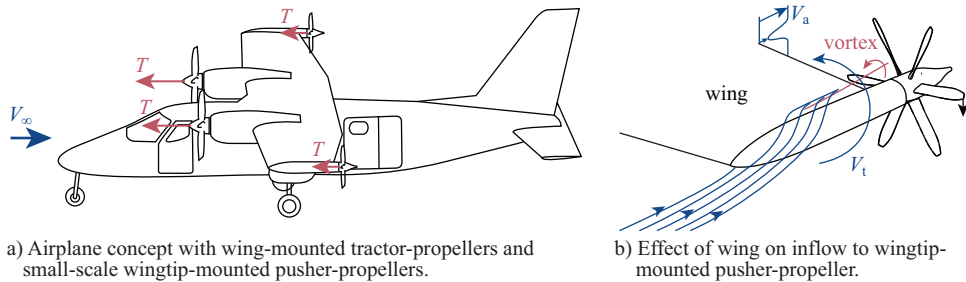
Interaction effects change when the propeller is moved more outboard to the tip of the wing. Wingtip-mounted propellers have been envisaged for their favourable interaction effects. However, adverse aeroelastic effects due to the large weight of an engine at the tip of a wing, high wing mass due to inertia loads and the large yawing moment arm of the thrust vector in case of a one-engine-inoperative condition have prevented the application of wingtip-mounted propellers up to now. The emergence of electric propulsion in aircraft allows almost penalty free downscaling of the propeller due to the scale independence of the electric motor [87]. This makes it possible to distribute the propulsion for instance through a hybrid-electric architecture, and enables to scale down the wingtip-mounted propeller like proposed for the X-57 Maxwell [88] that was shown in Fig. 1.6. An impression of such a concept, combining e.g. fuselage boundary layer ingestion and wingtip-mounted tractor-propellers through a hybrid electric architecture, is shown in Fig. 2.7 a. A more conventional airplane layout with small-scale



a) Airplane concept with wingtip-mounted tractor-propellers and a boundary layer ingestion pusher propeller.

b) Effect of wingtip-mounted tractor-propeller on wing flowfield.

Figure 2.7: Impression of an airplane concept, a modified LearAvia Lear Fan 2100, and a sketch depicting the flowfield experienced by the wing for a wingtip-mounted tractor-propeller configuration.



a) Airplane concept with wing-mounted tractor-propellers and small-scale wingtip-mounted pusher-propellers.

b) Effect of wing on inflow to wingtip-mounted pusher-propeller.

Figure 2.8: Impression of an airplane concept, a modified Tecnam P2012 Traveller, and a sketch showing the flowfield experienced by a wingtip-mounted pusher propeller.

wingtip-mounted pusher-propellers is sketched in Fig. 2.8 a.

For the tractor-propeller variant, for a given wing lift the interaction of the wing with the slipstream results in a reduction of the wing drag if the rotation direction of the propeller is opposite to that of the wingtip vortex [14–16]. In Fig. 2.8 b the change in inflow for the wing is depicted. Similar to the conventional wing-mounted propeller, the wing still experiences an increased dynamic pressure from the axial velocity increase in the slipstream, increasing locally lift and drag. However, now the wing only experiences an increase in angle of attack if the propeller rotation direction is inboard up, as the α decreasing part of the slipstream is outboard of the wing. This tilts the resultant force vector locally forward in thrust direction, opposing drag. A detailed experimental study of these interaction effects can be found in Sinnige et al. [16].

The pusher-propeller variant experiences a reduction in shaft power due to the swirling vortex inflow from the wingtip in case the propeller rotates against the direction of the wingtip vortex [15, 34–36]. Moreover, the modification of the wingtip vortex may reduce wing induced drag as well. In Fig. 2.8 b the effects of the wing on the inflow to the pusher variant are sketched. Next to the rotational flowfield depicted by V_t , the propeller also experiences reduced axial velocity V_a in the wake of the wing. Furthermore, the wingtip vortex trails downstream, impinging on the propeller disk. In Table 2.3 the importance of flowfield phenomena for wingtip-mounted propellers is also summarized.

In this research only propellers mounted at the wingtip will be treated and not at

Table 2.3: Flowfield phenomena relevant for a tractor or pusher propeller interacting with a wing or wingtip. Darker means stronger effect on average (avg) or local (loc) propeller loading as defined in Table 2.1.

		Wing		Wingtip	
		tractor	pusher	tractor	pusher
$-\Delta p_t$ from momentum sink	avg				
	loc				
$+\Delta p_t$ from momentum source	avg				
	loc				
Δq or $\Delta \alpha$ from potential effect	avg				
	loc				
Rotational flowfield	avg				
	loc				
Impinging vortices	avg				
	loc				

other wing locations. Although the pusher variant is more interesting from the point of view of interaction effects for the propeller and the focus is largely on this layout, the tractor-propeller layout serves as a validation case due to the presence of detailed wind-tunnel data. Furthermore, the very strong interaction effect for the wing deserves attention in a work on interaction dominated flowfields. Chapter 5 is dedicated to propeller interaction with the wingtip. The scope of this research is presented in the next two sections.

Apart from the wingtip-mounted configuration, other concepts exist in which the propeller is located on the tip of an aerodynamic surface with similar interactions, e.g. pylon-mounted propellers [50, 89] and propellers installed at the tip of the horizontal tailplane [90, 91]. Some of the aspects of the research done in this dissertation on wingtip-mounted propellers may be relevant for these layouts, and *visa versa*.

2.3.1. WINGTIP-MOUNTED TRACTOR-PROPELLER

CFD simulations based on the RANS equations provide the right ingredients to model the interaction between a propeller slipstream and a wingtip vortex, because of the capability to capture both vortex interaction effects and viscous interaction effects, contrary to potential-flow and Euler methods. For the wingtip without propeller, research has shown that RANS CFD is capable of predicting the wingtip vortex with sufficient detail, although the large gradients in flow variables require locally dense grids [92]. For conventional wing-mounted tractor propellers, RANS CFD has proven to adequately capture the transient propeller-wing interaction effects [85, 86, 93]. When the propeller is moved to the tip of the wing, the complexity of the flowfield increases due to the interaction of the propeller blade vortices and wingtip vortex, necessitating an evaluation of the accuracy of RANS simulations for this particular configuration.

Simulating a propeller interacting with an aerodynamic surface is computationally costly when resolving the propeller blades. This is especially relevant in a preliminary design phase, during which multiple concepts or design iterations need to be evaluated. Modelling of the propeller in a RANS simulation by adding sources of momentum and energy in a time-averaged sense with an actuator-disk (AD) model instead of resolving the propeller blades has been shown to reduce the computational cost of propeller-wing interaction simulations [94]. These sources can also be introduced in a time-accurate

sense with an actuator-line (AL) model, as has been applied for wind turbines [95, 96] and helicopter rotors [97]. In an actuator-line model, the propeller blades are replaced with distributions of momentum and energy sources along lines representing the blades. Next to the assessment of the accuracy of RANS simulations for wingtip-mounted propellers, it is especially interesting to evaluate the capability of these actuator models (AM). If proven to be sufficiently accurate, such modelling methods enable quicker design evaluations in propeller interaction studies. Therefore, the following two research questions were posed, which will be addressed in Section 5.1:

Q2a: *How do full-blade (FB) RANS simulations of a wingtip-mounted tractor-propeller compare to experimental data from an in-house wind-tunnel test in terms of flowfield and wing loading?*

Q2b: *How accurately can actuator-disk (AD) and actuator-line (AL) models in RANS simulations represent a propeller in interaction with the wingtip in tractor configuration and by how much can they reduce computational cost compared to FB simulations?*

The use of electric motors that give the freedom to scale wingtip-mounted propellers, can also be used for energy generation. During for instance descent, when less thrust is required, the propellers can operate as airborne wind turbines. Instead of a momentum source, the propeller acts as a momentum sink, changing the loading on the downstream wing. Some previous research has been done on this topic for soaring applications [98–100] and actual application of this principle has been confirmed by the use on the Pipistrel Alpha Electro trainer [101]. The consequence of windmilling and energy harvesting operation for the wingtip-mounted tractor-propeller is researched as part of this dissertation in Section 5.2 by addressing the research question:

Q3: *What are the consequences of windmilling and energy harvesting on the wing loading for a wingtip-mounted tractor-propeller?*

2.3.2. WINGTIP-MOUNTED PUSHER-PROPELLER

The design freedom to scale wingtip-mounted propellers and to distribute propulsion when electric propulsion is used, results in a non-unique thrust requirement. For example, the propeller can be designed to balance just the induced drag of the wing or balance the entire cruise drag of the aircraft. The resulting performance benefit of propeller installation at the wingtip may depend on the thrust level. Up to now, only research on a full scale wingtip-mounted pusher-propeller has been performed, with a propeller not specifically designed for this task [35]. The inflow to the propeller is non-uniform, especially when the propeller becomes smaller relative to the wingtip flowfield. For a boundary layer ingestion propeller, Ref. [63] has shown that maximizing the propulsive efficiency gain requires a different design to cope with the non-uniform inflow experienced on the aft fuselage. Analogue to that, the wingtip-mounted pusher-propeller may also benefit from design optimisation. Scale and design aspects of wingtip-mounted pusher-propellers are therefore researched in Section 5.3 by answering the following research questions:

Q4a: *How does the propeller size and thrust level influence the propulsive efficiency benefit and the upstream aerodynamic loading on the wing for a wingtip-mounted pusher-propeller?*

Q4b: *To what extent can the propulsive efficiency benefit be increased by designing the propeller for the non-uniform inflow experienced at the wingtip?*

2.4. INTERACTION WITH STATOR OR ROTOR

2.4.1. STATOR

Not only a wing can benefit from the swirl in the propeller slipstream, also a dedicated set of stator vanes is capable of utilizing this rotational kinetic energy loss. A sketch of these so-called swirl-recovery-vanes (SRVs) for a wing-mounted tractor-propeller is shown in Fig. 2.9. The objective of SRVs is an additional thrust force at no cost of shaft power. Motivated by the 1970's energy crisis, SRVs have been extensively investigated numerically and experimentally by NASA and partners [9, 102–104] behind an isolated propeller. The experimental effort of Gazzaniga and Rose [9] has shown a propulsive efficiency gain of 1.7% in the design cruise condition, reaching up to 4.4% for higher propeller thrust conditions. Research on the aerial application of SRVs has recently gained renewed interest [105–108]. The flowfield which SRVs experience is fully dominated by the slipstream of the propeller. For the propeller the interaction with downstream SRVs is estimated to be small, but the close proximity of the SRVs to the propeller may result in a small upstream pressure effect. However, the very strong interaction effect for the SRVs deserves attention in a work on interaction dominated flowfields. While in the MSc thesis of the author [107] a design methodology and analysis of the performance gains was presented for SRVs behind an isolated propeller and a wing-mounted tractor-propeller, in this work an analysis of the unsteady loading effects for the propeller and the stator vanes is performed. The following research question is addressed in Section 6.1:

Q5: *What are the steady and especially unsteady aerodynamic interaction effects between a propeller and swirl-recovery-vanes in terms of propeller and vane loading?*

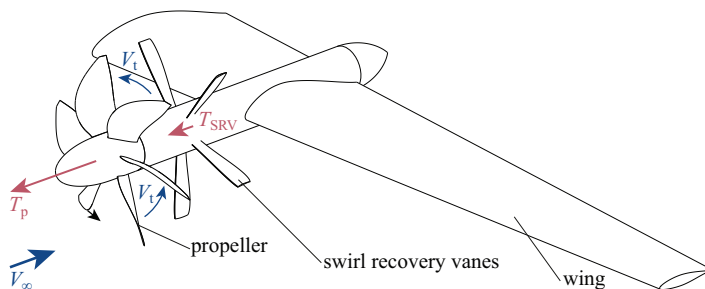


Figure 2.9: A sketch of swirl-recovery-vanes in the slipstream of a wing-mounted tractor-propeller.

Although not covered in this dissertation, the reverse situation can also be relevant, where a stator is placed upstream of the propeller as sketched by Weinig [109]. By giving

the propeller a rotational velocity field opposing that of the propeller rotation, the shaft power that normally is put into angular momentum can be put into axial momentum. Contrary to SRVs, these vanes produce a force opposing propeller thrust. In the maritime world, such pre-swirl vanes have been applied to ship propellers, resulting in a few percent efficiency gains [110]. The inflow field these pre-swirl vanes present to the propeller also contains wakes from the vanes and possibly vane tip vortices, depending on their radius. For both downstream and upstream stators, in Table 2.4 the relevant flowfield phenomena for the propeller are indicated and their effect on the propeller loading are estimated.

2.4.2. ROTOR

Not only stators but also rotors can be used to recover the swirl loss. The contra-rotating open-rotor (CROR) is generally thought to recover the loss better with gains in propulsive efficiency in the order of 8% [8], but also with increased complexity. Motivated by this efficiency gain, a considerable amount of research has been performed in recent years on this topic, e.g. Refs. [50, 111–113]. In such a configuration, especially the rear rotor but also the front rotor experience a flowfield dominated by interaction from the other rotor. A lot of the research is focussed on noise aspects of this interaction.

Interaction between rotors is also a topic very applicable to helicopters. The interaction of the main rotor with the tail rotor for conventional helicopters is a prime example of this [114]. Furthermore, the interaction between the two main rotors for co-axial helicopters [115] is a relevant case. Tandem helicopters also experience rotor-rotor interaction, especially in forward flight [116–119].

A relatively unexplored topic for interaction between propellers, where the research in this dissertation is focussed on, is that of eVTOL vehicles. A number of eVTOL vehicle concepts with different layouts are presented by Johnson et al. [42] and Silva et al. [48] as reference vehicles for technology development. In the work of Johnson et al. [42] it is stressed that performance issues with rotor-rotor interaction is one of the research areas for UAM aircraft development. When aircraft have two or more main rotors, rotor-rotor interaction can have significant impact on among others performance and noise, and this is dependent on their arrangement. Performance effects as a function of rotor or propeller arrangement are the focus of the research in this dissertation. Besides the impact on vehicle performance, interaction between propellers can also be a significant source of noise due to blade-vortex interaction. The article of Silva et al. [48] focusses on vehicles for UAM for 550 kg payload weight or up to six passengers design mission. They mention the development of a wind-tunnel test rig to study propeller interactional aerodynamics at small scale. Despite the scale effects and lack of dynamics, such wind-tunnel test is thought to be appropriate to evaluate aerodynamic interaction phenomena. Their experimental approach is also taken in this research.

Besides the eVTOL concepts in Refs. [42, 48], in Ref. [44] a conceptual design study is performed for another three eVTOL concepts. Many more different concepts have been designed by industry. Although the variety in eVTOL concepts is large, two key propeller interaction types are distinguished that occur on many of them. The Aurora Passenger Air Vehicle [120] and the Airbus Vahana [47] are taken as examples, and their propulsion

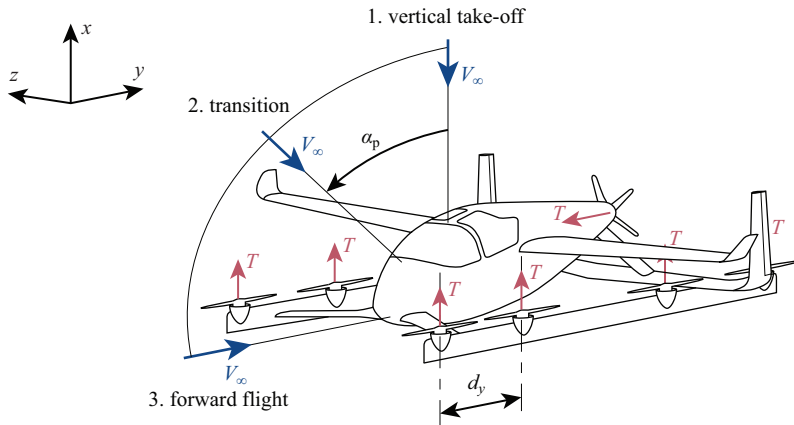


Figure 2.10: Sketch of the side-by-side (SBS) propeller configuration on an eVTOL vehicle based on the Aurora Passenger Air Vehicle [120].

layout is sketched in Figs. 2.10 and 2.11, respectively. For the concept from Aurora, eight propellers are used for lift at vertical take-off and during transition to forward flight. The propellers that are placed side-by-side (SBS) with their propeller planes coinciding, experience a zero propeller angle of attack α_p inflow of the freestream velocity at vertical take-off. The close proximity of the propellers and their slipstreams, in case of a small lateral distance d_y , may affect propeller performance. The vertical take-off is followed by a transition phase where α_p changes from 0 deg to approximately 90 deg. Concepts where a wing is used for lift often do not deploy such propellers for lift in forward flight, but for multicopter eVTOL concepts, a third flight condition to consider for propeller interaction is forward flight at angles around $\alpha_p = 90$ deg. Of particular interest are propellers positioned in a line in the flight direction like in the sketched concept, and not next to each other in spanwise direction. In transition and forward flight one can expect an interaction of the slipstream of the front propeller with the slipstream of the rear propeller, or even direct impingement of the slipstream from the front propeller on the rear propeller. Among others, the quadrotor concept and Lift+Cruise eVTOL aircraft presented by Silva et al. [48] are relevant side-by-side interaction cases. The Side-by-Side urban air taxi concept as presented by Ventura Diaz et al. [121] is however not covered in terms of propeller interaction despite its name, as the two rotors are distributed in spanwise direction.

The second key propeller interaction type, sketched in Fig. 2.11, is where propellers are placed one-after-another (OAA) with their propeller planes not coinciding. Using tiltwings and multiple rotors, the Airbus Vahana [47] hovers like a helicopter, then transitions, and cruises like an airplane. On this vehicle, during cruise or the last stage of transition, the rear propellers may ingest partly or fully the slipstream of the front propellers. In the RANS CFD simulation results shown in Ref. [47] this propeller interaction is visible between the front and rear propellers during transition. The Joby S2 Electric VTOL PAV concept [122] is another example where one-after-another propeller interac-

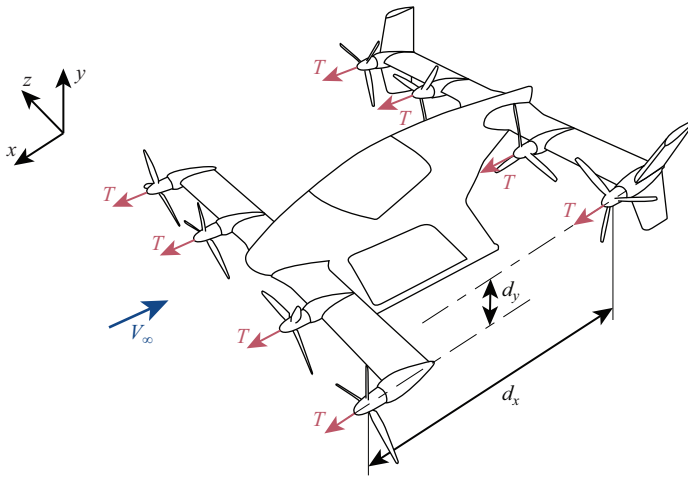


Figure 2.11: Sketch of the one-after-another (OAA) propeller configuration on an eVTOL vehicle based on the Airbus Vahana [47].

tion may occur in certain flight conditions between propellers mounted on the wing and on the tail surfaces. A similar interaction, but at much smaller axial distance d_x , also occurs for multicopter concepts during vertical take-off if the propellers are partially overlapping, or for propellers mounted with overlap or staggered on for instance the wing like for the high-lift propellers of the X-57 Maxwell that was shown in Fig. 1.6 [88].

Some relevant previous research exists that may be applicable to determine propeller performance effects for eVTOL vehicles. In terms of aerodynamic interaction effects, depending on the layout of the propellers on the eVTOL vehicle, already a lot can be learned from previous research on tandem-rotor helicopters, tiltrotors, tiltwings, and multicopter concepts. However, results from tandem-rotors are not necessarily applicable to propellers as they feature articulated, high-aspect ratio blades with no or low twist, while the studied rigidly mounted propeller blades have high twist and are of lower aspect ratio. A large part of the literature treats aerodynamic interaction between rotors in the hover condition, e.g. Refs. [123–127].

For a tandem-rotor in forward flight, Heyson [116] established experimental flowfield interaction results, reporting downwash angles and visualizing the flowfield with a five-hole probe survey. These results are relevant for side-by-side interaction at $\alpha_p = 90$ deg. Performance results of this experiment were reported by Dingeldein [117]. In forward flight the rear rotor, located at $d_y/R_p = 2.06$ behind the front rotor, is seen to operate in a region of increased downwash of the front rotor, increasing its power requirement to maintain the same thrust compared to the same rotor in an isolated configuration. The front rotor operates in the upwash from the rear rotor, reducing the effective downwash for the front rotor and increasing its thrust for unchanged operating conditions. According to Dingeldein [117], the front rotor could be modelled with fair agreement using isolated rotor theory in the freestream and the rear rotor using isolated rotor theory when modelled in the fully developed downwash of the front rotor.

Stepniewski and Keys [118] describe how for tandem-rotors in forward flight, the rear rotor operates in the wake of the front rotor and experiences a flow with higher axial velocity component than the isolated rotor, resulting in a higher induced power. It is shown how the distance of the rear rotor to the front rotor wake influences the rear rotor performance, and a maximum induced power is found when the front rotor wake passes through the rear rotor. This power penalty reduces when the wake passes above or below the rear rotor. The largest penalty for a hypothetical tandem-rotor results in a 23% increase in shaft power and occurs at the airspeed of minimum power, and decreases at lower or higher speeds. Lee et al. [119] also presents predictions of performance drawback of (overlapping) tandem-rotors in forward flight with a free-wake panel method.

A very relevant case of rotor interaction is found on the Bell Boeing Quad tiltrotor [128] which, depending on the flight condition, experiences side-by-side interaction at various angles of attack or one-after-another interaction for an axial distance of $d_x/R_p \approx 2$. Transition and forward flight was studied with RANS CFD simulations. Just like for the tandem-rotor, the rear rotor is affected by downwash of the front rotor in a side-by-side interaction, resulting in a slight reduction of thrust of the rear rotor during transition. Also changes in rear rotor loading in forward flight are reported when the rotors are in a one-after-another configuration, especially in the region where the hub vortex of the front rotor impinges on the rear rotor. In this region, the maximum in rear rotor thrust was found as a result of the high tangential velocity and low axial velocity component in the flow.

Relevant research on propeller interaction has also been performed on much smaller scale for UAV applications. The small propellers used for these applications are often quite flexible and operate at a low rotational speed for their size, resulting in aerodynamic twist and relatively low blade section Reynolds numbers compared to full-scale propellers on eVTOL vehicles. Despite these drawbacks, the interaction phenomena at small-scale and full-scale may be similar. A considerable amount of research has been done on the performance of overlapping rotors for UAV in hover condition, e.g. Refs. [129–132]. These studies, relevant for one-after-another interaction, all conclude that compared to isolated propellers either the power demand of the rear rotor increases with increasing overlap for equal thrust or that the thrust reduces for equal power.

The performance effects of propeller interaction in side-by-side configuration have also been studied for UAV applications, mainly again in hover condition in e.g. Ref. [133]. Alvarez and Ning [134] simulated the experiment from Ref. [133] using a viscous vortex particle method. For three Reynolds numbers in forward flight, a range of advance ratios were simulated for $\alpha_p = 0$ deg. It was found that, when propellers are in close proximity, propeller interaction is detrimental for the propulsive efficiency, resulting in a maximum efficiency drop of almost 3%. This drop in performance was more accentuated at low advance ratios.

The only UAV results in forward flight with $\alpha_p = 90$ deg are presented by Ventura Diaz and Yoon [135], showing detached eddy simulation results of a quadcopter UAV with side-by-side interaction. They found that in forward flight the propeller interaction is stronger than in hover because the wakes of the front propellers interfere with the rear propellers. They experimented successfully with different mounting to get the propellers out of same plane in order to reduce interaction effects.

Table 2.4: Flowfield phenomena relevant for a propeller interacting with a downstream (downstr.) or upstream (upstr.) stator or rotor. Darker means stronger effect on average (avg) or local (loc) propeller loading as defined in Table 2.1.

		Stator		Rotor	
		downstr.	upstr.	downstr.	upstr.
$-\Delta p_t$ from momentum sink	avg				
	loc				
$+\Delta p_t$ from momentum source	avg				
	loc				
Δq or $\Delta \alpha$ from potential effect	avg				
	loc				
Rotational flowfield	avg				
	loc				
Impinging vortex	avg				
	loc				

The relevant flowfield phenomena identified for interaction of propellers with other rotors are summarized in Table 2.4. Although there is already a large body of knowledge on aerodynamic interaction effects between propellers, it is often limited to a hover condition and especially studies of transition and forward flight are lacking. Furthermore, there is a lack of studies with non-articulated rotors with well defined geometry. In general, a reference data set with effects of interaction on in-plane forces and out-of-plane moments does also not exist. Therefore, the following research question was established that will be addressed in Section 6.2:

Q6: *How does propeller interaction in side-by-side and one-after-another propeller configuration affect propeller performance, in terms of thrust, power, in-plane forces and out-of-plane moments, and how do those performance effects depend on propeller spacing defined by d_x and d_y ?*

2.5. COMBINED INTERACTION

Often propellers are not interacting with a single object, but encounter interaction from multiple sources. For instance, interaction between propellers on eVTOL vehicles, as discussed in the previous section, often includes interaction with wings or tailplanes in a realistic application. A specific layout where interaction between a propeller and rotor is also complemented by interaction with a wing is that of the Airbus RACER compound helicopter concept that was shown in Chapter 1 in Fig. 1.8. In Fig. 2.12 a sketch is shown of the helicopter, without main rotor and tailplanes.

Because of the close proximity of the box-wing and main rotor, the propellers experience various aerodynamic interactions. These interactions significantly differ for each flight condition. The propeller installation effects for this compound helicopter have been described to some extent by Refs. [136, 137]. In the cruise condition the interaction between the main rotor and propellers is limited since their slipstreams are separated, as sketched in Figure 2.13. However, the proximity of a main rotor with slipstream may have potential flow effects, changing flow incidence angle and dynamic pressure for the propeller. Orchard and Newman [138] underline that propellers are particularly advantageous as propulsion device for compound helicopters considering their high efficiency

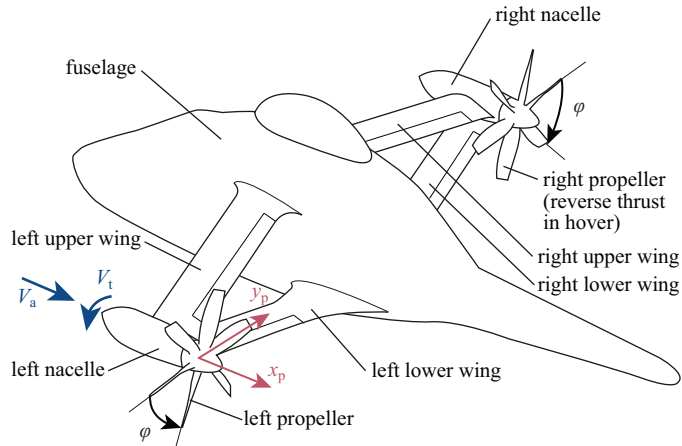


Figure 2.12: Sketch of the Airbus RACER compound helicopter configuration without main rotor and tailplanes. Propeller blade phase angle φ and axial and tangential velocity components V_a and V_t are indicated.

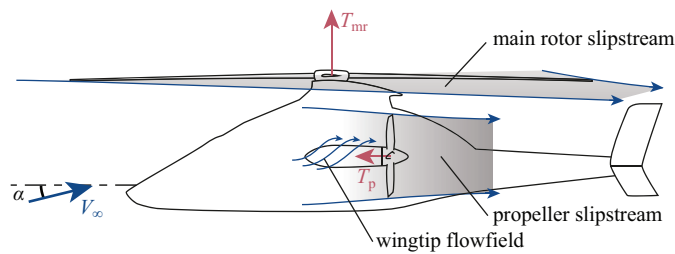


Figure 2.13: Sketch of main rotor, box-wing and propeller aerodynamic interaction in cruise, indicating the direction of the main rotor thrust T_{mr} and propeller thrust T_p .

at the moderate cruising speed. An additional efficiency advantage for these propellers can be expected because of the installation on the wingtip in pusher configuration, potentially resulting in wingtip vortex energy recovery by the propellers and wing induced drag reduction as discussed for planar wings in Section 2.3. Each wing-half is equipped with a flap, which allows a change in the ratio of wing lift to main rotor lift in forward flight. The impact of the novel box-wings and their lift on the propeller efficiency benefits is yet unknown.

The importance of flowfield phenomena for the propeller in the cruise condition are rated in Table 2.5, also for a fictitious tractor-propeller variant. Compared to the conventional-wingtip mounted propeller (Table 2.3), the same effects play a role, but slightly more pronounced as they originate from more sources. In Section 7.1 results for the cruise condition are presented to answer the following research questions:

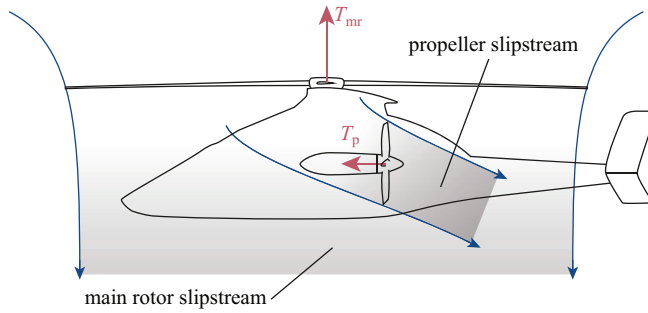


Figure 2.14: Sketch of main rotor and propeller aerodynamic interaction in hover, indicating the direction of the main rotor thrust T_{mr} and propeller thrust T_p .

Q7.1: *How does the box-wing affect the loading and efficiency of the propellers on the compound helicopter configuration in cruise, with varying flap deflection and varying angle of attack and sideslip, and how is the lift and drag of the box-wing altered?*

Q7.2: *What role does the main rotor play in the loading on the propellers of the compound helicopter configuration in cruise?*

Although propellers may be beneficial in the cruise condition where the main rotor slipstream generally passes over them, the lack of shielding of the propellers may pose a problem at low airspeed and particularly in the hover condition where the main rotor slipstream impinges on the propellers as sketched in Figure 2.14. It is known from Orchard and Newman [138] that bending moments of the propeller blades due to this skewed inflow may be significant. Furthermore, a propeller close to the main rotor may affect the rotor flapping amplitude and bending moments due to its pressure field, as is known from the extensive experimental investigation of Bain and Landgrebe [139]. Not only the propellers but also the wings experience a large variation of angle of attack in the flight envelope as shown by Lynn [140]. The wings may cause an additional disturbance to the inflow of the propellers. Again an estimated impact of the flowfield phenomena on the propeller loading is presented in Table 2.5. In Section 7.2 the impact of this complex interactional flow on the propeller performance and unsteady aerodynamic loading is investigated by addressing the following research questions:

Q8: *What is the influence of the main rotor and box-wing on the loading on the propellers of the compound helicopter configuration in hover?*

As this interaction with a main rotor and wing in hover is relatively unknown, the interaction effects are also investigated experimentally. This is complemented with RANS CFD simulations. An approximation of the interaction on the compound helicopter was realised by installing a tractor propeller at 90 deg angle of attack in an 3/4 open jet wind tunnel and placing a separate planar wing with flap upstream of the propeller, such that the wingtip aligned with the propeller axis, see Fig. 2.15 b. In this setup the main rotor flow is approximated with the wind tunnel jet. The goal is to investigate the specific

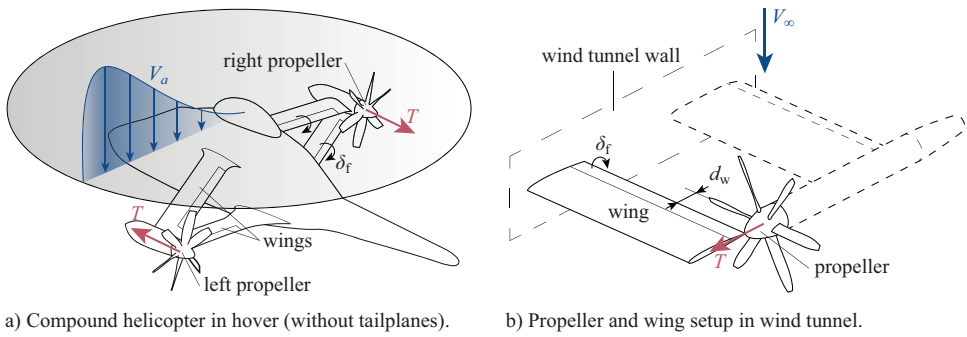


Figure 2.15: Comparison of the compound helicopter to experimental setup of propeller and wing.

interaction problem in a simplified form by means of an experiment, in order to verify the numerical findings that are found for more complicated geometry. The following research question is addressed in Section 7.3:

Q9: *How does wing distance and flap deflection influence the loading on a wingtip-mounted pusher-propeller subject to flow perpendicular to the wing planform?*

The results of this interaction problem may also be relevant for eVTOL concepts with wingtip-mounted pusher-propellers in the transition phase from vertical take-off to cruise.

This setup neglects any of the transient effects that the main rotor blade tip vortices and wakes have on the propeller loading as described by Thiemeier et al. [137]. Therefore, in terms of main rotor flow this wind tunnel dataset is of similar fidelity as the computational results for the compound helicopter, where the main rotor flow is approximated with a steady non-uniform actuator-disk. Furthermore, the experiment approximates the main rotor slipstream flowfield as uniform in space, while in reality a strong radial variation in axial induced velocity exists (as sketched in Fig. 2.15 a) and a much smaller tangential velocity component is present too. The effect of this non-uniformity is investigated numerically, but the tangential component is not considered.

Table 2.5: Flowfield phenomena for a propeller interacting with a helicopter main rotor and wingtip for a compound helicopter in cruise and hover. Darker means stronger effect on average (avg) or local (loc) propeller loading as defined in Table 2.1.

		Cruise		Hover	
		tractor	pusher	tractor	pusher
Δq from momentum sink	avg				
	loc				
Δq from momentum source	avg				
	loc				
Δq or $\Delta \alpha$ from potential effect	avg				
	loc				
Rotational flowfield	avg				
	loc				
Impinging vortex	avg				
	loc				

3

ANALYSIS METHODS AND MODELS

This chapter describes the various methods that were used to analyse propeller interaction. These can be split in experiments and computations. Wind tunnel experiments were used for validation of the taken numerical approaches. Furthermore, they made quick parametric variations possible to gain improved insight in the dependency of the interaction results on the operating condition and geometric variables of the configuration. On their turn, the validated numerical simulations allowed investigation of the transient loading on and the complete flowfield around the configurations. Since the computations often used geometry from the experiments, first the experimental approach is discussed in Section 3.1 and after that the numerical approach in Section 3.2.

3.1. EXPERIMENTAL APPROACH

This section on the experimental approach is split in a description on the propellers in Section 3.1.1, an overview of the wind tunnel facilities in Section 3.1.2 and an explanation of the models and measurement techniques in Section 3.1.3.

3.1.1. PROPELLERS

Four existing experimental propeller models have been used, which are depicted in Fig. 3.1 and summarized in Table 3.1. The largest is the APIAN (Advanced Propulsion Integration Aerodynamics and Noise) propeller [141], featuring 6 highly swept blades with a radius of $R_p = 0.2540$ m, representative of a high-speed design. The blade pitch angle was set to $\beta_{0.7R_p} = 42.0$ deg ($\beta_{0.75R_p} = 40.4$ deg). The blade design is shown in Fig. 3.2 a in terms of radial distributions of chord and blade pitch based on Ref. [142]. The aerodynamic properties of the isolated propeller are discussed in Section 4.1.4. This propeller was used in the computational propeller–SRV interaction study in Section 6.1, since the validating experiment used this propeller. The sweep is incorporated to postpone the onset of compressibility losses and thus be able to fly at a high Mach number of $0.7 < M_\infty < 0.8$ [85]. This propeller features sections with relatively large chord lengths

Parts of this chapter have been adapted from Refs. [64, 65, 67–71].

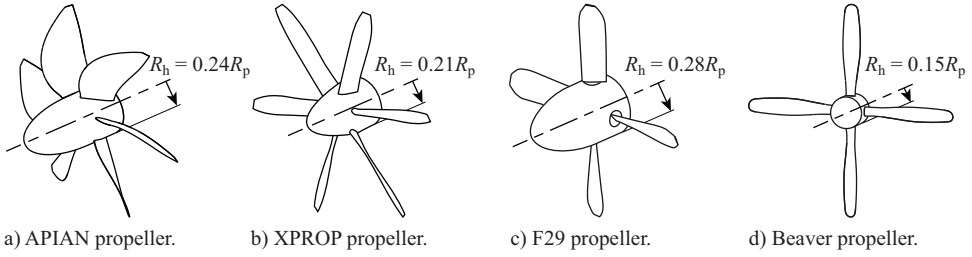


Figure 3.1: Isometric view of the four experimental propeller models with spinner.

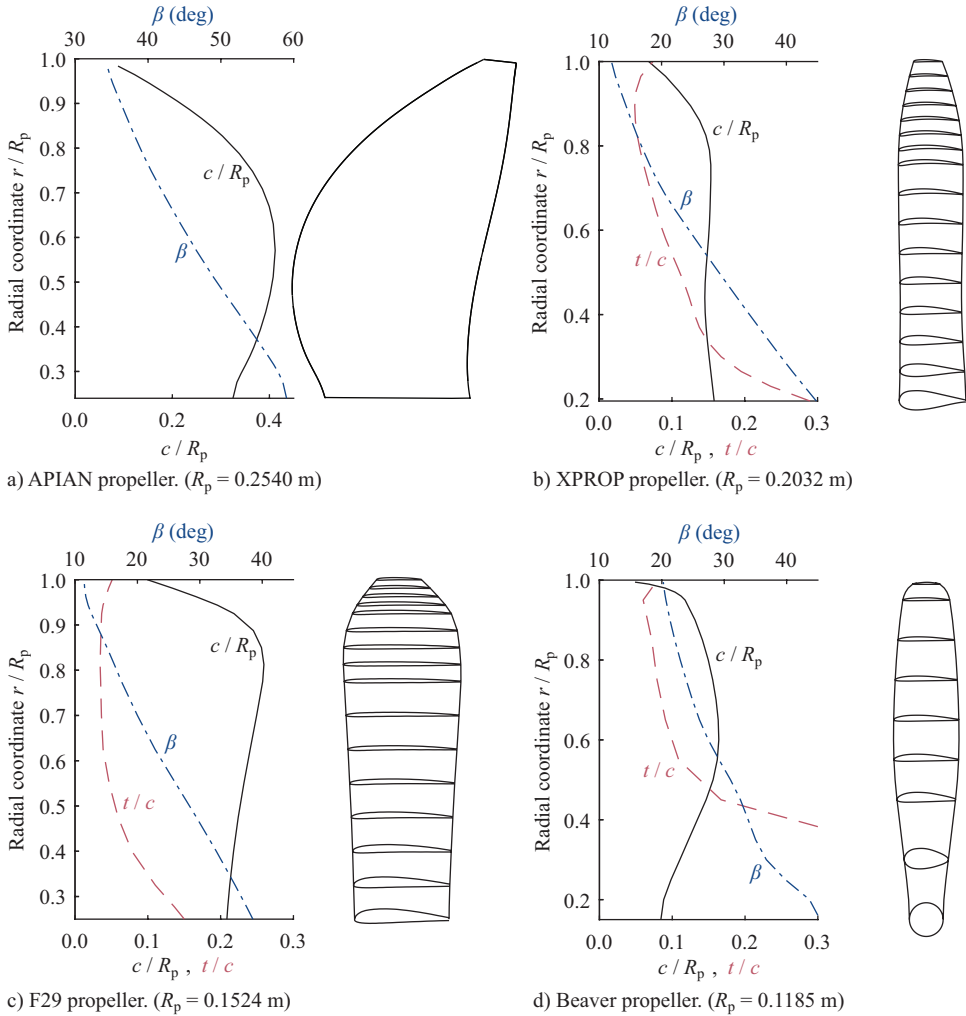


Figure 3.2: Blade description of the experimental propeller models with untwisted blade geometry and airfoils.

such that it can be highly loaded to produce the thrust needed at these speeds. As a result it induces a strong rotational flowfield in the slipstream, which makes it very suitable for the application of swirl-recovery-vanes that act on this rotational kinetic energy loss.

The second largest propeller is the 6-bladed XPROP propeller from Delft University of Technology, used by e.g. Refs. [143, 144]. It is a propeller with a blade radius of $R_p = 0.2032$ m, and it was used in an experiment at a blade pitch of $\beta_{0.7R_p} = 20.0$ deg and 30.0 deg and in computations also at other blade pitch angles. The blade design is shown in Fig. 3.2 b in terms of radial distributions of chord, thickness, blade pitch and airfoils and is typical for current turboprop airplanes, except for the lack of sweep. Compared to the APIAN propeller, it does not feature sweep and the section chord lengths are much smaller. This means that it is not suitable for very high subsonic speed and the loading on the propeller is generally lower. Furthermore, the blade pitch angle it was tested at is considerably smaller to avoid flow separation, since it was tested in static condition and at freestream speeds lower than for the APIAN propeller. Results for the isolated propeller are shown in Section 4.1.1 at zero angle of attack and in Section 4.2.1 at an angle of attack up to 90 deg. This propeller is also used as the reference propeller in the design study for a wingtip-mounted pusher-propeller in Section 5.3 as it is a well-defined modern propeller. At last, with this propeller the interaction occurring for the compound helicopter in hover was replicated experimentally, as this propeller has the same blade count and is of similar design to those of the compound helicopter, except for the smaller radius. These results can be found in Section 7.3.

The third largest is the F29 propeller. Two 4-bladed models with a radius of $R_p = 0.1524$ m and blade pitch of $\beta_{0.7R_p} = 20.0$ deg were used in an experiment. It was previously used by Veldhuis et al. [145] in 4- and 8-bladed variants, and defined by the Fokker Aircraft Company in their internal F29 project. The propeller has also been used by Refs. [146, 147] in an 8-bladed variant. The propeller blade geometry is defined in Fig. 3.2 c. It is similar to the XPROP propeller blade, but it has relatively larger chord lengths and is thinner. The F29 propeller was selected for reason of availability, as two identical propeller models were needed to study interaction between propellers. Isolated results for this propeller are shown in Sections 4.1.2 and 4.2.2 and results in interaction in Section 6.2.

The smallest tested propeller is the Beaver propeller. This 4-bladed propeller features a radius of $R_p = 0.1185$ m, with a blade pitch angle of $\beta_{0.7R_p} = 24.9$ deg ($\beta_{0.75R_p} = 23.9$ deg). The propeller design is representative of older, low-speed propellers, as the root section of the propeller blade is circular and transforms to an airfoil over the root

Table 3.1: Experimental propeller models.

Prop #	Name	B	R_p (m)	$\beta_{0.7R_p}$ (deg)	characteristic features
1	APIAN	6	0.2540	42.0	highly-swept, thin and very large chord length
2	XPROP	6	0.2032	20.0, 30.0	no sweep, medium chord length
3	F29	4	0.1524	20.0	no sweep, thin and large chord length
4	Beaver	4	0.1185	24.9	no sweep, circular root

part of the blade. The propeller blade geometry is defined in Fig. 3.2 based on Ref. [142] and the aerodynamic characteristics of the isolated propeller are discussed in Section 4.1.3. This propeller was used in a validating experiment for a wingtip-mounted tractor-configuration and was therefore also used in the numerical analyses of the same configuration in Sections 5.1 and 5.2.

3.1.2. WIND-TUNNEL FACILITIES

The experiment featuring the APIAN propeller was performed at the large low-speed facility of the German–Dutch wind-tunnels (DNW–LLF). This closed-circuit low-speed wind-tunnel was operated in the open-jet configuration, with an outlet of 8.00×6.00 m. At the selected freestream velocity of 60 m/s, the turbulence intensity is 0.24% in the longitudinal direction and 0.13% in the lateral direction.

The XPROP and F29 propellers were used in experiments in Delft University of Technology's Open Jet Facility (OJF). This open-jet closed-circuit wind-tunnel features a maximum freestream velocity of about 30 m/s from the octagonal outlet of 2.85×2.85 m. The settling chamber is equipped with a honeycomb flow rectifier and five screens to remove spatial velocity deviations and to reduce the turbulence level of the flow. This results in velocity deviations below 0.5% in the vertical plane at 2 m downstream of the outlet, and a longitudinal turbulence intensity level below 0.24%. The contraction and outlet of the tunnel can be seen in Fig. 3.5 b for the XPROP propeller setup and Fig. 3.7 a for the F29 propeller setup.

The data set used for the validation and comparison of the wingtip-mounted tractor-propeller simulations with the Beaver propeller was obtained in the Low-Turbulence Tunnel (LTT) at Delft University of Technology. This low-speed, closed-return wind tunnel features a test section with cross-section of 1.80×1.00 m in case a reflection plane is installed in the top part of the test section, as done for the measurements discussed here. At the selected freestream velocity of 40 m/s, the turbulence level is below 0.1%. Transition was forced on the reflection plane with a zig-zag transition strip.

3.1.3. MODELS AND MEASUREMENT TECHNIQUES

The models and measurement techniques are described in the next paragraphs for the four propellers. The APIAN propeller was used for a setup to investigate interaction with swirl-recovery-vanes (SRVs). The XPROP propeller was tested at large angle of attack with and without the influence of a wing to investigate interaction occurring for the compound helicopter in hover. The F29 propellers were used to study interaction between propellers. At last, with the Beaver propeller, the interaction for a wingtip-mounted tractor-propeller was investigated.

APIAN PROPELLER SETUP FOR INTERACTION WITH SRVS

Since the experimental data was only used for validation of the APIAN CFD simulations in isolation and in interaction with SRVs, for a detailed description of this experiment the reader is referred to Refs. [68, 142]. A short summary is presented here.

The APIAN propeller and downstream SRVs were mounted on a support structure in the wind-tunnel. Their geometry is sketched in Fig. 3.3. The SRVs were designed to achieve a positive efficiency increase for advance ratios up to $J = 1.75$. Although not opti-

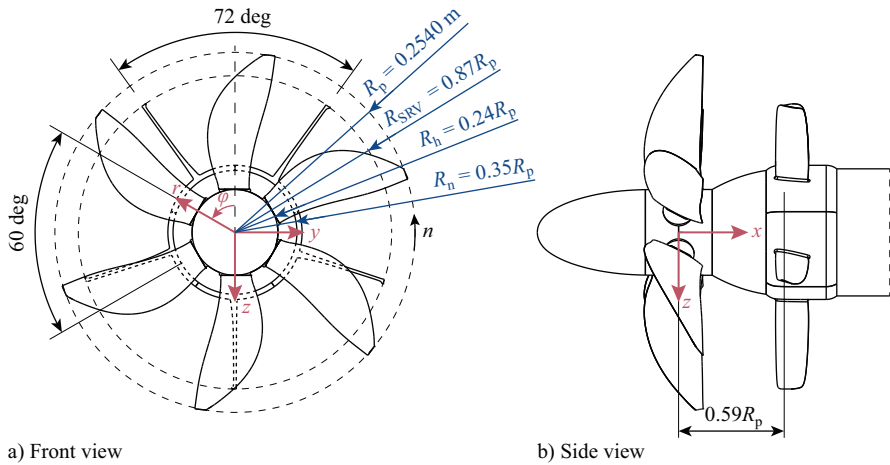


Figure 3.3: Sketch of the APIAN propeller setup geometry with SRVs.

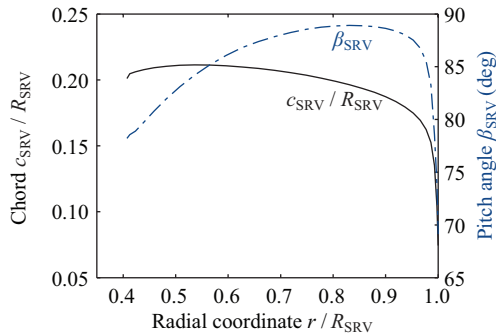


Figure 3.4: Radial distributions of the chord and pitch angle of the SRVs.

mized for maximum aerodynamic or aeroacoustic performance, the used SRV geometry introduced all flow phenomena relevant to a typical propeller–SRV configuration, and therefore is considered adequate for the purpose of this research. The radial distributions of the chord and pitch of the SRVs satisfying the design objective were defined using an in-house developed, low-fidelity design method based on the propeller analysis and design program XROTOR [148]. In this process, the number of SRVs, the SRV radius, and the propeller–SRV spacing were fixed. A total of five vanes was chosen to limit interaction noise by reducing the number of both total and concurrent interactions compared to an axisymmetric propeller–SRV configuration with six SRVs. The SRVs were distributed around the nacelle at circumferential angles of $\varphi_{SRV} = [36, 108, 180, 252, 324]$ deg. To minimize additional noise due to the interaction between the tip vortices of the propeller blades and the SRVs, the radius of the SRVs was set to 90% of the local contracted slipstream radius, resulting in an SRV radius of 87% of that of the propeller. The spacing between the propeller and the SRVs was equal to approximately 60% of the propeller radius. The selected distributions of the SRV chord and pitch angle are shown in Fig. 3.4.

The pitch angle β_{SRV} is defined here in the same way as used for the propeller blade. A symmetrical airfoil was selected for the entire vane; manufacturing constraints on the minimum thickness led to the selection of an NACA 0009 profile. Later studies [63, 143], performed after the experiment had been completed, showed that cambered airfoils typically provide better performance.

The propeller was connected to a rotating shaft balance (RSB), which provided measurements of the propeller thrust and torque during operation. Surface-pressure transducers were integrated into the propeller blades to obtain phase-accurate pressure distributions. The SRVs were not instrumented, but the effects of the SRVs on the flow-field in the propeller slipstream were quantified using stereoscopic particle-image velocimetry (PIV). The measurements were taken in longitudinally adjacent planes, located slightly below the propeller axis at a vertical position of $Z/R_p = 0.03$ due to a small misalignment of the setup.

All presented results are at a freestream velocity of $V_\infty = 60$ m/s, which is the default setting for acoustic measurements at DNW-LLF. Symmetric inflow conditions were considered ($\alpha = \beta = 0$ deg), while three different propeller operating conditions were evaluated, corresponding to high, medium, and low thrust conditions. The associated advance ratios were $J = 1.05, 1.40,$ and 1.75 , leading to measured propeller thrust coefficients of $C_T = 0.51, 0.36,$ and 0.18 , respectively.

XPROP PROPELLER SETUP FOR INTERACTION WITH WING AT LARGE ANGLE OF ATTACK

The XPROP propeller was driven by a TDI 1999 turbine air motor, mounted in a nacelle on top of a pylon, see Fig. 3.5 a. The dimensions of this setup are shown in Fig. 3.6. The pylon was fixed to a turn table to allow change of propeller angle of attack α_p from 0 deg to 90 deg. No angle larger than 90 deg was considered, since at larger angles the exhaust of the air motor at the rear of the nacelle would have been disturbed by the wind tunnel jet. The bottom wall of the wind-tunnel contraction outlet was extended beyond the pylon, effectively creating a 3/4 open jet test section.

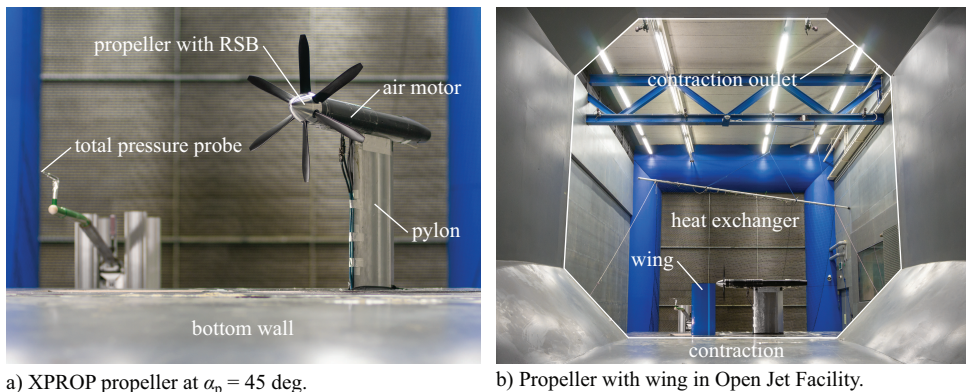


Figure 3.5: Photos of experimental setup for the XPROP propeller in the Open Jet Facility (OJF) at Delft University of Technology.

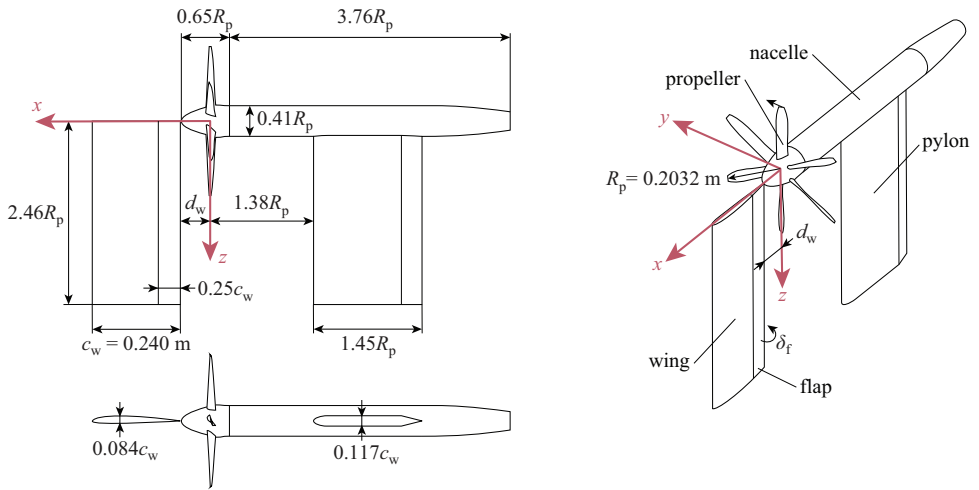


Figure 3.6: Side, bottom and isometric view of XPROP propeller setup at $\alpha_p = 90$ deg with wing, including dimensions.

A wing was used to study interaction effects typical for the investigated compound helicopter in hover. The straight, cambered wing of chord $c_w = 0.240$ m with $0.25c_w$ flap was positioned in front of the propeller for $\alpha_p = 90$ deg with the wing planform perpendicular to the freestream flow, see Fig. 3.5 b. Its dimensions are also provided in Fig 3.6. The chordwise distance of the wing to the propeller d_w and the flap deflection δ_f could be varied, as this was of interest to see if the effect of the wing on the propeller performance could be reduced.

The measurements consisted mainly of force and moment measurements of the propeller with spinner. This was achieved with a custom 6-component rotating shaft balance [149]. This sensor has a range of ± 344.1 N for the thrust, ± 200 N for the in-plane forces, ± 28.7 Nm for the torque and ± 20 Nm for the out-of-plane moments. The root mean square (rms) full scale error in a rotating reference frame, obtained from applying a series of static load cases with known weights, are 0.02% for the thrust, 0.23% and 0.14% for the in-plane forces, 0.05% for the torque, and 0.13% and 0.10% for the out-of-plane moments, respectively. The sensor was attached to two 24 bit data acquisition cards with custom LabVIEW data acquisition software and data was gathered at each measurement point with 10,000 Hz sampling frequency in a sweep of rotational speeds. An up-and down-sweep in rotational speed and a separate up-sweep was performed for each measurement condition with a measurement time of 10 s and 15 s respectively for cases without wing and 15 s and 20 s respectively for cases with wing. Different measurement times were chosen for the same measurement condition to establish confidence that the measurement time was sufficient to average out unsteady effects. The cases with wing were measured for a longer time because of the increased unsteadiness of the propeller loading due to the wing.

A zero measurement was taken before and after each sweep to minimize the effect

of drifts on the results. The zero measurements were applied to the data using a linear fit based on the zeros and the measurements timestamps. With an air supply control system, the rotational speed of the air motor was set. All measurements were taken at frequencies above the eigenfrequency of the propeller test stand and multiples of the eigenfrequency were also avoided. The rotating components, so the propeller blades, hub, spinner and the RSB have been spin balanced on a Schenck type M466 balancing machine according to ISO standard 1940. Maximum peak-to-peak fluctuations in rotational speed of typically 0.5% were found during the measurements for the cases without wing and 1.1% for the cases with wing. Based on the recorded one-per-revolution trigger signal, the force and moment data was phase-averaged, a reference frame transformation was applied from a rotating reference frame to a stationary frame, and the data was corrected for the mass of the propeller with spinner. Based on the three repeated measurements of the same condition, 95% simultaneous confidence bands were calculated. Confidence intervals based on these bands are plotted in the results throughout the dissertation.

The propeller performance includes the loading on the blades and spinner, i.e. no blades off aerodynamic tares have been subtracted from the results. This choice was motivated partly from the observations of Ortun et al. [72] for an isolated propeller at angle of attack, which showed that the aerodynamic loading on the propeller blades cannot be separated experimentally from the loading on the spinner, except if both elements are instrumented with their own balance. The pressure field resulting from the loading on the blades determines part of the loading on the spinner.

Besides the balance measurements, a Kiel probe was used to measure total pressure for reference as shown in Fig. 3.5 a. Furthermore, the wing was instrumented with tufts to visualise the shearlines on its surface under the influence of the propeller. The loading on the wing was not measured as this study focused on propeller performance effects.

Several wind-tunnel wall corrections should be considered when testing in an open jet tunnel with a propeller model. First, an inflow velocity correction due to blockage was considered based on Sayers and Ball [150]: This resulted in a corrected advance ratio of $J_c \approx 1.03J$ with a blockage area of 4.3% of the contraction outlet cross-sectional area, based on the worst case scenario of the propeller setup and wing at 90 deg angle of attack. Furthermore, a correction of the advance ratio is needed due to the sink effect of the propeller when operating at small angle of attack. The method discussed by Hackett et al. [151] for a closed-section wind-tunnel was extended for application to an open jet tunnel [152]. The corrected advance ratio in this method is equal to:

$$J_c = \frac{J}{1 + \frac{S_p}{S_{ts}} \left(\sqrt{1 + \frac{8}{\pi} T_C} - 1 \right)} \quad (3.1)$$

where S_p is the area of the propeller disk, S_{ts} the contraction outlet cross-sectional area and T_C the thrust coefficient based on freestream. This correction was applied to the wind-tunnel data with freestream flow without wing, and correction results are shown in Section 4.1.1. For measurements at angle of attack, only the component of the thrust in the wind-tunnel axial direction was considered in Eq. (3.1).

The last considered wall correction corrects the angle of attack when operating the propeller at large angle of attack following the method of Langer et al. [153]. The method assumes that the propeller thrust is equivalent to lift in the classical Glauert wall correction method. The required angle of attack correction then is:

$$\Delta\alpha_p = \frac{2\delta_w C_{T_r} S_p}{\mu^2 S_{ts}} \quad (3.2)$$

where δ_w is the boundary correction factor, C_{T_r} the thrust coefficient as defined for helicopter rotors, and μ the ratio of freestream to blade tip speed. A value of $\delta_w = -0.14$ was assumed, slightly reduced compared to the open jet tunnel value in Langer et al. [153] since this setup is effectively a 3/4 open jet and based on observation of the values in Barlow et al. [154]. Note that this assumption is quite uncertain. The angle of attack correction was also applied to the wind-tunnel data with freestream flow without wing, and correction results are shown in Section 4.1.1. For measurements at angle of attack, only the component of the thrust perpendicular to the wind-tunnel axial direction was considered in Eq. (3.2).

A correction for buoyancy was not considered in this research, since the body of interest has a relatively small dimension in the wind-tunnel axial direction.

F29 PROPELLER SETUP FOR INTERACTION WITH PROPELLER

For this experiment two custom propeller units were designed and manufactured. Each propeller was driven by an electric motor that was mounted inside an aluminium nacelle. One of the propeller units (propeller unit A) was instrumented with a static 6-component force/torque (F/T) sensor for performance measurements, while the other unit (propeller unit B) was not instrumented with an F/T sensor. An exploded view of propeller unit A (with F/T sensor) is shown in Fig. 3.8. In order to measure the aerodynamic loading on the propeller blades, hub and spinner, the electric motor was mounted to the F/T sensor, and the sensor on its turn to the nacelle. The motor shaft passed through a hole in the center of the F/T sensor. On the front of the nacelle an optical rotary encoder was mounted to the shaft to measure rotational speed.

To keep the temperature of the electric motor low and to prevent too large variations in F/T sensor temperature, a copper watercooling coil was wound around the electric motor. Each electric motor was driven by an electronic speed controller connected to a 5kW DC power supply. Both were controlled via custom LabVIEW control software, programmed to maintain a constant desired rotational speed. Maximum peak-to-peak fluctuations in rotational speed of typically 0.3% were found during the measurements. The dimensions of the propeller unit are given in Fig. 3.9 a in terms of propeller radius.

The propeller units were tested in three different configurations:

- as isolated (ISO) propeller,
- in one-after-another (OAA) configuration,
- and in side-by-side (SBS) configuration.

These configurations are sketched in Fig. 3.9 a, b and c, respectively. For the SBS configuration, as shown in Fig. 3.10 a, both propeller units were in tractor configuration,

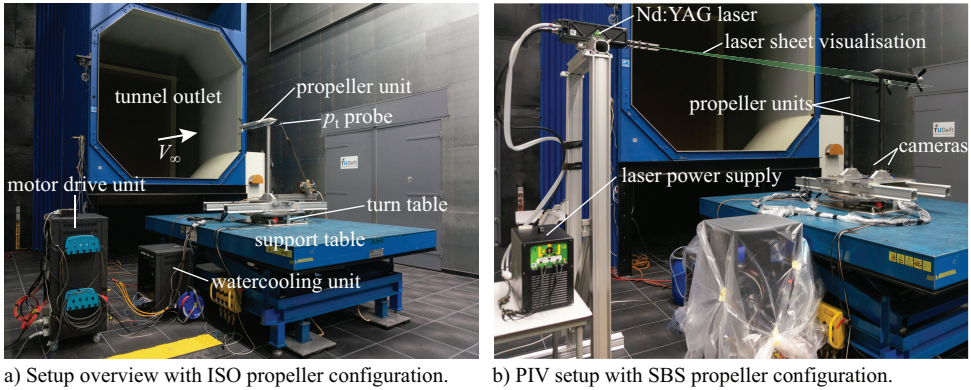


Figure 3.7: Overview of F29 propeller experimental setup in the Open Jet Facility (OJF) at Delft University of Technology.

clamped next to each other on sliding platforms attached to two beams on a turn table, to allow for change of both d_y and α_p . For the OAA configuration, as shown in Fig. 3.10 b, the front propeller unit was placed in a pusher configuration to avoid any disturbing elements between the two propellers. In this way, the pylon of the front propeller was furthest away from the rear propeller. To convert the propeller unit from tractor to pusher configuration, the unit was turned 180 deg, the spinner was interchanged with the nacelle aftbody, and the propeller blade pitch was changed by 180 deg. Since the rotation direction of the motor was switched, the propeller rotated in the same direction in tractor and pusher configuration. A NACA 65-021 fairing was placed over the steel pylon to reduce the wake impinging on the propeller in pusher configuration, see Fig. 3.8. This profile was chosen to align the profile maximum thickness with the pylon, while the profile leading edge reached up to the front of the nacelle.

A sideview sketch of the OAA and SBS configuration in the wind-tunnel is shown in Fig. 3.11 a and b respectively, clarifying the relative positioning of the propeller units with respect to the tunnel outlet. The height adjustable support table with turn table enabled the correct positioning and orientation of the propeller units. Furthermore, change of d_y was achieved by clamping the sliding platform of the rear propeller at different locations on the beams and change of d_x was done by mounting of the rear propeller unit including beams at a different position on the support table.

The sensor used to measure propeller performance was an ATI-IA Mini45 Titanium 6-component F/T sensor with SI-240-12 calibration. Variants of this sensor have also been used for propeller performance measurements in Refs. [155–160]. This sensor has a range of ± 480 N for the thrust, ± 240 N for the in-plane forces and ± 12 Nm for all moments. The typical effective resolution and factory tested full-scale error, established by taking the average error of a series of different calibration load cases, are 1/15 N and 0.06% for the thrust, 7/60 N and 0.23% for the in-plane forces, 1/8000 Nm and 0.04% for the torque, and 3/2000 Nm and 0.15% for the out-of-plane moments respectively. The F/T sensor was attached to two 24 bit data acquisition cards with custom LabVIEW data

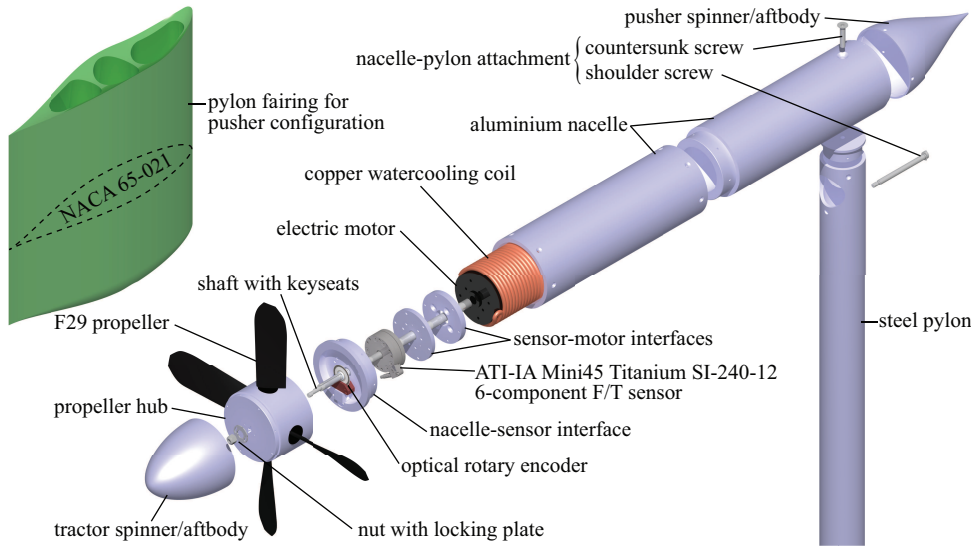


Figure 3.8: Exploded view of the F29 propeller unit A (with F/T sensor), indicating the various components.

acquisition software and data was gathered at each measurement point for 10 s with 10,000 Hz sampling frequency in a sweep of different rotational speeds.

In line with the findings of Gunasekaran et al. [156], the sensor was found to be prone to drifts, especially in thrust direction. This was mostly a result of temperature changes caused by the electric motor during testing. To minimize the effect of drifts on the results, short rotational speed sweeps were taken of maximum nine points, and a zero measurement was taken before and after each sweep. The zero measurements were applied to the data using a linear fit based on the zeros and the measurement timestamps. Four non-consecutive sweeps, two up- and two down-sweeps, were performed for each condition, and 95% simultaneous confidence bands were calculated based on those four measurements per condition. Confidence intervals based on these bands are plotted in the performance results throughout the dissertation. In Gunasekaran et al. [156], also a systematic error is discussed which seems related to off-axis loading of the sensor. Considering that our setup can be categorized as an axial mount according to their definition, no such error should arise for our setup. A small reference frame transformation in axial direction was needed to obtain the propeller performance results from the sensor reference center to the propeller center.

The propeller performance includes the loading on the blades, hub and spinner as defined in Fig. 3.8, i.e. no blades off aerodynamic tares have been subtracted from the results. Similar to the XPROP propeller setup, the pressure field resulting from the loading on the blades determines part of the loading on the hub and spinner. Furthermore, for the presented cases where aerodynamic interaction occurs between the propellers, the flowfield experienced by the spinner and hub is a function of the loading on both propellers. Therefore a blades off tare would not be representative of the loading on the

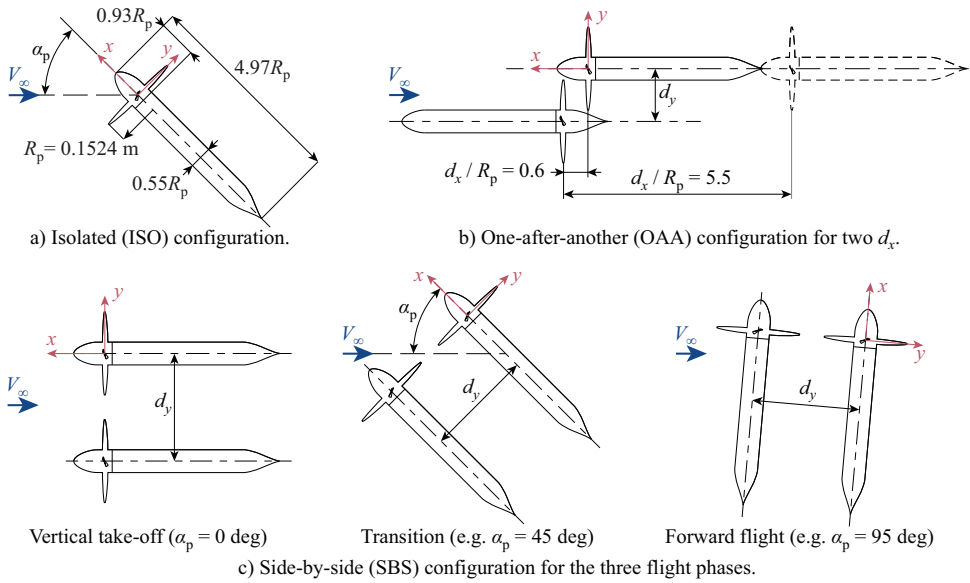


Figure 3.9: Top view sketch of the ISO, OAA and SBS F29 propeller configurations, including dimensions of the tractor propeller unit.

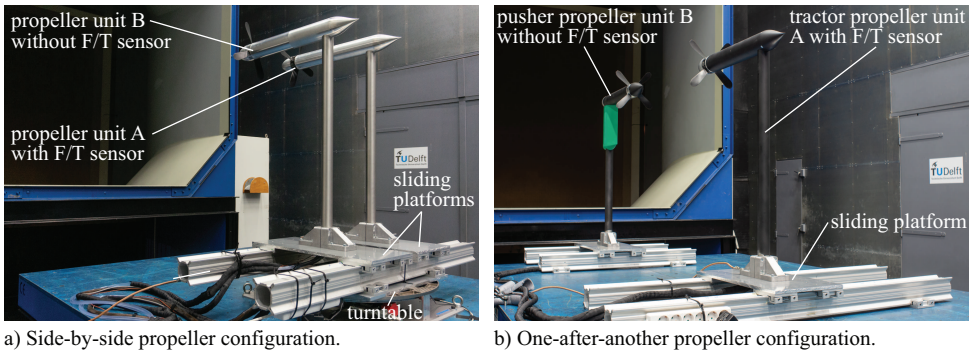


Figure 3.10: Experimental setup of the F29 SBS and OAA propeller configurations.

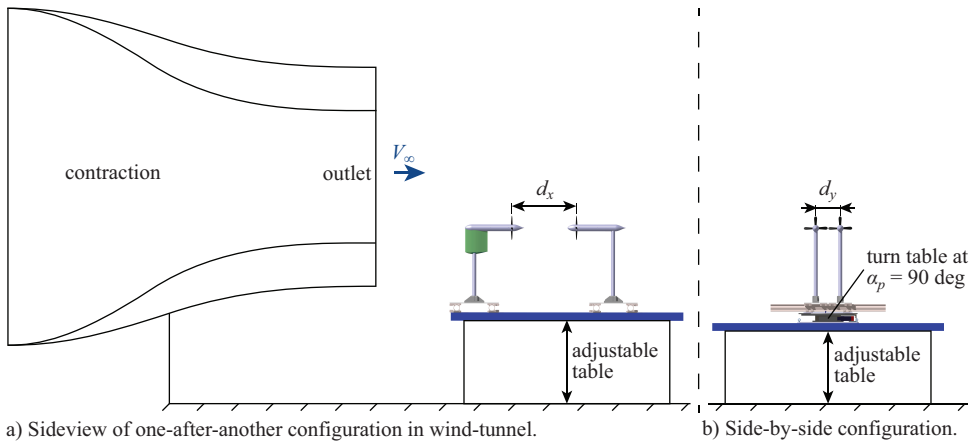


Figure 3.11: Sideview sketch showing the positioning of the OAA and SBS configuration in the wind-tunnel.

spinner and hub with blades installed.

Operating a propeller in a wind-tunnel requires wall corrections. Methods for correction of propeller performance data at small and large angle of attack in the same wind tunnel were discussed for the XPROP propeller setup in the previous section. Corrections on advance ratio and propeller angle of attack were considered due to blockage from results of Sayers and Ball [150], due to the sink effect of the propeller when operating at small angle of attack and due to the lift by the propeller when operating at large angle of attack following the method of Langer et al. [153]. While blockage for this experiment was negligible, a maximum advance ratio reduction of 1% should be considered by the reader in the interpretation of the results due to the sink effect for the lowest J at $\alpha_p = 0$ deg, and a maximum angle of attack reduction of 0.5 deg due to lift by the propeller for the lowest J at $\alpha_p = 95$ deg.

Total pressure measurements were performed behind the ISO propeller units to verify the F/T sensor thrust measurement, to verify the blade pitch setting of propeller unit B (without F/T sensor) through its thrust, and to establish a quantitative, time-averaged description of the slipstream flowfield. A total pressure probe was traversed through the slipstream just behind the propeller as shown in Fig. 3.7 a and was connected to a digital pressure gauge with a range of -1000 Pa to $+3500$ Pa and a full-scale accuracy of 0.03%. Measurements were taken for 10 s at a 3 Hz sampling frequency.

Flowfield measurements were taken in the wake of the propellers for the SBS configuration at $\alpha_p = 90$ deg using planar particle-image velocimetry (PIV). Figure 3.7 b illustrates the positioning of the PIV measurement plane with respect to the models. Details of the measurement and postprocessing characteristics of the PIV setup are given in Table 3.2. Only phase-uncorrelated measurements were taken, with a total number of 1000 image pairs to achieve convergence of the mean flowfields. Postprocessing was performed using an iterative multi-grid approach [161], with a final window size of 16×16 pixel and 75% overlap. The resulting vector spacing of 0.4 mm was sufficient to

Table 3.2: Measurement and postprocessing characteristics of the PIV setup for the F29 propeller test.

Parameter	Value
Laser	Nd:YAG 200 mJ
Cameras	2 × 5.5 Mpx sCMOS
Objective	50 mm $f/8$
Field-of-view size	270 × 227 mm
Pulse separation	30 μ s
Max. particle displacement	10 pixel
Image pairs	1000
Final interrogation window size	16 × 16 px
Window overlap factor	75%
Vector spacing	0.4 mm
Uncertainty instant. velocity	0.050 V_∞
Uncertainty mean velocity	0.011 V_∞

characterize the slipstream development and identify the dominant flow structures in the wake of the propellers. The method by Wieneke [162] was used to calculate the uncertainty of the instantaneous velocity components, while the statistical uncertainty of the mean velocity components was obtained from the variations between uncorrelated samples at each vector location and the local number of samples available for averaging. This was calculated for the results at a medium propeller thrust level ($J = 0.62$). Table 3.2 includes the resulting uncertainty values averaged over the field of view. Note that the statistical uncertainty of the mean also contains a contribution due to turbulence (next to the contribution due to uncertainty of the instantaneous velocity fields).

BEAVER PROPELLER SETUP FOR INTERACTION WITH WINGTIP

For this experiment, a tip-mounted propeller configuration was installed in the wind tunnel by connecting a tractor propeller mounted on a nacelle to the tip of a symmetrical wing model. The geometry used for the validation experiment dictated the geometry used for the simulations. Therefore, the setup of the experiment is summarized here. The full details of this experimental campaign are discussed by Refs. [16, 142]. Velocity and total-pressure data measured with the same propeller and nacelle in a sting-mounted configuration were taken from Sinnige et al. [163] and used to validate the simulations of the isolated propeller configuration.

Technical drawings of the propeller–wing configuration are provided in Figs. 3.12 and 3.13. The straight, symmetrical wing model had a chord length of 0.240 m, a semi-span of $s_w = 0.327$ m, and a NACA 64₂A015 profile with a rounded trailing edge of $0.0025 t_w$ radius. The distance from the propeller center to the wing leading edge was fixed to 43% of the propeller diameter, and boundary-layer transition was forced on the wing at 12% of its chord using silicon carbide particles. A 25%-chord plain flap, integrated into the wing model, was used to simulate the effects of camber. The model was connected to a turn table integrated into the reflection plane, allowing for measurements at nonzero angle of attack.

The integral forces and moments generated by the propeller–wing configuration were acquired using an external six-component balance. The wing model contained 408 pressure taps, providing local measurements of the pressure distribution along the chord at

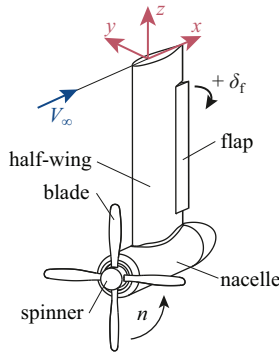


Figure 3.13: Isometric view of the wingtip-mounted tractor-propeller test setup with Beaver propeller.

number based on the wing chord and freestream velocity of $6.6 \cdot 10^5$. Only data measured at an angle of attack of 0 deg were considered, in order for the propeller to be at zero incidence with respect to the freestream and thus simplify the problem. Flap deflections of $\delta_f = +10$ deg and $\delta_f = -10$ deg were selected to represent the cases for which the rotation direction of the wingtip-vortex is opposite or equal to that of the propeller slipstream swirl. In other words, they represent inboard-up and outboard-up propeller rotation for a wingtip-mounted tractor-propeller. These flap deflections maximized the wing lift without significant separation on the flap. Measurement data with the blades installed were used at an advance ratio of 0.8, as well as data with the blades removed.

3.2. NUMERICAL APPROACH

This section on the numerical approach is split in a description on the propeller modelling methods in Section 3.2.1, an overview of RANS CFD solvers used in this dissertation in Section 3.2.2, the geometry, domains and boundary conditions of the various studies in Section 3.2.3 and a description of the grid generation and grid dependency studies in Section 3.2.4.

3.2.1. PROPELLER MODELLING METHODS

A range of propeller modelling methods are used in this dissertation. They can be split in methods involving RANS CFD simulations and lower order methods. In terms of RANS CFD methods, a split can be made between resolving the propeller in the grid or modelling the propeller with an actuator-disk or actuator-line approach. RANS CFD simulations form the backbone of this work. For design optimisation and quick analysis, also a blade element momentum and lifting line method have been utilized. The specifics of all propeller modelling methods are discussed in the next sections.

RESOLVING PROPELLERS IN RANS SIMULATIONS

Two propeller models are used in which the blades are resolved in the simulation. The most accurate and computationally costliest method uses grid motion to rotate the propeller. A rotating subdomain around the propeller and spinner is connected to the stationary part of the domain via sliding mesh interfaces. On these interfaces, interpolation

of the flow quantities takes place. This is a common method used for propellers or rotors, e.g. in Refs. [91, 97, 164–166]. This method inherently requires the problem to be solved transient. This approach is sometimes referred to as full-blade model in this dissertation.

An alternative to grid rotation is simulation with a multiple reference frame model (MRF) or frozen rotor interface. By applying a reference frame transformation to the sub-domain around the propeller and slipstream, propeller motion can be simulated. If the geometry and inflow is axisymmetric, the problem can be simulated approximately as a steady problem, reducing the computational cost considerably. Of course, this steady approximation is only valid if no significant flow separation occurs with a time dependent character from for instance the propeller blade root or nacelle. This method is found sometimes in literature for propeller simulation, e.g. in Refs. [167, 168]. This approach is applied to obtain isolated propeller performance at zero angle of attack with a single blade passage. It is needed to also apply the rotating reference frame to the slipstream domain as the propeller is not effectively moving and thus otherwise not the correct helix angle would be obtained for the blade tip- and root-vortices and wakes. A moving wall, stationary in the absolute frame, is then applied to the nacelle in case of a tractor-propeller, to enforce a no-slip condition with respect to the stationary frame.

ACTUATOR-DISK AND ACTUATOR-LINE MODELLING IN RANS SIMULATIONS

Instead of resolving the propeller, its effect can be modelled in the simulation by sources of momentum and energy. In the so-called actuator-line model, the propeller blades are replaced with distributions of momentum sources and energy sources along lines representing the blades. Figure 3.14a provides the definition of the propeller reference frame located in the propeller plane with n the rotational speed and \vec{T} and \vec{Q} the thrust and torque vector respectively. Let $T'(r, \varphi_b)$ and $Q'(r, \varphi_b)$ be the radial thrust and torque distributions per unit of length acting along blade b with φ_b the azimuthal location or phase angle of blade b . For cell c in Fig. 3.14 b, the momentum source term vector $\vec{F}(x, r, \theta)$ and energy source term $S(x, r, \theta)$ per unit of time and volume can then be written as:

$$\vec{F}(x, r, \theta) = \eta_x \eta_\theta \left(T' \vec{n}_T + \frac{Q'}{r} \vec{n}_Q \right) \quad (3.3)$$

$$S(x, r, \theta) = \eta_x \eta_\theta \vec{F} \cdot \vec{V} \quad (3.4)$$

where \vec{n}_T is a unit vector opposing the thrust direction and $\vec{n}_Q(\theta)$ a unit vector opposing the local torque direction. The energy source term is equal to the work done on the fluid per unit of time and volume. The terms η_x and η_θ are regularization functions to smoothly distribute the source terms in the volume in axial and azimuthal direction to avoid singular behaviour. A one-dimensional Gaussian kernel was chosen for each of them, based on the work of Sørensen et al. [169], in which a three-dimensional Gaussian kernel was successfully used for an actuator-disk application. In the radial direction no regularization function is required, since the thrust and torque distributions are prescribed per unit of radial length. The regularization functions in axial and azimuthal direction are defined as:

$$\eta_x(x) = \frac{1}{\varepsilon \sqrt{\pi}} e^{-\left(\frac{|x|}{\varepsilon}\right)^2} \quad (3.5)$$

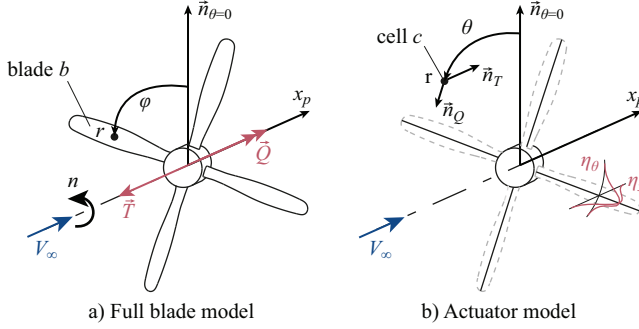


Figure 3.14: Propeller reference frame definition and actuator model variables.

$$\eta_\theta(r, \theta) = \sum_{b=1}^B \frac{1}{\varepsilon \sqrt{\pi}} e^{-\left(\frac{|\theta - \varphi| r}{\varepsilon}\right)^2} \quad (3.6)$$

where φ_b is the azimuthal location of blade b of the total of B blades and ε is a constant to adjust the strength of the regularization functions. For each of the cells in the domain, the actuator-line model calculates the x , r and θ location in the propeller reference frame. By updating φ_b at each timestep and updating the azimuthal regularization function for each cell, actuator-line movement is simulated. The regularization constant ε was kept equal to the local cell size as recommended Sørensen et al. [169]

Instead of representing the blades by lines, in the actuator-disk model their averaged effect on the propeller disk is modelled, taking into account radial and azimuthal variations in loading. While the actuator-line model is inherently time-dependent, a simulation with the actuator-disk model can be solved as a steady problem. The source terms are the same as in the actuator-line model, except for the azimuthal regularization function $\eta_\theta(r, \theta)$, which is replaced by:

$$\eta_\theta(r) = \frac{B}{2\pi r} \quad (3.7)$$

For the actuator-disk and actuator-line model, the propeller blade loading as a function of radius and azimuth is required from some source. An option is to extract the loading from full-blade propeller simulations. Since this requires full-blade simulations, no gain in computational cost would be achieved by this. However, it does allow evaluation of the applicability of actuator models in their most accurate form. In Section 5.1 this approach is followed to simulate a wingtip-mounted tractor-propeller. An approximation to this can be made in case the propeller sees a relatively freestream flow, by taking data from full-blade isolated propeller simulations and applying it with an actuator model to an installed propeller problem. In Section 5.2 the effects of windmilling for the wingtip-mounted tractor propeller are investigated in this way. Propeller blade loading can also be obtained from lower order methods like a blade element momentum or lifting line method, which is the approach taken in Section 5.3 for a wingtip-mounted pusher-propeller to investigate the upstream effect on the wing. Although not applied in

this dissertation, detailed experimental wake measurements behind the propeller would also be an applicable source of data for an actuator model.

The most promising approach to use actuator models is by predicting the loading on the propeller and applying that to the actuator model as a response to the propeller inflow occurring in the CFD simulation. This would require a database of propeller blade sectional data as function of Mach number and Reynolds number, a tip and hub loss model in case of the actuator-disk approach, and a model like the empirical model by Snel et al. [170] to correct two-dimensional sectional data for three-dimensional rotational effects. For propellers, such approach has mainly been used with the actuator-disk model by for instance Márquez Gutiérrez et al. [171], but application to the actuator-line approach is even more promising to simulate fully unsteady interaction problems. Also a slight variation to the actuator-line model exists, the actuator-surface model, where the sources are distributed in chordwise direction. A first application of an actuator-line model for propellers is found by Schollenberger et al. [172], and for helicopter rotors and wind turbines, research into this topic is also ongoing [173–175]. The difficulty lies in the extraction of the flowfield variables [173, 176], since the local effect of the source terms on the inflow needs to be corrected for. It is recommended for future research to further look into such model with propeller interaction problems.

LIFTING LINE AND BLADE ELEMENT MOMENTUM METHODS

Two lower order propeller methods are used in this dissertation. The first model uses a lifting line representation for the propeller blades. To perform quick propeller analyses and to aerodynamically design the propeller for optimized performance for the wingtip-mounted pusher-propeller problem in Section 5.3, a PROPELLER analysis and OPTIMISATION Routine named *PROPR* was set up based on XROTOR [148]. The software program uses discrete line vortices forming a semi-rigid wake to iteratively determine the induced velocities and has been used before by Refs. [63, 82, 177–179] for both uniform and non-uniform inflow.

All details of *PROPR* are described in the work of Nootbos [180] and a short summary follows here. A flowchart for propeller performance analysis with the tool is shown in Fig. 3.15. First, the propeller blade is defined in terms radial distributions of chord $c(r)$, twist distribution $\beta(r)$ and section profiles. The inflow to the propeller is not uniform as the tool was used for propeller analysis and design of a wingtip-mounted pusher-propeller. The flowfield behind the isolated wingtip was extracted from a RANS simulation, circumferentially averaged and provided to the tool in terms of radial distribution of axial $V_a(r)$ and tangential velocity $V_t(r)$. Circumferential non-uniformities are averaged as these result in time-dependent blade loading, which can not be analysed with XROTOR. Then XFOIL [181] is used to create a database with airfoil characteristics for the desired range of Reynolds numbers experienced over the advance ratio range. The tool then queries the database while calling XROTOR for propeller performance analyses for each desired J .

Twenty radial sections were used to define the propeller geometry and provide XROTOR with airfoil data. Fully turbulent flow for the airfoil data was assumed to allow comparison with the fully turbulent CFD simulations and to increase stability of running XFOIL in an optimisation framework. The non-linear part of the lift curve was modi-

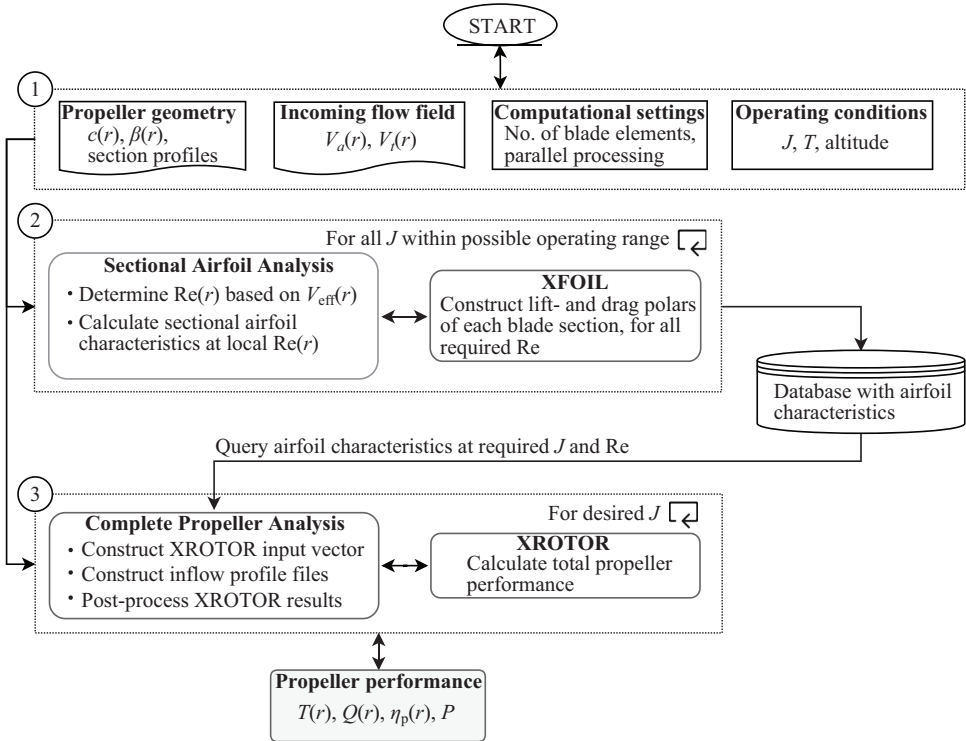


Figure 3.15: Flowchart of PROPR propeller performance analysis routine, modified from Ref. [180].

fied using an empirical model by Snel et al. [170] to correct two-dimensional data for three-dimensional rotational effects.

An optimisation routine was built around this propeller analysis tool using the non-linear programming solver *fmincon* in Matlab R2017b [182]. The optimisation objective was minimisation of the shaft power while an inequality constraint was set to obtain the desired thrust. The optimisation variables included the rotational speed and the radial distribution of blade twist and chord length. The number of blades and blade radius were varied parametrically.

The second lower order model was developed in the work of Usai [183]. A blade element momentum (BEM) model was extended to include the effects of OAA propeller interaction. Results of this model are plotted alongside the experimental results for this configuration in Section 6.2, to show that such a method can be used to predict performance. The model consists of four steps:

1. The front propeller loading distribution is determined with a BEM model.
2. The velocity distribution in the slipstream of the front propeller is calculated with a contraction model.
3. Induced velocities in the slipstream of the front propeller are superimposed on the rear propeller disk.

4. The rear propeller loading distribution is determined with a BEM model using the flowfield from step 3.

The blade element momentum model is based on the theory by Glauert [51] and uses the Prandtl tip and hub loss factor. Lift and drag predictions for each blade section were supplied from 2D analyses with RFOIL [170] at the correct Reynolds number and Mach number. This viscous-inviscid coupled solver with Karman-Tsien compressibility correction, developed for wind turbine research, includes an estimation of the rotational effects experienced on a rotating blade by formulation of a quasi 3D system of boundary layer equations that include the leading terms due to rotation. Free transition from a laminar to a turbulent boundary layer was estimated with a critical amplification factor of four, chosen based on the freestream turbulence level of the wind-tunnel. In case of non-uniform inflow, quasi steady results were calculated and then used as input to obtain an unsteady solution using non-stationary airfoil theory from Sears [184, 185]. This was similarly applied by Ref. [146] for the unsteady blade response of a propeller in the wake of a pylon.

The slipstream estimated by momentum theory at the front propeller disk was contracted using a model from Chandrasekaran [186]. Given the flow characteristics at the front propeller disk, it was possible to compute the evolution of the slipstream geometry and axial and tangential velocity components along the slipstream axis. These were then interpolated to the rear propeller disk at the desired d_x and d_y distance. A BEM analysis with the same model resulted in the performance of the rear propeller. Any upstream effect on the front propeller was not accounted for. Further details of this extended BEM model can be found in Ref. [183].

3.2.2. RANS CFD SOLVER SETUP

Three RANS CFD solvers were used for the results throughout this work:

- ANSYS[®] CFX release 16.0 [187] used in Sections 4.1.4 and 6.1, an unstructured, element-based, node-centered, finite-volume solver.
- ANSYS[®] Fluent version 16.0 [188] used in Sections 4.1.3, 5.1 and 5.2 and version 18.1 [189] in Sections 4.1.1, 4.2.1, 5.3 and 7.3. This is a commercial, unstructured, cell-centered, finite volume solver.
- ENFLOW used in Sections 7.1 and 7.2, a multiblock structured solver by NLR [165, 190–192].

The choice for these solvers has been a matter of availability, capabilities and requirements. Initially, CFX was used by the author for its profile transformation capability across interfaces, useful for propeller–stator simulations. Fluent provided more flexibility for the development of actuator models using user defined functions and therefore a switch was made to this solver. To use the computational resources at NLR for simulation in the PROPTER project, ENFLOW was utilized for the compound helicopter simulations, alongside single blade passage isolated propeller simulations using Fluent for comparison.

Although basic, a requirement to get simulations in line with the experiment is to provide the right boundary and flow conditions. Therefore a recap is given here. For all

simulations, the ideal-gas law was applied as equation of state, whereas the dynamic viscosity was obtained with Sutherland's law using standard atmospheric conditions [193]:

$$T = \frac{p}{\frac{R}{M_w} \rho} \quad (3.8)$$

$$\mu = \mu_{\text{ref}} \left(\frac{T}{T_{\text{ref}}} \right)^{3/2} \frac{T_{\text{ref}} + S}{T + S} \quad (3.9)$$

where T is static temperature, p static pressure, R universal gas constant, M_w molecular weight, ρ density, μ dynamic viscosity, μ_{ref} reference dynamic viscosity, T_{ref} reference temperature and S Sutherland temperature. Following the ideal gas assumption, the heat capacity at constant pressure C_p was calculated using:

$$C_p = \frac{\gamma \frac{R}{M_w}}{\gamma - 1} \quad (3.10)$$

where γ is the specific heat ratio. The values of all reference values and constants can be found in Table 3.3. The static pressure and density have to be selected in accordance to the standard atmosphere at the given height. This results in the following speed of sound a and Mach number M , given an airspeed V :

$$a = \sqrt{\gamma \frac{R}{M_w} T} \quad (3.11)$$

$$M = \frac{V}{a} \quad (3.12)$$

Following isentropic relations, the total pressure p_t and total temperature T_t are obtained with:

$$p_t = p \left(1 + \frac{\gamma - 1}{2} M^2 \right)^{\frac{\gamma}{\gamma - 1}} \quad (3.13)$$

$$T_t = T \left(1 + \frac{\gamma - 1}{2} M^2 \right) \quad (3.14)$$

This results in the following gauge pressure with respect to the operating pressure Δp_t for total pressure inlet boundary conditions:

$$\Delta p_t = p_t - p \quad (3.15)$$

For the swirl-recovery-vane simulations in CFX in Section 6.1, discretization of the advection term was done with an upwind scheme using the Barth—Jespersen boundedness principle [194] to be close to 2nd order accurate. The spatial derivatives of all diffusion terms were evaluated using shape functions following the standard finite-element approach. The alternate rotation model was selected, meaning the absolute velocity is used for the advection term instead of the relative frame velocity. To capture the unsteady aerodynamic interaction between the propeller and the SRVs, the governing equations were solved in a time-dependent manner by a 2nd order backward Euler scheme.

Table 3.3: Flow reference values and constants for RANS CFD simulations.

Parameter	Value
Universal gas constant R	8314.32 J/kmolK
Molecular weight M_w	28.9644 kg/kmol
Ref. dynamic viscosity μ_{ref}	$1.78938 \cdot 10^{-5}$ kg/ms
Ref. temperature T_{ref}	288.15 K
Sutherland temperature S	110.4 K
Specific heat ratio γ	1.4

Also for all simulations with Fluent, discretization of the advection term was done with an upwind scheme using the Barth–Jespersen boundedness principle [194] and time-dependent solutions were found by a 2nd order backward Euler scheme. Steady solutions were obtained using the pseudo transient under-relaxation method. Initial conditions were calculated using the full multigrid initialization method, where the Euler equations for inviscid flow are solved using first order-discretization on a series of reduced size grids to obtain an approximate solution.

For ENFLOW, the flow equations were discretized in space by a 2nd order cell-centred finite-volume method, using central differences and artificial diffusion. The steady flow equations were solved by a multi-grid scheme, using as relaxation operator a Runge-Kutta scheme. For transient solutions, the flow equations were integrated in time by a 2nd order implicit scheme, using the dual-time stepping method.

In general, a timestep equivalent to 1 deg of propeller rotation was used for the transient results as commonly found in propeller research [72, 86]. An exception was formed by the results in Section 5.1 and 5.3 for which a time step equivalent to 2 deg of propeller rotation was selected to reduce computational cost, at the cost of temporal resolution. Furthermore, for the most complex configuration of XPROP propeller setup in Section 7.3, a simulation was performed with a timestep equivalent to 0.5 deg and 2 deg of propeller rotation, to check the temporal resolution.

Three turbulence models were used throughout the dissertation. Initially, for the swirl-recovery-vane simulations in Section 6.1, the two-equation eddy viscosity $k - \omega$ model with shear stress transport correction [195] ($k - \omega$ SST) was used as often found in literature for propeller simulations [72, 196–198]. For the wingtip mounted propeller simulations in Chapter 5 the turbulence model was selected based on the findings of Kim and Rhee [92], who tested several turbulence models to simulate the wingtip vortex of an isolated wing. From the eddy viscosity models tested, the turbulence model in their research that best agreed with experimental data in terms of static pressure and axial velocity in the wingtip-vortex core was the Spalart–Allmaras (SA) one-equation model [199] with modification proposed by Dacles-Mariani et al. [200] to prevent build-up of turbulence viscosity in vortex cores. This model was therefore selected. Only a computationally more expensive Reynolds stress model performed slightly better, but that was out of the scope of the research. The $k - \omega$ SST model was also considered, although this model agreed poorly in terms of static pressure and axial velocity in the wingtip-vortex

core in the research of Kim and Rhee [92]. A comparison is presented between these two turbulence models for the isolated propeller and wing in Section 5.1.

Following the conclusions of the wingtip mounted propeller work, for the large angle of attack simulations with the XPROP propeller in Chapter 4 and XPROP propeller interaction with wing in Section 7.3 also the SA model was used. For the most complex configuration a simulation was performed with the $k - \omega$ SST to check the effect of turbulence modelling on the results.

Values for the inlet turbulence quantities were based on the recommendations by Spalart and Rumsey [201] for general use for most typical external aerodynamic applications, which resulted in an eddy viscosity ratio of 0.21044 for the SA model. For the $k - \omega$ SST model, the turbulence kinetic energy k and turbulence dissipation rate ω were calculated using [201]:

$$k = 1 \cdot 10^{-6} V^2 \quad (3.16)$$

$$\omega = 5 \frac{V}{L} \quad (3.17)$$

where L is a reference length, for instance the wing chord in case of the wingtip-mounted propeller simulations.

A third turbulence model was used for the compound helicopter simulations in ENFLOW. To model turbulence in the cruise condition, an explicit algebraic Reynolds-stress was selected for the Reynolds-stress tensor (EARSIM), combined with the TNT $k - \omega$ model to determine the relevant turbulent time and length scales [202]. For the hover condition the $k - \omega$ SST model was used again to promote convergence of this complex flowfield [195], as the flow was fully driven by the propellers and main rotor and large wakes were present below the wings and fuselage.

3.2.3. GEOMETRIES, DOMAINS AND BOUNDARY CONDITIONS

This section describes the geometry, computational domains and boundary conditions for each interaction problem for which RANS simulations were performed. Every case is treated in a separate section below.

APIAN PROPELLER SETUP FOR INTERACTION WITH STATOR

For the APIAN propeller, isolated propeller simulations and simulations with stator interaction were performed to study the effects of propeller – stator interaction on the flowfield and loading. The computational domain is illustrated in Fig. 3.16. For the isolated propeller simulations, only a single blade was simulated in a 60 deg wedge-shaped domain with cyclic periodic boundary conditions. The inlet and farfield were placed at a distance of $5R_p$ from the propeller, similar to the approach taken by Ortun et al. [72] for the same propeller, while the outlet was placed further away at $10R_p$ to reduce disturbances in the static pressure field. The simulation data were analysed to verify that the domain was sufficiently large. In terms of boundary conditions, the total pressure was prescribed on the inlet. On the outlet, the static pressure was specified to be on average over the outlet equal to the freestream static pressure. Finally, the farfield was modelled with a slip-wall boundary condition. The inlet conditions matched the experimental conditions, except for the turbulence quantities.

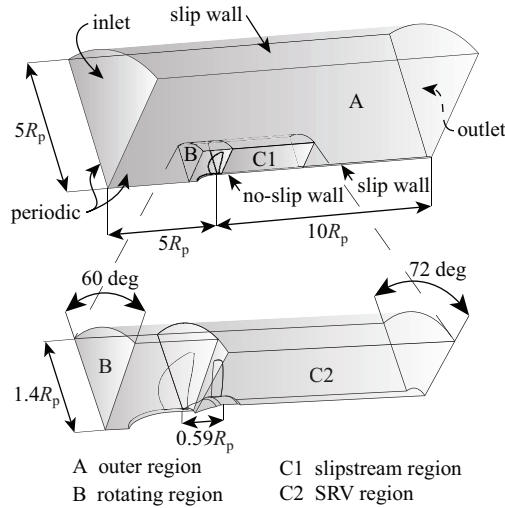


Figure 3.16: Definition of the computational domain for the APIAN propeller. With SRVs installed, the full annulus was simulated.

For the propeller–SRV simulations periodicity is not applicable, hence the full annulus was simulated. An exception was made to reduce computational cost for the grid convergence study of the SRVs, for which a profile transformation was applied to couple the rotating region (B in Fig. 3.16) and the SRV region (C2 in Fig. 3.16). In this way, the unequal pitch of the propeller and SRV domains was mitigated by a scaling of the flow profile across the interface between the propeller and the SRVs. This allowed for a simulation of a single blade and SRV to be made [187], which significantly reduced the computational cost of the unsteady simulations performed for the grid convergence study. The simulations were performed for 840 deg of propeller rotation, of which only the last 120 deg were used to eliminate startup effects.

XPROP PROPELLER SETUP FOR INTERACTION WITH WING AT LARGE ANGLE OF ATTACK

The XPROP propeller was used in an experiment to investigate the interaction with a wing representative of the interaction occurring on the compound helicopter in hover. Furthermore, isolated propeller performance was measured in static condition and with freestream flow at angle of attack. Five different geometries have been simulated with RANS CFD simulations alongside these experimental results:

SBP Single blade passage of the propeller and nacelle at $\alpha_p = 0$ deg.

PN Full annulus propeller and nacelle without pylon at various α_p .

PNP Full annulus propeller and nacelle with pylon at various α_p .

PNW Full annulus propeller and nacelle with wing without pylon at $\alpha_p = 90$ deg, $d_w = 0.4$ and $\delta_f = 0$ deg.

PNWP Full annulus propeller and nacelle with wing and pylon at $\alpha_p = 90$ deg, $d_w = 0.4$ and $\delta_f = 0$ deg.

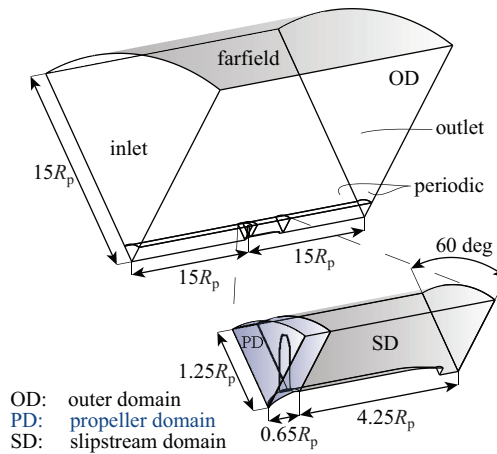


Figure 3.17: Sketch of computational domain for a single blade passage of the isolated XPROP propeller at zero angle of attack.

The geometry was the same as in the experiment as shown in Figs 3.2 b and 3.6. A simplification was present near the blade root, which has a cutout at the trailing edge in the experiment and continues to the spinner wall in the simulations. The wing flap was not modelled as only zero degree flap deflection cases were simulated.

Two different computational domains were used, a domain for a single blade passage (SBP) of the isolated propeller and nacelle at $\alpha_p = 0$ deg and a domain for all full annulus propeller simulations. The single blade passage domain including boundary conditions and dimensions is shown in Fig. 3.17. Since the wake of a propeller with axisymmetric nacelle is cyclic with the number of the blades, only a single blade could be modelled with periodic boundary conditions in a 60 deg wedge domain to reduce the computational cost. The outer dimensions of the domain were chosen to be sufficiently large with respect to the propeller radius, in order to minimize the influence of the boundary conditions on the flow properties near the propeller.

For simulations with freestream flow, at the domain inlet a total pressure was set to reach the desired freestream airspeed. Furthermore, the freestream total temperature was specified. At the domain outlet, the static pressure was prescribed to be on average equal to the freestream static pressure. A Riemann-invariant pressure farfield condition was specified with a Mach number, static pressure and static temperature complying with the inlet conditions.

For simulations at static condition, on the inlet, farfield and outlet the static pressure was prescribed to be on average equal to the undisturbed static pressure. Especially this condition required the large $15R_p$ distance of the boundaries from the propeller. By applying a reference frame transformation to the subdomain around the propeller (PD) and slipstream (SD) with the multiple reference frame model (MRF), propeller motion was simulated. A sliding mesh interface was present around the propeller domain. The propeller and spinner walls were modelled with a no-slip condition and the nacelle was

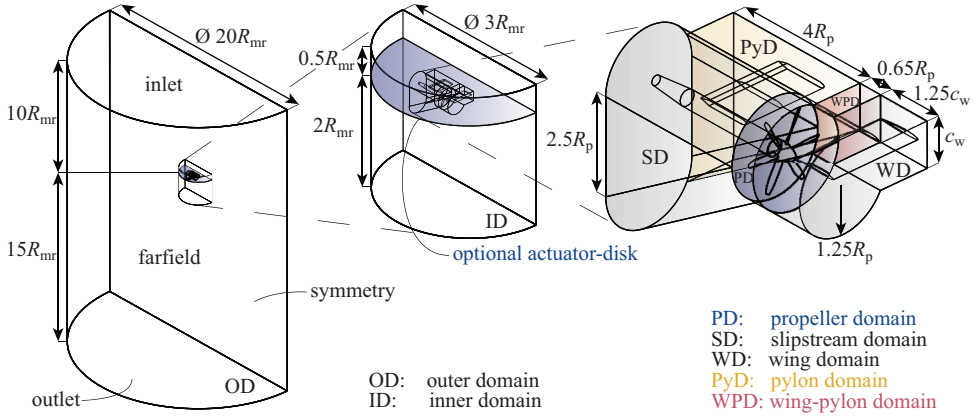


Figure 3.18: Sketch of computational domain for full annulus XPROP propeller at angle of attack and propeller-wing simulations with freestream or actuator-disk approach.

modelled with a moving wall, stationary in the absolute frame to counter the local reference frame transformation.

The propeller domain was copied and rotated to arrive at a full annulus propeller. The domain for the full annulus propeller simulations is shown in Fig. 3.18. This half cylindrical domain featured a symmetry boundary condition on the rectangular face, to approximate the single wind-tunnel wall in the 3/4 open jet configuration. For the simulations without wing and for some of the simulations with wing where a freestream airspeed was present, the same inlet, outlet and farfield conditions were set as for the single blade passage simulations. For the other simulations with wing, an actuator-disk was used to replace the freestream flow, to simulate the axial and radial flow of a helicopter main rotor in hover. For these simulations the static pressure on the inlet, farfield and outlet was prescribed to be on average equal to freestream static pressure. The actuator-disk approach from Ref. [64] was used with a thrust loading distribution based on the experimental data of the UH60 blade presented in Srinivasan et al. [203]. The UH60 data provides a realistic main rotor loading distribution in hover to introduce a typical radial non-uniform downwash distribution. Only the radial shape of the loading was used as the thrust level was tuned such that the downwash farfield velocity V_d was equal to the freestream airspeed V_∞ in the wind-tunnel following simple momentum theory [204]:

$$T_{mr} = \frac{1}{2} \rho_\infty V_d^2 S_{mr} = \frac{1}{2} \rho_\infty V_\infty^2 \pi R_{mr}^2 \quad (3.18)$$

The main rotor diameter was chosen equal to the width of the contraction outlet, resulting in $R_{mr} = 1.425$ m. The actuator-disk center coincided with the wing quarter-chord line and the distance between the main rotor and propeller was similar to the compound helicopter in Ref. [69]. The outer dimensions of the domain were chosen sufficiently large with respect to the main rotor radius ($\geq 10R_{mr}$), larger than the $5R_{mr}$ distance in Potsdam and Strawn [205] and larger than the largest tested distance of $9R_{mr}$ in Strawn and Djomehri [206].

The wing, pylon and wing-pylon domain were only present when these parts were simulated. For the simulations without wing, the propeller, slipstream and pylon domain could be turned to achieve the desired propeller angle of attack. The slipstream domain was shaped such that it captured the propeller slipstream for all tested angles of attack and operating conditions. Grid rotation of the propeller domain with sliding mesh interfaces was used to simulate propeller motion. All geometry walls were modelled with a no-slip condition.

3

BEAVER PROPELLER SETUP FOR INTERACTION WITH WINGTIP

For this setup to study interaction of a wingtip-mounted tractor-propeller, simulations were performed where the propeller was resolved in the grid, as well as simulations where the propeller was simulated with an actuator-disk and actuator-line model. Three different configurations were studied:

Isolated propeller configuration The isolated propeller configuration contained the propeller, spinner and nacelle. Unlike the wind-tunnel setup from Sinnige et al. [163], no sting was present. Considering the axisymmetry of the configuration, only a 90 deg wedge was modelled containing one propeller blade. The geometry is the same as used in the wind-tunnel model as shown in Fig. 3.13, but without the wing. The coordinate system for this configuration is located in the propeller plane with the x -axis through the rotation axis pointing in downstream direction as presented in Fig. 3.14a.

Wing configuration The wing configuration consists of all the components shown in Fig. 3.13 except the propeller blades, and the transition strip was not modelled since the simulations were modelled fully turbulent. The gaps around the flap that were present in the experiment were also incorporated in the numerical model: Along the leading edge of the flap, a gap was present with a width of $0.027 t_w$. A gap of the same width was implemented along the inboard flap edge. In the experiment, the outboard flap edge was flush with the wing and thus no gap was modelled there other than the gap arising from a flap deflection.

Propeller-wing configuration The propeller-wing configuration contained all components drawn in Fig. 3.13. The propeller was present for the full-blade representation of the propeller, while for actuator-disk and actuator-line representations, a spinner without blades was used like in the wing configuration.

A sketch of the domain including boundary conditions and dimensions used for the isolated propeller configuration is shown in Fig. 3.19. Since the wake of a propeller with axisymmetric nacelle is cyclic with the number of the blades, only a single blade was modelled with periodic boundary conditions in a 90 deg wedge domain to reduce the computational cost. This implies that the simulations were not performed in the wind-tunnel domain, as was done for the other configurations. The effect of neglecting the wind-tunnel walls was checked with a simulation and found to be insignificant for the considered propeller operating condition. The outer dimensions of the domain were chosen to be sufficiently large with respect to the propeller radius in order to minimize the influence of the boundary conditions on the flow properties near the propeller. At

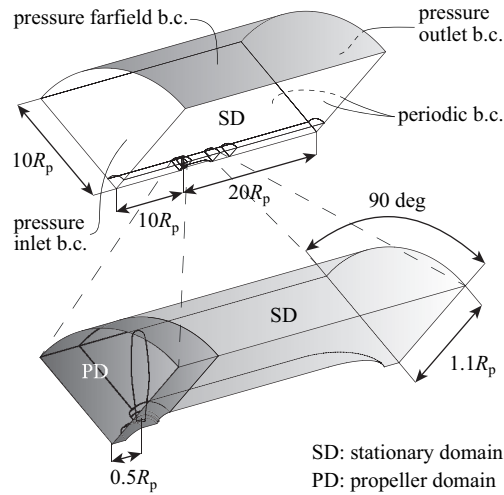


Figure 3.19: Computational domain and boundary conditions (b.c.) for the isolated Beaver propeller configuration.

the domain inlet, a total pressure was set to reach the freestream velocity of 40 m/s. Furthermore, the undisturbed total temperature was specified.

At the domain outlet, the static pressure was prescribed to be on average equal to undisturbed static pressure over the outlet. On the top of the domain, a Riemann-invariant pressure farfield condition was specified with a Mach number, static pressure and static temperature complying with the inlet conditions. The propeller blade, spinner and nacelle were modelled as no-slip walls. Due to geometrical overlap, the front part of the nacelle was in the propeller domain and was modelled by a moving wall, being stationary in the absolute frame. On the sides of the domain, a conformal periodic boundary condition was specified to avoid interpolation and introduction of associated errors.

The wing and propeller-wing configurations were installed in a domain representing the wind-tunnel test section, as shown in Fig. 3.20. The upstream and downstream extent of the domain and the inlet and outlet boundary conditions were the same as for the isolated propeller configuration. The propeller blades, spinner, nacelle, wing and flap were defined as no-slip walls and the front part of the nacelle was again modelled by a moving wall. Part of the top wall of the wind-tunnel domain was also modelled as a no-slip wall to account for the interaction of the boundary layer on the wind-tunnel ceiling with the wing. All other wind-tunnel walls were set as slip walls. The flap could be deflected, after which remeshing of the inner domain was required. Interfaces were present between the wind-tunnel domain, the inner domain and the propeller domain. To simulate the wing only or apply the actuator models, the propeller domain was replaced by a domain with only a spinner.

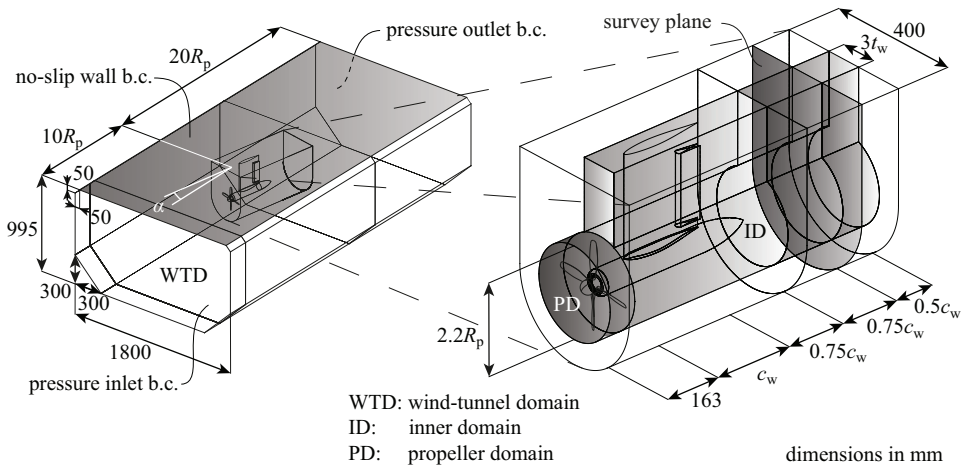


Figure 3.20: Computational domain and boundary conditions for the wing and propeller-wing configurations of the Beaver propeller.

WINGTIP-MOUNTED PUSHER-PROPELLER

For the wingtip-mounted pusher-propeller investigation, four different types of RANS CFD simulations were performed in order to establish the wing performance and wingtip flowfield, to estimate the upstream effect of the propeller on the wing and to verify the accuracy of PROPR (PPropeller analysis and OPTimisation Routine):

- Isolated wing simulations,
- isolated propeller simulations,
- wing simulations with actuator-disk propeller representation, and
- a propeller-wing simulation.

The wing used for these simulations was derived from the Tecnam P2012 Traveller [207], a twin-prop 9-passenger commuter airplane with a maximum take-off mass of 3600 kg. Only the wing was taken into account, without the original propeller and nacelles. A sketch of the wing is shown in Fig. 3.21 a. A minimum radius nacelle was added at the tip of the wing, extending aft of the trailing edge to accommodate a propeller in pusher configuration. The nacelle radius was kept equal to the propeller hub radius R_h . Hence, so far there is no provision to accommodate an electric motor. The wing parameters are given in Table 3.4 and are partly based on Ref. [208].

The propeller in the isolated propeller and propeller-wing simulations is the earlier described 6-bladed XPROP propeller shown in Fig. 3.21 b. The spinner was modified to convert it into a pusher propeller. The propeller was used in its original size with a radius of $R_{p,ref} = 0.2032$ m and modified hub radius of $R_h = 0.23R_{p,ref}$. Simulations were also performed with proportionally scaled versions of smaller and larger size.

The computational domain and boundary conditions for the wing simulations are shown in Fig. 3.22. The outer dimensions of the domain were chosen to be sufficiently large with respect to the wing chord, in order to minimize the influence of the boundary

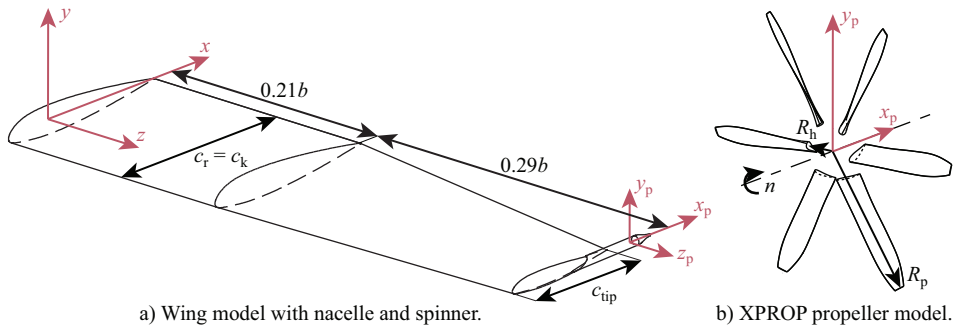


Figure 3.21: Isometric view of the wing and XPROP propeller for the wingtip-mounted pusher configuration.

Table 3.4: Wing model parameters for the wingtip-mounted pusher-propeller configuration.

Parameter	Value
Span b	13.55 m
Root and kink chord c_r, c_k	2.06 m
Tip chord c_{tip}	1.38 m
$c/4$ sweep, dihedral, twist	0°
Root and kink airfoil	NACA23015
Tip airfoil	NACA23012
Cruise speed	80 m/s
Cruise altitude	3048 m
Cruise angle of attack	3°
Cruise lift coefficient	≈ 0.35

conditions on the flow properties near the wing. At the domain inlet, a total pressure was set to reach the cruise speed. Furthermore, the undisturbed total temperature was specified. At the domain outlet, the static pressure was prescribed to be on average equal to the undisturbed static pressure. On the outboard side of the domain, a Riemann-invariant pressure farfield condition was specified with a Mach number, static pressure and static temperature complying with the inlet conditions. On the inboard side, a symmetry boundary condition was imposed. The wing, nacelle, propeller and spinner were modelled as no-slip walls.

The computational domain was divided in several domains for refinement of the grid. The propeller domain (PD) was connected to the other domains through sliding mesh interfaces to allow grid rotation for simulation of propeller motion. This domain could be replaced by a domain without propeller blades for the isolated wing simulations and wing simulations with actuator-disk representation of the propeller. The earlier described actuator-disk model was used, requiring the propeller blade radial distribution of thrust and torque as input.

The computational domain for the isolated propeller simulations is already described for the XPROP propeller. Since the wake of a propeller with axisymmetric nacelle is cyclic with the number of the blades, only a single blade was modelled in the wedge shaped domain with appropriate boundary conditions from Fig. 3.17. The movement of the propeller and spinner was simulated with a rotating reference frame.

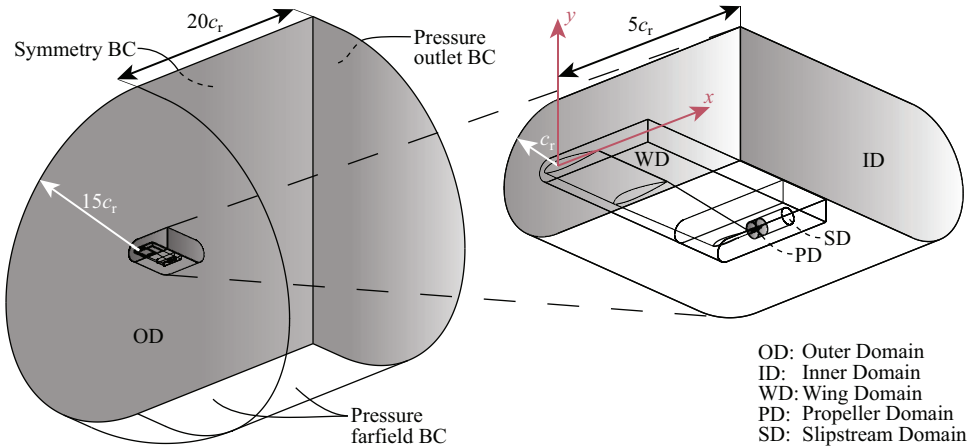


Figure 3.22: Computational domain and boundary conditions for the wingtip-mounted pusher-propeller simulations.

COMPOUND HELICOPTER

The aerodynamic interaction effects for the Airbus RACER compound helicopter were investigated through a series of RANS CFD simulations. In Fig. 3.23 the various simulated configurations are depicted and a more detailed sketch of the geometry was shown in Fig. 2.12. By leaving away different airframe components in the simulations, a quantitative indication of the aerodynamic interaction effects could be established. The helicopter fuselage with box-wings was simulated with two fully resolved six-bladed tip-mounted propellers turning inboard-up, all represented by no-slip walls. All four wing halves were equipped with plain flaps over the majority of the span. In the remainder of the dissertation this body without the propeller blades is referred to as the *airframe*.

The model was simplified by removal of the tail unit and the time-averaged effect of the main rotor was introduced by an actuator-disk implementation, similar to i.e. Batrakov et al. [209], which consists of radially and circumferentially varying momentum and energy jump conditions based on provided blade loading distributions. Note that rotor and rotor-head wake interactions with the tail unit and resulting design optimisation of the tail unit have been studied separately by Lienard et al. [32] and Salah el Din et al. [210] respectively. Adaptive mesh refinement techniques such as described by Öhrle et al. [211] would enable the full simulation of the main rotor with reduced computational cost, but for this project a large quantity of simulations were needed to study the interactions in the various operating conditions, necessitating the more computational cost effective actuator-disk approach.

For the PNWFR, PNR and PNWF configurations (P: propeller; N: nacelle; W: wing; F: fuselage; R: rotor), transient simulations were performed, while the NWFR configuration was simulated steady to reduce computational cost. For the PN configuration, transient simulations were performed whenever the propeller was at angle of attack. For zero angle of attack, a single blade passage was modelled in a steady simulation with cyclic periodic boundary conditions to reduce computational cost. The propellers and spinner

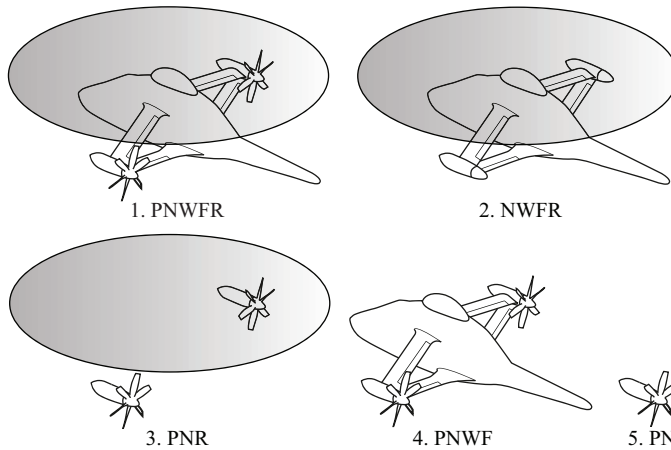


Figure 3.23: The five different simulated compound helicopter configurations including labels (P: propeller; N: nacelle; W: wing; F: fuselage; R: rotor).

were in a separate domain from the rest of the airframe to allow propeller motion with a sliding mesh interface. A sliding mesh interface was also present around the propeller blade to allow change of propeller blade pitch without redefinition of the structured grid.

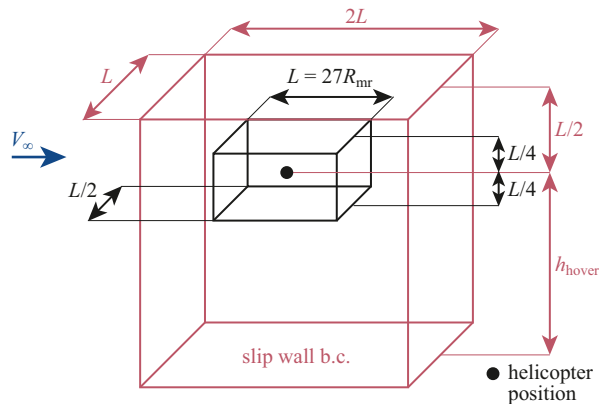


Figure 3.24: Comparison of the compound helicopter domain for the cruise condition and enlarged domain for the hover condition.

The domain for the cruise condition and the enlarged domain for the hover condition are sketched in Figure 3.24. For the cruise condition the dimension in the freestream direction L was chosen larger than the other dimensions to diminish the effect of the boundary conditions on the flowfield near the helicopter. Furthermore, on all boundaries, general free stream boundary conditions were prescribed based on Riemann invariants. The freestream airspeed in the cruise condition was set to 220 kt (113.2 m/s)

with a static temperature of 276.3 K and density of 1.024 kg/m^3 . For the hover condition, a larger domain was required to prevent unwanted recirculation and thus unwanted influence of the boundary conditions on the flowfield near the helicopter. The bottom boundary condition was placed at a distance equal to the hover altitude h_{hover} and modelled as a slip wall. A very small freestream velocity was prescribed to further reduce recirculation in the domain and the static temperature was set to 306.2 K and density to 1.112 kg/m^3 .

3

3.2.4. GRIDS AND GRID DEPENDENCY STUDIES

For all simulations with the unstructured solvers CFX and Fluent, unstructured grids were constructed by means of ANSYS® Meshing. For the simulations with ENFLOW, the ENGRID utility was used to create structured grids. Both approaches are described below.

Grids for all simulations except for the compound helicopter were constructed by means of ANSYS® Meshing. For regions adjacent to no-slip walls, the unstructured grid was made up of a triangular wall mesh, followed by layers of semi-structured prismatic elements of the inflation layer. For the remainder of the domain tetrahedral elements were used. An exception is formed by the wingtip-mounted tractor-propeller simulations in Sections 5.1 and 5.2, where in the slipstream of the propeller an unstructured hexagonal mesh was used to reduce the grid size. Grid density in the whole domain was controlled by wall refinement of all no-slip walls, volume refinement of the domains, a 1st layer thickness of the inflation layers, and growth rates of the inflation layers and the remainder of the grid.

The 1st layer thickness was tuned to comply with the y^+ requirement of the turbulence models of $y^+ \leq 1$. An exception to this was the part of the no-slip wind-tunnel wall outside of the inner domain for the wingtip-mounted tractor-propeller, for which wall functions were used. Furthermore, for the propeller-SRV interaction study in Section 6.1, wall functions were used on all no-slip walls to reduce computational cost, with a y^+ of 11 on average and 30 at maximum. The number of inflation layers was in general tuned to encapsulate the boundary layer. The grids on periodic boundaries were in general conformal to avoid interpolation. For full annulus propeller simulations, the grid from a single blade was copied and rotated to achieve periodicity in the grids.

For each simulation setup, grid dependency results are presented alongside the results. All refinements were varied systematically in the grid dependency study, except for the inflation layer which was kept constant in line with Roache [212]. To estimate discretization uncertainty, the least-squares version of the grid convergence index (GCI) proposed by Eça and Hoekstra [213] was applied. The grid size and refinement ratios h_i/h_1 for the considered grids were first calculated, where h_i is the average cell size of grid i and h_1 that of the finest grid. Richardson extrapolation of solutions ϕ_i on the grids was performed by means of a least-squares approach. In case of oscillatory convergence or divergence, the least-squares approach cannot be followed and an error estimate based on the maximum difference of the solutions Δ_M was used. A small deviation from the method of Eça and Hoekstra [213] was introduced by only evaluating

solutions on the selected n_{sel} and more refined grids to avoid penalizing evaluation of coarser grids:

$$\Delta_M = \max(|\phi_i - \phi_j|) \text{ with } 1 \leq i \leq n_{\text{sel}} \wedge 1 \leq j \leq n_{\text{sel}} \quad (3.19)$$

The resulting estimated error U_ϕ depends on the observed order of accuracy p and is equal to:

$$U_\phi = \begin{cases} \min(1.25\delta_{\text{RE}} + U_s, 1.25\Delta_M) & 0 < p < 0.95 \\ 1.25\delta_{\text{RE}} + U_s & 0.95 < p < 2.05 \\ \max(1.25\delta_{\text{RE}}^* + U_s^*, 1.25\Delta_M) & p \geq 2.05 \\ 3\Delta_M & p < 0 \text{ or oscillatory} \end{cases} \quad (3.20)$$

3

where δ_{RE} is the difference between the estimated exact solution and the solution on the chosen grid, U_s is the standard deviation of the fit and δ_{RE}^* and U_s^* are based on a least-squares fit with the theoretical order of convergence. Since all discretization methods were 2nd order accurate, the theoretical order of convergence is $p = 2$. This error analysis was performed for relevant quantities. The results for the grid dependency studies can be found in the respective results chapters.

For the compound helicopter simulations with ENFLOW in Sections 7.1 and 7.2, block structured grids were constructed. The grid for the complete configuration consisted of about 153 million cells in the cruise condition and about 163 million cells in the hover condition. Due to the larger domain and the need for a different first layer thickness, the grid size of the hover condition was slightly larger. In order to comply with the turbulence models, the dimensionless wall distance y^+ on all no-slip walls of the model was less than one.

In order to assess the dependency of the results on the grid, the grid convergence index was evaluated using three grid levels. A medium and coarse grid were obtained by structured grid coarsening by combining 8 cells, resulting in a refinement ratio of 2. As only three grid levels were available, the least squares method from Ref. [213] simplified to the standard GCI method without least-squares approximation. Since the grid was refined in a structured manner and the solver is 2nd order accurate, also grid-dependent uncertainties based on Richardson extrapolation E_ϕ could be calculated [212], where the assumption is made that the order of accuracy is $p = 2$. The advantage of this latter uncertainty estimate is that it does not depend on the coarse grid, which might be out of the asymptotic range because of the large refinement ratio. Grid dependency results using both uncertainty estimators are shown alongside the results.

4

AERODYNAMICS OF THE ISOLATED PROPELLERS

In this chapter the isolated aerodynamic characteristics of the propellers are discussed. These results are used as the reference in later chapters to determine and describe propeller interaction effects. Throughout this chapter, RANS CFD and experimental results are presented in order to answer research question 1a as posed in Section 2.1:

Q1a: *What are the aerodynamic characteristics of the propellers used in this research as a function of advance ratio and angle of attack in terms of thrust, power, in-plane forces, out-of-plane moments and resulting slipstream?*

Furthermore, RANS CFD and lower order model results are validated against the experimental results in order to use these models in later chapters. This includes grid convergence results for the isolated propellers. Specifically for the Beaver propeller the consequences of actuator-disk and actuator-line modelling on the propeller slipstream are discussed as in Section 5.1 a similar study is performed in interaction with a wingtip. With these results the following research question is addressed:

Q1b: *How do the RANS CFD and lower order propeller models compare with experimental results in terms of isolated propeller performance and flowfield and what grid uncertainties are associated with the CFD results?*

Results in static condition (zero airspeed) and at low subsonic airspeed at zero angle of attack are covered in Section 4.1 for all of the experimental propellers. Angle of attack effects are described up to very large angles ($\alpha_p = 95$ deg) in Section 4.2 for the XPROP and F29 propellers.

4.1. CHARACTERISTICS AT ZERO ANGLE OF ATTACK

Two distinctions are made in terms of propeller operating conditions:

The contents of this chapter have been adapted from Refs. [64–68, 71].

1. In static condition, and
2. with non-zero airspeed.

The characteristics of both conditions are discussed in the following subsections at zero angle of attack. For the XPROP and F29 propeller, performance characteristics are shown in the next two Sections 4.1.1 and 4.1.2 as function of propeller rotational speed and airspeed. For the Beaver propeller, both positive and reverse thrust cases are investigated with a non-zero airspeed in Section 4.1.3. For the APIAN propeller, the focus in Section 4.1.4 is mainly on the slipstream characteristics as this is important for the interaction study with the downstream swirl-recovery-vanes.

4.1.1. XPROP PROPELLER

For the XPROP propeller model an extensive experimental database of isolated propeller performance was established to investigate performance effects with angle of attack. These results are presented in this chapter. It is also used to study interaction effects with a wing relevant for a compound helicopter in hover in Section 7.3. Furthermore, it serves as the reference propeller in the analysis and design of a small-scale wingtip-mounted pusher-propeller in Section 5.3.

BASELINE PROPELLER PERFORMANCE

The baseline XPROP propeller integral performance at zero angle of attack is plotted in Figs. 4.1 and 4.2 in the static condition and at non-zero airspeeds of $V_\infty = 6$ m/s, 12 m/s and 18 m/s respectively. Thrust C_T and power coefficient C_P are plotted versus tip Mach number M_{tip} in static condition and advance ratio J with freestream airspeed for two blade pitch angles $\beta_{0.7R_p}$. The raw experimental data are plotted together with 3rd order polynomial fits with 95% confidence bands. Furthermore, RANS CFD predictions with GCI uncertainty are shown from steady simulations with the MRF approach, using the domain from Fig. 3.17. The sizes of the grids used to obtain the GCI are given in Table 4.1, of which the densest grid was used for the final results.

The performance measured experimentally in static condition is characterized by a very small dependency on tip speed. This is partly due to the relatively small range that could be achieved in the experiment. This is in line with McLemore and Cannon [73], where a much larger range of tip Mach number was tested and also only minor dependency of C_T and C_P on tip speed was found for most blade pitch angles. A small increase in thrust and power coefficient is visible for both blade pitch angles with increasing tip Mach number or section Reynolds number. While C_{T_0} increases by 10% when increasing blade pitch angle from $\beta_{0.7R_p} = 20$ deg to 30 deg, C_{P_0} increases much more, by 100%. This

Table 4.1: Grid sizes for the grid dependency study of the single blade passage (SBP) configuration of the XPROP propeller.

grid	# of cells	h_i/h_1
4	757,740	2.06
3	1,382,195	1.68
2	2,829,218	1.33
1	6,605,436	1.00

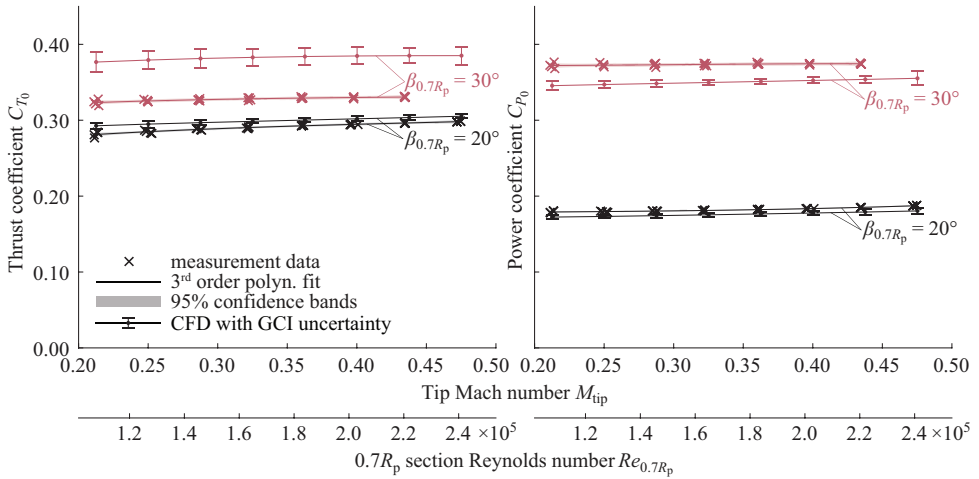


Figure 4.1: XPROP propeller thrust and power coefficient comparison between experiment and CFD for $V_\infty = 0$ m/s.

indicates flow separation for the larger blade pitch angles, as will be shown later. The CFD prediction for $\beta_{0.7R_p} = 20$ deg is very accurate both in terms of power and thrust for the whole tip speed range, while for $\beta_{0.7R_p} = 30$ deg the thrust is largely over-predicted and the power under-predicted. The earlier mentioned expected flow separation is the likely cause of this difference. The GCI uncertainty is also considerably higher for the larger blade pitch angle, especially in terms of thrust.

At the lowest advance ratio for $V_\infty = 6$ m/s, the experimental thrust and power coefficients in Fig. 4.2 are very similar to those in static condition. With increasing advance ratio through decreasing rotational speed, both C_T and C_P decrease. The data for the three freestream airspeeds ($V_\infty = 6, 12$ and 18 m/s) in Fig. 4.2 follow the same trends with advance ratio, but small differences for the overlapping advance ratios are noticeable. These differences are a result of Reynolds number differences. The increase in thrust coefficient with increase in blade pitch angle is larger for higher advance ratios, while for the power coefficient the increase remains more or less constant. This indicates that flow separation is likely less severe for these higher advance ratios. The maximum error in the CFD prediction for thrust occurs at the lower advance ratios for $\beta_{0.7R_p} = 30$ deg. The GCI uncertainty in the CFD prediction is also higher in that area. For $\beta_{0.7R_p} = 20$ deg the maximum error in the CFD prediction for thrust occurs at the higher advance ratios. The CFD prediction for power is generally better than the thrust prediction.

To investigate what is happening on the propeller blades in the CFD simulations, in Fig. 4.3 the thrust and power distribution along the radius are plotted for two specific conditions for both blade pitch angles. Furthermore, in Fig. 4.4 the shearlines (lines following the shear stress vector direction) and pressure distribution on the blade are shown for the same conditions. Results at the same rotational speed for $V_\infty = 0$ m/s and 18 m/s are plotted alongside each other. For $\beta_{0.7R_p} = 20$ deg in static condition, the thrust distribution is characterized by a maximum relatively outboard at $r/R_p = 0.93$ compared

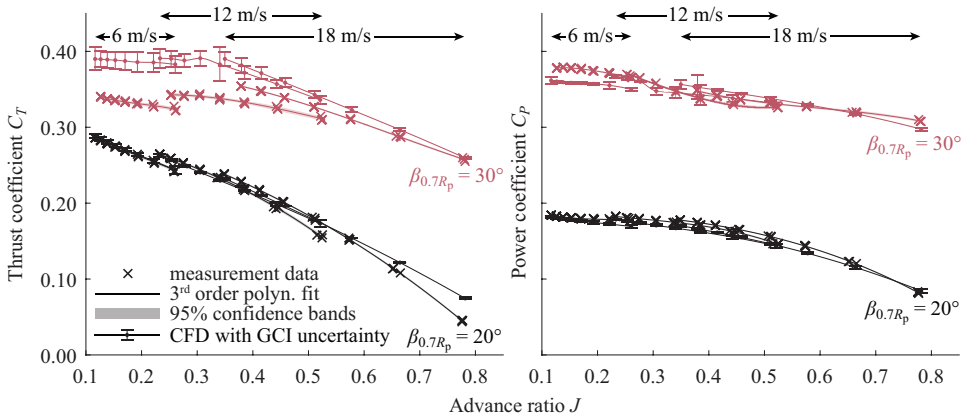


Figure 4.2: XPROP propeller thrust and power coefficient comparison between experiment and CFD at non-zero freestream airspeeds for $\alpha_p = 0$ deg.

to at $r/R_p = 0.85$ with the non-zero airspeed. For both conditions at $\beta_{0.7R_p} = 20$ deg, a narrow peak is visible near the tip of the blade, resulting from the low static pressure in the vicinity of the tip vortex. This is also visible in the static pressure contour by the region of negative $C_{p,r}$ along almost the entire chord near the tip. For the power coefficient, a maximum in both conditions is found around $r/R_p = 0.8$ with again narrower peaks near the tip. For these conditions, no significant flow separation is indicated by the shearlines, only a small region of flow separation near the trailing edge for $r/R_p < 0.6$ in static condition.

For $\beta_{0.7R_p} = 30$ deg in static condition, the peak in thrust moves inboard to $r/R_p = 0.9$ and the peak at the blade tip disappears, as flow separation over the entire chord occurs in the tip region and furthermore near the trailing edge for lower radial locations. As a result, the power coefficient increases drastically, and its maximum occurs at $r/R_p = 0.9$ in the region with significant flow separation. At $V_\infty = 18$ m/s, the thrust and power distribution for $\beta_{0.7R_p} = 30$ deg are very similar in terms of shape to that of $\beta_{0.7R_p} = 20$ deg. For the larger blade pitch angle, a region of trailing edge separation is indicated by the shearlines, which does not seem to change the loading characteristics significantly.

In conclusion, for $\beta_{0.7R_p} = 20$ deg, CFD predictions of the propeller performance are accurate and only minor flow separation occurs. For $\beta_{0.7R_p} = 30$ deg, especially in static condition or for very low advance ratios, the CFD predictions contain significant errors with respect to the experiment, likely due to differences in predicting the occurring flow separation. Since propeller performance at large angle of attack is characterized by similar blade loading as in static condition during parts of the azimuth as the component of the velocity normal to the propeller becomes small, at angle of attack only results for $\beta_{0.7R_p} = 20$ deg are shown in Section 4.2.1.

VALIDATION OF PROPELLER ANALYSIS ROUTINE OF PROPR

To establish confidence in the propeller analysis and optimisation routine PROPR (see Section 3.2.1), two comparisons were made with the XPROP propeller. The first was with

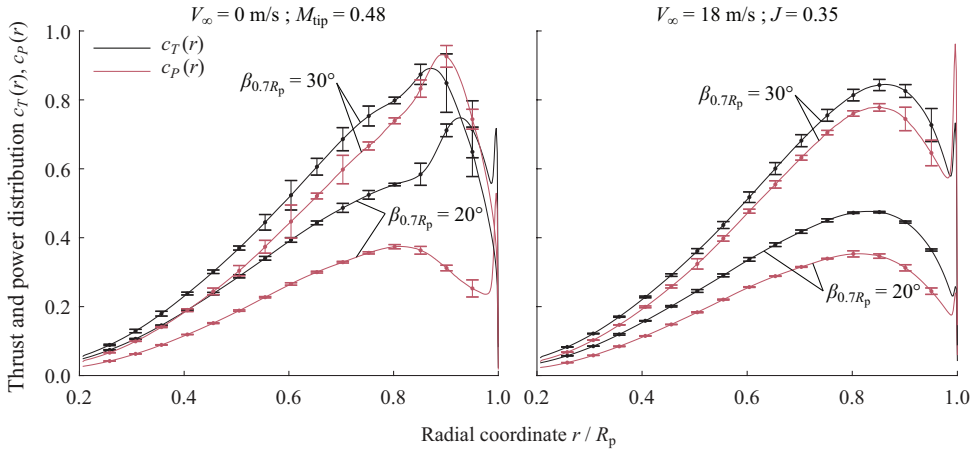


Figure 4.3: CFD result showing XPROP propeller thrust and power coefficient distribution for four selected conditions at $\alpha_p = 0$ deg.

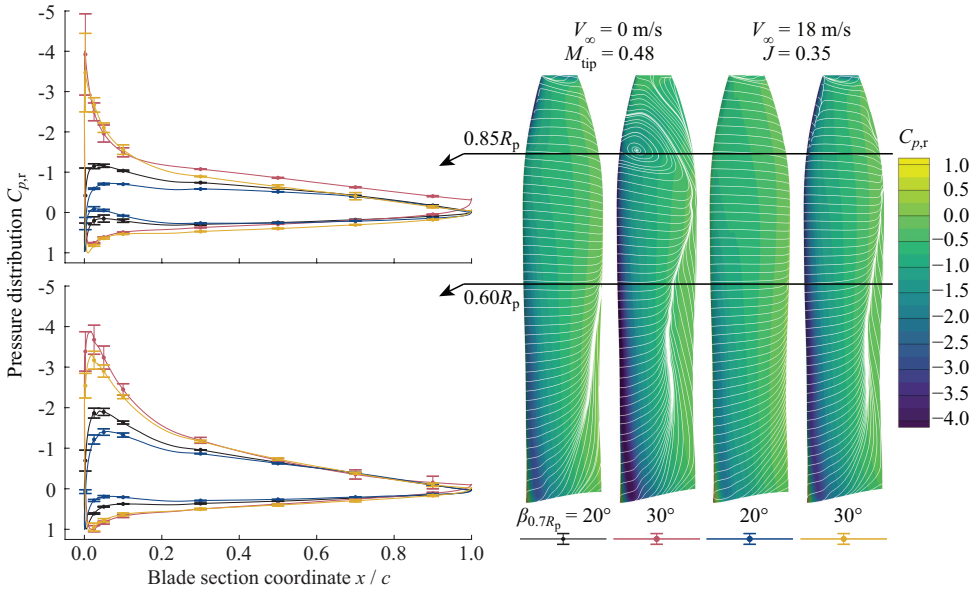


Figure 4.4: CFD results showing XPROP propeller blade shearlines and pressure coefficient distribution with discretization uncertainty for four selected conditions at $\alpha_p = 0$ deg.

wind-tunnel data of the XPROP propeller in uniform flow. In Fig. 4.5 a comparison is presented of the thrust and torque coefficient versus advance ratio for $V_\infty = 30$ m/s. Although at high advance ratios a significant deviation starts to appear for both thrust and torque coefficient, in the region of interest where C_T is higher, the match with the experimental data is satisfactory.

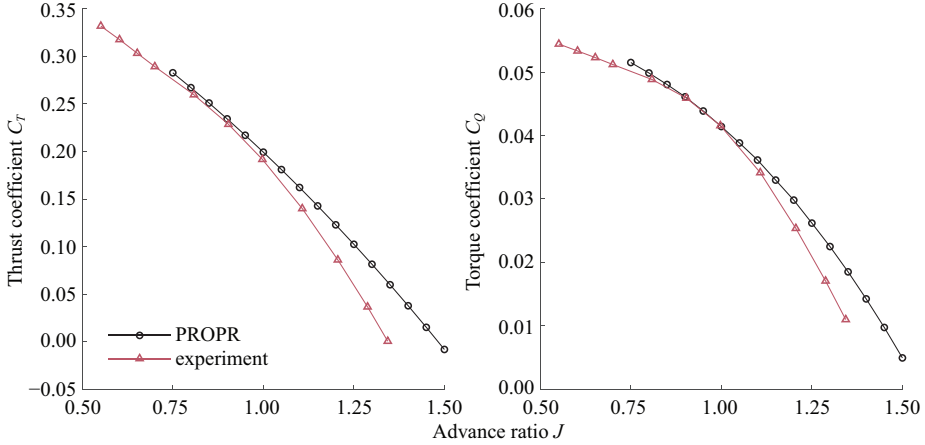


Figure 4.5: XPROP propeller performance from PROPR and wind-tunnel test for $V_\infty = 30$ m/s and $\beta_{0.7R_p} = 30^\circ$.

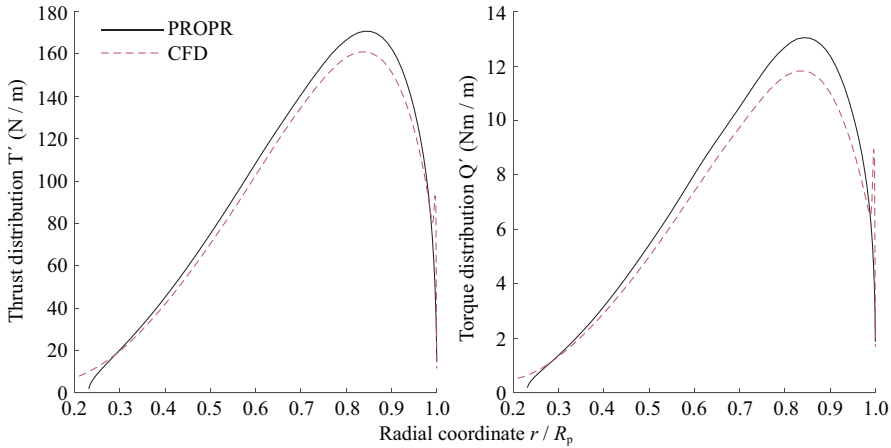


Figure 4.6: XPROP propeller blade loading distributions from PROPR and CFD model for $V_\infty = 30$ m/s, $\beta_{0.7R_p} = 30^\circ$ and $J = 0.74$.

The second comparison was made with the CFD model of the isolated propeller. In Fig. 4.6 the thrust and torque distribution over a propeller blade are plotted for both PROPR and the CFD model for $V_\infty = 30$ m/s and an advance ratio of $J = 0.74$. The integrated loading is overestimated by PROPR with 4.5% and 7.6% in thrust and torque respectively. The shape of the thrust and torque distribution from PROPR and the CFD model are very similar except for at the tip of the blade. The local rise in thrust and torque in the CFD model due to the tip vortex is not captured in the PROPR results because of the single lifting line representation of the blade. Considering that in these comparisons acceptable agreement was found, the PROPR model was deemed acceptable for the subsequent design study that is discussed in Section 5.3.

4.1.2. F29 PROPELLER

The F29 propeller model was used in an experiment to study interaction effects for eVTOL vehicles, of which the interaction results are presented in Section 6.2. In this experiment, two propeller units were used, of which unit A was instrumented with an F/T sensor to measure propeller performance. Unit B without F/T sensor was both set up in a tractor and pusher configuration. First the baseline propeller performance in tractor configuration is discussed, and after that the performance of propeller unit B is verified. At last, the consequences of operating the propeller in pusher configuration are discussed.

BASILINE PROPELLER PERFORMANCE

For the F29 propeller similar integral performance plots were created as for the XPROP propeller. In Fig. 4.7 the baseline propeller performance in static condition is shown. Raw F/T sensor data is shown and 3rd order polynomial fits are presented including 95% confidence bands. Results are plotted for a range of M_{tip} from 0.237 to 0.405, where M_{tip} was based on the rotational speed. The respective Reynolds number $Re_{0.7R_p}$ at the $r = 0.7R_p$ blade section is indicated as well for reference. The Reynolds number range is comparable to that of the XPROP experiment, as the F29 propeller has relatively large section chords despite being of smaller diameter.

While the thrust coefficient C_{T_0} is almost independent of M_{tip} , the power coefficient C_{P_0} increases slightly with increasing M_{tip} . Although in the remainder of the dissertation only results are shown for this propeller at a freestream airspeed of $V_\infty = 20$ m/s, the propeller performance at static condition is a relevant reference, especially at large propeller angle of attack α_p , when the freestream axial velocity component ($V_\infty \cos(\alpha_p)$ in Fig. 2.4) for the propeller becomes small, zero or even negative. Furthermore, the power in static condition serves as a baseline for eVTOL vehicles, similar to hover power for a helicopter. While the confidence band for C_{P_0} is very narrow, the C_{T_0} measurements show quite some scatter and thus have a wider confidence band to consider. This is related to the sensor drift for which especially the thrust measurement is susceptible, as discussed in Section 3.1.3. As can be observed, the measurements seem to form two groups, depending on whether an up- or down-sweep in rotational speed was performed.

Figure 4.8 presents the fitted F/T sensor data for C_T and C_P at $\alpha_p = 0$ deg together with C_T values obtained from integration of total pressure wake measurements. In ad-

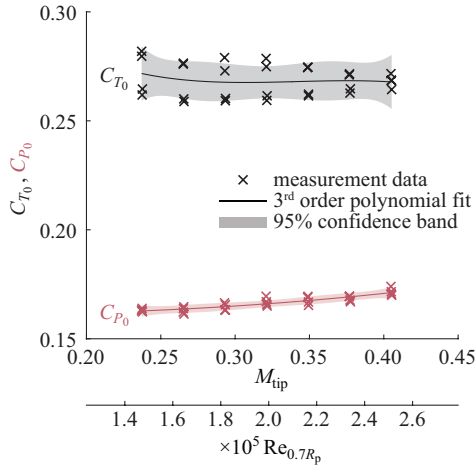


Figure 4.7: F29 propeller thrust and power coefficient versus M_{tip} for $V_\infty = 0$ m/s, measured with the F/T sensor.

dition, results from the BEM model (presented in Section 3.2.1) are included to validate the performance predictions. The investigated range of advance ratio was smaller than in the XPROP experiment, since only one freestream airspeed of $V_\infty = 20$ m/s was selected. C_T and C_P decrease with increasing J , similar to the XPROP results in Fig. 4.2.

The F/T sensor data were verified by comparison with total-pressure measurements in the propeller slipstream. A total pressure sweep was performed in a single radial direction at $x/R_p = 0.48$ behind the propeller, and the corresponding results are shown in Fig. 4.9. In order to obtain a thrust force, the same radial total pressure distribution was assumed at each azimuthal location, i.e. an axisymmetric slipstream. A thrust force was obtained by integration of the total pressure, with the freestream total pressure subtracted, over the slipstream cross-section. This thrust estimation from the total-pressure data was then corrected to account for the contraction effect. First, the local slipstream radius R_s at the total pressure measurement plane was estimated from the radial distribution of total pressure coefficient in Fig. 4.9. R_s was estimated by drawing a tangent through the point of steepest descent of the piecewise cubic hermite interpolating polynomial (PCHIP) fit of the data and finding the intersection with $C_{pi} = 0$. The integrated thrust was then corrected by multiplication with the area ratio $\pi R_p^2 / \pi R_s^2$.

The C_T values calculated from the total pressure measurements in Fig. 4.8 compare reasonably well with those from the F/T sensor, although a non-negligible offset can be observed, especially towards the highest J . The total pressure measurements do not account for any spinner loading effects and very close to the nacelle no pressure measurement was done, both leading to an error in C_T . Furthermore, the contraction correction may have introduced an error as well. The F/T sensor data confidence bands are quite large, indicating an uncertainty in the measured C_T as well. Overall, the reasonable agreement verifies the correct operation of the F/T sensor. In Fig. 4.8 also results from the BEM model are included to validate the performance predictions by this model. The BEM model predictions agree well with the F/T sensor data in terms of C_P . In terms of

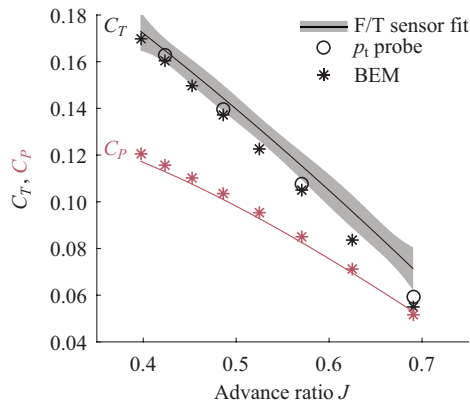


Figure 4.8: Comparison of measured and predicted ISO F29 propeller performance for $V_\infty = 20$ m/s and $\alpha_p = 0$ deg.

C_T an offset is visible, especially towards the highest J . Part of the offset may be a result of spinner loading as the BEM model prediction does not include spinner loading. This BEM model is used for performance prediction in the OAA configuration in Section 6.2.

VERIFICATION OF PERFORMANCE OF PROPELLER UNIT B (WITHOUT F/T SENSOR)

Propeller unit B was not equipped with an F/T sensor as it was only used to introduce the interaction effect for propeller unit A (with F/T sensor). The blade pitch angle of both propellers was set to match each other on a blade pitch angle measuring bench. As an additional check, the total pressure distribution behind the propellers is compared in this section.

Four radial sweeps of total pressure coefficient were obtained behind propeller unit A (with F/T sensor) for different J . These sweeps are shown in Fig. 4.9. Typical distributions of increased total pressure are found, resulting from the momentum addition to the flow by the propeller. With decreasing advance ratio, the total pressure rise increases. Contraction of the slipstream, for which a correction of the data was needed to obtain integrated thrust, is clearly visible when looking at the edge of the slipstream, especially at high loading conditions. Therefore, the maximum thrust on the blade is more outboard from the maximum C_{p_t} . For $J = 0.49$, data are also plotted for propeller unit B (without F/T sensor). Good agreement between the measurements behind the two propeller units A and B is obtained, with a difference in thrust of 0.4%, indicating a correct blade pitch angle setting.

COMPARISON OF PUSHER AND TRACTOR PROPELLER SLIPSTREAM

When propeller unit B was used in pusher configuration and thus turned by 180 deg compared to the tractor propeller configuration, the blades were turned by 180 deg as well to arrive again at the same blade pitch angle. Therefore, the blade pitch setting is checked again in this section by means of total pressure measurements in the slipstream. However, the comparison is not straightforward as the pusher propeller sees a different inflow than the tractor propeller, since its inflow is disturbed by the wakes of the nacelle

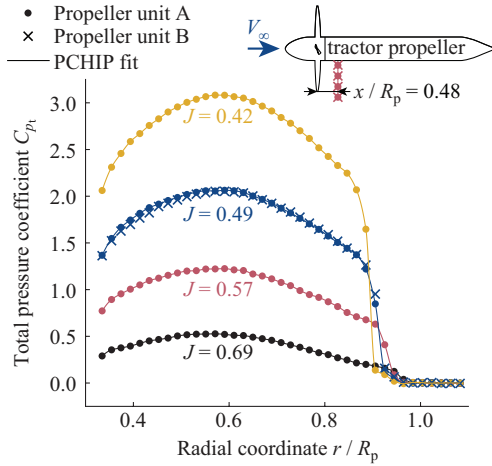


Figure 4.9: Radial distribution of C_{pt} at $x/R_p = 0.5$ behind the two F29 propeller units for $V_\infty = 20$ m/s and $\alpha_p = 0$ deg with piecewise cubic hermite interpolating polynomial (PCHIP) fit.

and pylon with fairing (see Figs. 3.8 and 3.10 b). Furthermore, the development of the slipstream for the pusher propeller is different from that of the tractor propeller since for the pusher propeller the spinner contracts, while the nacelle behind the tractor propeller has a constant radius in the vicinity of the propeller.

Taking these differences into consideration, a comparison was made of total pressure behind the pusher and tractor propeller in Fig. 4.10. A total pressure measurement sweep was performed in a direction perpendicular to the pylon and fairing, reducing the effect they may have on the local slipstream flowfield. Note that the distance of the total pressure probe behind the propeller for the pusher propeller ($x/R_p = 0.6$) is not exactly the same as for the tractor propeller ($x/R_p = 0.5$). Instead, it was chosen to coincide with the location of the rear propeller for the OAA configuration at close d_x . Although increased contraction can be seen for the pusher propeller, partially forced by the contraction of the spinner, the maximum in C_{pt} is very similar to that of the tractor propeller for the two advance ratios. The integrated difference in thrust is +0.8% at $J = 0.57$ and -0.6% at $J = 0.49$, indicating the correct setting of blade pitch angle of propeller unit B in pusher configuration.

Although for the OAA configuration a pusher propeller was chosen as the front propeller to avoid having the pylon and fairing in the slipstream, the effect of the pylon and fairing on the slipstream is not negligible. This is illustrated in Fig. 4.11 with total pressure measurements. The first comparison is between a lateral pressure sweep below and above the propeller center at a distance of $x/R_p = 0.6$ behind the propeller. In the lower sweep (x symbol), the effect of the fairing is visible by a drop in total pressure at slightly negative y-coordinate. This drop in total pressure is a result of the drop in total pressure in the wake of the fairing, that is only partially compensated by the increased total pressure jump by the propeller: The thrust and thus the total pressure jump by the propeller is locally higher as a result of the reduced axial inflow velocity from the wake. The shift to

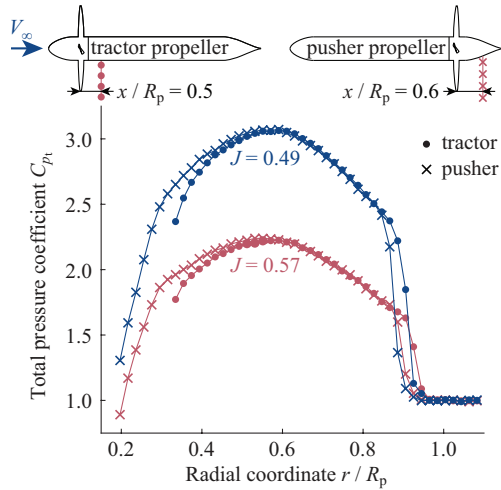


Figure 4.10: Comparison of radial distribution of C_{p_t} in the slipstream of the F29 propeller in pusher and tractor configuration for $V_\infty = 20$ m/s and $\alpha_p = 0$ deg.

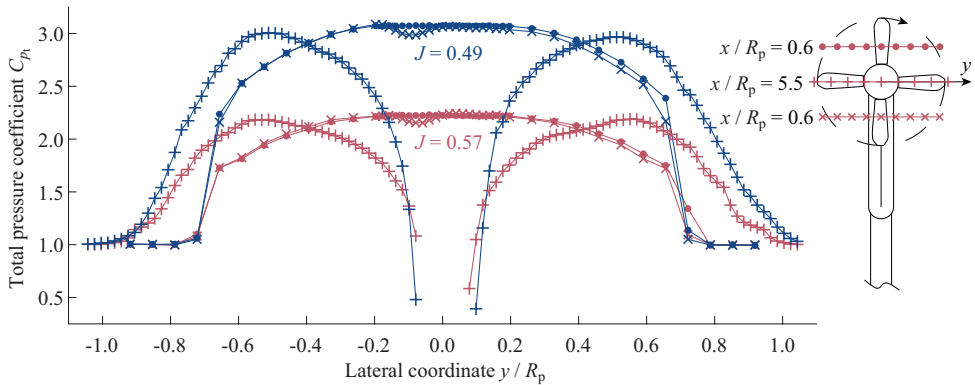


Figure 4.11: Lateral distribution of C_{p_t} at $x/R_p = 0.6$ behind the F29 pusher propeller for data offset from propeller center and at $x/R_p = 5.5$ for data across the center; for $V_\infty = 20$ m/s and $\alpha_p = 0$ deg.

negative y -coordinate is a result of the swirl component in the slipstream, displacing the fairing effect in azimuthal direction. The effect of the upstream fairing on the slipstream characteristics is however not very pronounced, and thought to be less pronounced than the reverse setup with a tractor propeller and fairing in the slipstream, as for such setup the fairing wake is not partially filled by the propeller.

In Fig. 4.11 also the total pressure is shown in a sweep across the propeller center at a distance of $x/R_p = 5.5$. This measurement coincides with the rear propeller location for the OAA configuration at the far d_x , and is plotted to quantify the slipstream seen by this propeller. Comparing the total pressure at negative and positive y -coordinate, a slight asymmetry of the slipstream edge can be observed. This could have been introduced by the fairing. In the slipstream core, no total pressure measurement was possible with the used probe due to vibrations as in this area a hub vortex was likely formed from the blade root vortices. When comparing the slipstream edge in this figure at $x/R_p = 5.5$ with the measurements in Fig. 4.10 at $x/R_p = 0.6$, an increased slipstream contraction is clearly present at $x/R_p = 5.5$. This will have an influence on OAA interaction, that was studied with the rear propeller at both axial distances.

4

4.1.3. BEAVER PROPELLER

The Beaver propeller is used to study the aerodynamic interactions occurring for a wingtip-mounted tractor-propeller. Both numerical and experimental results were established for this propeller. First the effect of grid size on the isolated propeller flowfield is investigated, after which a comparison with the experiment is presented. In this comparison, also results from propeller modelling in RANS CFD simulations with an actuator-disk and actuator-line model (introduced in Section 3.2.1) are presented. These results form the baseline for the study in interaction in Section 5.1. At last, the effects of windmilling and energy harvesting on the isolated propeller loading and flowfield are discussed. This is later used as the reference in Section 5.2. All results in this section were measured/computed at an airspeed of 40 m/s.

GRID CONVERGENCE

For the isolated propeller at $J = 0.8$, Table 4.2 presents the considered grid sizes in the grid dependency study. Grid 3 was selected based on this grid convergence study. In Table 4.3 grid study results are shown comprising of the solutions on the different grids, the corresponding observed order of convergence, standard deviation of the fits and estimated discretization error of grid 3.

Table 4.2: Grid sizes for the computational domain of the isolated Beaver propeller configuration.

grid	# of cells	h_i/h_1
5	3,547,253	1.82
4	4,529,662	1.68
3	7,373,636	1.43
2	12,451,486	1.20
1	21,447,859	1.00

Grid convergence for the isolated propeller configuration was verified by analyzing the radial distributions of blade thrust and torque, and the axial velocity distribution in

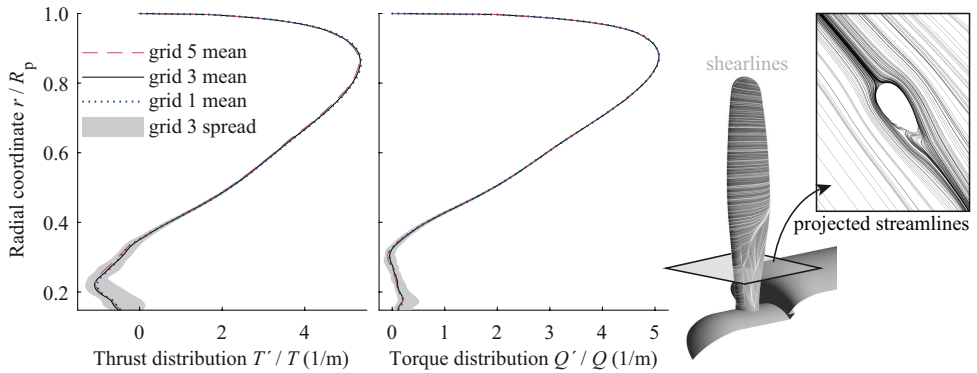


Figure 4.12: Beaver propeller blade radial thrust and torque distributions at $J = 0.8$. Shearlines on the blade and projected streamlines on a plane at $r/R_p = 0.3$ indicate flow separation at the blade root.

the slipstream. Figure 4.12 presents the radial thrust and torque distributions for three of the five considered grids. The intermediate grids 2 and 4 have been omitted for clarity. The average loading distribution is plotted over the last 2 propeller rotations of a total of 4.5 rotations, while for grid 3 also the spread over time is shown. Note that the root section of the propeller blade is circular and transforms to an airfoil over the root part of the blade [163]. This shape results in flow separation with time-varying loading. A discretization uncertainty was quantified for the maxima of the thrust and torque distribution, T'_{\max} and Q'_{\max} (Table 4.3). These quantities were chosen instead of the integrated loads in order to avoid the noise due to the blade-root flow separation. For T'_{\max} converging behaviour is found with an observed order of 4.80, resulting in the use of the theoretical order to estimate the discretization error according to Eq. 3.20. Note that the standard deviation of the fit with the theoretical order is only marginally larger than that of the observed order and is relatively small, so a good fit was achieved. It is concluded that the propeller blade loading is converged well for grid 3, with a 1.1% estimated discretization error for T'_{\max} and 0.2% for Q'_{\max} , for which oscillatory convergence is observed.

To study grid convergence for the axial velocity in the slipstream, a phase-locked

Table 4.3: Grid dependency study for the isolated Beaver propeller configuration at $J = 0.8$.

	T'_{\max}/T (1/m)	Q'_{\max}/Q (1/m)	u_{\max}/V_{∞}	$u_{0.7R_p}/V_{\infty}$
ϕ_5	5.311	5.070	1.295	1.248
ϕ_4	5.337	5.074	1.314	1.250
ϕ_3	5.346	5.076	1.342	1.250
ϕ_2	5.356	5.077	1.365	1.249
ϕ_1	5.366	5.074	1.386	1.246
p	4.80	— [¶]	1.51	— [¶]
U_s (%)	0.12	-	0.09	-
U_s^* (%)	0.15	-	0.17	-
U_{ϕ_3} (%)	1.14	0.16	9.75	0.82

[¶]Oscillatory convergence observed

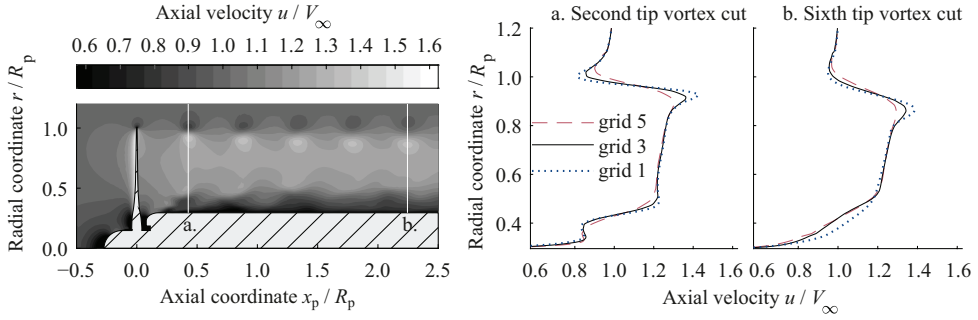


Figure 4.13: Axial-radial contour plot through the Beaver propeller blade pitch axis showing phase-locked axial velocity for grid 3 at $J = 0.8$. Radial profiles provide comparison with solutions on other grids.

4

contour plot of the axial velocity was constructed for each grid on an axial-radial plane through the blade pitch axis. In Fig. 4.13 this contour plot is presented for grid 3 and radial profiles through the second and sixth tip-vortex core are shown for three of the five grids. In order to remove some of the unsteadiness stemming from the flow separation over the propeller blade root and from the front of the nacelle, again an average was taken over the last 2 propeller rotations of a total of 4.5 rotations. However, still some variation is present between the different grids in the region up to $r/R_p = 0.5$ as the result of this unsteadiness. Overall, the flowfield for grid 3 is converged well except in the tip-vortex region around $r/R_p = 1.0$. There, the steep velocity gradients due to locally large values of vorticity were not entirely captured as a result of numerical diffusion. A discretization error was estimated for the maximum in axial velocity u_{\max}/V_∞ and the axial velocity at $r/R_p = 0.7$ for the radial profile through the second tip-vortex (Table 4.3). For u_{\max}/V_∞ , an observed order of $p = 1.51$ was found, resulting in a relatively large discretization error of 9.8% for grid 3, while for $u_{0.7R_p}/V_\infty$, oscillatory convergence was observed with a much smaller discretization error of 0.8%. Unfortunately, the numerical methods found in typical 2nd order CFD solvers require extremely dense grids to avoid numerical diffusion and preserve the tip-vortex strength, resulting in excessively high computational cost [214]. Exploration of higher-order schemes for this type of flow and means of local grid refinement were out of the scope of this research. The qualitatively good agreement of the flowfield in the tip-vortex region and the quantitatively good agreement in the remainder of the slipstream of grid 3 compared to the denser grids were considered sufficient for the analysis discussed in this research.

COMPARISON OF COMPUTATIONAL AND EXPERIMENTAL RESULTS

The purpose of the analysis of the isolated propeller configuration is to compare and validate the propeller modelling methods without the interaction with the wing. Differences in modelling without interaction should become clear to later differentiate from differences due to interaction of the slipstream with the wing. To this end, a comparison was made of the time-averaged flowfield just aft of the propeller and the time-accurate development of the slipstream more downstream. Figure 4.14 presents the radial distribution of total-pressure coefficient and tangential velocity, averaged over the circumfer-

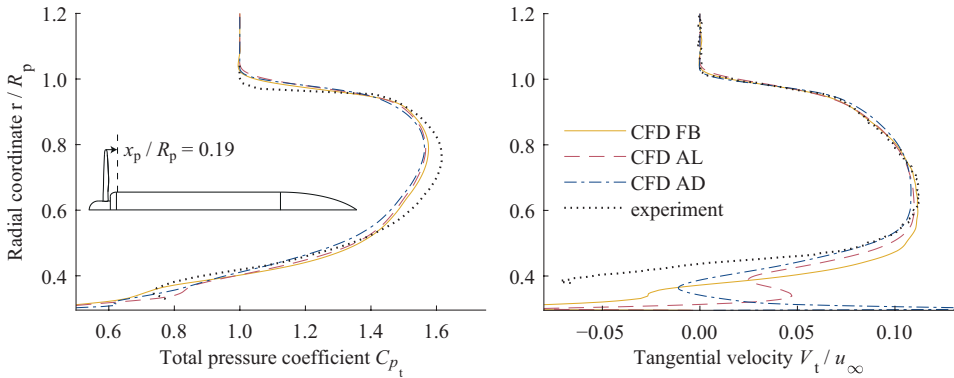


Figure 4.14: Radial variation of time-averaged total-pressure coefficient and tangential velocity at $x/R_p = 0.19$ for the Beaver propeller at $J = 0.8$.

ence just downstream of the propeller disk at $x/R_p = 0.19$. In the experiment, a total-pressure measurement was performed by traversing a total-pressure probe in the radial direction [163]. Stereo PIV measurements from the same experiment in an axial-radial plane provided the time-averaged tangential velocity profile.

Comparing the results of the full-blade (FB) simulation and the experiment, qualitative agreement is found in the total-pressure profile. The main differences are that in the experiment the total pressure in the region $0.5 < r/R_p < 0.9$ was higher and the total-pressure gradient near the nacelle and at the slipstream edge was steeper than in the simulations. The differences in the maximum of the total-pressure coefficient in the simulations with respect to the experiment are quantified in Table 4.4 and is found to be -3.1% for the full-blade model. The differences between the numerical and experimental data are likely not a result of a model error in the propeller blade loading, but are thought to be due to numerical diffusion of the blade tip and root vortices in the CFD simulations, as discussed in the previous section. The reduced vortex strengths result in a slight reduction in contraction of the slipstream compared to the experiment as is visible in Fig. 4.14, but not in a reduction of momentum in the slipstream. The lack of change in momentum in the slipstream was confirmed by analysis of the integral of total pressure over the evaluation disk, which was found to deviate approximately 1% from the experiment for all models (Table 4.4).

Table 4.4: Difference in C_{p_t} quantities from Fig. 4.14 with respect to the experimental data for the Beaver propeller at $J = 0.8$.

difference of	CFD FB	CFD AL	CFD AD
C_{p_t} maximum (%)	-3.08	-3.68	-3.82
C_{p_t} integral (%)	-0.81	-0.85	-1.22

Comparing the actuator-model results with the full-blade result, minor deviations are observed, especially near the nacelle in the region $0.3 < r/R_p < 0.45$. These deviations are the result of two differences between the full-blade and actuator models. First, the blade loading supplied to the actuator models was extracted from the last 2 rotations

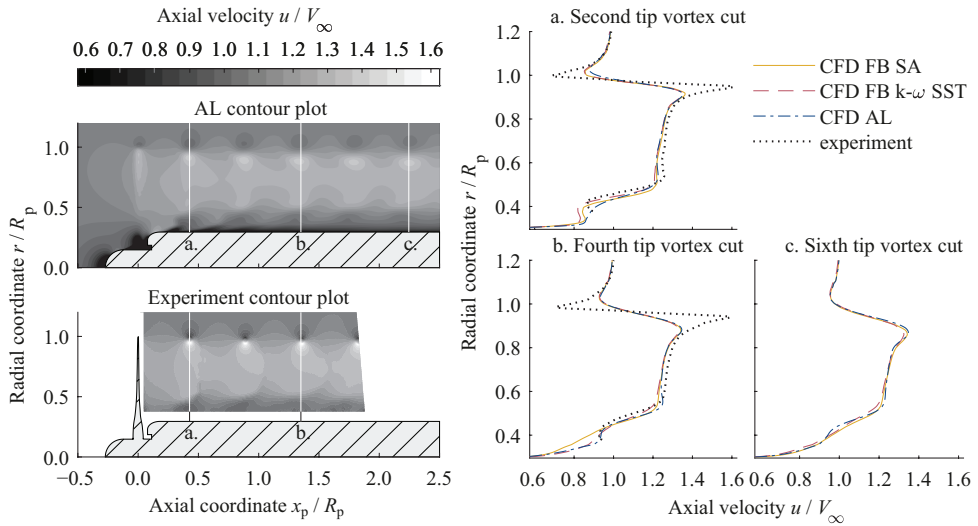


Figure 4.15: Axial-radial contour plots through the Beaver propeller blade pitch axis showing the phase-locked axial velocity for the actuator-line model and experiment at $J = 0.8$. Radial profiles provide comparison with the full-blade model.

of the full-blade simulation after which it was phase-averaged to obtain a time-averaged loading distribution at each azimuthal position. However, as was shown in Fig. 4.12, flow separation on the root part of the blade resulted in time-varying loading, which was removed by phase-averaging from the actuator models. Second, neglecting the finite thickness of the blade in the introduction of momentum and energy sources for the actuator models may have resulted in a different interaction with the front of the nacelle because of its close proximity.

Figure 4.14 also presents in the radial distribution of tangential velocity. Comparing the full-blade model result with the experiment, quantitative agreement is found for $r/R_p > 0.45$. Near the nacelle again a steeper gradient in the tangential velocity in the experiment is observed. The tangential velocity profiles for the actuator-line (AL) and actuator-disk (AD) models agree well with that of the full-blade model for $r/R_p > 0.5$. Closer to the nacelle again differences are present with the same causes as explained for the total-pressure profile. Moreover, in this area the direction of the time-accurate velocity vector varied strongly, which explains the larger differences compared to the total-pressure profile.

The time-accurate agreement of slipstreams computed for the the full-blade model and actuator-line model with that of the experiment can be observed in Fig. 4.15. Contour plots of the phase-locked axial velocity are shown for the actuator-line model and for the experiment obtained by PIV. Note that the corresponding contour plot obtained for the full-blade model was shown before in Fig. 4.13. Alongside the contour plots, radial profiles through three tip vortices provide a quantitative comparison of the results. For the full-blade model not only results obtained with the Spalart–Allmaras (SA) turbulence model are shown, but also with the $k-\omega$ SST turbulence model. The choice of these

models was discussed in Section 3.2.2. The main difference between the CFD results and the experiment is that the extrema in axial velocity in the tip vortices are reduced in the CFD results. In the grid dependency study a discretization error of 9.8% was found for the maximum of the axial velocity associated with the second tip vortex, as a result of numerical diffusion. Based on the extrapolated grid value, a model error for the full-blade model with respect to the experiment remains of 7.0%. Outside the tip vortices, a good match is observed with the same differences as for the distribution of total-pressure coefficient in Fig. 4.14. No large effect of the turbulence model is found for the plotted axial range, although it was observed that further downstream in the same plane the velocity gradients in the tip vortices for the $k - \omega$ SST model kept decaying while they remained constant at the level of the sixth tip vortex for the SA model. Comparing the actuator-line model with the full-blade model, it is concluded that a good match is obtained in terms of the time-accurate flowfield.

WINDMILLING AND ENERGY HARVESTING EFFECTS

A propeller operating in windmilling condition produces net drag. When connected to an electric motor, a propeller can be used to generate electric power and thus 'harvest energy' in such condition. This can for instance be used on a (hybrid-) electric plane during descent to regenerate some of the energy and charge the batteries. Operating a propeller in windmilling condition not only changes the loading on the propeller but also changes the slipstream drastically. In case of a wing-mounted propeller this has consequences for the wing loading. As these effects are investigated in Section 5.2 for a wingtip-mounted tractor-propeller configuration with the Beaver propeller, the characteristics of the isolated propeller in windmilling condition are investigated here.

Figure 4.16 displays the performance of the isolated propeller in terms of thrust and torque coefficient versus advance ratio for constant airspeed. The data were obtained from the CFD simulations of the isolated propeller. Figure 4.16 a provides the thrust and power coefficients referenced to the rotational speed of the propeller ($C_T = T/\rho_\infty n^2 D^4$ and $C_P = P/\rho_\infty n^3 D^5$). For the installed configuration, the thrust coefficient of the rotor C_T does not relate directly to the interaction effects at the wing. Therefore, in Fig. 4.16 b the alternative definition of the thrust coefficient, $T_C = T/q_\infty D^2$, is used. This coefficient represents the average disk loading over the propeller.

The propeller response at positive thrust is as expected and was described in the previous section for $J = 0.8$ and for other advance ratios in Ref. [16]. From an advance ratio of approximately 1.0 onward, the thrust becomes negative. In this regime, the lift and drag forces on the blade sections both contribute to the force in negative thrust direction (l and d in Fig. 2.2 c). Therefore, the slope of the thrust coefficient C_T versus advance ratio steepens compared to that in positive-thrust conditions. The propeller power coefficient displays a comparable trend as the thrust coefficient, even though in the negative-thrust regime the drag force opposes the negative torque. The cross-over advance ratio from positive to negative power occurs at higher advance ratio than for the thrust. This is because the lift coefficients are small but positive at the zero thrust condition, thus contributing to a positive torque. For J above approximately 1.4, the thrust and power response flatten, because the cambered airfoil sections of this propeller (see Fig. 3.2 d) are not designed for operation at relatively large negative angles of attack. This was also

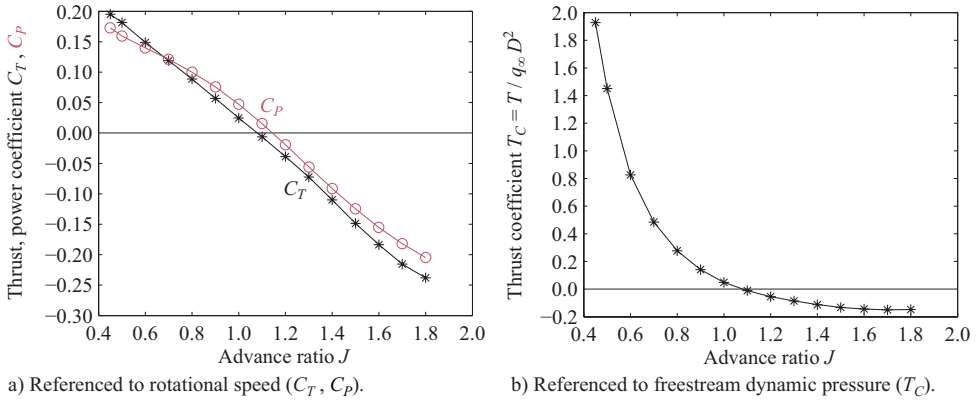


Figure 4.16: Isolated Beaver propeller thrust and power coefficient versus advance ratio at $V_\infty = 40$ m/s.

observed in previous work for windmilling fans [215], and is caused by local separation on the blades.

To visualize the differences in flow separation on the blades between typical propulsive and energy-harvesting conditions, Fig. 4.17 plots distributions of skin friction coefficient and shearlines on the blades at $J = 0.8$ and $J = 1.6$. Note that the colorbars in the two subfigures do not have the same scale. It can be seen that the cambered blade sections are not efficient for operation at negative loading conditions. In propulsive mode (Fig. 4.17 a), the flow is attached over the largest part of the blade, except for trailing-edge stall on the inboard radial sections. This is due to the locally inefficient blade design, and would not occur on more modern blade designs at comparable conditions. In energy-harvesting mode (Fig. 4.17 b), additional flow separation can be observed near the trailing edge of the blade at about 40% and 90% of the radius. Shape optimisation would be required to make the blade design more robust for efficient energy harvesting.

The high negative thrust and torque (power) on the blades and associated separation in energy-harvesting conditions leads to local distortions in the blade loading distributions. This is shown in Fig. 4.18 for the radial distributions of thrust and power. At negative thrust conditions, the shape of the loading distributions clearly differs from the typical result for minimum-induced loss in the positive thrust regime. Moreover, the flattening of the blade response at high advance ratio, observed before in Fig. 4.16, can clearly be recognized when for example comparing the blade loading distributions at $J = 1.6$ and $J = 1.8$.

The distorted blade-loading distribution affects the slipstream characteristics and thus the interaction effects on a downstream aerodynamic surface immersed in the slipstream. Figure 4.19 provides the radial distributions of axial and tangential velocity in the slipstream at $0.19R_p$ downstream of the propeller center. These distributions are instrumental in the interpretation of the data for the propeller-wing configuration in

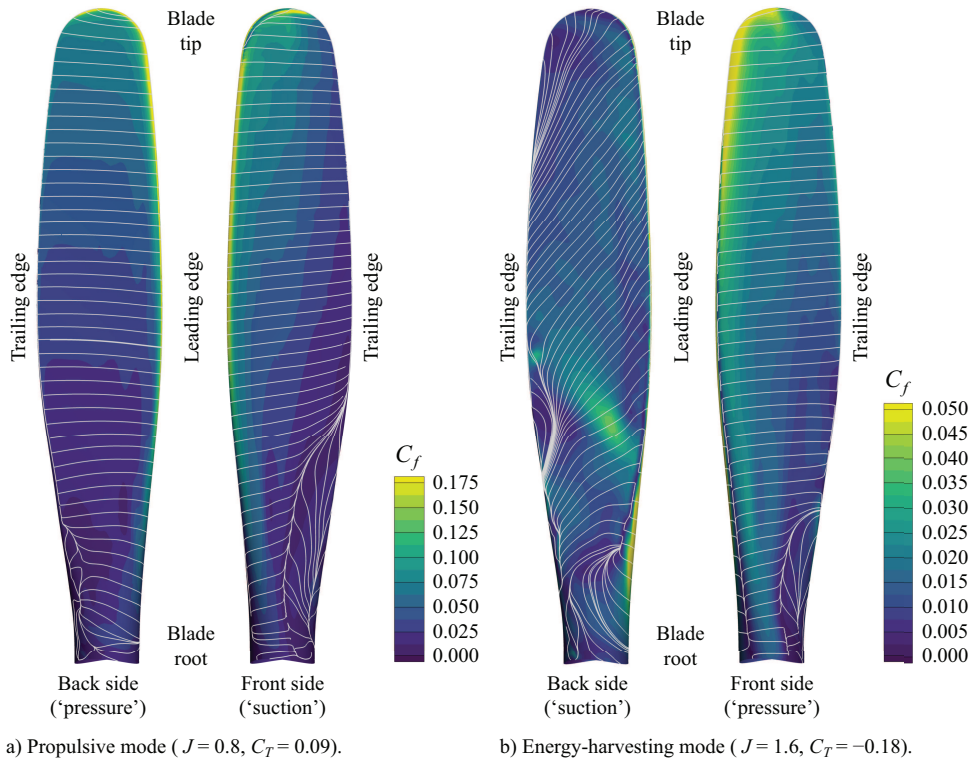


Figure 4.17: Visualization of flow separation on the Beaver propeller blades by contours of skin friction coefficient and shear lines.

Section 5.2. The edge of the nacelle is located at $r/R_p = 0.295$. The distribution of the axial velocity displays the expected decrease in velocity with decreasing thrust setting (increasing advance ratio). At negative loading conditions, the axial velocity in the slipstream is lower than in the freestream. This will cause a decrease in the lift on surfaces immersed in the slipstream. Comparing the results at positive and negative power coefficients (for example $J = 0.8$ versus $J = 1.6$), it can be seen that the tangential velocity reverses. This is as expected considering the opposite direction of the propeller torque in both conditions. Since the tangential velocity in the slipstream modifies the effective angle of attack perceived by the downstream wing, this will have a pronounced impact on the wing loading of the installed configuration.

The power coefficient used in Figs. 4.16 and 4.18 does not provide a clear insight into the absolute power consumption or generation by the propeller. Therefore, an alternative power coefficient, $P_C = P/\rho_\infty V_\infty^3 D^2$, was defined to assess the energy-harvesting performance of the propeller. Furthermore, an energy-harvesting efficiency was defined as [216]:

$$\eta_{eh} = \frac{P}{\frac{1}{2}\rho_\infty\pi R^2 V_\infty^3} \quad (4.1)$$

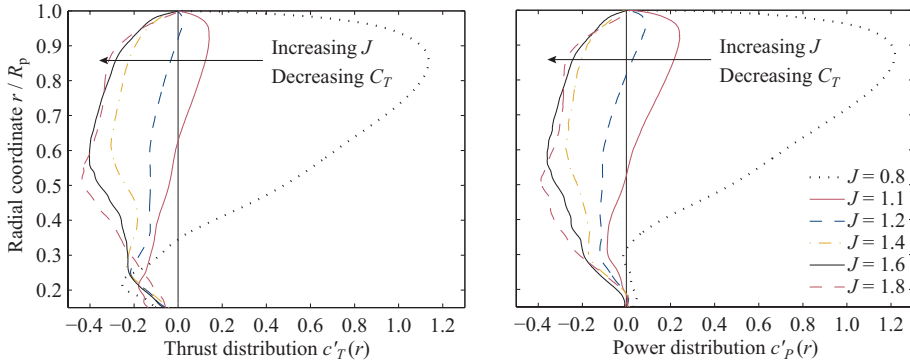


Figure 4.18: Beaver propeller thrust and power blade loading distributions for various advance ratios.

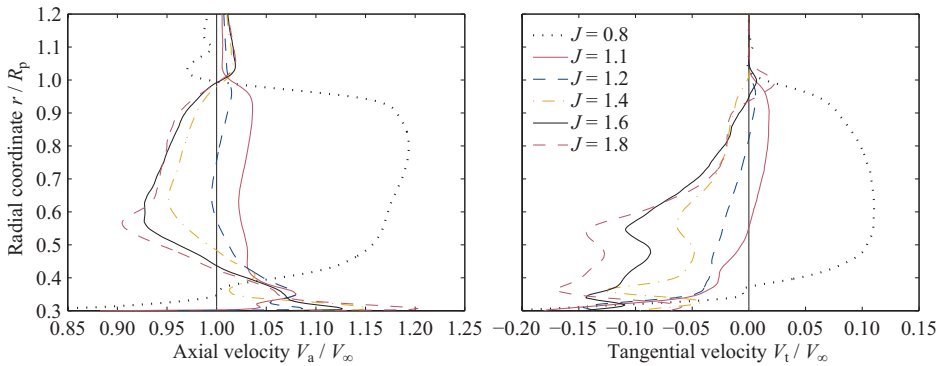
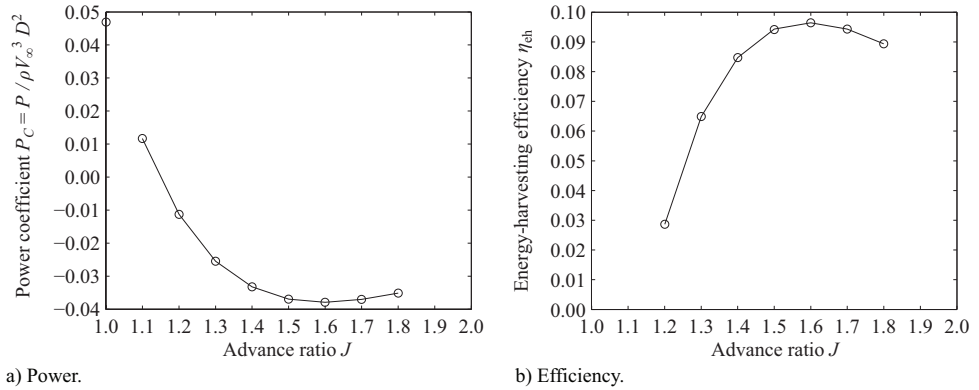


Figure 4.19: Radial distributions of axial and tangential velocity in the Beaver propeller slipstream at $0.19R_p$ downstream of the propeller center.

with P the power generated by the rotor, and the term in the denominator representing the power available in the flow for energy conversion, defined following the typical convention for horizontal-axis wind turbines. Figure 4.20 displays the corresponding results from CFD. It can be seen that in both cases maximum regenerative power and energy-harvesting efficiency is obtained around $J = 1.6$. At the considered blade pitch setting, the maximum energy-harvesting efficiency predicted by the CFD data was about 10%. This is low compared to modern large-scale horizontal-axis wind turbines, for which values of up to around 50% can be reached [216].

For small wind turbines the efficiency is already considerably lower due to the reduction in lift-to-drag ratio of the blade sections with decreasing Reynolds number [216]. Furthermore, the Beaver propeller used for the analyses was not designed for operation at negative thrust conditions. Therefore, the energy-harvesting efficiency could be improved by changing the blade design, while taking into account that the propulsive performance should not be degraded. Ref. [101] has already proven the potential success of such a multi-objective design effort, in that case applied to a fixed-pitch energy-harvesting propeller on a small electric aircraft. Despite this low efficiency, the propeller

Figure 4.20: Energy-harvesting performance by the Beaver propeller at $V_\infty = 40$ m/s.

introduces the characteristic features in the slipstream (reverse tangential velocity, reduced axial velocity, slipstream expansion) needed to study the interaction with the wing in Section 5.2.

4.1.4. APIAN PROPELLER

The APIAN propeller was used to study interaction with downstream swirl-recovery-vanes (SRVs) as the validating experiment featured this propeller. This section discusses the isolated performance and slipstream of the APIAN propeller. All results are at a freestream airspeed of $V_\infty = 60$ m/s. First grid study results for the RANS CFD simulations are presented, after which the CFD results are discussed and compared to the experimental results from Ref. [68]. The interaction of the APIAN propeller with the downstream swirl-recovery-vanes is treated in Section 6.1.

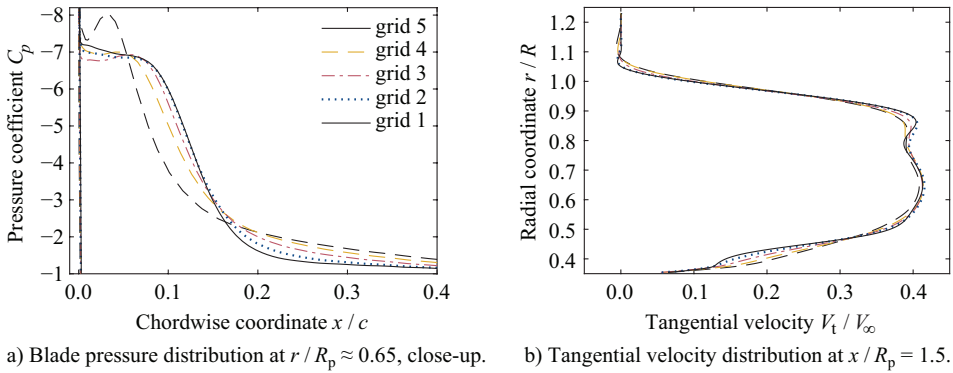
GRID CONVERGENCE

For the grid convergence study of the isolated propeller, five grids were created for the wedge-shaped domain from Fig. 3.16. The grid sizes are reported in Table 4.5.

Table 4.5: Grid sizes of wedge-shaped domain from Fig. 3.16 for the isolated APIAN propeller.

grid	# nodes	h_i/h_1
5	1,509,555	2.41
4	2,219,976	1.97
3	3,406,920	1.58
2	5,461,761	1.27
1	9,084,698	1.00

Figure 4.21a displays the effect of grid refinement on the pressure distribution on the front part of the blade's suction side at $r/R_p \approx 0.65$. The isolated propeller is considered at a high loading condition ($J = 1.05$). The effect of grid refinement is small and only noticeable in an area of reduced pressure just aft of the suction peak. This is the result of a leading-edge vortex occurring at this advance ratio. This vortex and its pressure gradient

Figure 4.21: Effect of grid refinement for the isolated APIAN propeller at $J = 1.05$.

are captured better with grid refinement [217], resulting in small changes in thrust and torque coefficient of the propeller blade. To assess the effect of grid refinement on the flowfield in the propeller slipstream, the time-averaged radial distribution of tangential velocity in a plane at $x/R_p = 1.5$ is shown in Fig. 4.21b. Differences between the solutions obtained using the different grids are only noticeable in the regions of the tip vortex and the root vortex, while outside of these regions the velocity profile remained practically unchanged. The sensitivity of the vortical flow structures to the grid size is a well-known characteristic of 2nd order schemes, and is caused by numerical diffusion in the solution algorithm [214], as was discussed earlier for the Beaver propeller.

Table 4.6: Grid dependency of APIAN propeller performance at $J = 1.05$.

	C_T	C_Q
p	2.42	3.81
U_s (%)	0.21	0.20
U_s^* (%)	0.23	0.31
ϕ_0	0.523	0.157
U_{ϕ_3} (%)	2.44	1.97

The grid dependency of the propeller thrust coefficient and propeller torque coefficient is summarized in Table 4.6. The study for the isolated propeller was performed at $J = 1.05$, since this is the most stringent operating condition in terms of loading of the propeller blades. For this case, monotonic convergence was observed. Minor changes in thrust coefficient and torque coefficient occurred due to grid refinement. The apparent order of convergence was higher than the theoretical order of the scheme, resulting in the use of the theoretical order ($p = 2$) to estimate the error. For grid 3, the estimated discretization errors for the thrust coefficient and torque coefficient are 2.44% and 1.97%, respectively. It is concluded that grid 3 provides a sufficiently converged solution to use for the remainder of this study.

COMPARISON OF COMPUTATIONAL AND EXPERIMENTAL RESULTS

To validate the CFD results, the computed pressure distribution on the propeller blade at $r/R_p \approx 0.65$ was compared to the experimental result, as shown in Fig. 4.22a for the high thrust condition ($J = 1.05$). The wide suction peak on the front part of the profile is due to the previously mentioned leading-edge vortex, which is visualized in Fig. 4.22b by means of streamlines and an isosurface of the turbulent kinetic energy. This vortex is caused by the high sweep and thin leading edge of the propeller blade in combination with a large local angle of attack, and has been observed before in experiments on a propeller with a geometry comparable to the APIAN propeller [218]. Near the trailing edge, a small suction region can be observed on the lower side of the blade. This is caused by the local curvature of the blade profile, which features a rounded trailing edge. The agreement between the experimental and numerical data is reasonably good, especially on the pressure side of the blade and around the suction region near the leading edge of the profile. The unexpected increase of the suction observed in the experimental data at $x/c = 0.7$ may have been caused by calibration shifts between the different pressure sensors instead of a physical phenomenon.

In Fig. 4.23 the computed tangential velocity is presented by means of a contour plot at the position of the PIV measurement plane. Experimental data is shown alongside for comparison. These measurements were taken in longitudinally adjacent planes, located slightly below the propeller axis at a vertical position of $z/R_p = 0.03$ due to a small misalignment of the setup. The CFD results were extracted from the same plane. The intermediate thrust condition ($J = 1.40$) is considered. The experimental results were acquired phase-locked to the propeller blade position and the CFD data were extracted such that they correspond to the same circumferential position of the blade. In the slipstream in general a positive tangential velocity can be observed, moving in the propeller rotation direction by the momentum added to the flow by the propeller. One can observe the wakes of the propeller blades by the vertical bands of increased tangential velocity. When moving downstream, these wakes deform by the non-uniform velocity distribution in the slipstream. The effect of the propeller blade tip vortices can be observed around $y/R_p \approx 1.0$ by the pairs of increased and decreased tangential velocity.

Qualitative agreement is obtained between the experimental and numerical data. Compared to the PIV data, the CFD results suffer from numerical diffusion, smoothing the velocity gradients in the wakes and tip vortices of the propeller blades. As a result, these flow structures appear more spread out in the numerical data. Apart from the effects due to numerical diffusion, also a phase shift can be observed between the experimental and numerical results by comparing the axial locations of the blade tip vortices and wakes. To provide a quantitative comparison between the experimental and numerical data, profiles of the time-averaged tangential and axial velocity were extracted from the evaluation plane, at $x/R_p = 1.5$ downstream of the propeller. The corresponding results are given in Fig. 4.24, which includes the data for all considered propeller thrust settings. The uncertainty of the experimental data is indicated by the gray shading.

With decreasing advance ratio, the axial and tangential velocity increase in magnitude as the loading on the propeller becomes larger. Good quantitative agreement is obtained between the tangential velocity PIV measurements and the CFD evaluations for the intermediate and low propeller thrust settings ($J = 1.40$ and $J = 1.75$) in the middle

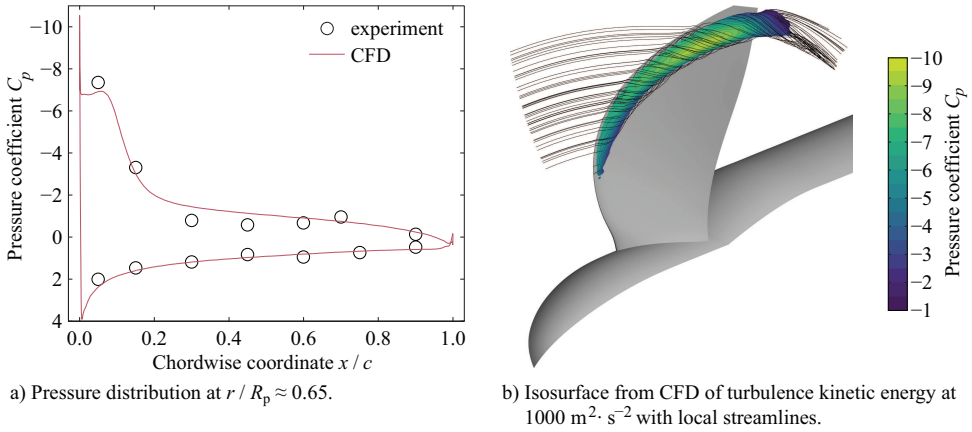


Figure 4.22: Pressure distribution on the APIAN propeller blade at $J = 1.05$ with visualization of leading-edge vortex occurring in this condition.

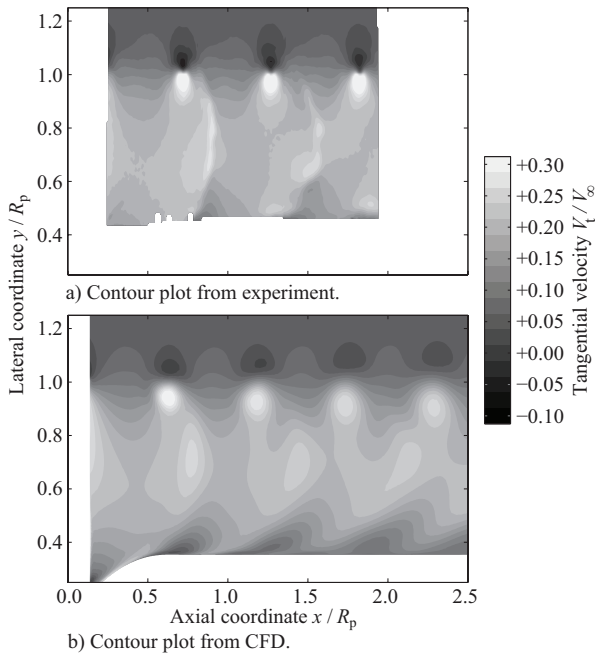


Figure 4.23: Comparison of the slipstream of the APIAN propeller, visualised by contour plots of the phase-locked tangential velocity at $z/R_p = 0.03$ for $J = 1.40$.

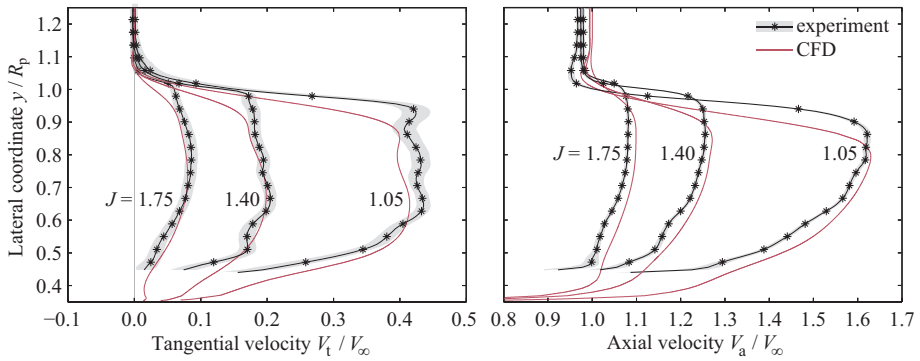


Figure 4.24: Comparison of the time-averaged velocity in the slipstream of the APIAN propeller at $x/R_p = 1.5$ and $z/R_p = 0.03$.

part of the slipstream ($0.5 < y/R_p < 0.9$). At more outboard lateral coordinates, near the slipstream edge, the CFD results suffered from numerical diffusion, as discussed before in relation to Fig. 4.23. Comparing the experimental and numerical data for the axial velocity in the same figure, differences are again observed near the edge of the slipstream due to the smearing of the velocity gradients induced by the tip vortices of the propeller in the simulations. Away from the slipstream edge, the measured velocity is consistently lower than the simulated value. This could point at an upstream effect of the support structure used in the experiment, which was not included in the simulations. However, considering the changes to the velocity distributions caused by the change in J , it is observed that the simulations predict the same trends as measured in the experiment.

4.2. ANGLE OF ATTACK EFFECTS

Angle of attack effects for the isolated propeller are discussed for the XPROP and F29 propeller as these propellers are later used in interaction studies where they experience a large angle of attack on top of the interaction effects. For the XPROP propeller, experimental results are complemented with RANS CFD results for selected conditions. For the F29 propeller, only experimental performance results are presented.

4.2.1. XPROP PROPELLER

For the propeller at angle of attack, the propeller reference frame, angle of attack α_p , blade phase angle φ and forces are defined in Fig. 4.25. The performance quantities are shown in the (tilted) hub frame of reference.

An angle of attack range from 0 deg to 90 deg was investigated experimentally for the isolated propeller. The performance data and 3rd order polynomial fits with 95% confidence bands are presented in Fig. 4.26 as function of advance ratio for all angles of attack and freestream airspeeds. The results for the different freestream airspeeds do not match exactly as expected, because of differences in Reynolds number. With decreasing advance ratio, the thrust and power coefficient curves for different α_p all converge to the values found in static condition (Fig. 4.1). While for the smaller angles of attack

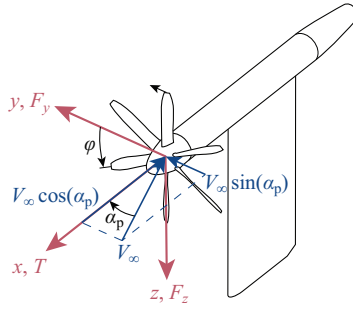


Figure 4.25: Sketch of XPROP propeller setup without wing, including definition of propeller reference frame, angle of attack α_p , blade phase angle φ and forces.

4

C_T and C_P decrease with J , for $\alpha_p > 60$ deg they increase. In terms of in-plane forces, C_{F_y} is the dominating component compared to C_{F_z} as the angle of attack is formed by rotation around the propeller z -axis. For all advance ratios, with increasing angle of attack C_{F_y} increases up to a certain maximum angle, which for the highest J is found at an angle smaller than 90 deg. The effect of angle of attack on the performance quantities is larger for higher J , as the contribution of the freestream airspeed to the effective velocity becomes relatively larger due to the lower propeller rotational speed. The out-of-plane moments follow similar trends as the in-plane forces, with C_{M_y} the more dominant component compared to C_{M_z} . The mechanisms behind the angle of attack effects are discussed later in this section by means of the CFD results.

Since the experimental data were obtained in an open jet wind-tunnel, wall corrections need to be considered. In Fig. 4.27, an estimation of the angle of attack and advance ratio correction are presented for the data in Fig. 4.26 based on Eqs. (3.1) and (3.2). This figure gives an indication of the required correction and all other results in this section are uncorrected. The advance ratio correction is presented as the difference between the corrected and measured advance ratio $\Delta J = J_c - J$. The data at the freestream airspeed of 6 m/s require a large angle of attack correction while at the highest advance ratio for 18 m/s the correction is almost negligible. The effect of these large corrections for 6 m/s on the performance data is however small as in Fig. 4.26 it was shown that the dependency of the performance results on angle of attack for 6 m/s is relatively small. Furthermore, the advance ratio correction is relatively small for all operating conditions, although most pronounced again for the lowest airspeed of 6 m/s. Based on these correction estimates, for the interaction study with the wing in Section 7.3 only results at 12 m/s and 18 m/s are presented.

Not only the wind-tunnel itself, also the propeller setup possibly introduces an unwanted disturbance in the performance data through the presence of the pylon. To investigate the effect of the pylon, in Fig. 4.28 CFD results are shown of the blade thrust evolution over the azimuth with and without presence of the pylon. Data are shown for an advance ratio of $J = 0.35$ at $V_\infty = 18$ m/s for four angles of attack. At $\alpha_p = 45$ deg GCI uncertainty is shown to illustrate the possible uncertainty introduced by the grid. The

4.2. ANGLE OF ATTACK EFFECTS

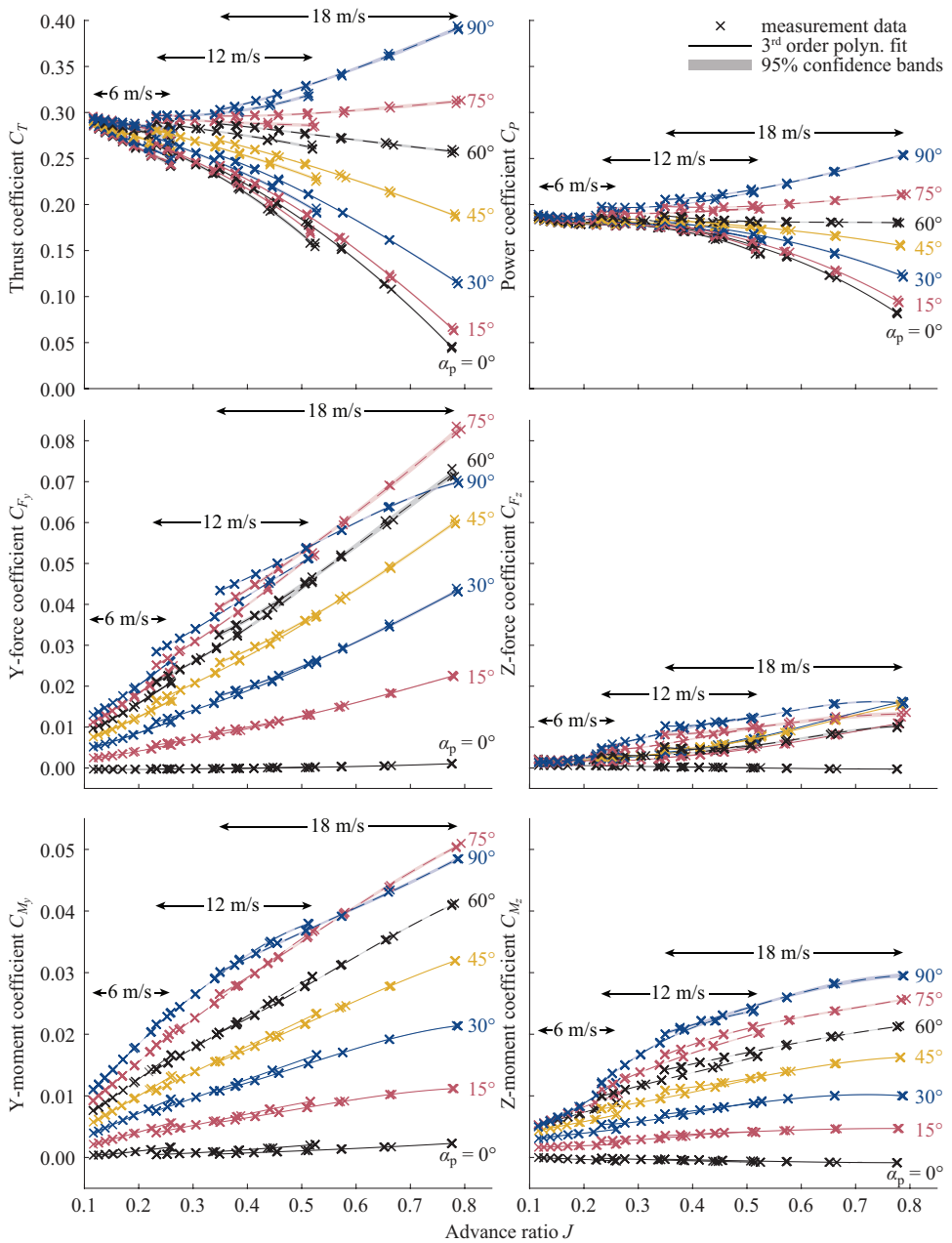


Figure 4.26: Experimental result for the XPROP propeller showing thrust, power, in-plane force and out-of-plane moment coefficients for $\beta_{0.7R_p} = 20$ deg.

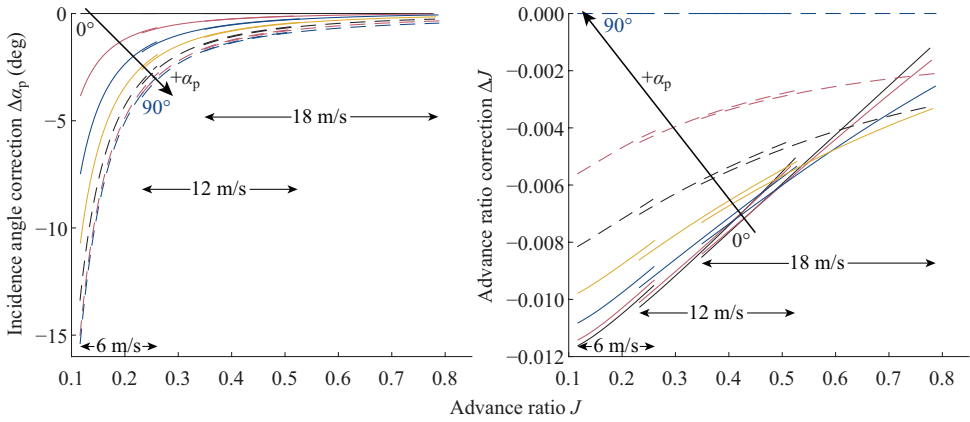


Figure 4.27: Angle of attack and advance ratio wind-tunnel wall corrections for the XPROP experimental results for $\beta_{0.7R_p} = 20$ deg; linestyle and color of Fig. 4.26 maintained.

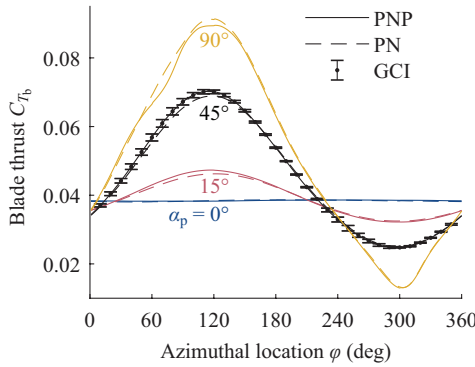


Figure 4.28: CFD simulation results showing XPROP propeller blade thrust evolution with azimuth angle with and without pylon for $J = 0.35$, $V_\infty = 18$ m/s and $\beta_{0.7R_p} = 20$ deg. Azimuthal location φ is defined in Fig. 4.25.

CFD data were simulated using a transient scheme with a sliding mesh approach in the domain as presented in Fig. 3.18. The effect of the pylon can be noticed in the data when the blade sweeps past the pylon around $\varphi = 90$ deg. For $\alpha_p = 0$ deg there is purely an upstream pressure effect due to blockage, increasing the blade thrust by on average 0.2%. For $\alpha_p = 15$ deg and 45 deg the blade thrust is slightly increased by on average 0.6% and 0.7% respectively due to the pylon, likely caused by the increased angle of attack due to the upwash from the lift on the pylon. At $\alpha_p = 90$ deg a small reduction in blade thrust of on average 1.1% occurs. As the pylon was normal to the flow causing considerable blockage, it might have induced a slight angle of attack reduction.

The integrated CFD data are plotted in Fig. 4.29 alongside experimental data as a function of α_p for all propeller performance quantities. Results for the propeller with and without pylon effect are shown and these include the loading on the spinner. Also results with pylon effect excluding the spinner loading are presented, to show the con-

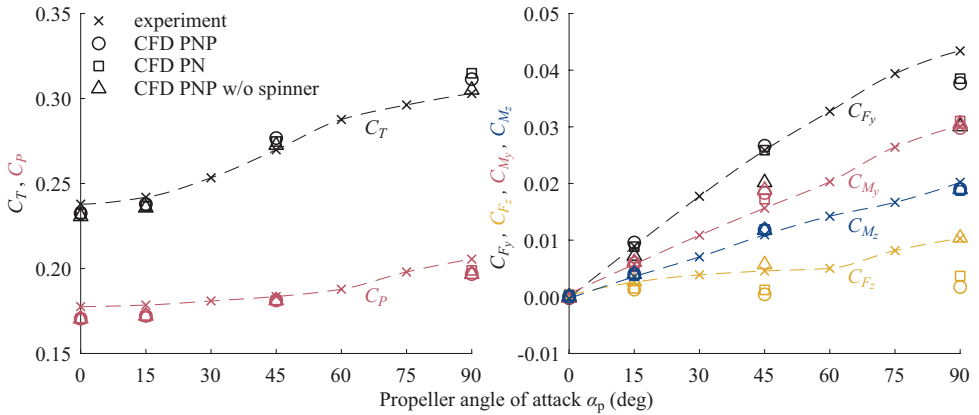


Figure 4.29: XPROP propeller performance comparison between CFD and experiment as function of α_p for $J = 0.35$, $V_\infty = 18$ m/s and $\beta_{0.7R_p} = 20$ deg.

tribution of the spinner on the performance quantities. For $\alpha_p = 45$ deg in Fig. 4.30 the distribution of thrust and in-plane force coefficients are plotted over the propeller disk. The corresponding time-averaged flowfield is given in Fig. 4.31 in terms of axial and tangential velocity and approximated blade section angle of attack. The flowfield was obtained by time-averaging the flowfield $0.07R_p$ upstream and downstream of the propeller for a full blade passage, and taking the average of these two flowfields to obtain approximately the flowfield experienced by the propeller.

The CFD predictions of thrust and power in Fig. 4.29 are close to the experimental values. A rise in thrust and power is seen with increasing angle of attack. In Fig. 4.30 a the thrust distribution is plotted as a ratio with the thrust distribution at zero angle of attack. An area of increased thrust ($(c_T(r)/(c_T(r))_{\alpha_p=0} > 1)$) and decreased thrust ($(c_T(r)/(c_T(r))_{\alpha_p=0} < 1)$) can be observed. Two effects play a role. With non-zero angle of attack, the in-plane component of the freestream, $V_\infty \sin(\alpha_p)$, results in negative and positive tangential velocity for the advancing and retreating blade side respectively (Fig. 4.31 b). The tangential velocity is defined positive in the rotation direction of the propeller. The negative tangential velocity results in an increase in blade section angle of attack and thus in an increase in thrust and vice versa (Fig. 4.31 c). The second effect is that the axial component of the freestream, $V_\infty \cos(\alpha_p)$, reduces over the complete propeller disk, resulting in increased blade section angle of attack. The net effect is an increase in integrated thrust, and a likewise increase in power. The loading on the spinner only plays a minor role for the thrust and negligible role for the power.

For the largest in-plane force coefficient C_{F_y} , the CFD prediction is close to the experimental values for all propeller angles of attack except for $\alpha_p = 90$ deg where a 13% under-prediction is found. C_{F_y} increases from zero to positive values with non-zero angle of attack. This is because the positive contribution to C_{F_y} on the advancing blade side is larger than the negative contribution on the retreating blade side (Fig. 4.30 b). This imbalance in tangential force between the advancing and retreating blade side is coming from the imbalance in thrust explained in the previous paragraph. As shown in

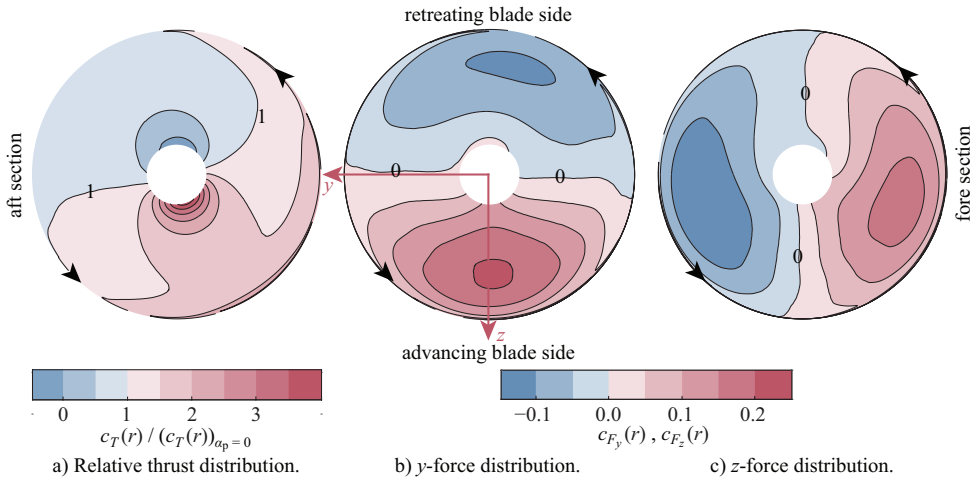


Figure 4.30: CFD result showing thrust and in-plane force coefficient distributions for the XPROP propeller at $\alpha_p = 45$ deg without pylon for $J = 0.35$, $V = 18$ m/s and $\beta_{0.7R_p} = 20$ deg.

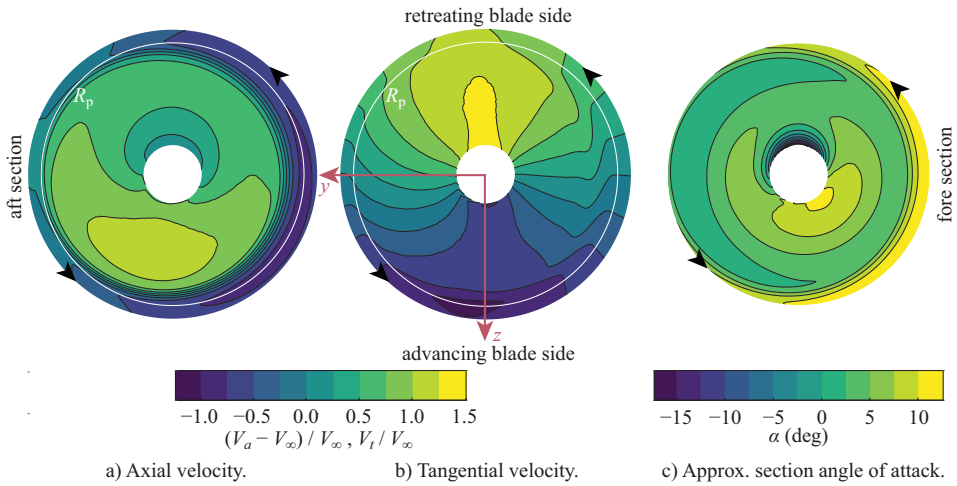


Figure 4.31: CFD result showing time-averaged XPROP propeller flowfield at $\alpha_p = 45$ deg without pylon for $J = 0.35$, $V = 18$ m/s and $\beta_{0.7R_p} = 20$ deg.

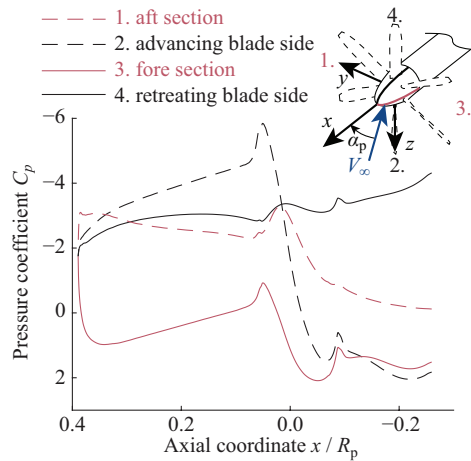


Figure 4.32: CFD result showing the time-averaged pressure coefficient distribution C_p on the XPROP spinner in a horizontal and vertical plane at $\alpha_p = 45$ deg without pylon for $J = 0.35$, $V = 18$ m/s and $\beta_{0.7R_p} = 20$ deg.

Fig. 4.29, at the larger angles of attack a considerable portion of C_{F_y} is formed by loading on the spinner. This is resulting from the skewed inflow to the spinner, causing a pressure difference between the fore and the aft section of the propeller. To illustrate this, in Fig. 4.32 the time-averaged pressure coefficient distribution along the spinner is plotted along lines in the horizontal and vertical plane. Clearly, the large suction on the aft section compared to the fore section results in a net force in positive y -direction, adding to the positive y -force by the propeller blades.

The smaller in-plane force coefficient C_{F_z} is only about 20% of C_{F_y} on average. In the CFD simulations, this component is considerably underestimated. A very large part of this force component is a result of spinner loading. The part of C_{F_z} from the propeller blades results from the imbalance in tangential force between the fore and aft section, causing an area of larger positive z -force on the fore section than negative z -force on the aft section (Fig. 4.30 c). The larger positive z -force is caused by the phase lag in the thrust, especially for the outboard sections (Fig. 4.30 a). The dominant mechanism behind this phase lag are variations in induced velocity across the propeller disc as discussed by Ortun et al. [72]. On the aft section the propeller experiences higher axial velocities and vice versa (Fig. 4.31 a), because the propeller vortex system is displaced in this direction. This results in relatively larger blade section angles of attack on the fore section (Fig. 4.31 c) and thus in a larger thrust and tangential force component. The contribution of the spinner to C_{F_z} is a result of the higher static pressure jump on the advancing blade side than on retreating blade side from the difference in thrust [72]. In Fig. 4.32 the pressure coefficient distribution on the advancing and negative retreating blade side are also plotted. Upstream of the propeller, the increased suction on the advancing blade side results in a positive z -force, while downstream of the propeller the opposite occurs. The pressure difference between the advancing and retreating blade side is larger downstream of the propeller and the integrated z -force on the spinner is therefore negative, decreasing C_{F_z} . Note that the large under-prediction of C_{F_z} in the

CFD simulation may be originating from the spinner loading if this pressure balance is slightly different in the experiment, although this is unclear and cannot be derived from any of the experimental or CFD results.

The prediction of the out-of-plane moment coefficients in the CFD simulations is very accurate. The spinner loading only play a minor role for these moment components. Both components increase with increasing α_p . The positive values for C_{M_y} are resulting from the imbalance in thrust distribution between the advancing and retreating blade side as plotted in Fig. 4.30 a. Likewise, the positive values for C_{M_z} originate from the imbalance in thrust distribution between the fore and aft section.

4.2.2. F29 PROPELLER

Similar to Fig. 4.26 for the XPROP propeller, Fig. 4.33 presents the performance at a freestream airspeed of $V_\infty = 20$ m/s at various angles of attack from $\alpha_p = 0$ deg to 95 deg. The raw F/T sensor data is shown and 3rd order polynomial fits are presented including 95% confidence bands. This isolated propeller performance is directly used as the reference performance for the cases with interaction discussed in Section 6.2. The propeller thrust and power coefficient C_T and C_P , the in-plane force coefficients C_{F_y} and C_{F_z} and the out-of-plane moment coefficients C_{M_y} and C_{M_z} are plotted versus advance ratio J . The three dashed lines of constant advance ratio at $J = 0.49, 0.57$ and 0.69 are the main conditions used in the interaction results. Also for the data at angle of attack, the thrust coefficient has the widest confidence bands because of scatter in the data, followed by those for C_{F_y} . All other quantities have significantly less scatter. The data match with typical propeller performance behaviour with angle of attack in line with the XPROP propeller data in Fig. 4.26. At zero angle of attack, C_T decreases with increasing J . With increasing angle of attack the $C_T - J$ curve slope reduces, until from a certain α_p , in this case around 60 deg, the slope changes sign. For a given J , C_T increases with increasing α_p . When one would extend the curves for different α_p to the left, they seem to merge at a level very similar to the C_T in static condition from Fig. 4.7. The behaviour of C_P with variation of J and α_p is similar to that of C_T , albeit at a different level.

The in-plane force component in the direction of the angle of attack, defined as the y-force coefficient C_{F_y} by the axis system shown in Fig. 3.9 a, is zero at zero α_p and increases with increasing α_p . It is possible that a maximum in C_{F_y} is reached for $\alpha_p < 90$ deg as was found for the XPROP propeller for the higher advance ratios. The in-plane force coefficient C_{F_z} is again much smaller than C_{F_y} . The out-of-plane moment coefficients C_{M_y} and C_{M_z} correlate again to C_{F_y} and C_{F_z} respectively.

To investigate the relation between thrust and power with varying J and α_p , in Fig. 4.34 the power coefficient is plotted versus the thrust coefficient, made non-dimensional with the rotational speed in Fig. 4.34 a and with the freestream airspeed in Fig. 4.34 b. In the $C_P - C_T$ plot the data collapses approximately to an almost linear line, i.e. variations in J and α_p only marginally affect the $C_T - C_P$ ratio for the presented conditions. As rotational speed is varied to change advance ratio and the freestream airspeed is constant, the $P_C - T_C$ plot is more indicative of propeller performance. It can be seen that with increasing α_p the power required by the propeller reduces for a given thrust level.

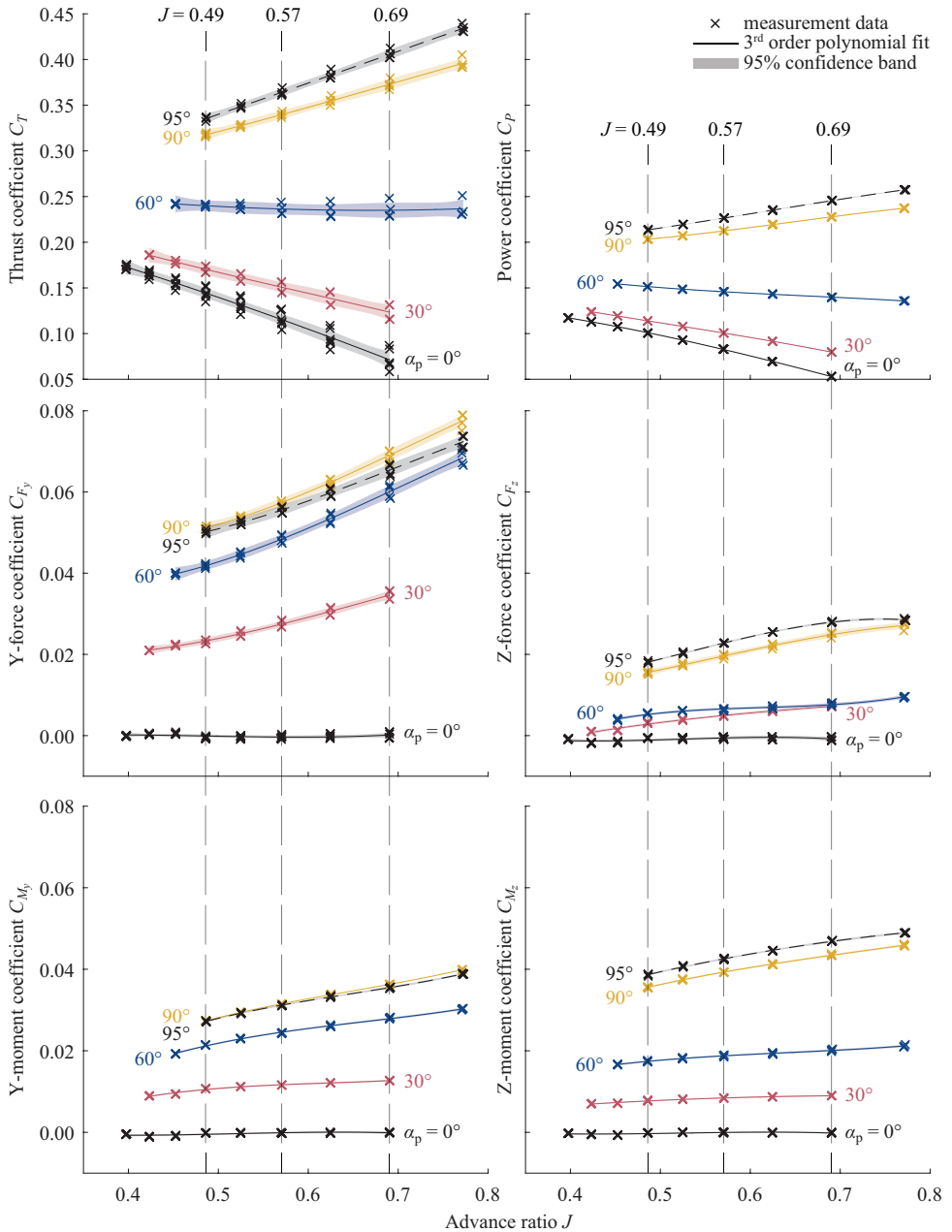


Figure 4.33: Isolated F29 propeller performance versus J at various propeller angles of attack for $V_\infty = 20$ m/s, measured with the F/T sensor.

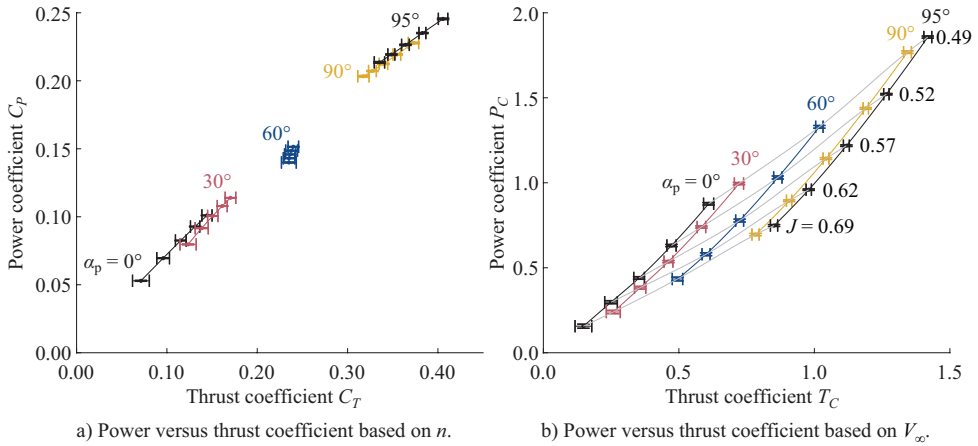


Figure 4.34: Isolated F29 propeller power versus thrust at various J and propeller angles of attack for $V_\infty = 20$ m/s, measured with the F/T sensor.

4.3. CONCLUSIONS

The aerodynamic characteristics of the propellers in this research were described in this chapter as a function of advance ratio J and angle of attack α_p , answering the first research question **Q1a**. Propeller operation in static condition, in forward flight, at very large angle of attack and in windmilling and energy harvesting condition were discussed in terms of performance and slipstream. These results will be used as the reference in the following chapters where aerodynamic interactions are introduced.

With the XPROP and F29 propellers, the propeller performance was studied for a wide range of advance ratios and angle of attack. In static condition (zero inflow speed), the thrust and power coefficient remain almost constant with increasing tip speed, although small increases were found for the investigated range of tip speeds likely due to Reynolds number and/or compressibility effects. For the investigated range of advance ratios, it was found that at zero angle of attack, the thrust coefficient decreases with increasing J . With increasing angle of attack the slope of the thrust coefficient versus J curve reduces, until from a certain α_p , in the case of the F29 propeller around 60 deg and for the XPROP propeller slightly higher, the slope changes sign. For a given J , the thrust coefficient increases with increasing α_p . When one would extend the curves for different α_p to the left, they seem to merge at a level very similar to the the thrust coefficient in static condition. The behaviour of the power coefficient with variation of J and α_p is similar to that of the thrust coefficient, albeit at a different levels. With increasing α_p the power required by the propeller reduces for a given thrust level. The in-plane force component in the direction of the angle of attack is zero at zero α_p and increases with increasing α_p . It is possible that a maximum is reached for $\alpha_p < 90$ deg as was found for the XPROP propeller for the higher advance ratios. The other in-plane force coefficient is much smaller. The out-of-plane moment coefficients correlate to their respective in-plane force coefficients.

For the Beaver and APIAN propellers, the slipstream at positive thrust was characterised. The typical increase of the axial velocity component in the slipstream results in contraction, especially noticeable at high thrust. Furthermore, the propeller introduces a tangential velocity component in the direction of rotation. Blade tip vortices and blade wakes were identified as well. For the APIAN propeller, a leading edge vortex was present as a result of its leading edge sweep. Especially at high loading, this caused a wide suction peak near the leading edge.

With the Beaver propeller, windmilling was investigated. In this negative thrust regime, both the lift and drag forces acting on the blade sections contribute to the force in the thrust direction. Consequently, the slope of the thrust coefficient with advance ratio is higher than in the positive thrust regime. Beyond a certain advance ratio, the negative thrust and torque responses flatten to a smaller gradient with advance ratio than in positive-thrust conditions. The cambered airfoil sections of this propeller are not optimized for operation at relatively large negative angles of attack, thus causing separation and associated viscous losses. As the thrust and torque change sign, the axial velocity component in the slipstream is reduced compared to the freestream and the tangential velocity component changes sign. The distribution of these velocity components is different from the distributions at positive thrust as the propeller blade loading distribution is also different. The peaks are found more inboard.

Also research question **Q1b** was addressed. In general it has been shown that resolving propellers in CFD compares reasonably well with experimental data from wind tunnel tests in terms of propeller performance and slipstream. For the XPROP propeller it was shown that the prediction of flow separation on propeller blades at high blade loading, for instance when the propeller operates in static condition without freestream flow, comes with an error in propeller performance (approximately 15% in thrust and 6% in power) due to modelling and due to discretization. These errors reduce significantly (approximately 2% in thrust and 3% in power) when reducing blade pitch and thus blade loading to a regime where flow separation on the blades is less present.

For the Beaver and APIAN propellers it was shown that slipstream predictions by resolving the propellers in CFD agree well with experimental data except for in the tip vortex region. There, a significant error due to discretization is present due to numerical diffusion. Since these propellers are of very different geometry, this conclusion may be generalized. Unfortunately, the numerical methods found in typical 2nd order CFD solvers require extremely dense grids to avoid numerical diffusion and to preserve the tip-vortex strength. This error also resulted in reduced contraction of the slipstream. For the Beaver propeller the Spalart–Allmaras turbulence model only showed differences from the $k-\omega$ SST turbulence model in the downstream part of the slipstream (more than two blade radii downstream of the propeller), where numerical diffusion in the vortex cores was less for the SA model.

Propeller performance at angles of attack up to very large angles can be reasonably well predicted by the CFD model (on average approximately 3% difference in thrust and power and 8% difference in the primary in-plane force and the out-of-plane moments over de angle sweep), although for the XPROP propeller differences in the loading on the spinner may have introduced deviations from the experimental data, especially in terms

of the secondary in-plane force coefficient (on average approximately 60% difference over the angle sweep, partly due to the very small values). Loading on the spinner is an important factor to consider for the in-plane forces.

Considering propeller modelling in CFD, the actuator-disk and actuator-line models of the Beaver propeller provided an accurate time-averaged slipstream, only deviating from the full-blade model close to the nacelle. The remaining difference is thought to be due to the difference in modelling the close interaction of the blade root and nacelle by neglecting the blade thickness, and due to the lack of the time dependence of the flow separation from the blade root in both models. The actuator-line model agreed almost one-to-one with the full-blade model in a time-accurate sense.

In terms of lower-order propeller modelling, the blade element momentum model of the F29 propeller and the propeller analysis routine of PROPR for the XPROP propeller were found acceptable for isolated propeller performance prediction.

5

INTERACTION WITH WINGTIP

This chapter treats aerodynamic interaction of a propeller with the wingtip. Two layouts are investigated, a tractor and pusher variant. For the tractor variant the largest interaction effects are expected for the wing as it experiences the propeller slipstream and visa versa for the pusher propeller as it operates in the wing wake and wingtip flowfield. In the first Section 5.1, RANS CFD and validating experimental results are presented in order to answer research question 2a and b as posed in Section 2.3:

Q2a: *How do full-blade (FB) RANS simulations of a wingtip-mounted tractor-propeller compare to experimental data from an in-house wind-tunnel test in terms of flowfield and wing loading?*

Q2b: *How accurately can actuator-disk (AD) and actuator-line (AL) models in RANS simulations represent a propeller in interaction with the wingtip in tractor configuration and by how much can they reduce computational cost compared to FB simulations?*

With the same CFD model with actuator-disk, question 3 is answered in Section 5.2:

Q3: *What are the consequences of windmilling and energy harvesting on the wing loading for a wingtip-mounted tractor-propeller?*

In Section 5.3 the pusher variant is investigated. A propeller design framework is established and verified with RANS CFD simulations, both with the actuator-disk model from the previous sections and with blade resolving simulations. With this design study, question 4a and 4b are answered:

Q4a: *How does the propeller size and thrust level influence the propulsive efficiency benefit and the upstream aerodynamic loading on the wing for a wingtip-mounted pusher-propeller?*

Q4b: *To what extent can the propulsive efficiency benefit be increased by designing the propeller for the non-uniform inflow experienced at the wingtip?*

The contents of this chapter have been adapted from Refs. [64–66].

5.1. ANALYSIS AND MODELLING OF A WINGTIP-MOUNTED TRACTOR-PROPELLER

In this section, the accuracy of RANS simulations for a wingtip-mounted tractor-propeller is investigated. Not only blade resolving (full-blade) simulations are performed and compared to experimental results using the setup shown in Figs. 3.12 and 3.13, but also the capability of actuator-disk (AD) and actuator-line (AL) modelling are investigated for this interaction case. If proven to be sufficiently accurate, such propeller modelling methods enable quicker design evaluations in propeller interaction studies. The focus of this section is not on the interaction effects occurring as this is covered in Refs. [16, 219] for the same configuration.

For this research the Beaver propeller was used. For the isolated propeller configuration, grid convergence results and a comparison with the experiment were already presented in Section 4.1.3. The isolated wing configuration is treated in the next Section 5.1.1 to establish confidence in the chosen grid and to analyse differences with the experiment occurring already without interaction. The main interaction results with the propeller-wing configuration are discussed in Section 5.1.2. The results obtained using the full-blade model are compared to the experimental data to validate RANS modelling of the tip-mounted tractor propeller. The results obtained using the actuator models are compared to the experimental data and full-blade computational data to quantify the error introduced by the actuator models. The theory behind the actuator models was discussed in Section 3.2.1.

The wing model was equipped with a flap and flap deflection was used to generate lift on the wing. Two flap deflections of $\delta_f = +10$ deg and $\delta_f = -10$ deg were used to generate positive and negative lift respectively. The positive flap deflection represents inboard-up propeller rotation against the direction of the wingtip vortex and the negative flap deflection represents outboard-up rotation. All results were obtained with a freestream velocity of 40 m/s with zero angle of attack.

Since the final goal of the actuator models is to reduce the cost of propeller simulations, in Table 5.1 an overview of the grid size, number of iterations and estimated computational cost is shown for all configurations and propeller models. The estimated

Table 5.1: Grid sizes, number of iterations and estimated computational cost for the different configurations and propeller models.

configuration	model	# of cells	# of iterations		comp. cost w.r.t.
			steady	unsteady	iso. prop. FB
isolated propeller	FB	7,595,822	4,000	28,350	1.00
	AL	5,491,152	4,000	28,350	0.72
	AD	5,491,152	4,000	-	0.09
wing	-	41,749,592	8,500	-	1.44
propeller-wing	FB	50,387,027	8,500	39,375	9.82
	AL	41,749,592	8,500	39,375	8.13
	AD	41,749,592	8,500	-	1.44

computational cost is given relative to the full-blade (FB) isolated propeller configuration, and was calculated by the multiplication of the number of cells with the summation of steady and unsteady number of iterations. Because the propeller blades were not modelled in the actuator-line (AL) model simulations, the reduced grid size resulted in a 28% and 17% reduction of computational cost for the isolated propeller and propeller-wing configuration respectively compared to the full-blade model simulations. One should note that the demand of a high grid resolution in the slipstream all the way downstream to the survey plane led to a relatively large grid size. For a similar problem without this requirement, the reduction of computational cost could have been larger. For the actuator-disk (AD) model no unsteady iterations were required, resulting in a reduction of computational cost of 91% and 85% for the isolated propeller and propeller-wing configuration respectively compared to the full-blade model simulations. Note that this is only an indication of the computational cost reduction, since in a future application a lower order propeller model is envisioned which supplies the actuator models with the propeller loading distributions, instead of the requirement of full-blade model results for that purpose.

5.1.1. ISOLATED WING CONFIGURATION

The CFD domain for the isolated wing configuration was presented in Fig. 3.20. The propeller domain was replaced with a similar domain without propeller blades. First, grid convergence results are presented to establish confidence in the chosen grid. After that, a comparison with experimental results of the isolated wing is made.

GRID CONVERGENCE

Table 5.2 provides the grid size and refinement ratios h_i/h_1 for the five considered grids of the isolated wing configuration. Table 5.3 presents the solutions on the different grids, the corresponding observed order of convergence, standard deviation of the fits and estimated discretization error of the chosen grid 3.

Table 5.2: Grid sizes of the isolated wing configuration domain.

grid	# of cells	h_i/h_1
5	21,186,092	1.71
4	27,771,270	1.57
3	40,951,865	1.38
2	63,484,270	1.19
1	106,614,585	1.00

Grid convergence for the wing configuration was tested for the $\delta_f = +10$ deg condition by evaluating the overall lift and drag coefficients, C_L and C_D . While the best fit for C_L was found to be divergent, the solutions for the large range of grid sizes are very close to each other and noticeable scatter is present, making this a poor fit. A discretization error of 1.1% was estimated for grid 3. For the drag coefficient, convergence was found resulting in a comparable discretization error of 1.0%.

A comparison of the total-pressure coefficient C_{p_t} in the wake of the wing at the location of the survey plane is presented in Fig. 5.1 for three of the five grids. A contour plot for grid 3 is given together with lateral total-pressure profiles, cutting the inboard

Table 5.3: Grid dependency study for the isolated wing configuration, $\delta_f = +10$ deg.

	C_L	C_D	$(C_{p_t})_{\min}$ flap	$(C_{p_t})_{\min}$ wingtip
ϕ_5	0.1997	0.0411	0.7774	0.3858
ϕ_4	0.2000	0.0410	0.7741	0.3703
ϕ_3	0.1999	0.0409	0.7722	0.3633
ϕ_2	0.2001	0.0408	0.7726	0.3473
ϕ_1	0.2006	0.0408	0.7727	0.3441
p	-5.05	5.42	- [¶]	3.10
U_s (%)	-	0.08	-	1.03
U_s^* (%)	-	0.13	-	1.16
U_{ϕ_3} (%)	1.09	1.02	0.20	16.02

[¶]Oscillatory convergence observed

and outboard flap-edge vortices, the flap wake at midspan and the wingtip vortex. Good agreement is found between the profiles of different grids outside the vortex cores. The minima of total pressure in the flap wake at midspan and in the wingtip vortex were analyzed quantitatively (Table 5.3). Oscillatory convergence was observed in the flap wake with a marginal error of 0.2% for grid 3, while convergence was found for the total pressure in the core of the wingtip vortex with a large error of 16.0%. This latter error is a result of numerical diffusion, although it should be taken into account that this error is presented with respect to the relatively low total-pressure coefficient in the vortex core; relative to the freestream total-pressure coefficient this error reduces to 5.8%.

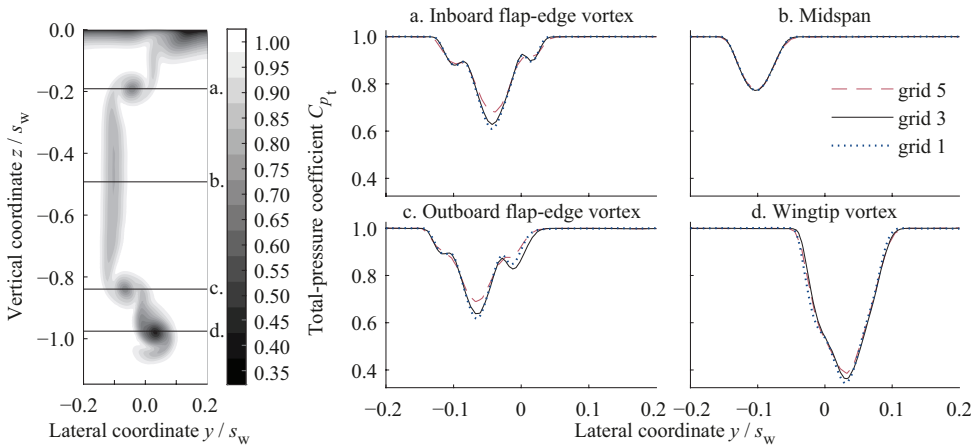


Figure 5.1: Contour plot of the total-pressure coefficient in the survey plane for grid 3, $\delta_f = +10$ deg. Lateral profiles provide comparison with solutions on other grids.

Based on the above grid dependency studies, it was concluded that grid 3 is well converged in terms of propeller and wing loading, slipstream flowfield, and wing wake, except for the vortex cores where a considerable discretization error needs to be taken into account. Hence, grid 3 was used for the results presented in the remainder of the section.

COMPARISON OF COMPUTATIONAL AND EXPERIMENTAL RESULTS

The loading and wake characteristics of the wing configuration were assessed to validate modelling of the wing without propeller interaction. Results were obtained for both the SA and $k - \omega$ SST turbulence models.

The overall loading on the wing and nacelle including turntable was obtained by balance measurements in the experiment, allowing for a comparison of the overall lift and drag coefficient with the CFD results. The computed and measured lift and drag coefficients are compared in Table 5.4 for the wing configuration with $\delta_f = \pm 10$ deg. While the lift for the positive and negative flap deflection should be exactly the opposite, for the experiment this was not the case. The likely reason is a small offset of the wing and the nacelle in terms of the angle of attack. The lift coefficient found from the CFD SA simulation is in between these values. The drag coefficient is slightly higher for the CFD SA result compared to the experiment, which is expected due to the fully turbulent modelling of the boundary layer, compared to the forced transition at $x'/c_w = 0.12$ in the experiment. The drag is relatively high for the given lift, because it includes the drag of the turntable, which amounted to about 1/3 of the total drag. The lift coefficient predicted with the $k - \omega$ SST turbulence model is considerably lower than found in the experiment, while the drag is slightly higher, also compared to the CFD result obtained with the SA turbulence model. The remainder of this section only considers the case with $\delta_f = +10$ deg.

Table 5.4: Overall lift and drag coefficients for the wing configuration.

		CFD SA	CFD $k - \omega$ SST	experiment
$\delta_f = +10$ deg	C_L	0.200	0.161	0.189
	C_D	0.041	0.042	0.040
$\delta_f = -10$ deg	C_L	-0.200	-0.161	-0.205
	C_D	0.041	0.042	0.040

To get more insight into the agreement of the CFD results and the experimental data, Fig. 5.2 displays the chordwise pressure distributions at the flap midspan and near the outboard flap edge. The coordinate x' changes with flap deflection as depicted in Fig. 3.12a. For the location at the flap midspan, also streamlines around the flap are shown. Again, both the SA and $k - \omega$ SST turbulence models are considered in the comparison with the measured data from the experiment. Very good agreement is found between the CFD results computed with the SA turbulence model and the experimental data. A small difference is present on the suction side around $x'/c_w = 0.12$ where the upstream effect of the transition strip results in a slight increase in pressure for the experiment. However, this should be considered as an artifact of the experimental data. The pressure distribution for the $k - \omega$ SST turbulence model at the flap midspan section deviates over the entire suction side of the flap due to flow reversal, as shown by the streamlines. This was also true for the section near the flap edge, although to a lesser extent due to reduced flow separation.

To validate the characteristics of the wing wake, a comparison of the total-pressure coefficient C_{p_t} in the wake of the wing at the location of the survey plane is presented in

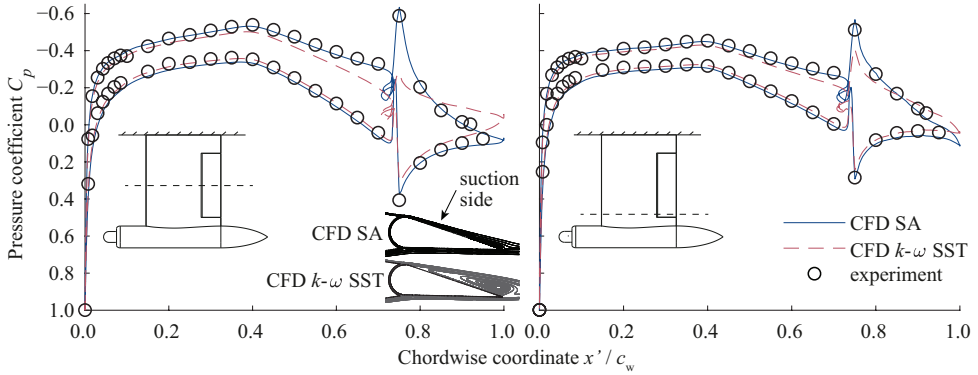


Figure 5.2: Pressure distributions at the flap midspan and near the outboard flap edge, $\delta_f = +10$ deg.

5

Fig. 5.3. A contour plot is shown for the experimental data, together with lateral total-pressure profiles which also include the CFD results for both considered turbulence models. These profiles run through the inboard and outboard flap-edge vortices, the flap wake at midspan and the wingtip vortex. The corresponding CFD contour plot obtained with the SA turbulence model was shown before in Fig. 5.1. Comparing those results with the experimental data in Fig. 5.3, very good agreement in the total-pressure deficit distribution is found, closely matching the locations of the flap vortices, the wingtip vortex and the wing wake. Note that at $z/s_w = 0$ a boundary layer is formed on the reflection plane of the wind-tunnel section, which is only visible in the CFD results since no total-pressure measurement could be performed in that region. The lateral total-pressure profiles show that the flap wake is slightly wider and the total-pressure deficit slightly larger in the CFD SA result compared to the experiment. Again, this is likely due to the fully turbulent modelling of the wing compared to the experiment.

For the $k-\omega$ SST turbulence model, the lateral location of the flap wake is offset from the experiment and the difference in total-pressure deficit is even larger, both a direct result of the flow reversal on the suction side of the flap for this turbulence model. The reduced pressure difference between the suction and pressure side for the $k-\omega$ SST turbulence model (Fig. 5.2) is also visible in the lower total-pressure deficit of the flap-edge vortices, while again with the SA turbulence model closer agreement with the experiment is found. The wingtip vortex is slightly better modelled by the $k-\omega$ SST turbulence model, although both turbulence models show a similar increased pressure deficit compared to the experiment. The fully turbulent modelling of the wing and nacelle and the higher lift (Table 4.4) compared to the experiment may be the reason for this difference. Note that numerical diffusion affected the strength of the flap-edge vortices and wingtip vortex as discussed in the grid dependency study.

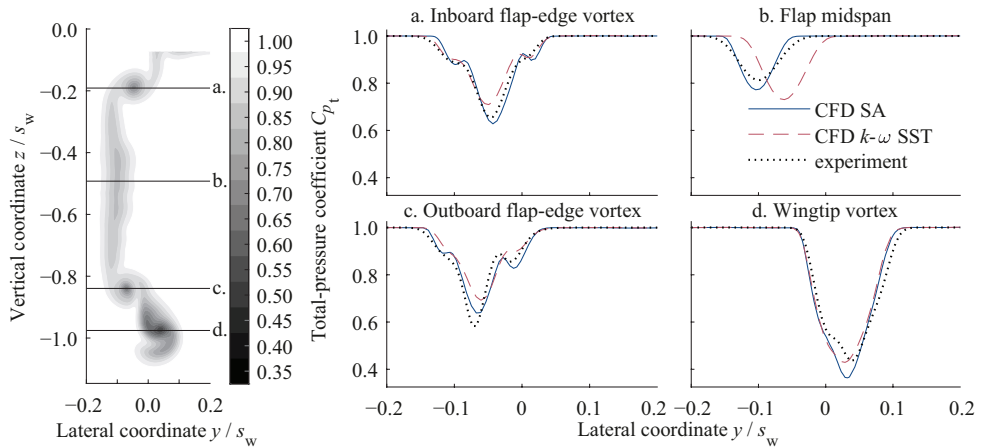


Figure 5.3: Contour plot of the total-pressure coefficient measured in the survey plane in the experiment, $\delta_f = +10$ deg. Lateral profiles provide comparison with CFD results.

5.1.2. PROPELLER–WING CONFIGURATION

The propeller–wing configuration was assessed for the flap deflections of $\delta_f = +10$ deg and $\delta_f = -10$ deg in terms of wing loading and wake flowfield. Since the wing has a symmetric airfoil and it is tested at $\alpha = 0$ deg, the positive flap deflection represents inboard-up propeller rotation and the negative flap deflection outboard-up rotation for a real application of wingtip-mounted propellers. All full-blade and actuator-line results were obtained by taking the average over the last rotation of a total of 6.25 rotations, while the actuator-disk results were converged to a steady state. The SA turbulence model was selected based on the comparison of turbulence models for the wing configuration and isolated propeller configuration. For the wing configuration, it was concluded that the SA turbulence model predicted flow separation on the flap better than the $k-\omega$ SST turbulence model and therefore also predicted the wake better. For the isolated propeller configuration, the SA model showed less decay of the velocity gradients in the tip vortices in the downstream direction.

LOADING

The propeller blades in installed condition experience an upstream effect of the wing, resulting in a small azimuthal variation and very small increase in time-average blade loading. This effect is described in Refs. [16, 219]. The effect of the propeller on the

Table 5.5: Overall lift and drag coefficients for the complete propeller–wing configuration. The full-blade propeller model is used and for the CFD model also results without propeller loading are given.

		CFD	experiment	CFD w/o prop
$\delta_f = +10$ deg	C_L	0.259	0.257	0.259
	C_D	-0.173	-0.180	0.040
$\delta_f = -10$ deg	C_L	-0.180	-0.180	-0.178
	C_D	-0.167	-0.177	0.043

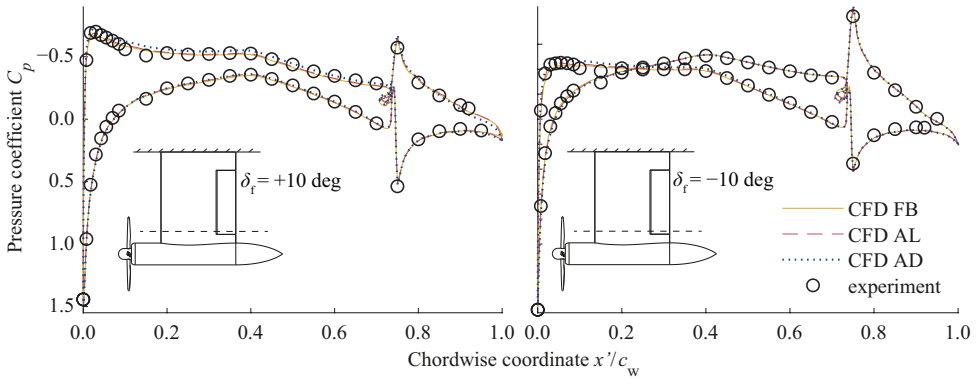


Figure 5.4: Time-averaged pressure distributions at a section near the outboard flap edge, $\delta_f = \pm 10$ deg.

5

overall lift and drag coefficient can be observed in Table 5.5 for the simulation with the full-blade modelling method and the experiment. Compared to the results for the wing configuration (Table 5.4), the lift coefficient for the positive and negative flap deflection changes by a positive increment due to the combined effect of the swirl and dynamic pressure rise in the slipstream. The lift coefficient obtained from the CFD and experiment are very similar, with a maximum difference of 0.002. The drag coefficient becomes negative, since it includes the propeller thrust, which is much larger than the wing, nacelle and turntable drag. For both flap deflections, the drag coefficient predicted by the CFD simulation is somewhat less negative than that from the experiment. This is for a large part explained by the choice of grid and the corresponding discretization error in the propeller thrust and wing drag as given in the grid dependency studies (Sections 4.1.3 and 5.1.1). In Table 5.5 also lift and drag coefficients are given for the CFD model without propeller loading. Compared to the wing configuration (Table 5.4), improved wing performance is noticeable for $\delta_f = +10$ deg, as C_L is higher and C_D is lower.

To get a better insight into the agreement and differences between the data obtained with the CFD models and measurements obtained in the experiment, the pressure distributions on the wing and the flowfield behind the wing were investigated. The time-averaged effect of the propeller slipstream on the wing loading and the effect of the direction of the flap deflection are both noticeable in the pressure distribution near the outboard flap edge, which is presented in Fig. 5.4. Compared to the case of the isolated wing (Fig. 5.2), a suction peak is present near the leading edge as a combined result of the swirl and dynamic pressure rise in the slipstream. Note that the pressure coefficient at the stagnation point is larger than unity since the section is located in the slipstream, while the freestream dynamic pressure is used to define the pressure coefficient. For both flap deflections a good match is found between the measurements and the CFD results, for all propeller modelling methods. However, over the majority of the suction side, a slightly lower pressure (increased suction) is noticeable for the actuator-disk model compared to the other two CFD results.

This lower pressure is also reflected in the lift distribution over the semi-span of the setup, shown in Fig. 5.5 for the positive flap deflection. The drag distribution is plot-

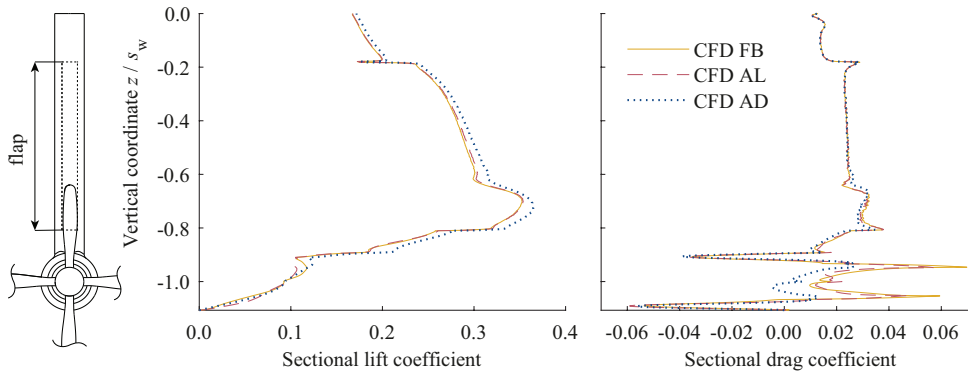


Figure 5.5: Time-averaged spanwise lift and drag distribution, $\delta_f = +10$ deg.

ted alongside. While the actuator-line and full-blade model results are almost the same, a slightly increased lift coefficient is shown for the actuator-disk model at all spanwise sections except on the nacelle. The corresponding increase in integrated lift coefficient over the semi-span compared to the full-blade model is 3.9%. The drag coefficient, on the other hand, remained practically the same, except for a reduction at the nacelle. Since the actuator-disk and actuator-line models are based on the same propeller blade loading distributions, the time dependency of the slipstream is the expected origin for the different lift distribution. Apparently, the time-average of the unsteady response of the wing to the slipstream is not equal to the response of the wing to the time-averaged slipstream. A similar observation was made by Thom and Duraisamy [220], who compared the inviscid response of a wing to an unsteady and time-averaged slipstream for a midspan-located tractor propeller. The only other two reasons for the offset in the lift distribution computed with the actuator-disk model could have been transient wing loading effects caused by for instance flow separation, which were not correctly captured in the steady-state solution, or differences already present in the slipstream prior to interaction with the wing. The former was checked with a transient simulation of the actuator-disk model, but no difference in wing loading was found compared to the steady-state solution. The latter was checked earlier with the isolated propeller model, for which the time-averaged slipstream (Fig. 4.14) was shown to be very similar for the two actuator models. Therefore, the difference in wing lift is likely a result of a difference in the propeller-wing vortex interaction. The vorticity is inherently more distributed in the slipstream computed by the actuator-disk model compared to the full-blade and actuator-line model. Therefore, the vortex interaction with the wing will likely result in differences in deformation of the vortex structure and consequently the wing loading obtained with the actuator-disk model will deviate from the other propeller model results.

The difference between the steady and time-accurate response of the wing can be observed in Fig. 5.6. The inherently steady pressure distribution obtained by applying the actuator-disk model is compared to the time-accurate results computed with the other two models at the spanwise section where the propeller blade tip-vortices im-

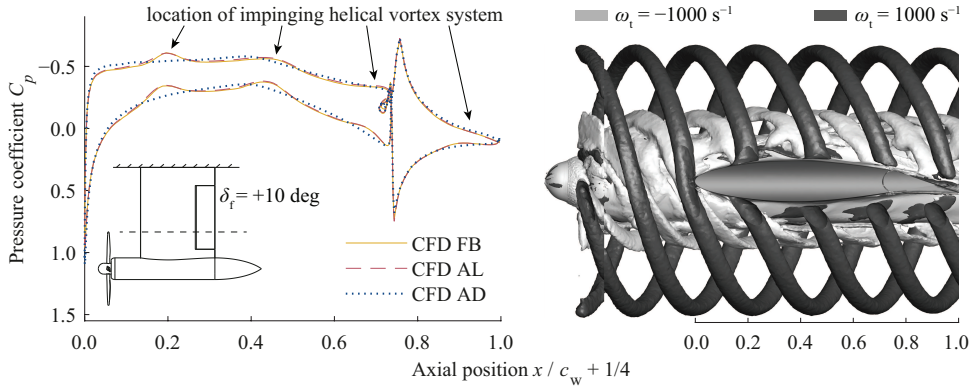


Figure 5.6: Time-accurate (FB and AL) and steady (AD) pressure distribution at the slipstream edge at $r/R_p = 0.99$, $\delta_f = +10$ deg for propeller orientation as shown in Fig. 3.13. Tangential vorticity isosurfaces indicate location of impinging helical vortex system.

5

pinge on the wing. The location of the impinging helical vortex system is visualized by isosurfaces of positive and negative tangential vorticity component as computed with the actuator-line model. In the positive tangential vorticity isosurface a clear axial deformation is visible between the wing suction and pressure sides. Moreover, a deformation in spanwise direction occurs, which was also observed by Sinnige et al. [163] At each tip-vortex core, a suction peak is noticeable in the pressure distribution on both sides of the airfoil. The locations as well as the magnitudes of these suction peaks agree well for the full-blade and actuator-line model, and thus the helical tip-vortex system and its deformation match well between these models.

FLOWFIELD

The flowfield behind the wing is the result of the interaction of the slipstream with the wing and thus can give further insight into this interaction. A comparison of the computed and measured total-pressure coefficient C_{pt} in the wake and slipstream at the location of the survey plane is presented in Fig. 5.7 for $\delta_f = +10$ deg. Alongside, radial total-pressure profiles are displayed for two azimuthal locations. The contour plots highlight the increased total pressure in the slipstream, masking part of the wing wake. In general, the full-blade model result agrees well with the experimental data. The most prominent difference is visible in the area of reduced total-pressure in the core of the slipstream. This area is influenced by vortex shedding from the root of the propeller blades and the front of the nacelle due to flow separation, as discussed in Section 4.1.3. The averaging period was found to be slightly too short to properly capture the time-average of these phenomena in the simulations. Furthermore, a slightly lower total pressure can be observed in the outer part of the slipstream for the full-blade model compared to the experiment. This difference was already present for the isolated propeller and was thought to be a result of decreased contraction due to the decay of the tip vortices in the simulations, as explained in Section 4.1.3. The wingtip vortex is identified by the largest pressure deficit in all contours and the outboard flap-edge vortex is also still visible. For

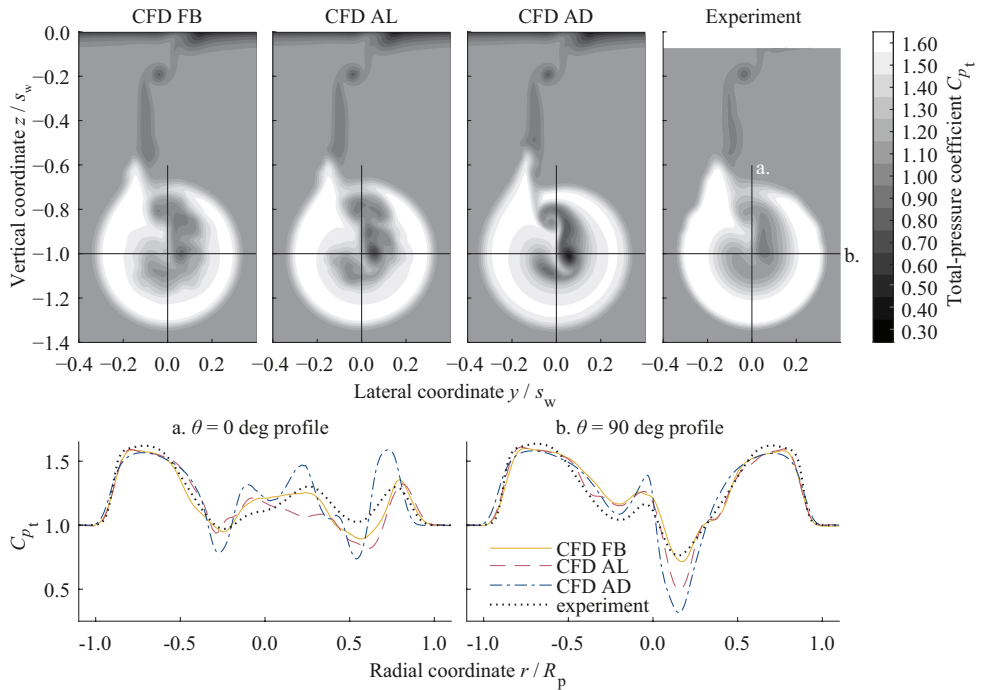


Figure 5.7: Time-averaged total-pressure coefficient at the survey plane, $\delta_f = +10$ deg.

the actuator-disk model, these vortices are more clearly recognizable than for the other methods and the experiment. The pressure deficit in the wingtip vortex is also larger, especially compared to the full-blade model and experiment. This can be explained by two effects. First, the higher wing loading for this model (Fig. 5.5) results in a stronger tip vortex with larger pressure deficit. Second, the time-dependent vortex field shed from the propeller for the other methods and the experiment may result in a time-dependent interaction with the wingtip vortex, moving the vortex location over time, and thus showing up as a reduced pressure deficit over a wider area in these time-averaged contours. Also for the actuator-line model a slightly larger total-pressure deficit is found in the wingtip vortex. Since phase-averaged blade loading is used for the actuator-line model, less spatial variation in the vortex shedding is present for this model, resulting again in a more concentrated wingtip-vortex in this time-averaged plot.

The phase-locked PIV data provide the opportunity to also compare the time-accurate flowfields in the wake and slipstream, as shown in Fig. 5.8 for the axial velocity. The actuator-disk model is not included due to the steady nature of this model. Radial profiles of the phase-locked axial velocity are provided as well. The phase at which the data were extracted was chosen such that a tip vortex aligns with the 90 deg radial profile. In the phase-locked contours, a good qualitative agreement is observed between the simulations and the experiment, with the locations of the blade-tip vortices matching well. However, the phase-locked profiles and contour plots again reveal the large difference

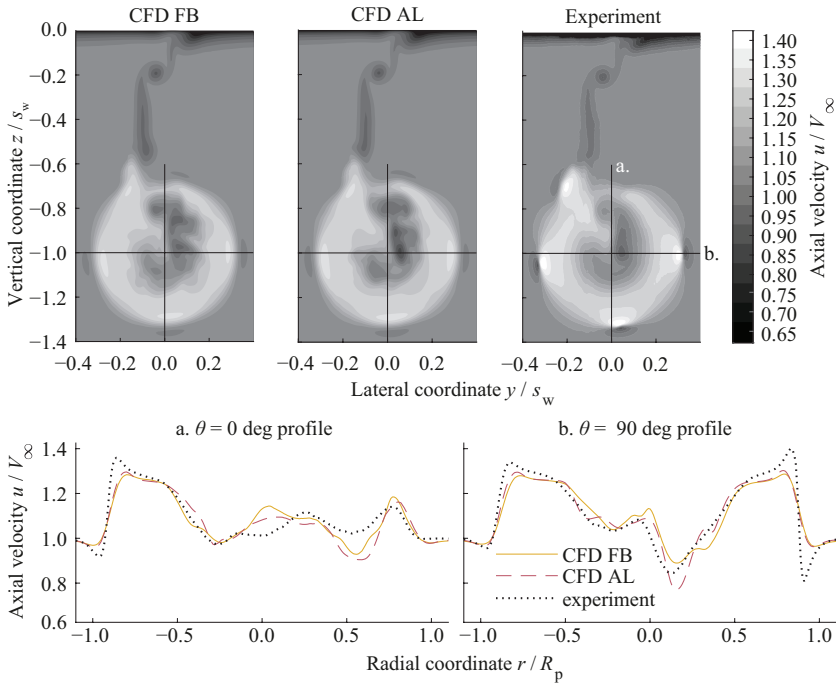


Figure 5.8: Phase-locked axial velocity at the survey plane, $\delta_f = +10$ deg.

between the computed and experimental results in the velocity gradients in the blade-tip vortex cores. One additional vortex structure is noticeable in the computational results in the top of the slipstream just right of profile line a, which is absent in the result from the experiment. This originates from the interaction of the propeller tip vortices with the pressure side of the wing. However, the vortex structure is visible in the experiment at a slightly different phase angle, which indicates a small phase shift between the computations and experiment.

So far, results of the flowfield in the wake and slipstream have been shown for a positive flap deflection of $\delta_f = +10$ deg, where the slipstream swirl opposes the direction of rotation of the wingtip vortex. This is the most relevant case for wingtip mounted propellers, since it is beneficial in terms of wing induced drag. [14–16] The other case, with the swirl turning in the same direction as the wingtip vortex, was simulated by means of a negative flap deflection of $\delta_f = -10$ deg and provides the opposite interaction. The difference between these two cases becomes clear in the time-averaged tangential velocity component in the slipstream as provided in Fig. 5.9. For all propeller modelling approaches and the experiment, the tangential velocity in the slipstream is on average lower for the positive flap deflection than for the negative flap deflection. The rotation of the flow around the wingtip, as a result of the pressure difference between the suction and pressure side, opposes the propeller swirl for the positive flap deflection, while the contrary occurs for the negative flap deflection. As a combined result of the gradients in

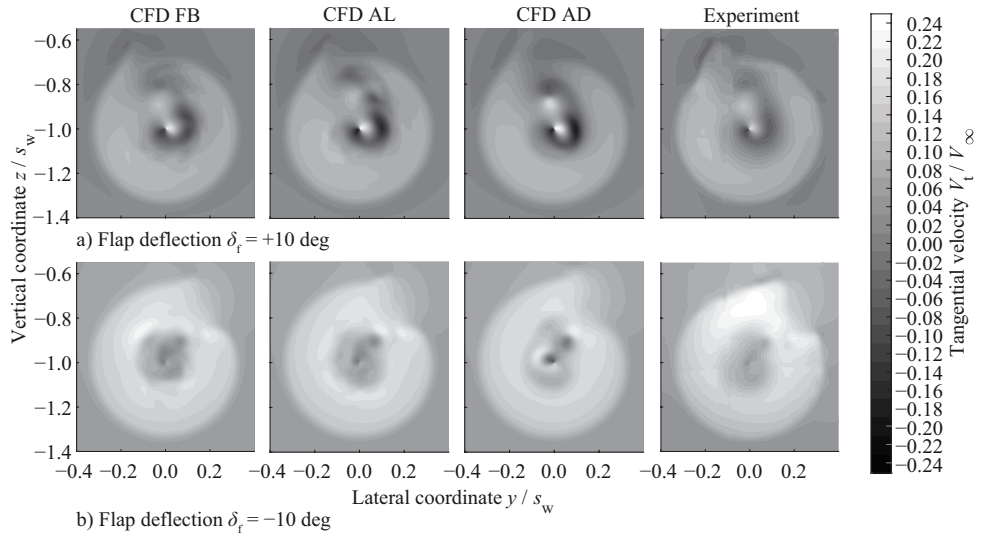


Figure 5.9: Time-averaged V_t/V_∞ in the propeller reference frame at the survey plane, $\delta_f = \pm 10$ deg.

the spanwise wing-loading distribution and the rotation of the flow around the wingtip, a spanwise shearing of the slipstream occurs. This shearing is also visible in the contours of tangential velocity and is found to be stronger for the negative flap deflection, since the two effects amplify each other, while they oppose each other for the positive flap deflection, similar to the situation at positive and negative angle of attack as shown in Ref. [163].

Very similar flowfields are obtained with the propeller models compared to the experiment. The main difference in the tangential velocity for the positive flap deflection is found in the wingtip vortex in the center of the slipstream, which is more negative for the actuator-line and especially actuator-disk models. This is again thought to be a difference due to decreased movement of the wingtip vortex because of the reduced time dependence of propeller blade vortex shedding, explained for the total-pressure coefficient in Fig. 5.7.

For the negative flap deflection an additional difference of the propeller models compared to the experiment is found in the inboard part of the slipstream, where an area with considerably higher tangential velocity is located in the experiment. This is discussed in more detail by van Arnhem et al. [219] In order to explain it, the interaction of the blade tip vortices with the wing should be considered first. As shown in Fig. 5.6 and also explained in Refs. [163] and [220], the propeller tip vortices deform upon impact with the leading edge of the wing. On the side of the wing to which the blade is moving, this results in an increase in the axial vorticity component of the tip vortices, while on the side of the wing from which the blade is moving away the axial vorticity is decreased to the extent that it changes sign. While at the survey plane the unaffected part of the blade tip vortices change location over time and therefore do not show up clearly in the time-averaged tangential velocity contour plots, the part of the vortices affected by the

Table 5.6: Ratio of rotational to total kinetic energy flow through the survey plane in the propeller reference frame, integrated up to $r/R_p = 1.1$.

	$\Delta\dot{E}_{k_{rot}} / \Delta\dot{E}_{k_{tot}}$	
	$\delta_f = +10$ deg	$\delta_f = -10$ deg
full-blade model	0.0104	0.0492
actuator-line model	0.0115	0.0480
actuator-disk model	0.0115	0.0459
experiment	0.0088	0.0537

interaction with the wing leading edge, trail downstream of the flap in mostly the axial direction. Therefore, they have a fixed location in the survey plane, resulting in a concentrated effect in the contour plots. Together with the outboard flap-edge vortex, which consists of mainly an axial vorticity component of negative sign, a strong positive tangential velocity is induced. This effect is much less visible for the CFD results, likely due to numerical diffusion.

5

The significance of the deviations in the flowfield between the CFD results and the experiment is best observed in the integral of the kinetic energy flow through the survey plane. Table 5.6 provides the ratio of rotational and total kinetic energy flow for $\delta_f = \pm 10$ deg. Note that the kinetic energy is only the addition of kinetic energy to the flow. The kinetic energy flow is calculated in the propeller reference frame and integrated up to $r/R_p = 1.1$. Although the ratio of rotational to total kinetic energy is not exactly the same for all propeller modelling methods and the experiment, the change of this ratio by the change in the flap deflection from about 0.05 to about 0.01 is observed for all cases, showing the ability of the CFD methods to quantify the relevant interaction effects of tip-mounted propeller configurations. The clearly reduced swirl loss for propeller rotation against the direction of the wingtip vortex shows the importance of choosing the correct rotation direction for wingtip-mounted propellers. For further reading, an elaborate investigation of the aerodynamic and performance benefits of this wingtip-mounted tractor-propeller configuration can be found in Refs. [16, 142], including comparison with a midspan-wing mounted configuration.

5.2. EFFECTS OF WINDMILLING FOR A WINGTIP-MOUNTED TRACTOR-PROPELLER

For this study, the propeller setup from Section 5.1 is investigated numerically for the propeller in windmilling condition. If electrically driven, windmilling can be used for energy harvesting during descent. It could also be used for yaw control or may occur in case of engine failure. The negative thrust produced by the propeller in windmilling and energy-harvesting conditions, as shown in Section 4.1.3, causes a drastic modification of the propeller-airframe interactions compared to the propulsive case that was discussed in the first section. This was investigated using actuator-disk simulations for both flap deflections $\delta_f = +10$ deg and $\delta_f = -10$ deg. The positive flap deflection represents again inboard-up propeller rotation against the direction of the wingtip vortex and the negative flap deflection represents outboard-up rotation.

The loading on the actuator-disk was assumed to be that of the isolated propeller as shown in Fig. 4.18, resulting in a small error: It was shown in Ref. [219] that for $J = 0.8$ the wing results in a 3% thrust increase compared to the isolated propeller thrust and causes a variation in blade thrust of 2% of the mean. The approximation by using the isolated propeller data was deemed acceptable for this study. In the first Section 5.2.1, the effects of this interaction on the wing loading are discussed and in the second Section 5.2.2 the effects on the slipstream flowfield are discussed. In line with the previous section, all results were obtained with a freestream velocity of 40 m/s with zero angle of attack. Note that here results are plotted with the wingspan horizontally, unlike the previous section where they were plotted vertically, in line with the experiment.

5.2.1. WING LOADING

To provide insight into the local effects of the propeller slipstream on the wing loading, the sectional loading characteristics were extracted. The pressure and skin-friction data from the CFD simulations were integrated to obtain both lift and drag distributions over the entire wing. Figure 5.10 presents the results at positive and negative thrust coefficient, in terms of section lift coefficient and corresponding lift-to-drag ratio. The spanwise coordinate was made dimensionless with the alternative wing semi-span of $s'_w = 292$ mm, starting from zero at the root of the model as defined in Fig. 3.12. The loading on the nacelle is thus not shown, unlike Fig. 5.5 where for the positive thrust case also the loading on the nacelle was shown. Note that the $J = 0.8$ case is used in Fig. 5.10 to represent the results in propulsive mode of the propeller that were earlier shown in Section 5.1. For that advance ratio, we saw an increase in section lift coefficient for the inboard up rotating propeller as a result of increased axial velocity in the slipstream of the propeller and the upwash from the swirl. The reduced axial velocity in the slipstream of the propeller at negative thrust ($J = 1.6$) that was shown in Fig. 4.19, results in a drop in wing lift compared to the propeller-off condition. For the considered inboard-up rotation case, this lift reduction is amplified by the downwash induced by the propeller swirl, which has changed direction compared to the propulsive case as the torque has changed sign.

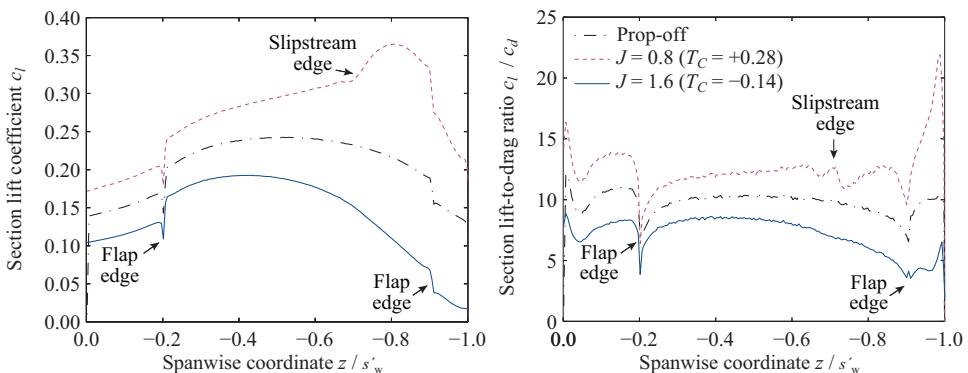


Figure 5.10: Effect of propeller thrust setting (inboard-up rotation) on the wing loading distribution.

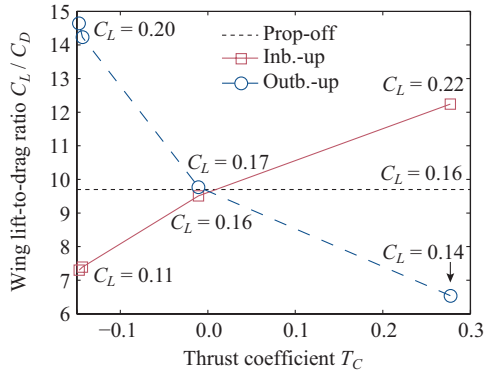


Figure 5.11: Effect of propeller thrust setting on the wing lift-to-drag ratio.

5

With inboard-up rotation, the upwash on the wing leads to enhanced section lift-to-drag ratio in propulsive mode, while the corresponding downwash in energy-harvesting mode decreases the section lift-to-drag ratio compared to the propeller-off configuration. The resulting change in wing lift-to-drag ratio was assessed by integrating the spanwise distribution (excluding the nacelle). Figure 5.11 provides the resulting lift-to-drag ratios of the wing as a function of thrust coefficient T_C , for both inboard-up and outboard-up rotation. Note that the datapoints are not at constant wing lift coefficient. For reference, the wing lift coefficients corresponding to each datapoint are indicated in the figure. The figure shows that the wing lift-to-drag ratio increased by about 25% when compared to the propeller-off configuration for the case with inboard-up rotation and the propeller in propulsive mode at a thrust coefficient of $T_C = 0.28$ ($J = 0.8$). With the same rotation direction in negative thrust conditions, on the other hand, the lift-to-drag ratio decreased by about 25% compared to the propeller-off result at thrust coefficients of about $T_C = -0.15$ ($J = 1.6$ to 1.8). At a condition of zero thrust (around $J = 1.1$), the propeller effect is negligible, as expected. The decreased lift-to-drag ratio in windmilling condition is not per se a drawback as in descent it is possible to realise a larger descent angle.

An opposite trend is observed for the case with outboard-up rotation. At positive thrust, the wing lift-to-drag ratio decreased by around 30% at $T_C = 0.28$ ($J = 0.8$). Due to the reversed swirl in the negative thrust regime, the wing lift-to-drag ratio increased with decreasing propeller thrust. At a thrust coefficient of $T_C = -0.15$ ($J = 1.6$ to 1.8), the increase in lift-to-drag ratio was near 50%. Note that this benefit is larger than the increase observed with inboard-up rotation in the positive thrust regime. This can partially be attributed to the different wing lift coefficients. Moreover, the reduced dynamic pressure in the slipstream of the windmilling propeller will reduce the friction drag on the wing compared to the propulsive case.

5.2.2. SLIPSTREAM FLOWFIELD

The effect of the propeller thrust condition on the slipstream flowfield is assessed in this section. Two survey planes were considered. The first was positioned at $0.19R_p$ downstream of the propeller center to assess the initial slipstream flowfield. A second survey

plane was defined at 1.5 wing chord lengths downstream of the wing trailing edge, corresponding to an axial location of $5.9R_p$ downstream of the propeller center (indicated survey plane in Fig. 3.12). In Fig. 5.12 the computed swirl-angle distribution is plotted in both planes as a function of the propeller operating condition for the case with inboard-up rotation. Figure 5.13 plots the same quantity for the outboard-up rotation case.

The figures display the expected change in swirl in the downstream plane at positive thrust. With inboard-up rotation the swirl decreases, while with outboard-up rotation the swirl increases, as shown before in Ref. [16] with experimental data. The results at negative thrust setting confirm the reversal of the interaction effects in the energy-harvesting condition that were observed in the loading data discussed in the previous section. The distortion of the slipstream is smaller in the negative-thrust condition than in propulsive mode. This is expected to be a consequence of the smaller distortion of the spanwise wing lift distribution (Fig. 5.10) in the energy-harvesting condition.

The swirl-angle distributions were integrated to obtain a single figure of merit for each configuration, using the following equation:

$$\theta_{\text{int}} = \frac{1}{S_{\text{ref}}} \int_0^{2\pi} \int_0^{1.1R_p} \theta r dr d\varphi, \quad (5.1)$$

with $S_{\text{ref}} = \pi(1.1R_p)^2 - \pi R_{\text{nac}}^2$ for the upstream survey plane (hence with the area inside the nacelle removed) and $S_{\text{ref}} = \pi(1.1R_p)^2$ for the downstream survey plane. The radial integration limit was set to $1.1R_p$ to capture the entire slipstream, also in cases with slipstream distortion resulting from the interaction with the wing. The resulting mean swirl angles are summarized in Table 5.7. The table shows that with inboard-up rotation, the positive swirl in the propeller slipstream at $T_C = 0.28$ ($J = 0.8$) (see upstream result) cancelled the negative swirl induced by the wing (see downstream propeller-off result), resulting in a near zero average swirl. At $T_C = -0.14$ ($J = 1.6$), on the other hand, the negative swirl in the propeller slipstream added to the negative swirl induced by the wing, thus leading to an increase in the absolute swirl angle compared to the propeller-off result. With outboard-up rotation, the results are reversed. At positive thrust, the swirl angle downstream of the propeller-wing configuration increases compared to the propeller-off condition, while with negative thrust the swirl decreases. As any rotational kinetic energy left downstream of the wing can be considered a loss, these results once more highlight the sensitivity of the system performance to the propeller rotation direction.

Table 5.7: Effect of propeller rotation direction and thrust setting on the mean swirl angle in the wake of the propeller-wing model.

Operating point		C_L		$\theta_{\text{int}}^{\text{ups}}$ (deg)		$\theta_{\text{int}}^{\text{dwms}}$ (deg)	
J	T_C	Inb.-up	Outb.-up	Inb.-up	Outb.-up	Inb.-up	Outb.-up
Prop-off	-	0.16	0.16	0.0	0.0	-3.0	-3.0
0.8	+0.28	0.22	0.14	3.3	-3.3	-0.3	-5.2
1.1	-0.01	0.16	0.17	0.1	-0.2	-2.7	-3.1
1.6	-0.14	0.11	0.20	-2.3	+2.3	-4.5	-1.5

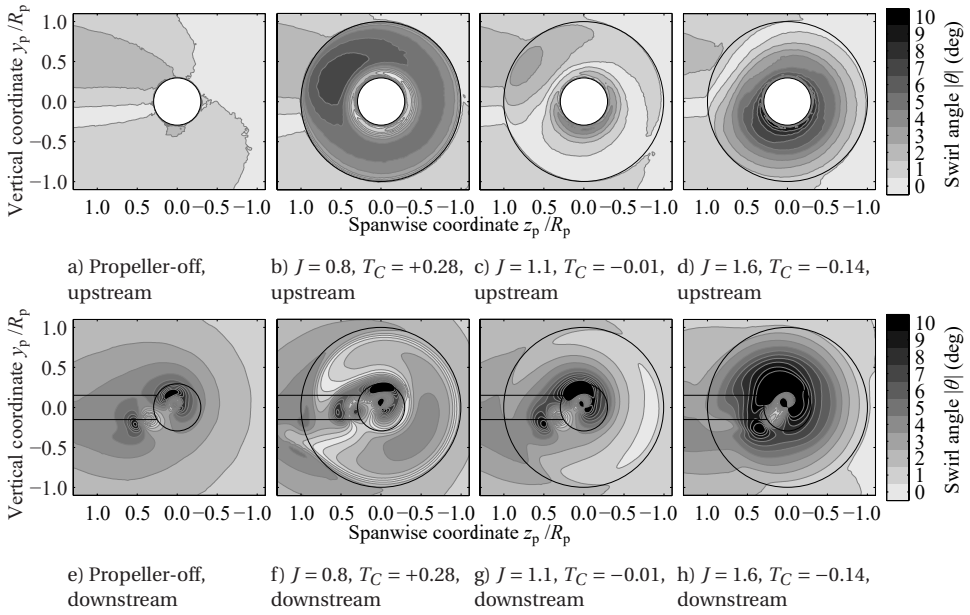


Figure 5.12: Effect of propeller thrust setting on the swirl-angle distribution upstream and downstream of the wing with inboard-up rotation ($0.19R_p$ and $5.9R_p$ downstream of propeller center).

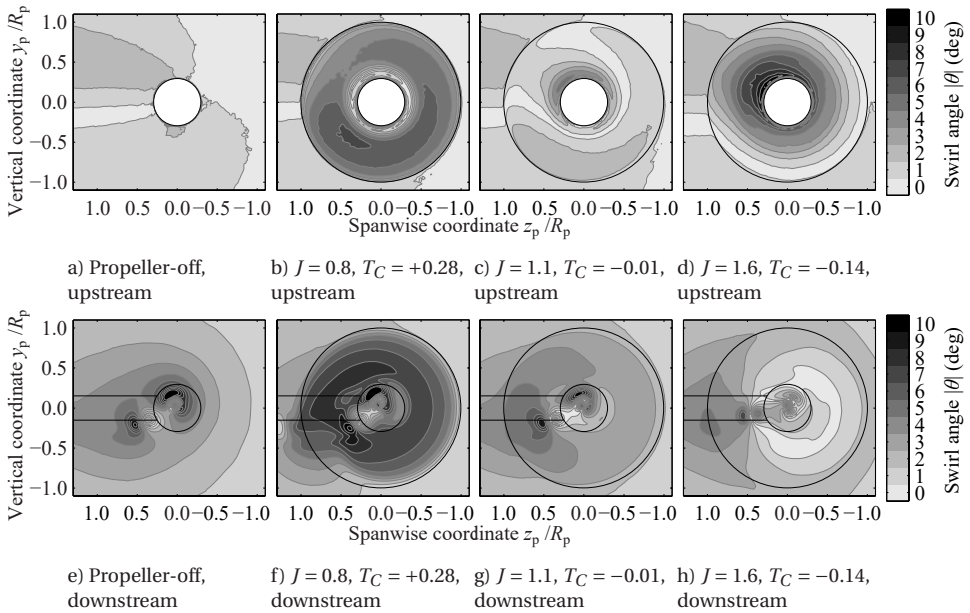


Figure 5.13: Effect of propeller thrust setting on the swirl-angle distribution upstream and downstream of the wing with outboard-up rotation ($0.19R_p$ and $5.9R_p$ downstream of propeller center).

5.3. ANALYSIS AND DESIGN OF A SMALL-SCALE WINGTIP-MOUNTED PUSHER-PROPELLER

In this section an analysis and design study is performed of a wingtip-mounted pusher-propeller. Such a propeller experiences a reduction in shaft power due to the swirling vortex inflow from the wingtip in case the propeller rotates against the direction of the wingtip vortex [15, 34–36]. In comparison with the tractor-variant, the main benefit for this layout is for the propeller and not the wing. Up to now, only research on a full scale wingtip-mounted pusher-propeller has been performed, with a propeller not specifically designed for this task [34, 35].

Electric motors give the opportunity to scale the propulsion source to smaller sizes without penalty in terms of engine weight or efficiency [87]. This allows distribution of propulsion and thus results in a non-unique thrust requirement, as the propeller can for instance be designed to balance just the induced drag of the wing or balance the entire cruise drag of the aircraft. Furthermore, the inflow to the propeller is non-uniform, especially when the propeller becomes smaller relative to the wingtip flowfield. The wingtip-mounted pusher-propeller may benefit from design optimisation for this non-uniform flowfield. Scale and design aspects of wingtip-mounted pusher-propellers are therefore researched in this section.

This study, which is regarded as an extension of Ref. [180], gives insight in research questions 4a and b by analysis of a specific wing, shown in Fig. 3.21, through the following steps:

1. RANS CFD analyses of the wing are performed in order to quantify the wing performance and extract the wingtip flowfield in the next Section 5.3.1.
2. A lower order propeller analysis and optimisation routine PROPR is established and validated for uniform inflow. (see Sections 3.2.1 and 4.1.1 respectively)
3. The wingtip flowfield is fed to PROPR for analysis and design optimisation in Section 5.3.2.
4. The upstream effect of the propeller designs on the wing performance is analysed through CFD analyses of the wing with an actuator-disk representation of the propeller in Section 5.3.3.
5. The accuracy of PROPR for the non-uniform wingtip flowfield is checked through a fully resolved propeller–wing CFD simulation in the last Section 5.3.4.

5.3.1. ISOLATED WING ANALYSIS

The wing used for these simulations was derived from the Tecnam P2012 Traveller [207]. Only the wing was taken into account, without the original propeller and nacelles. A sketch of the wing was shown in Fig. 3.21 a. There, also the other details regarding the geometry and setup were discussed. CFD analyses of the wing were performed at 3 deg angle of attack to represent a cruise condition. A grid dependency study was performed to estimate the discretization uncertainty and to select an appropriate grid density. Table 5.8 gives an overview of the grid sizes and wing lift and drag found for each grid. Table 5.9 presents the extrapolated lift and drag ϕ_0 , the standard deviation of the fit based on the

Table 5.8: Overview of grids and resulting isolated wing performance.

Grid	No. of cells	h_i/h_1	C_L [-]	C_D [-]
4	8,561,478	1.82	0.3434	0.01638
3	16,315,794	1.47	0.3440	0.01622
2	32,756,863	1.16	0.3447	0.01600
1	51,424,220	1.00	0.3452	0.01585

Table 5.9: Grid extrapolation results and estimated discretization uncertainties for grid 2.

	C_L	C_D
ϕ_0	0.3458	0.01568
U_s^* (%)	0.08	0.57
U_{ϕ_2} (%)	0.49	3.10

theoretical order of convergence U_s^* and the estimated discretization uncertainty U_{ϕ_2} for grid 2. The uncertainty of 0.49% and 3.10% for the lift and drag coefficient respectively was deemed acceptable for this study.

5

From the solution on grid 2 the flowfield that was fed to PROPR was extracted from the propeller plane, the plane where the propeller will be installed. The flowfield at the wingtip is visualised in Fig. 5.14 by means of streamtraces and the wingtip vortex is shown by an axial vorticity isosurface. On the isosurface and the propeller plane the velocity magnitude is plotted and on the wing surface the pressure coefficient distribution is shown.

In Fig. 5.15 this flowfield at the propeller plane is given for the left wingtip as seen from behind, by means of contour plots of the axial and tangential velocity components. These velocity components are most relevant for the propeller aerodynamic loading and, together with the propeller rotational speed and propeller induced velocities, determine the local blade section angle of attack and dynamic pressure. The tangential velocity component is defined positive in the rotation direction of the propeller, which is running counterclockwise for the left propeller when seen from behind. In PROPR, the inflow flowfield is radially varying but assumed to be circumferentially constant as the program is inherently steady in time. Therefore a circumferential average of this flowfield was taken, which will impact the resulting propeller response as follows.

In the axial velocity contour plot the reduced velocity in the wake of the wing is clearly visible and its effect on the propeller will be averaged. In the tangential velocity plot a region of strong negative velocity and a region of positive velocity can be observed which have an opposite effect on the propeller. These regions will also be circumferentially averaged in a net negative tangential velocity. As PROPR is used for propeller design optimisation, the optimised results are not fully optimal as the circumferential variations in the flowfield are not taken into account. It is however thought to be close to optimal as the propeller is optimised for the average of the circumferential variation. The resulting propeller designs for this flowfield are presented in Section 5.3.2 and the consequence of circumferential averaging will be further discussed in Section 5.3.4.

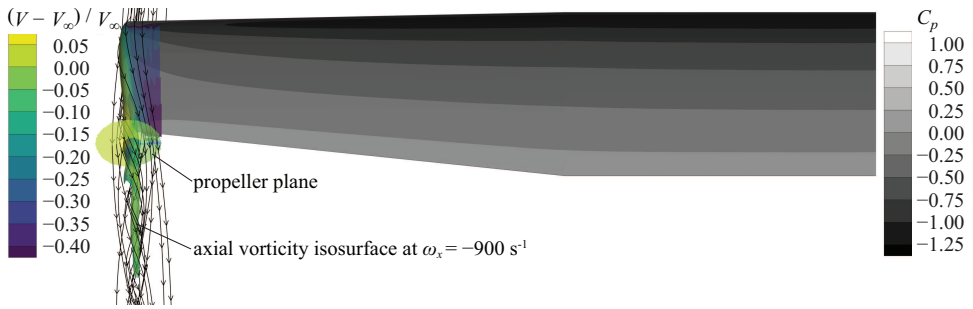


Figure 5.14: Visualisation of wingtip flowfield and pressure coefficient distribution on the wing surface without propeller.

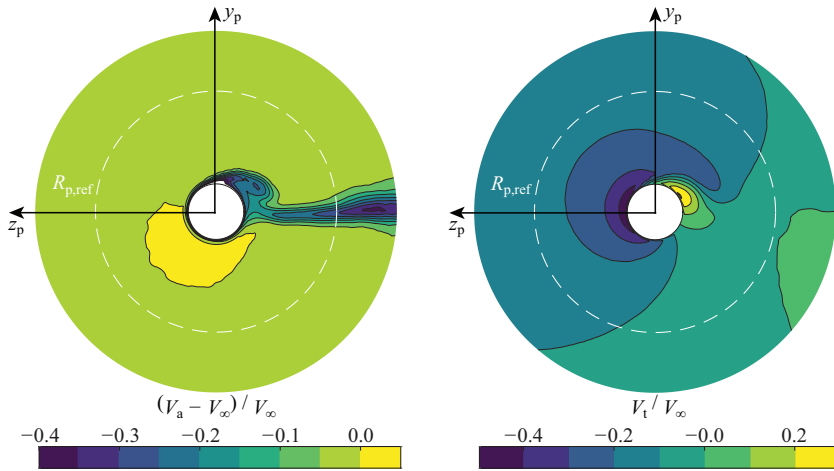


Figure 5.15: Contour plots of axial and tangential velocity components at the propeller plane behind the left wingtip. The dashed line shows the propeller disc area for the reference XPROP propeller.

5.3.2. PROPELLER DESIGN STUDY

In this section the design optimisation results from PROPR for a propeller placed in the wingtip flowfield are discussed. The different propeller designs are given in Table 5.10. The original XPROP propeller was tested in isolated and installed condition. The XPROP propeller was also optimised for minimum power in terms of blade pitch distribution and chord distribution, with an inequality constraint on the thrust to achieve the required thrust. The airfoil sections were kept the same as the original XPROP propeller. This was done for isolated and installed conditions, denoted isoOpt and insOpt respectively. The former was tested both in isolated and installed conditions, while the latter was only tested in installed conditions. Note that these optimisations were performed for each thrust level separately and that for each thrust level the performance is given for optimum operating conditions in terms of $\beta_{0.7R_p}$ and J .

Table 5.10: Overview of different propeller geometries used in design study.

Propeller name	Description
XPROP-iso	Original XPROP propeller operating in isolated condition
isoOpt-iso	Optimised for isolated condition, operating in isolated condition
XPROP-ins	Original XPROP propeller operating in installed condition
isoOpt-ins	Optimised for isolated condition, operating in installed condition
insOpt-ins	Optimised for installed condition, operating in installed condition

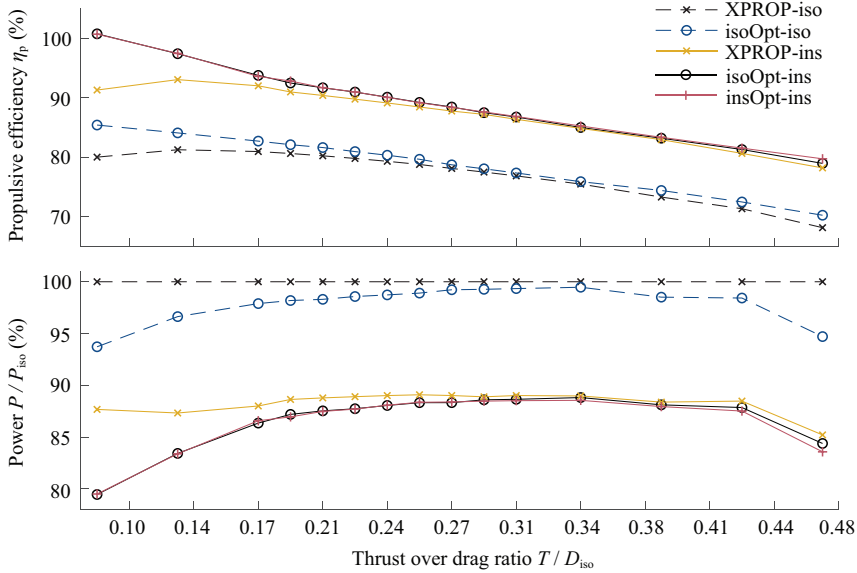


Figure 5.16: Propeller optimisation results for minimum power showing the propulsive efficiency and power versus the thrust to wing drag ratio at constant radius $R_p/R_{p,ref} = 1.00$ for isolated and installed conditions.

PROPELLER OPTIMISATION FOR CONSTANT RADIUS

First, a design sweep was performed for a range of thrust levels, keeping the propeller radius equal to that of the original XPROP propeller $R_{p,ref}$. In Fig. 5.16 the propeller performance is shown for a range of design thrust levels with respect to the isolated wing drag, T/D_{iso} . The propeller propulsive efficiency $\eta_p = TV_\infty/P$ is plotted, as well as the relative power required with respect to the XPROP-iso propeller, P/P_{iso} . Dashed lines refer to performance in isolated conditions, solid lines indicate installed propeller performance. Put in perspective, the wing induced drag is about 40% of the total wing drag in this condition, so a range of thrust levels is plotted from 25% up to 115% of the wing induced drag.

A number of trends can clearly be observed: The propulsive efficiency decreases with increasing design thrust in both the isolated and installed cases. This is expected since the propeller radius was kept constant. The possible efficiency gains due to installation and optimisation of the propeller are significant. Comparing insOpt-ins with XPROP-iso results, up to 20% increase in efficiency is achieved at lower design thrust levels by the

combined effect of optimisation and installation, decreasing to approximately 10% and remaining constant at higher thrust levels. Although, a fairer comparison is that of the insOpt-ins with the isoOpt-iso propeller, both optimised for their respective flowfield. Then, an efficiency increase up to 15% remains at the lowest thrust level, decreasing to 9% at the highest thrust level.

Looking at the plot showing the power ratio, the effectiveness of geometry optimisation in both isolated and installed conditions at low and high thrust levels is clearly visible. This effect diminishes at more average thrust levels, as the XPROP propeller is apparently designed for those thrust levels. The reduction in required power is significant when installing the propeller, even for the XPROP with non-optimised geometry. Reductions up to 20% are achieved when comparing insOpt-ins with XPROP-iso results, although looking at the most fair comparison with the isoOpt-iso propeller, a slightly lower maximum power reduction of up to 15% is found. Note that the installed propeller with optimised geometry for isolated conditions (isoOpt) yields almost identical power reductions compared to the installed propeller with optimised geometry for installed conditions (insOpt). Thus, effectively the propeller geometry is optimised for the required thrust level and to a lesser degree for the non-uniformity in the flowfield. Only at the very high design thrust levels of $T/D_{iso} \geq 0.42$ a noticeable difference in performance between the two different optimised propellers is observed.

With increasing thrust, the power reduction due to installation converges quickly to a nearly constant value, meaning that the effective power reduction that can be achieved by installation of the propeller almost does not change with thrust requirement. One would expect that the effective power reduction would decrease with increasing propeller design thrust, as there is only a finite amount of energy to be 'extracted' from the wingtip flowfield present in the installed case. Because of the limited maximum thrust that can be delivered by the XPROP propeller it is not possible to investigate the effective power decrease at even higher thrust levels for the current propeller radius. The experimental work done by Patterson Jr and Bartlett [35] gives already an indication of the power reduction found at higher thrust levels, considering that the size of that propeller and its thrust relative to the wing was much larger. At similar lift coefficient the power reduction was found to be 14%, although this was for a non-optimised propeller design. Considering that this is of similar order to what was found in this study thus far, it may be that over a larger thrust range this relative power reduction stays more or less constant. To confirm this, also the higher thrust regime up to a thrust equal to the cruise drag of the wing will be investigated with larger radius propellers.

BLADE LOADING AND GEOMETRY CHANGES DUE TO OPTIMISATION

The resulting changes in the propeller blade loading and geometry due to optimisation and installation are discussed for two different design thrust levels: $T = 0.21D_{iso}$ and $T = 0.39D_{iso}$. First, the results from optimisation of the XPROP propeller with $T = 0.21D_{iso}$ are discussed. In Fig. 5.17 the blade pitch angles, chord fractions, the profile efficiency and thrust distribution over the entire blade radius are shown. It is seen that the chord distribution of the insOpt and isoOpt propellers are nearly identical, even though the insOpt propeller was subjected to the non-uniform wingtip flowfield during optimisation. In both cases, the chord lengths were reduced by as much as 40% compared to the

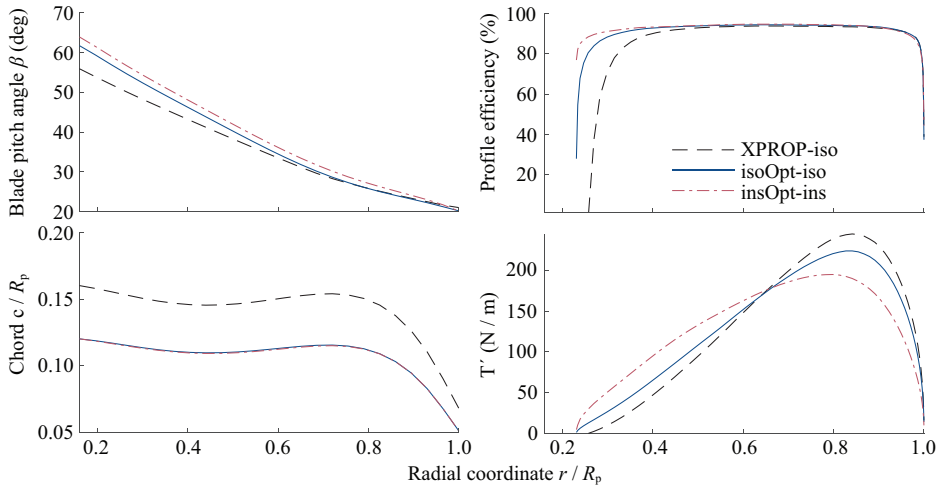


Figure 5.17: Propeller blade loading and geometry changes due to optimisation for $T = 0.21D_{iso}$.

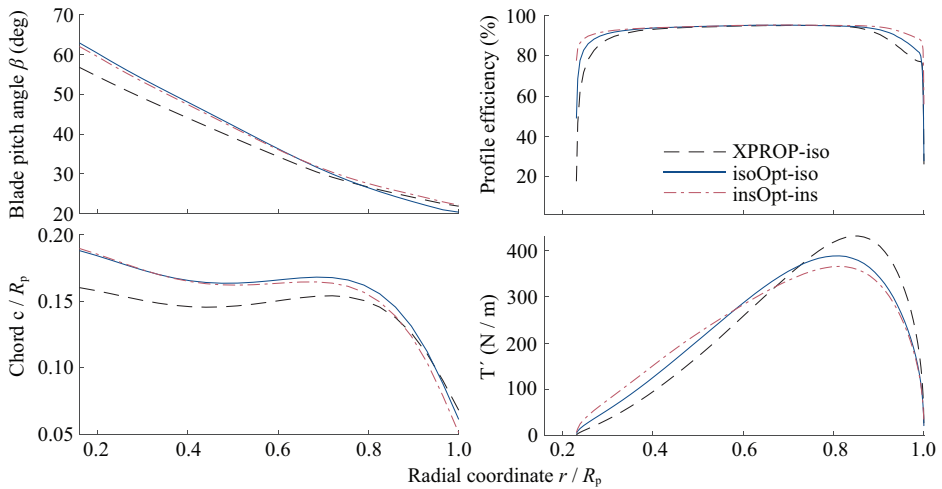


Figure 5.18: Propeller blade loading and geometry changes due to optimisation for $T = 0.39D_{iso}$.

XPROP propeller. A slight increase in blade pitch angle in the root sections is observed. Both the optimised isoOpt and insOpt propellers show significantly higher efficiency in the root sections. Presence of the non-uniform inflow enables further efficiency gains. Combined, this leads to a higher local profile efficiency for the insOpt propeller, especially for the root sections ($r/R_p < 0.4$). A clear trend is visible in the thrust distribution over the blade. Geometry optimisation of the XPROP propeller causes the thrust distribution to shift inboard towards the root. Furthermore, the maximum value decreases. The same behaviour to an even greater extent is observed when investigating the insOpt propeller. The combination of higher profile efficiency and the production of thrust there where the profile efficiency is higher makes this the most efficient propeller of the three.

Second, the optimisation results with $T = 0.39D_{iso}$ are discussed. In Fig. 5.18 it is seen that the local blade chord lengths are increased in both the isoOpt and insOpt propeller designs compared to the original XPROP propeller. This geometry change due to optimisation shows a reverse trend than what was seen for the lower design thrust in Fig. 5.17, where the chord fractions were decreased due to optimisation. This is a direct result of the higher thrust requirement. The local blade pitch angle is higher for both the isoOpt and insOpt propeller design, as was the case for the propellers optimised for $T = 0.21D_{iso}$. Also the improvements in local efficiency are similar, except for at the tip. Note that the efficiency of the XPROP propeller is relatively low in the tip region ($r/R_p > 0.85$) due to tip stall. Optimisation of the propeller geometry reduces this tip stall and the overall efficiency distribution is again an almost ideal constant distribution. Finally, again an inboard shift in thrust distribution is observed for the optimised propeller geometries.

PROPELLER OPTIMISATION FOR VARYING RADIUS

The performance of the propeller placed in the wingtip flowfield was also investigated for propeller radii different from the XPROP propeller. The radius was varied between $0.75 - 1.50R_{p,ref}$, where $R_{p,ref}$ is the radius of the XPROP propeller. A design thrust range up to $T = D_{iso}$ was analysed for the largest radius propeller, and again the power was minimized in an optimisation procedure. The hub dimension was kept constant and was not scaled with the propeller radius. In this analysis the performance of the propeller optimised for installed condition and operating in installed condition, insOpt-ins, was compared to a propeller of equal radius optimised for isolated condition operating in isolated condition, isoOpt-iso. This is the most fair comparison since both propellers are optimised for their respective flowfield. The propeller performance results are given in Fig. 5.19 as a function of thrust level. For any given thrust level, the propulsive efficiency η_p increases with increasing propeller radius for all propeller designs. This is a straight forward result since, with increasing radius and equal thrust, more mass is accelerated by the propeller but with a lower velocity increase. The corresponding advance ratio is also higher for larger radii propellers due to the large reduction in required rotational speed n .

The gain in efficiency by installation of the propeller at the wingtip, $\eta_p - \eta_{p,iso}$, varies less with propeller radius than η_p . Only for low thrust levels of less than 30% of the wing drag, significant differences occur in the efficiency gain. While the efficiency gain

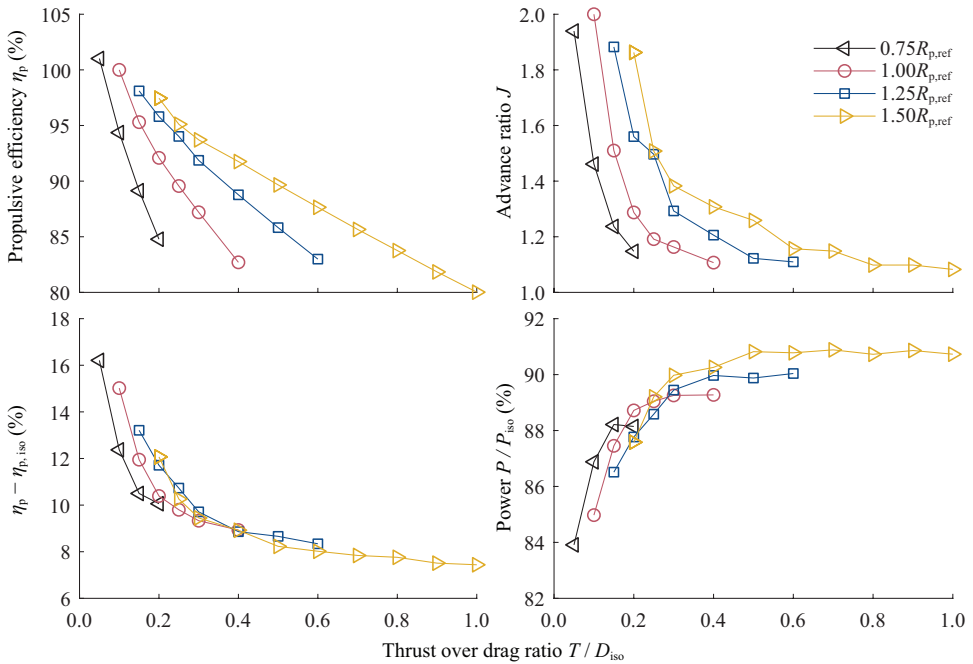


Figure 5.19: Optimisation results minimizing power with varying propeller radius for installed condition with insOpt-ins design compared to isolated condition with isoOpt-iso design.

decreases with thrust level, it does so at a reducing rate, decreasing to a still significant gain of 7.5% when the thrust equals the wing drag $T = D_{iso}$. As discussed earlier for the optimisation results at equal radius, the power ratio P/P_{iso} seems to level off to an approximately constant value at larger thrust levels. This is also happening for the other propeller radii, however the relative power reduction becomes less for larger propeller radii, decreasing to a 9% power reduction due to the wingtip flowfield for $1.50R_p$.

5.3.3. PROPELLER–WING ANALYSIS WITH ACTUATOR-DISK

The upstream effect of the propeller designs on the wing performance was analysed through CFD analyses of the wing with an actuator-disk representation of the propeller. These simulations are of similar computational cost as the isolated wing simulations but do provide the required time-averaged upstream effect of the propeller at much reduced computational cost compared to the fully resolved propeller–wing simulation in Section 5.3.4. In Fig. 5.20 the wing lift coefficient C_L and lift-to-drag ratio L/D are plotted as a function of propeller thrust for a number of cases with varying propeller radius from Fig. 5.19. Results are also shown for the isolated wing.

The changes in wing lift coefficient due to propeller thrust are quite small and are only just larger than the estimated discretization uncertainty given in Table 5.9. Despite this, an increasing trend in C_L is visible with increasing propeller thrust level. This could be explained by a slightly stronger suction over the wing due to the presence of the

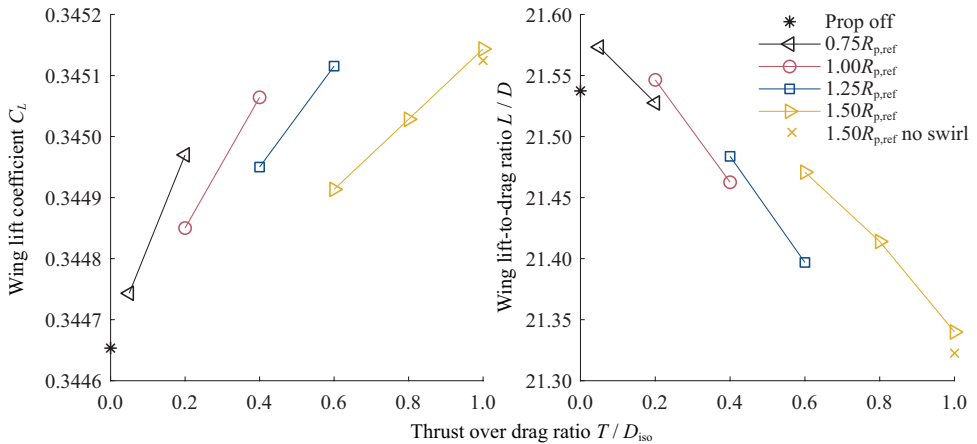


Figure 5.20: Wing performance as function of propeller thrust investigated with an actuator-disk.

propeller. Contrary to the lift coefficient, the lift-to-drag ratio decreases with increasing propeller thrust. Apparently the propeller slightly reduces the wing efficiency. Another observation is that with increasing propeller radius, the upstream effects of the propeller on the wing reduce.

For the $1.50R_p$ case an additional simulation was performed where no swirl component was introduced by the actuator-disk, denoted *no swirl*. It shows that the swirl component has only a minor impact on the wing loading. Thus, the reduction of swirl in the wingtip flowfield due to the propeller does not cause a significant change in wing loading and the observed changes are mainly an effect of the axial velocity increase. However in general, it is concluded that the upstream effect of the propeller on the wing loading is very limited for the investigated thrust range. Therefore, the taken approach of optimising the propeller for the isolated wing flowfield is valid. A closer look at the downstream interaction of the wing on the propeller is presented in the next section.

5.3.4. BLADE RESOLVING PROPELLER–WING ANALYSIS

To check the accuracy of PROPR for the non-uniform wingtip flowfield, and to investigate the unsteady behaviour of a wingtip-mounted pusher-propeller, a fully resolved propeller–wing CFD simulation was performed. The original XPROP propeller was simulated installed on the wingtip at optimum operating condition in terms of $\beta_{0.7R_p}$ and J at a thrust of $T = 0.30D_{iso}$.

In Fig. 5.21 a the normalized blade thrust and torque as function of blade phase angle are shown, as defined in Fig. 5.22 b. In addition, the mean of the thrust and torque obtained from the transient CFD simulation are shown, as well as the thrust and torque values calculated using PROPR. As expected, the blade thrust and torque vary considerably over a rotation due to the circumferential non-uniformities in the flowfield that were shown in Fig. 5.15. Following the trajectory of the blade, clear trends are observed:

- $\varphi = 0^\circ$: Initial position, blade pointing up and perpendicular to the wing surface.

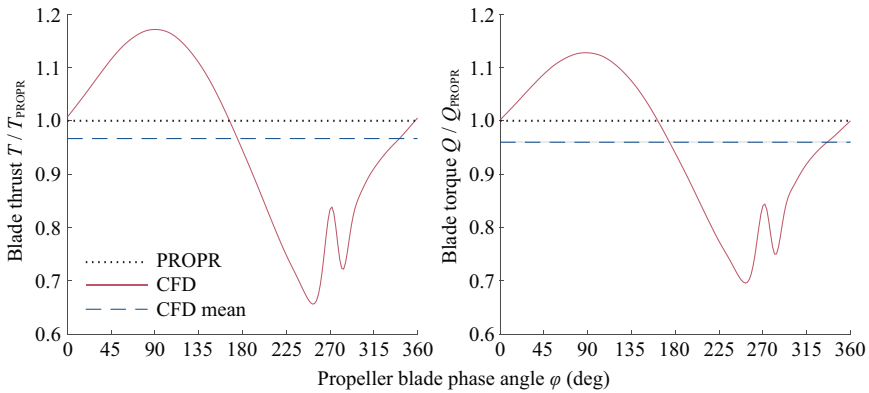
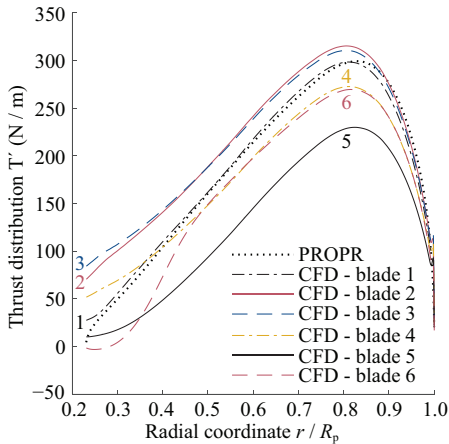


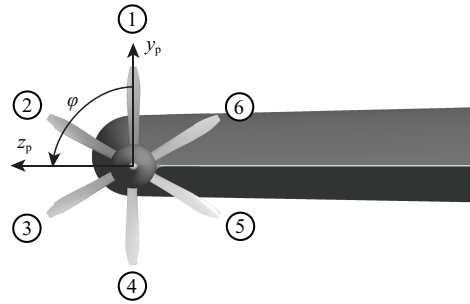
Figure 5.21: Installed XPROP propeller blade thrust and torque evolution over a complete rotation for $T = 0.30D_{iso}$.

5

- $\varphi = 90^\circ$: Blade is fully outboard and subjected to the largest negative tangential velocities, thus highest thrust.
- $\varphi = 180^\circ$: Blade is again perpendicular to the wing but now pointing down. Thrust delivered with inflow from under the wing is slightly lower.
- $\varphi = 270^\circ$: At this angle the blade is fully immersed in the wake region of the wing, showing a clear local peak in thrust of about 10% of the time-averaged blade loading, due to the lower axial velocity. This causes an increased angle of attack of the blade sections.



a) Propeller blade thrust distribution comparison.



b) Backview showing definition of blade positions.

Figure 5.22: Comparison of XPROP propeller blade thrust distributions at different blade positions for $T = 0.30D_{iso}$.

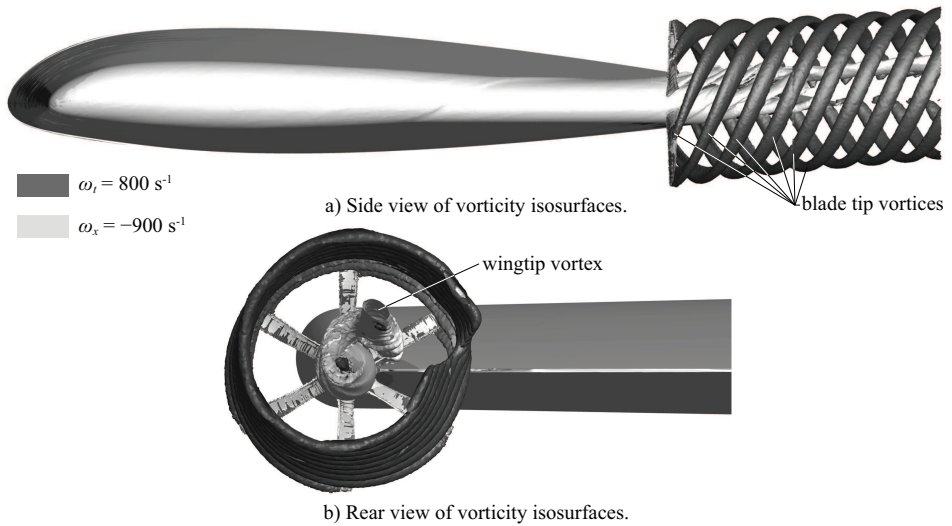


Figure 5.23: Vorticity isosurfaces identifying the XPROP propeller blade tip vortices and wingtip vortex.

Identical trends are observed when investigating the blade torque evolution. The mean blade thrust and torque are overestimated 3.3% and 4.0% by PROPR respectively. These differences in mean thrust and torque between CFD and PROPR are very similar to those obtained for the isolated propeller in Section 4.1.1. This provides confidence in the validity of PROPR given these non-uniform flowfields.

To get some more insight in the blade loading evolution, in Fig. 5.22 a the propeller blade thrust distribution is plotted at various blade positions as defined in Fig. 5.22 b. The blade distribution from PROPR is also shown. It is seen that the thrust distribution over the blade from PROPR is nearly identical to that found in the transient CFD simulation over blade 1. Blade 2 and 3 are subjected to the largest tangential velocity field and indeed show the highest thrust. Most notably, these blades experience a significantly higher thrust at the root sections of the blade. Blade 5 experiences the lowest blade loading because, as was shown in Fig. 5.15, the tangential velocity field at this location is near zero. A drop in thrust near the root occurring over blade 6 is seen, because it is immersed in a flowfield with locally positive tangential velocity. Blade 6 experiences this positive tangential velocity near the root, because it crosses the tip vortex of the wing. As the vortex was approximately aligned with the propeller axis and impinged off-center from the axis, the propeller blade experienced locally a decrease and increase of blade section angle of attack, depending on the radial location. This becomes clear from Fig 5.23, where a tangential and an axial vorticity isosurface is shown at such levels that they identify the propeller blade tip vortices and wingtip vortex respectively. The propeller blades are at the same position as in Fig. 5.22 b. It is clear that blade 6 is starting to cross the wingtip vortex.

5.4. CONCLUSIONS

In this chapter two configurations were studied, a wingtip-mounted tractor- and pusher-propeller configuration. The conclusions that may be drawn from the numerical and experimental data are treated separately and a small comparison of the interaction effects is given at the end.

TRACTOR-PROPELLER

For tractor variant a comparison was made of full-blade propeller simulations with a wind-tunnel experiment to answer research question **Q2a**. The Beaver propeller was used for this comparison. Furthermore, two reduced-order models for the propeller were tested to answer **Q2b**: an actuator-line and actuator-disk model. In order to distinguish modelling errors of the isolated propeller and wing from modelling errors of the propeller-wing interaction, also the isolated wing was investigated and in the previous chapter the isolated propeller was already treated.

For the isolated wing configuration, agreement in integrated lift and drag was found for the CFD model with Spalart-Allmaras turbulence model and the experiment. The main difference was a result of a small misalignment of the wing and nacelle in the experiment. The Spalart-Allmaras turbulence model predicted flow separation on the flap far better than the $k - \omega$ SST turbulence model, also resulting in a better match of the wake in terms of total-pressure coefficient. Both turbulence models suffered from reduced total-pressure deficits in the vortex cores due to numerical diffusion, except in the wingtip vortex.

For the propeller-wing configuration, agreement of the time-averaged pressure distributions on the wing in the slipstream was obtained by the full-blade and actuator-line models compared to the experiment, matching the good agreement obtained for the integrated lift coefficient (maximum difference of 0.8%). The actuator-disk result showed a slightly lower pressure on the suction side, likely due to a difference in slipstream-wing interaction as a result of the inherently time-averaged slipstream in this model. This resulted in a 3.9% increase in integrated lift, with no increase in drag. Almost no difference was found in the time-accurate pressure distribution on the wing at the slipstream edge between the full-blade and actuator-line models.

The slipstream and wake agreed well in a time-averaged and time-accurate sense for all the propeller modelling methods. Most of the differences were already present in the simulations of the isolated propeller and wing, and were mainly a result of numerical diffusion in the vortex cores. All results from the different CFD models and the experimental data showed a clear reduction in tangential velocity or swirl in the slipstream behind the wing for the case with the propeller rotating against the rotation of the wingtip vortex compared to the case with rotation with the wingtip vortex. With a change of flap deflection from $\delta_f = -10$ deg to $\delta_f = +10$ deg (or in other words from outboard-up to inboard-up rotation), for all CFD models and the experiment the ratio of rotational to total kinetic energy decreased from about 0.05 to about 0.01. This highlights the increase in performance that was found in Ref. [16] for the same configuration, as less rotational kinetic energy is left in the flow downstream of the wing.

It is concluded that RANS CFD with a simple one-equation turbulence model (Spalart-Allmaras) is capable of modelling the interaction of the wingtip-mounted propeller in

tractor configuration, provided that the uncertainty due to numerical diffusion is accounted for by a grid dependency study or reduced by local grid refinement. If the radial distribution of thrust and torque can be obtained for each azimuthal position of the blade by a lower-order method, the actuator-line model is fully capable of replacing the full-blade model with a 17% reduction in computational cost. The actuator-disk model provides the ability to further reduce the cost of the simulation with 85% by removing time dependency, with a small penalty in the accuracy of the time-averaged lift distribution and flowfield.

With this validated model, the consequences of windmilling were investigated as a concept to harvest energy in-flight, for instance during descent, to answer research question **Q3**. The aerodynamic interaction phenomena change drastically compared to the case at positive thrust setting. With inboard-up rotation ($\delta_f = +10$ deg), the lift and lift-to-drag ratio performance worsen with increasingly negative propeller thrust. This is due to the reduced dynamic pressure in the propeller slipstream compared to the freestream, and the reversal of the swirl compared to the conventional case with positive thrust. Whereas in the propulsive condition the wing lift-to-drag ratio increased by about 25% compared to the propeller-off case, in energy-harvesting mode a reduction of 25% was observed. Note that these numbers are very specific to this configuration. The increase in lift-to-drag ratio was reflected in the slipstream by a decrease in average swirl from upstream of the wing to downstream, and visa versa. For outboard-up propeller rotation, the interaction phenomena are reversed compared to the inboard-up rotation case. Improved wing performance can be achieved at negative thrust conditions as a maximum increase in wing lift-to-drag ratio of near 50% was obtained compared to the propeller-off case. This is however not at constant lift coefficient.

PUSHER-PROPELLER

For the wingtip-mounted pusher-propeller a design framework was established and verified with RANS CFD simulations. It was found that the following approach is valid: First a wingtip flowfield was extracted from an isolated wing simulation. Then, this flowfield was circumferentially averaged and used in a validated lifting line based propeller analysis and optimisation routine named PROPR for aerodynamic design optimisation. The upstream effect of the propeller on the wing performance was investigated with an actuator-disk representation of the propeller in multiple wing simulations and was found to be very limited for the tested thrust levels. This was a requirement for the taken approach as the propellers were designed using the flowfield from the isolated wing simulation. However, a trend of increasing wing lift coefficient and decreasing lift-to-drag ratio was observed with increasing propeller thrust, which may become significant for higher thrust levels than currently investigated.

At last, the resulting propeller performance from PROPR was in line with time-averaged propeller loading of fully resolved propeller-wing RANS CFD simulations, providing confidence in the validity of the approach. This was despite the large fluctuation found in the transient propeller blade loading due to circumferential non-uniformities in the inflow field. This large fluctuation was mainly caused by a circumferential variation in tangential velocity in the inflow, induced by the wing and from the angle of attack of the freestream. Also, a local peak in thrust of about 10% of the time-averaged blade loading

was present where the wing wake impinged on the propeller blade. Furthermore, the impingement of the wingtip vortex on the propeller blade caused a variation in the radial distribution of loading on the blade. As the vortex was approximately aligned with the propeller axis and impinged off-center from the axis, the propeller blade experienced locally a decrease and increase of blade section angle of attack, depending on the radial location. Due to the propeller rotation direction, the decrease occurred on the inboard side of the propeller blade.

With this design framework for wingtip-mounted pusher-propellers, various conclusions on propeller design for wingtip-mounted pusher-propellers are drawn to answer research question **Q4a** and **Q4b**. The possible propulsive efficiency gains for the propeller due to installation are significant: Up to 16% increase in efficiency was achieved at the lowest investigated thrust level of 5% of the wing drag, decreasing with a reducing slope to approximately 7.5% for the highest investigated thrust level of 100% of the wing drag. The propulsive efficiency gain was only significantly dependent on the propeller radius for low thrust levels of less than 30% of the wing drag. It was found that effectively the propeller geometry is optimised for the required thrust level and to a lesser degree for the non-uniformity in the flowfield. Propeller blade optimisation and installation resulted in higher profile efficiency in the blade root sections and a more inboard thrust distribution over the blade. Considering the propulsive efficiency benefits found in this study, wingtip-mounted pusher-propellers should be considered for (hybrid)-electric concepts. The propeller thrust should then be a design variable, determining together with the wing lift the resulting efficiency benefit from this aerodynamic interaction.

5

TRACTOR- VERSUS PUSHER-PROPELLER

It is still an unanswered question in literature whether the tractor or the pusher propeller configuration is aerodynamically 'better', although the analytical study by Miranda and Brennan [15] indicates that the same benefit can be obtained with either layout. We have seen that the tractor-propeller can enhance the wing lift-to-drag ratio considerably with only a minor upstream effect on the propeller, similar to that of conventional wing-mounted tractor-propellers. We have also seen that the wing can provide the pusher propeller with a more favourable inflow that reduces the power requirement for a given thrust. This came with a very minor upstream effect on the wing, very slightly reducing lift-to-drag ratio. In terms of unsteady effects, the wing experienced some variation in pressure distribution over time in the slipstream of the tractor propeller, while the pusher propeller blade loading varied significantly over a rotation. This may have different consequences for noise and vibrations. Considering that the two investigated configurations are very different, no conclusion on this open question can be made in this work either. Not only propeller blade optimisation but also wing shape optimisation for each case separately would be required for a fair comparison.

6

INTERACTION WITH STATOR OR PROPELLER

This chapter treats interaction of a propeller with a stator and with another propeller. The stator or swirl-recovery-vanes (SRVs) are designed to interact with the slipstream of the propeller to gain propulsive efficiency through a small thrust force. Interaction of a propeller with a stator is different from interaction with a wing from the previous chapter as a stator consists of many aerodynamic surfaces, which are of similar size as the propeller they are in interaction with. This is contrary to the wing which is only affected in a small region near the propeller. Therefore, stronger interaction effects can be expected for the stator. Research question 5 is addressed in Section 6.1 through a RANS CFD study (including validating experimental results) of the APIAN propeller in interaction with SRVs:

Q5: *What are the steady and especially unsteady aerodynamic interaction effects between a propeller and swirl-recovery-vanes in terms of propeller and vane loading?*

While SRVs are designed to interact with the slipstream of a propeller, interaction between propellers may be a side effect of a specific configuration and operating condition. The interactions investigated between propellers in Section 6.2 focus on two specific layouts, the side-by-side (SBS) and one-after-another (OAA) configurations identified in Section 2.4, which are common on many eVTOL vehicles but not limited to that. For these two configurations, research question 6 is answered by means of a wind-tunnel experiment with the F29 propellers:

Q6: *How does propeller interaction in side-by-side and one-after-another propeller configuration affect propeller performance, in terms of thrust, power, in-plane forces and out-of-plane moments, and how do those performance effects depend on propeller spacing defined by d_x and d_y ?*

The contents of this chapter have been adapted from Refs. [67, 68].

6.1. AN ANALYSIS OF PROPELLER–SWIRL-RECOVERY-VANE INTERACTION

In this section the interaction between the APIAN propeller and downstream swirl-recovery-vanes is investigated. These stator vanes operate in the non-uniform slipstream of the propeller to convert some of the rotational kinetic energy left by the propeller in axial kinetic energy. Their goal is to produce a net thrust force and in this way improve the system performance. This section will not focus on the possible benefits that SRVs can achieve, but rather discusses the aerodynamic interaction between the propeller and SRVs in terms of effects on the flowfield and the propeller and SRV (unsteady) loading. For more extensive analyses of the efficiency benefits of SRVs the reader is instead referred to Refs. [63, 108].

First a small grid convergence study is presented in Section 6.1.1 for the propeller and SRVs combined to provide confidence in the chosen grid. Then in Section 6.1.2 the flowfield around the propeller and SRVs is analysed by a comparison of the RANS CFD simulation results with validating experimental data from Ref. [68]. The effects of the interaction on the loading are investigated in Section 6.1.3, mainly by computational results. Results are shown for a freestream velocity of $V_\infty = 60$ m/s at zero angle of attack, for three different propeller operating conditions corresponding to high, medium, and low thrust conditions. The associated advance ratios were $J = 1.05, 1.40,$ and $1.75,$ leading to measured propeller thrust coefficients of $C_T = 0.51, 0.36,$ and $0.18,$ respectively.

6

6.1.1. GRID CONVERGENCE WITH INSTALLED SRVs

A grid study for the isolated APIAN propeller was already given in Section 4.1.4. In this section, a short grid convergence study with the SRVs installed is presented. The grid sizes are reported in Table 6.1. Again five grids were created for the wedge-shaped domain from Fig. 3.16, but now with region C2. As explained before, for the grid study with SRVs, a profile transformation was applied to connect the unequal pitch domains of the propeller blade and SRVs to significantly reduce computational cost. The results on the chosen grid in the next sections were however computed with a full annulus domain for accuracy. The grid study for the configuration with SRVs installed was carried out at $J = 1.75.$ At this setting, the propeller loading was least sensitive to the grid size, hence the effects of refinements near the SRVs could be studied best.

Table 6.1: Grid sizes of wedge-shaped domain from Fig. 3.16 for the APIAN propeller with SRVs.

grid	# nodes	h_i / h_1
5	2,367,946	1.74
4	3,356,779	1.55
3	4,966,426	1.36
2	7,630,369	1.18
1	12,188,588	1.00

The grid dependency of the propeller thrust coefficient, propeller torque coefficient and resultant force on the SRV is summarized in Table 4.6. For this case, oscillatory convergence occurred for the propeller thrust and torque. Therefore, a conservative error estimate was obtained by taking the maximum difference between the solutions ob-

Table 6.2: Grid dependency of the propeller and SRV performance at $J = 1.75$.

	C_T	C_Q	F_{SRV}
p	- [†]	- [†]	6.35
U_s (%)	-	-	0.36
U_s^* (%)	-	-	0.56
ϕ_0	-	-	5.946 N
U_{ϕ_3} (%)	1.26	1.91	2.55

[†]Oscillatory convergence observed

tained at all grids times an increased safety factor of 3 (See Eq. 3.20). This resulted in discretization errors of 1.26% and 1.91% for the thrust coefficient and the torque coefficient, respectively. The resultant force on the vane F_{SRV} converged with some noise. The order of accuracy was overpredicted by the best fit, and a fit with the theoretical order was used to estimate a discretization error of 2.55% for grid 3. All results presented in the following were obtained with grid 3.

6.1.2. SLIPSTREAM FLOWFIELD

In this section a comparison of the flowfield is made in the slipstream of the propeller between the experimental data and CFD simulations of the same configuration. In Fig. 6.1 the propeller and SRV tip vortices are visualized with isosurfaces of the axial vorticity component from CFD. Furthermore, an evaluation plane is shown. Figure 6.2 presents the same contours of measured and computed tangential velocity as Fig. 4.23, but now with the SRVs installed on this evaluation plane. Note that around $x/R_p = 0.6$ experimental data is lacking due to reflections from the nearby SRVs. It should also be mentioned that now the single evaluation plane considered in this figure is not necessarily representative of the velocity distribution in the entire slipstream as the SRVs are stationary.

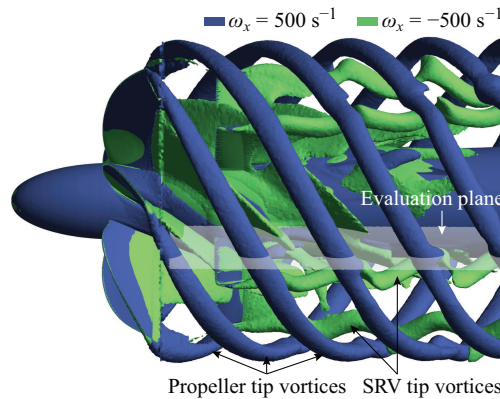


Figure 6.1: Interaction between the tip vortices of the SRVs and the propeller visualized by isosurfaces of the vorticity in axial direction at $J = 1.40$.

In the contour plot of the tangential velocity in Fig. 6.2 it is seen that the SRVs reduced the swirl in the propeller slipstream. The SRVs are located at $x/R_p = 0.6$ and downstream

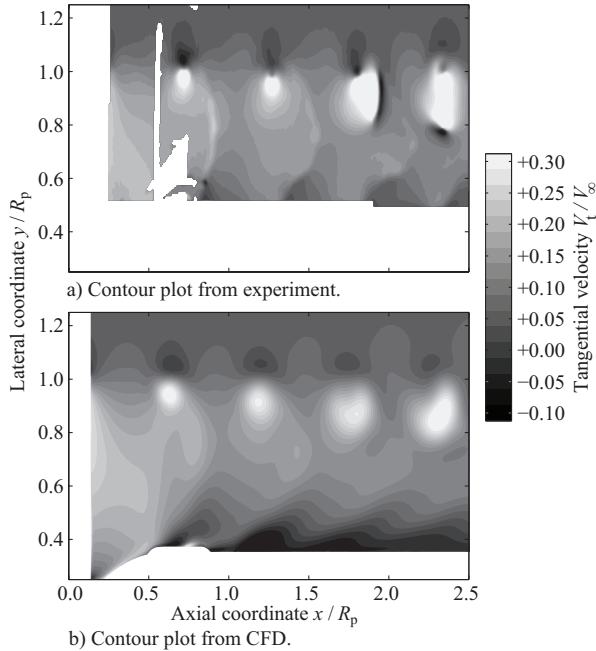


Figure 6.2: Comparison of the slipstream of the APIAN propeller with SRVs, visualised by contour plots of the phase-locked tangential velocity at $z/R_p = 0.03$ for $J = 1.40$.

6

a clear reduction is noticeable with respect to the flowfield upstream of the SRVs. Note that around $x/R_p \approx 2.0$, the tip vortex from the nearest SRV entered the measurement plane at $y/R_p \approx 0.9$. Figure 6.1 confirms that the tip vortex of the SRV approaches the evaluation plane directly downstream of one of the tip vortices of the propeller blades. Moreover, it can be seen that the trajectory of the tip vortex from the SRV is affected by the passage of the tip vortices of the propeller blades and vice versa, and as a result displays an oscillating behaviour. The entrance of the SRV tip vortex is hard to discern in the CFD data due to the earlier discussed numerical diffusion (in Section 4.1.4).

To provide a quantitative comparison between the experimental and numerical data, profiles of the time-averaged tangential and axial velocity were again extracted from the evaluation plane at $x/R_p = 1.5$. The corresponding results are given in Fig. 6.3. The computational data from Fig. 4.24 for the isolated propeller is plotted as well for comparison. It is seen that the reductions in swirl were obtained for $y/R_p < 0.9$ as the SRVs were cropped compared to the propeller to this radial position. For the low and medium thrust condition ($J = 1.75$ and $J = 1.40$) near the root even a change to negative tangential velocity can be observed. Apparently the SRVs overcompensated in recovering the swirl in the slipstream. Similar to the results for the isolated propeller, a good quantitative agreement is obtained between the PIV measurements and the CFD evaluations for the intermediate and low propeller thrust settings in the middle part of the slipstream ($0.5 < y/R_p < 0.9$). At more outboard lateral coordinates near the slipstream edge, the

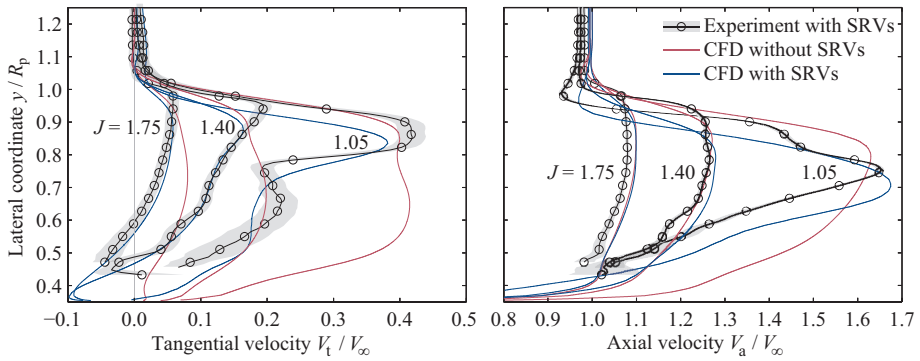


Figure 6.3: Comparison of the time-averaged velocity in the slipstream of the APIAN propeller with SRVs at $x/R_p = 1.5$ and $z/R_p = 0.03$. For reference also CFD results without SRVs from Fig. 4.24 are shown.

CFD results suffered again from numerical diffusion.

In terms of axial velocity, while for the low and medium thrust condition a small increase by the SRVs is observed, for the high thrust condition ($J = 1.05$) mainly a decrease can be noticed. As the SRVs operate by turning the tangential flow in axial direction, an axial-velocity increase is expected. From the CFD simulations it was found that the decrease in axial velocity at $J = 1.05$ resulted from leading edge flow separation over a large part of the span of the SRVs as the swirl angle and thus the local angle of attack was very high in this condition. Comparing the experimental and numerical data away from the slipstream edge, the measured velocity is consistently lower than the simulated value. This was discussed for the isolated propeller data and thought to be a result of an upstream effect of the support structure used in the experiment. However, it is observed that the simulations predict the same trends as measured in the experiment, at all thrust settings. Therefore, it is concluded that the numerical data can be used to assess the effects of the propeller–SRV interaction on the loading in the next section.

The presented results only show the effect of the SRVs on the flowfield in a single plane, which is not necessarily representative of the complete slipstream. To analyse the swirl recovery over the entire disk, Fig. 6.4 depicts the computed distribution of the tangential velocity in a plane perpendicular to the streamwise direction, again positioned at $x/R_p = 1.5$, for the intermediate thrust setting ($J = 1.40$) both with and without SRVs installed. As expected, the swirl recovery achieved by the installation of the SRVs occurred over the entire circumference of the slipstream. Since the SRVs are stationary, their wakes and tip vortices are clearly visible in the time-averaged flowfield by the strong local modification of the tangential velocity.

6.1.3. PROPELLER AND SRV LOADING

According to the CFD data, the SRVs used in this experiment were not very effective in turning the recovery of swirl into a useful thrust force. A maximum increase in propulsive efficiency was found of 0.7% for $J = 1.40$ [68], which is low compared to other findings [63, 108]. Despite this, these stator vanes do introduce the aerodynamic interaction of

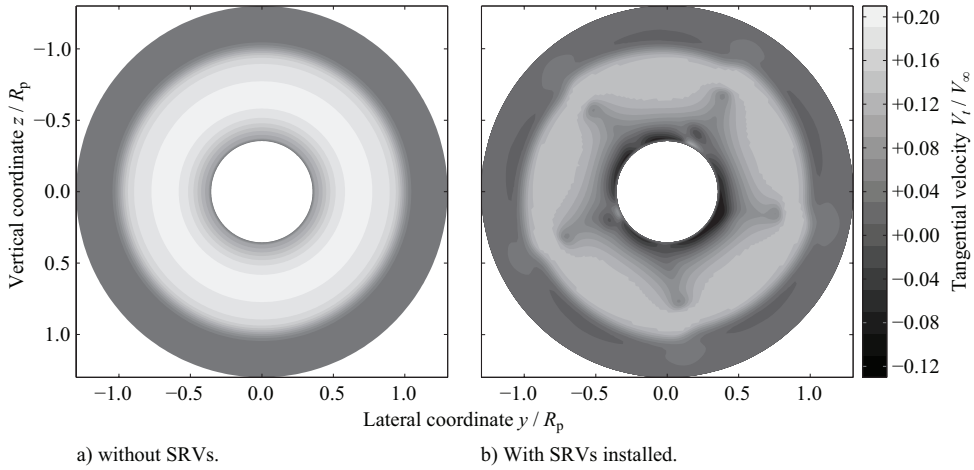


Figure 6.4: Effect of SRVs on the computed time-averaged tangential velocity in the propeller slipstream at $x/R_p = 1.5$ for $J = 1.40$.

6

interest in this study. From the CFD simulations it was found that there is only a small upstream effect of the SRVs on the time-averaged propeller performance. A 1% increase in propeller thrust and torque was found due to the upstream pressure effect of the SRVs. The SRVs also introduce temporal variations in the propeller loading. This can be seen in Fig. 6.5 from the unsteady component of the propeller blade normal-force coefficient c'_{n_p} at $r/R_p \approx 0.65$. A comparison is shown between experimental and CFD results. As the experimental results were obtained by integration of chordwise static pressure data, for consistency with the experimental results, the unsteady normal force extracted from the CFD data was computed using the pressure forces only, neglecting the influence of the viscous forces. The phase angle φ was defined in Fig. 3.3 and refers in this case to the leading edge position of the blade at $r/R_p \approx 0.65$. Five periodic loading cycles are visible over the complete azimuth in both the experimental and CFD results, equal to the number of vanes. As the blade passed a stator vane, the loading on the blade increased systematically for each operating condition. The peak-to-peak amplitude was about 0.8% of the time-averaged normal force for $J = 1.05$, and increased with increasing J to 2.3% for $J = 1.75$.

As expected, the effect of the propeller on the SRV loading is very significant as the SRVs are located in its slipstream. In Fig. 6.6 the time-averaged thrust distribution $c_{T_{SRV}} = T'_{SRV} / (\rho_\infty n^2 D_p^3)$ over the radius of a vane is shown. The figure also highlights the poor vane performance, as both the root and tip region only produce net drag for all conditions. For $J = 1.75$ the swirl in the slipstream was apparently too low to produce any significant thrust over the radius of the vane. It was found that in the tip region the rapid reduction of twist towards the tip (see Fig. 3.4) resulted in a net negative angle of attack. In the root region, flow separation over the vanes was the cause of the negative thrust.

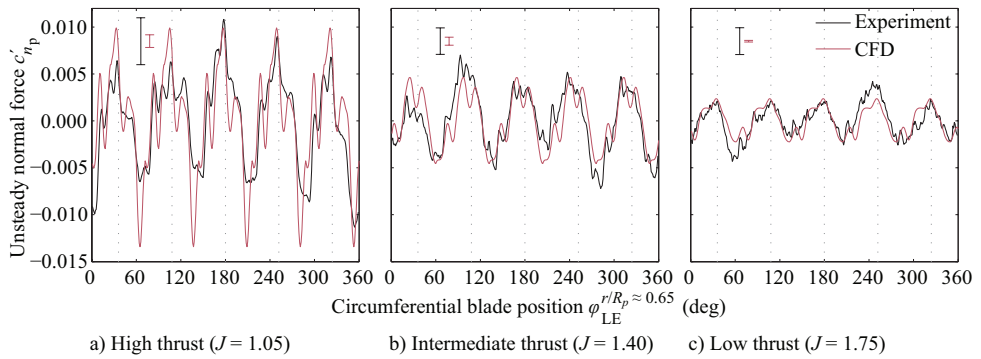


Figure 6.5: The upstream effect of the SRVs on the unsteady propeller blade loading at $r/R_p \approx 0.65$. The dotted lines indicate the locations where the blade passes a stator vane.

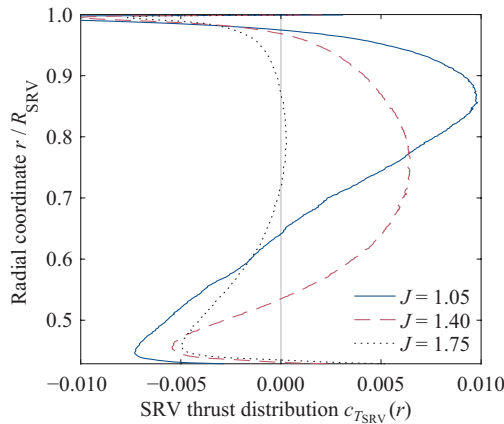


Figure 6.6: Time-averaged radial distributions of the thrust $c_{T_{SRV}}(r) = T'_{SRV} / (\rho_\infty n^2 D_p^3)$ on a single SRV.

In Fig. 6.2 we saw that the propeller slipstream is non-uniform in axial direction because of perturbations from the blade wakes and tip vortices. This unsteadiness in the slipstream results in temporal variations in SRV loading. To compare the unsteady loads on the SRVs to those occurring on the propeller blades from Fig. 6.5, the time-accurate sectional normal force on the SRVs was extracted from the CFD data. Figure 6.7 presents the results with the time-averaged loading subtracted, at radial stations $r/R_{SRV} \approx 0.74$ and $r/R_{SRV} \approx 0.99$. The data obtained at $r/R_{SRV} \approx 0.74$ are representative of the unsteady loading on the SRVs caused by the impingement of the blade wake, while the results at $r/R_{SRV} \approx 0.99$ are dominated by the interaction with the blade tip vortex. Since the unsteady SRV loading is periodic at the blade-passage frequency, only a single blade passage (60 deg) is displayed. The shaded areas represent the standard deviation computed per blade position, using all data available from the two blade passages (120 deg) from which the numerical data were extracted. Note that the scales on the vertical axes of the two subplots are different.

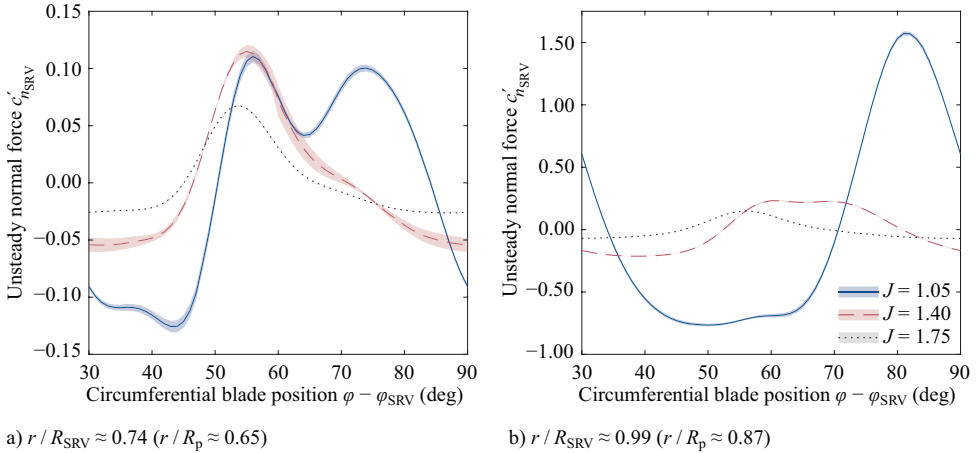


Figure 6.7: Unsteady SRV loading caused by the impingement of the propeller slipstream.

The time histories of the unsteady normal-force coefficient on the SRVs at $r/R_{SRV} \approx 0.74$ (Fig. 6.7a) reveal a peak in the unsteady loading occurring around $\varphi - \varphi_{SRV} = 55$ deg at all propeller thrust settings. At this position, the blade wake impinged on the downstream SRV, causing a sudden increase in local loading. The delay between the passage of the propeller blade in front of the SRV (at $\varphi - \varphi_{SRV} = 0$ deg) and the impingement of the blade wake on the SRV is caused by the finite distance between the propeller and the SRVs. This delay becomes larger with increasing propeller thrust setting due to the associated increase in the pitch angle of the slipstream helix. The pressure disturbance caused by the passing propeller blade itself might have amplified the unsteady loading due to the blade-wake impingement, but should not feature a phase shift with changing propeller thrust condition. Therefore, it can be considered as a secondary effect, dominated by the blade-wake impingement phenomenon.

At the highest thrust setting ($J = 1.05$), a secondary peak can be seen at about 20 deg after the primary rise in the loading. This peak is attributed to the induced velocities caused by the propeller-blade tip vortex, which trails the blade wake (see Fig. 6.2). The magnitude of this secondary peak in the unsteady SRV loading increases with increasing radial coordinate, as confirmed by Fig. 6.7b. Near the tip of the SRVs, the unsteady loading is about one order of magnitude larger than on the rest of the vane. At the low and intermediate thrust settings, the velocities induced by the tip vortex are smaller, hence their effect on the unsteady SRV loading is also smaller.

The importance of the interaction between the SRVs and the propeller tip vortices is highlighted in Fig. 6.8, which displays the spanwise distribution of the rms of the unsteady normal force on the SRVs for all considered propeller thrust settings. Especially at the high thrust condition ($J = 1.05$), a clear peak in the unsteady loading occurs near the tip of the SRV. With decreasing thrust, the strength of the tip vortices reduce. Furthermore, the slipstream contracts less and thus the spacing between the SRVs and vortex cores increases. The combined result is a significant decrease in the unsteady

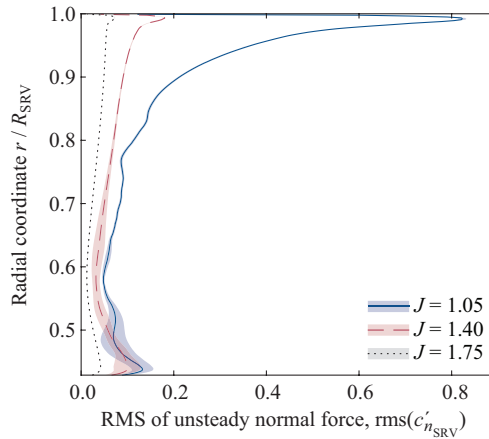


Figure 6.8: Spanwise distribution of the rms of the unsteady normal force on the SRVs.

loading with decreasing thrust. While for the highest thrust condition the fluctuations were highest in absolute sense, for all operating conditions the peak-to-peak amplitude of the unsteady loading was approximately 20% of the time-averaged value. This is an order of magnitude higher than the fluctuations experienced by the propeller blades.

6

6.2. INTERACTION WITH ANOTHER PROPELLER IN TYPICAL eVTOL CONFIGURATIONS

In this section the performance effects of propeller interaction with another propeller are investigated. As a propeller induces large changes to the flowfield, a propeller in the vicinity or in the slipstream may be experience altered propeller performance, in terms of thrust, power, in-plane forces and out-of-plane moments. An experimental setup was devised as described in Section 3.1.3 to parametrically investigate different propeller configurations quickly in a wind-tunnel, to see how these performance effects depend on propeller spacing. The considered cases were side-by-side (SBS) and one-after-another (OAA) propeller interaction. These two interaction cases were identified in Section 2.4 to possibly occur on eVTOL vehicles. The wind-tunnel configurations are however generic and not limited to specific eVTOL vehicle layouts, to fundamentally study the interaction effects on the propeller performance.

An overview of the test cases for performance measurement is given in Table 6.3. The reference isolated propeller performance was measured at $V_\infty = 0$ m/s, and at $V_\infty = 20$ m/s for $0 \leq \alpha_p \leq 95$ deg. The isolated propeller performance was already shown in Section 4.1.2 for zero angle of attack and in Section 4.2.2 for non-zero angle of attack. Up- and down-sweeps of propeller rotational speed were performed to vary helical tip Mach number M_{tip} at static condition and advance ratio when there was a freestream airspeed. The propeller blade pitch was set at $\beta_{0.7R_p} = 20.0$ deg to achieve considerable thrust for operation with freestream airspeed at zero propeller angle of attack, but prevent significant flow separation on the blades at large angle of attack or at static condition. The

Table 6.3: Overview of test cases for performance measurements in isolated and interacting configurations.

config.	F/T sensor loc.	V_∞ (m/s)	α_p (deg)	d_x/R_p	d_y/R_p
ISO	iso prop	0	0	-	-
ISO	iso prop	20	0, 30, 60, 90, 95	-	-
SBS	rear prop	20	0, 30, 60, 90, 95	-	2.25, 4
SBS	rear prop	20	90	-	2.1, 2.25, 2.6, 3, 4, 6
SBS	front prop	20	90	-	2.1, 2.25, 2.6, 4
OAA	rear prop	20	0	5.5	0, 0.25, 0.375, 0.5, 0.625, 0.75, 0.875, 1, 1.25, 1.5, 2, 3
OAA	rear prop	20	0	0.6	1.28, 1.5, 1.75, 2, 3

selected freestream airspeed of $V_\infty = 20$ m/s was a compromise to achieve considerable thrust with the chosen blade pitch angle and to reduce wind-tunnel wall corrections, as for the XPROP propeller it was shown that for lower airspeeds the corrections become more significant (Fig. 4.27).

All SBS and OAA configuration results were measured at a freestream airspeed of $V_\infty = 20$ m/s and only co-rotating propellers were considered due to the limitations of the setup. For the SBS configuration, lateral distance d_y (defined in Fig. 3.9) was varied in the experiment since this parameter differs considerably for eVTOL concepts. For selected lateral distances the same range of angle of attack as for the isolated propeller was considered with the SBS configuration, measuring the rear propeller performance. A more extensive sweep of lateral distance of $2.1 \leq d_y/R_p \leq 6$ for rear propeller measurements and $2.1 \leq d_y/R_p \leq 4$ for front propeller measurements was performed at $\alpha_p = 90$ deg. For $d_y/R_p = 2.6$ at this angle of attack, PIV measurements of the slipstream interaction were taken. Both propellers were operated at the same rotational speed, except for two special cases with both propellers at equal thrust. The results for the SBS configuration are discussed in Section 6.2.1.

Although in a realistic application OAA interaction may only occur when the aircraft is at an angle of attack, all measurements for this configuration were performed at $\alpha_p = 0$ deg for simplification. Two axial distances were considered, a far case at $d_x/R_p = 5.5$ and a close case at $d_x/R_p = 0.6$. Axial distance d_x was defined in Fig. 3.9. The far case corresponds for instance to the layout of the Airbus Vahana as sketched in Fig. 2.11 and the Joby S2 [122]. The close case is more relevant for propellers mounted with overlap or staggered on for instance the wing. The interaction for this case differs fundamentally from the far case, since the rear propeller experiences a slipstream that is not fully contracted yet. Lateral distances of $0 \leq d_y/R_p \leq 3$ were considered for the far case and a smaller range of $1.28 \leq d_y/R_p \leq 3$ for the close case, since the front propeller spinner was limiting any further overlap. The front propeller was operated at two different rotational speeds and a sweep of rear propeller rotational speed was performed each time. Only the performance of the rear propeller was measured as for the main axial distance of interest, $d_x/R_p = 5.5$, the upstream effect was assumed to be negligible. The effects of OAA interaction are investigated in Section 6.2.2.

6.2.1. SIDE-BY-SIDE (SBS) PROPELLER CONFIGURATION

This section discusses the results of one of the main interaction cases identified for eVTOL vehicles: side-by-side propeller interaction. This interaction type is of importance especially in the transition phase of eVTOL vehicles, when propeller thrust is used for lift when transitioning from climbing flight to forward flight. During this manoeuvre, large changes in propeller angle of attack occur, altering the direction of the slipstreams and as such the effects of aerodynamic interaction between the propellers. First, results are presented where both propellers operate at equal advance ratio, calculated using the freestream velocity and the rotational speed of each propeller. Second, results are shown for which the propellers operate at equal thrust or combined constant thrust, compensating for interaction effects. This enables the determination of required power changes to maintain thrust.

PROPELLERS AT EQUAL ADVANCE RATIO

Previous research has shown that when propellers operate at static condition in the same plane at very small distance from each other, a small reduction in thrust can be expected. Ref. [133] showed a reduction of less than 2% at $d_y/R_p = 2.1$, while Ref. [127] demonstrated a 4% reduction at $d_y/R_p = 2.2$ for the case of a quadcopter. In forward flight, this effect is thought to be even less since, unlike at static condition where air is drawn from all around the propeller, the inflow region is limited and less shared with the neighbouring propeller.

In Fig. 6.9 a performance comparison is plotted between the ISO configuration and SBS configuration as a function of α_p at $V_\infty = 20$ m/s and a constant advance ratio of $J = 0.57$. This figure is meant to illustrate propeller interaction during the transition phase for eVTOL vehicles, where $\alpha_p = 0$ deg represents take-off and $\alpha_p = 95$ deg forward flight with an aircraft angle of attack of 5 deg, see Fig. 3.9 c. Although in a realistic scenario, the inflow velocity to the propeller during transition is not constant and blade pitch and/or rotational speed may be adjusted to meet the required performance, for simplification the operating conditions were kept constant. In case of the SBS configuration results at non-zero α_p , performance is plotted of the rear propeller since for this propeller more significant interaction effects can be expected than for the front one. Two distances d_y were considered. At $\alpha_p = 0$ deg no significant performance effects can be observed as a result of SBS interaction. With increasing angle of attack, an increasing reduction in C_T and C_P with respect to the isolated propeller can be noticed for the rear propeller in SBS interaction. As expected, this decrease is worse for the propellers at close distance $d_y/R_p = 2.25$ than at the further distance $d_y/R_p = 4$. A maximum in C_T and C_P occurs around $\alpha_p \approx 90 - 95$ deg for the SBS case, while for the ISO configuration both performance parameters increase significantly in value beyond $\alpha_p = 90$ deg. The mechanism behind this reduction in C_T and C_P for the rear propeller is likely a reduction of effective α_p as a result of operating in the downwash of the front propeller, similar to what was found for tandem-rotors by Refs. [116, 117]. This situation is sketched in Fig 6.10 a for $\alpha_p = 90$ deg. The averaged effect of the downwash is a reduction in α_p as shown in Fig 6.10 b. From isolines of C_T and C_P (horizontal lines in Fig. 6.9 a and b), an estimation of the effective angle of attack can be made. For $\alpha_p = 95$ deg and $d_y/R_p = 4$, the effective angle of attack is estimated to be 15 deg less than the geometric, while for $d_y/R_p = 2.25$ it is even 27 deg less.

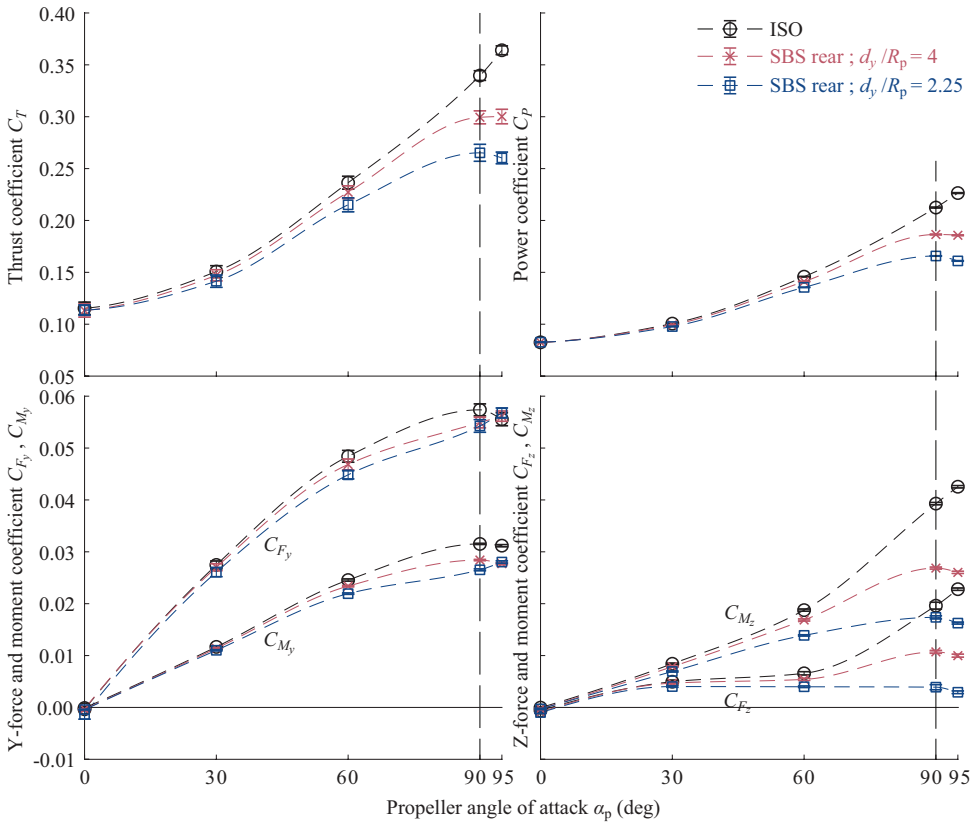


Figure 6.9: ISO and SBS rear propeller performance versus α_p for $V_\infty = 20$ m/s and $J = 0.57$, fitted from F/T sensor data.

The in-plane force coefficients C_{F_y} and C_{F_z} , and out-of-plane moment coefficients C_{M_y} and C_{M_z} are also plotted in Fig. 6.9. For $\alpha_p \leq 60$ deg the effect of SBS interaction on C_{F_y} of the rear propeller is similar to the effect on C_T . However, the results at $\alpha_p = 90$ deg and 95 deg do not follow the trend of increased reduction with angle of attack. A cross-over point can even be noticed near $\alpha_p = 95$ deg where C_{F_y} of the rear propeller in SBS interaction becomes larger than that of the ISO propeller. C_{M_y} follows the trend of C_{F_y} as it is a derivative effect, except for the cross-over. On the other hand, the effect of SBS interaction on C_{F_z} and C_{M_z} of the rear propeller is similar to the effect on C_T but amplified. To explain the interaction effects on C_{F_y} and C_{F_z} , the sketch in Fig. 6.10 is again used. From the fact that the interaction effects more downstream at $d_y/R_p = 4$ are smaller than at $d_y/R_p = 2.25$, it can be implied that the rear propeller sees a non-constant distribution of downwash in y-direction, reducing with distance from the front propeller. The gradient in downwash likely results in the secondary effect sketched in Fig. 6.10 c, where the thrust is relatively decreased on the side of the propeller disk closest to the front propeller, and relatively increased on the side that is further away. This asymmetry in thrust and the corresponding asymmetry in tangential forces causes a negative force

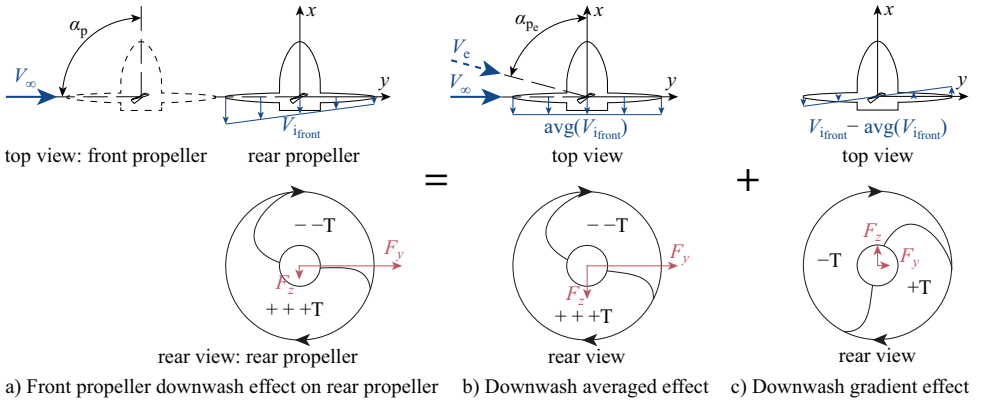


Figure 6.10: Sketch showing the typical effect of SBS interaction on rear propeller forces at $\alpha_p = 90$ deg, relative to isolated propeller at $\alpha_p = 0$ deg.

contribution in z -direction, opposing the z -force for the isolated propeller at angle of attack. A phase lag in this asymmetry can result in a positive force contribution in y -direction, possibly explaining the cross-over in C_{F_y} occurring at large angle of attack. It is thought that this phase-lag originates from variations in induced velocity across the propeller disc similar to the phase-lag in loading for a propeller at angle of attack [72].

At $\alpha_p = 90$ deg dashed lines are drawn in Fig. 6.9 for which in Fig. 6.11 performance plots are presented as function of d_y . In this figure the performance quantities are expressed as ratios between the quantity in interaction and the quantity for the isolated propeller at the same operating condition. Results are shown both for the rear and front propeller, as the propeller units were switched around in the experiment, and for both propellers at three advance ratios $J = 0.49, 0.57$ and 0.69 . While for the rear propeller C_T reduces as a result of the SBS interaction, for the front propeller a small increase is noticeable at small d_y . As was found by Refs. [116, 117] for a tandem-rotor, an upwash from the rear propeller slightly increases the front propeller angle of attack. The effect of the interaction for the rear propeller is dependent on the advance ratio, increasing in strength with increasing advance ratio, or decreasing rotational speed. This is explained by the increased gradient of $C_T - \alpha_p$ at higher advance ratios for the isolated propeller as was shown in Fig. 4.33. While the effect of interaction on the front propeller becomes negligible when d_y increases to 4, the effect on the rear propeller remains significant for the plotted range up to $d_y/R_p = 6$. Apparently the effective change in angle of attack by the front propeller extends far downstream. Exactly the same effects are seen for C_P .

As was discussed in relation to Fig. 6.9, the SBS interaction effect for C_{F_y} is smaller than for C_T for the rear propeller. Figure 6.11 shows that this conclusion is true for the whole tested range of d_y . The trend of interaction effect with advance ratio is reversed compared to that for C_T . For the highest plotted advance ratio, C_{F_y} is even slightly increased with respect to the isolated configuration. This is explained by the fact that a propeller operating at higher J is relatively more influenced by inflow velocity changes,

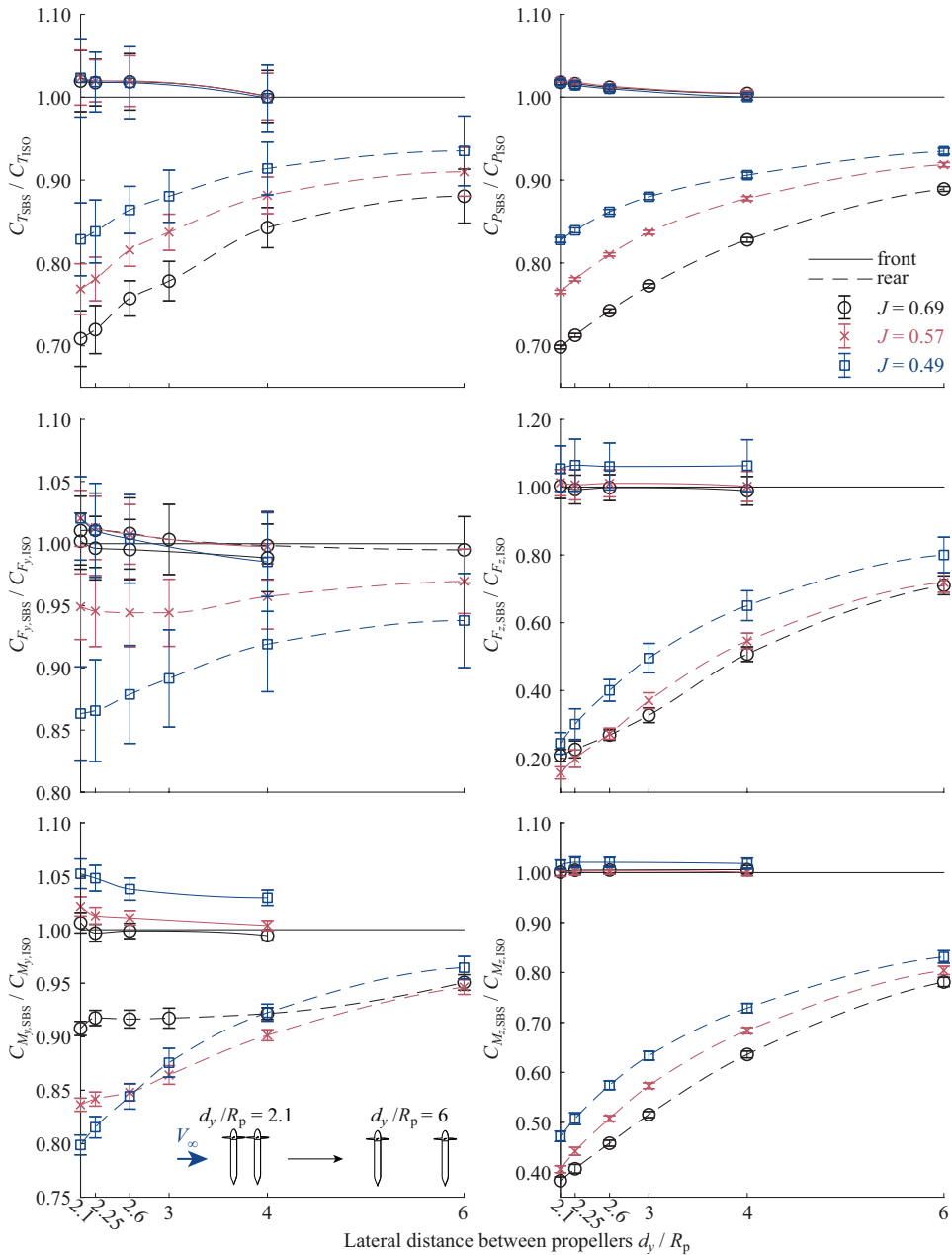


Figure 6.11: Front and rear propeller performance change due to SBS interaction as function of d_y for $V_\infty = 20$ m/s and $\alpha_p = 90$ deg (forward flight) at three advance ratios, fitted from F/T sensor data.

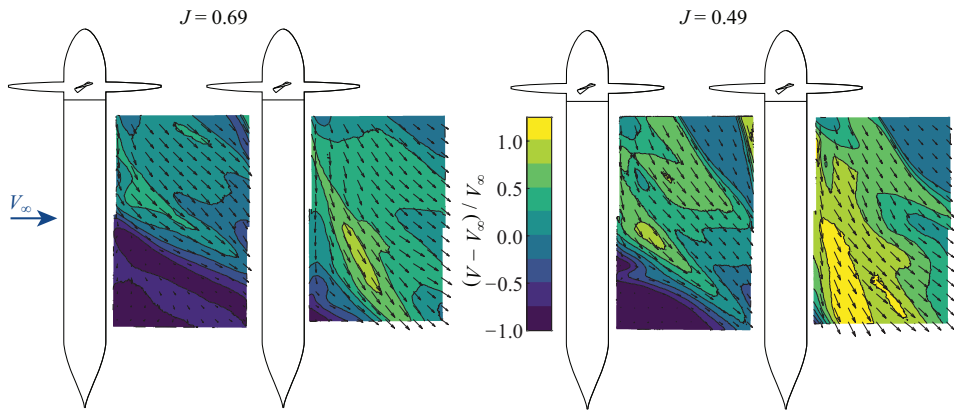


Figure 6.12: Time-averaged flowfield from planar PIV measurements behind propellers in SBS interaction for $V_\infty = 20$ m/s, $\alpha_p = 90$ deg and $d_y/R_p = 2.6$.

like the interaction effect sketched in Fig. 6.10 c that is thought to increase C_{F_y} . In line with C_T , the interaction effect on the front propeller is small for C_{F_y} . Similar results are shown for C_{M_y} .

For C_{F_z} the interaction effect is stronger than for C_T for the whole range of d_y . At $d_y/R_p = 2.1$ the force component is reduced to just 20% of its value without interaction. However, the absolute values are relatively small compared to the other force components. The effect on the front propeller is again small. C_{M_z} follows the trends of C_{F_z} .

Considering the large observed effects on the propeller forces and moments, SBS interaction can have significant consequences for the aircraft stability. This however very much depends on the location of the rear propeller with respect to the center of gravity (CG). One can imagine if thrust is lost at a far distance from the CG, its moment arm can induce a pitch up or pitch down moment. The dependency of the interaction effect on d_y and the direct dependency of stability on the rear propeller location through d_y , make it also hard to draw any general conclusions. However, the found interaction results enable the reader to make a first estimation of stability effects for specific eVTOL layouts.

For the lowest and highest advance ratio plotted in Fig. 6.11, at $d_y/R_p = 2.6$ the time-averaged slipstream flowfield in a plane perpendicular to the propeller disk and parallel to the freestream velocity is shown in Fig. 6.12, as measured with the PIV setup (see Section 3.1.3). Note that this velocity field only contains the in-plane velocity components and the out-of-plane component is not included. For both advance ratios, a mixing of the front and rear propeller slipstream can be observed. As expected, for lower J , the impingement of the front propeller slipstream on the rear propeller slipstream happens more downstream. This is a result of the higher induced axial velocity due to the higher thrust at the lower J . Despite the lower thrust of the rear propeller as a result of the interaction, the rear propeller slipstream seems to form an angle with the rotation axis equal or smaller than for the front propeller. This indicates that the effective angle of

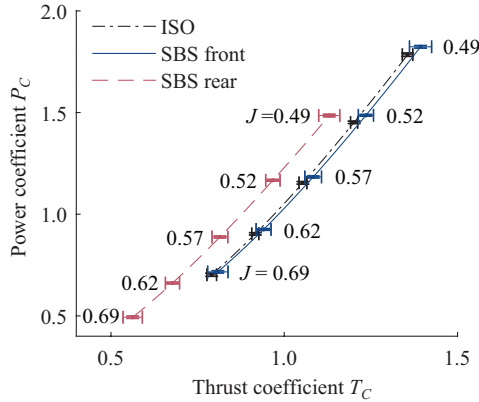


Figure 6.13: ISO and SBS front and rear propeller power versus thrust coefficient for $d_y = 2.1$, $V_\infty = 20$ m/s and $\alpha_p = 90$ deg, fitted from F/T sensor data.

attack for the rear propeller is indeed reduced by the downwash of the front propeller, confirming the mechanism sketched in Fig. 6.10. Another observation is that the velocity distribution in the slipstreams is rather non-uniform. This is likely induced by the very non-uniform loading on the propeller due to this skewed inflow. Note that below the propeller slipstreams large velocity deficits are noticeable in the PIV measurements, which are the wakes of the nacelles.

Figure 6.11 does not directly highlight any changes in efficiency. Therefore, in Fig. 6.13, a $P_C - T_C$ plot is given for the ISO and SBS configuration at $d_y/R_p = 2.1$ and $\alpha_p = 90$ deg. Note that, since in the SBS configuration the front and rear propeller are in aerodynamic interaction and their advance ratio was kept equal, the results for the front and rear propeller can only be compared at constant advance ratio. However, comparison with the ISO configuration is valid for unequal advance ratio. Clearly, for a given T_C , a higher shaft power is required for the SBS rear propeller compared to the ISO configuration, while for the SBS front propeller the required power reduces slightly. The shift between the ISO and the SBS rear result is very similar to a decrease in propeller angle of attack in Fig. 4.34 b, while the shift between the ISO and the SBS front result resembles an angle of attack increase. Further analysis on the efficiency is done in the next section by keeping thrust constant between the front and rear propeller.

PROPELLERS AT EQUAL THRUST

In order to assess the effects of SBS interaction on the power demand, the lost thrust due to interaction for the rear propeller needs to be compensated. For $\alpha_p = 90$ deg and $d_y/R_p = 2.6$ an experiment was performed where the rotational speed of the front propeller was fixed at two specific advance ratios, $J = 0.77$ and $J = 0.62$, and the rotational speed of the rear propeller was varied to obtain the same thrust as the front propeller. T_C was used instead of dimensional thrust to remove any effects of change in freestream temperature or static pressure during the experiment. The front propeller T_C was assumed to be equal to that found with the rear propeller at the same J , thus ignoring the

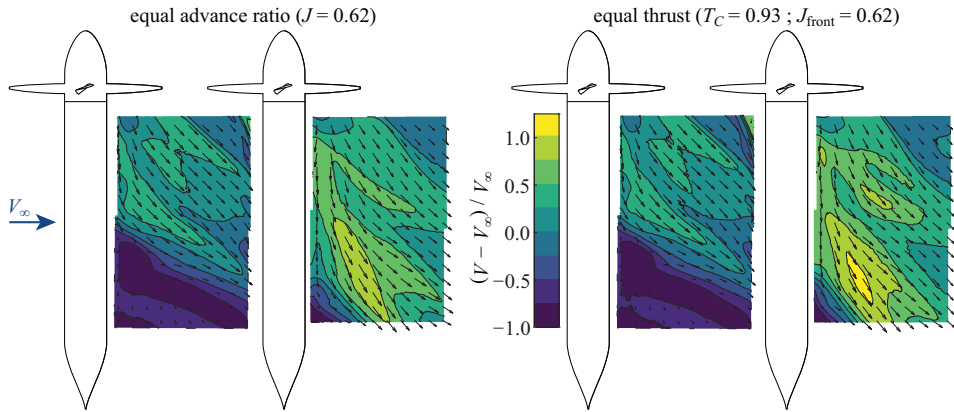


Figure 6.14: Time-averaged flowfield from planar PIV measurements behind propellers in SBS interaction at equal J and equal T_C for $V_\infty = 20$ m/s, $\alpha_p = 90$ deg, $d_y/R_p = 2.6$.

secondary effect of the increase in rear propeller thrust on the front propeller loading. For $J = 0.77$ an increased power of 7.3% is found due to the interaction effect for the propellers combined. For $J = 0.62$ this is slightly lower at 5.8%. For the latter advance ratio the slipstream flowfield is visualised in Fig. 6.14, both for equal advance ratio and equal thrust. The rear propeller slipstream for the case at equal thrust forms an even smaller angle with respect to the propeller rotation axis. This shows that the decreased deflection with decreasing J observed in Fig. 6.12 not only depends on the front propeller setting and the resulting downwash on the rear rotor (mechanism sketched in Fig. 6.10), but also on the rear propeller setting. When the propellers are operating at equal thrust, the slipstream deflection difference between the front and rear propeller is even larger than when operating at equal advance ratio, indicating again a reduced effective angle of attack for the rear propeller.

A second strategy that can be thought of to maintain equal thrust compared to the situation without interaction, is to keep the front and rear propeller operating at equal advance ratio but reduce this advance ratio to compensate for the loss in combined thrust. The reference thrust in this case is chosen to be the thrust of the isolated propeller at $J = 0.62$, $V_\infty = 20$ m/s and $\alpha_p = 90$ deg, so the same reference condition as in the previous paragraph. For this analysis the front propeller performance is assumed equal to the isolated propeller performance. In Fig. 6.15 the power at this thrust is plotted for three cases, the ISO propeller configuration and the average of the front and rear propeller in SBS configuration with $d_y/R_p = 4$ and $d_y/R_p = 2.25$. The power is plotted relative to the isolated propeller power at static condition at the same thrust, so a value higher than 1 means more power is required than hover power. For the ISO configuration, at $\alpha_p = 0$ deg, 40% more power is required than hover power since the freestream velocity of $V_\infty = 20$ m/s can be seen as a climbing flight. This power requirement reduces with increasing α_p to a situation where only 80% of the hover power is required at $\alpha_p = 95$ deg. With interaction, a similar trend is followed but at reduced slope, meaning that especially at large α_p the SBS interaction results in a power penalty with re-

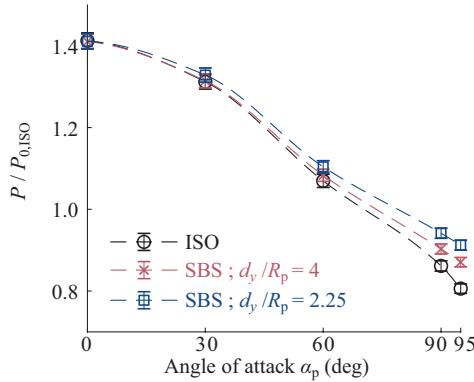


Figure 6.15: Power in three scenarios at equal $T_C = 0.93$ for $V_\infty = 20$ m/s, fitted from F/T sensor data: The ISO propeller and the average of the front and rear propeller in SBS interaction at $d_y/R_p = 4$ and 2.25.

spect to the ISO configuration of up to 8.0% and 13.2% at $\alpha_p = 95$ deg for $d_y/R_p = 4$ and $d_y/R_p = 2.25$ respectively. In any case, SBS interaction is neutral or detrimental for the performance.

6

6.2.2. ONE-AFTER-ANOTHER (OAA) PROPELLER CONFIGURATION

This section discusses the results of the second interaction case identified for eVTOL vehicles: one-after-another propeller interaction. This interaction type is of importance especially in cruise flight of eVTOL vehicles, where propeller thrust is used to propel the vehicle. While in the design cruise condition of eVTOL vehicles the slipstream of one propeller may not impinge on another propeller, during manoeuvres or due to angle of attack changes, such situations may arise. An analysis of the performance effects of this interaction is therefore important. First, results are presented for the case with both propellers operating at equal advance ratio. Second, results are shown for the case with the propellers operating at equal thrust, in order to determine the required power change compared to the situation without interaction. Results are shown for two axial distances between the propellers, a far case with $d_x/R_p = 5.5$ and a close case with $d_x/R_p = 0.6$. The far case represents for instance interaction found between a propeller mounted on a wing and one on a tailplane. The close case is representative for propellers mounted with an overlap on for instance the wing leading edge. The interaction effects in this section are limited to the effects for the rear propeller. Predictions of the interaction effects on thrust and power with the extended blade element momentum (BEM) model are shown alongside the results.

PROPELLERS AT EQUAL ADVANCE RATIO

In Fig. 6.16 the thrust and power coefficient of the rear propeller in OAA interaction are plotted as function of lateral distance d_y for two advance ratios $J = 0.57$ and $J = 0.49$. The performance is plotted as a ratio with the isolated performance in the denominator. Results are shown for both the far and close case with $d_x/R_p = 5.5$ and $d_x/R_p = 0.6$ respectively. Measurements are shown in Fig. 6.16 a and predictions with the extended

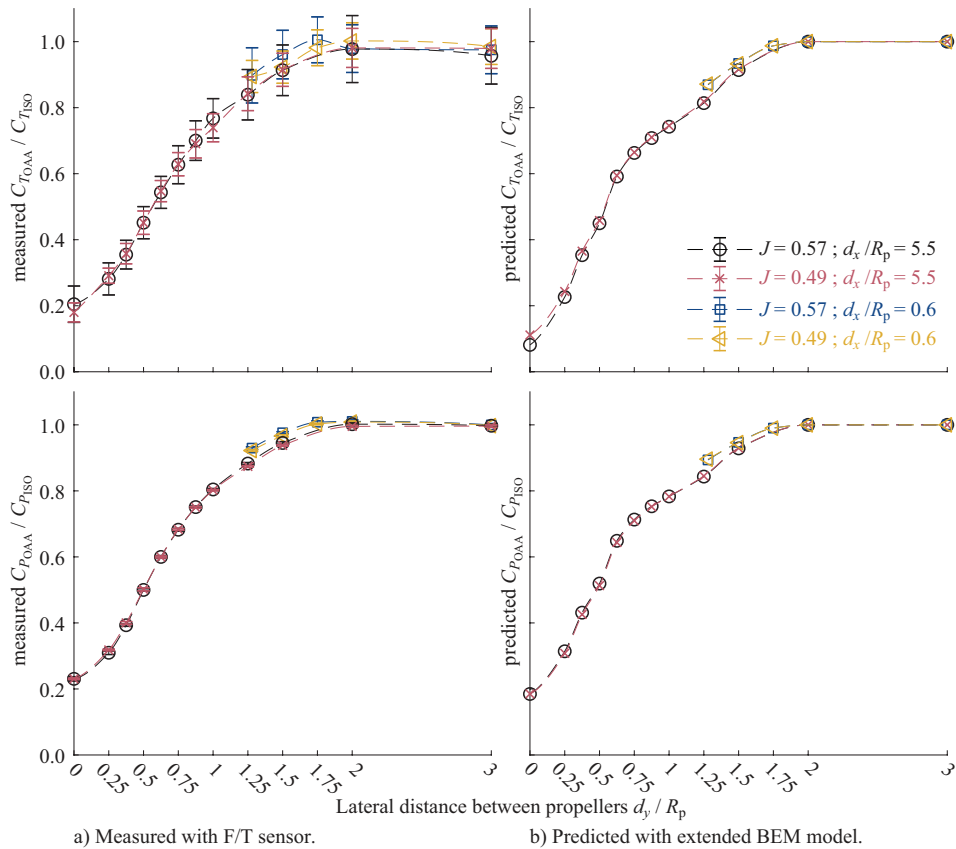


Figure 6.16: Change of rear propeller C_T and C_P due to OAA interaction as function of d_y for $V_\infty = 20$ m/s, $\alpha_p = 0$ deg.

BEM model in Fig. 6.16 b. For the furthest lateral distance $d_y/R_p = 3$, no significant interaction effect on C_T and C_P was measured. The BEM model prediction is in agreement since with its formulation the rear propeller sees an undisturbed freestream inflow for this d_y . For $d_x/R_p = 5.5$, the interaction effect is still negligible when the lateral distance is decreased to $d_y/R_p = 2$. This is in line with the observation that the slipstream of the front propeller contracts (Fig. 4.11) and thus at $d_y/R_p = 2$ the rear propeller does not experience the induced velocities in the slipstream of the front propeller.

For any of the measurements with d_y smaller than 2, interaction effects can be expected. Since the front propeller slipstream increases the axial velocity inflow to a part of the rear propeller, the effective advance ratio of the rear propeller increases and thus its C_T and C_P reduce, as can be deduced from Fig. 4.33. The more the propellers overlap, the more this effect on C_T and C_P is accentuated. However, the front propeller also introduces a swirl or tangential velocity component in the slipstream, and the effect of this induced velocity component on the rear propeller performance depends on the location of slipstream impingement.

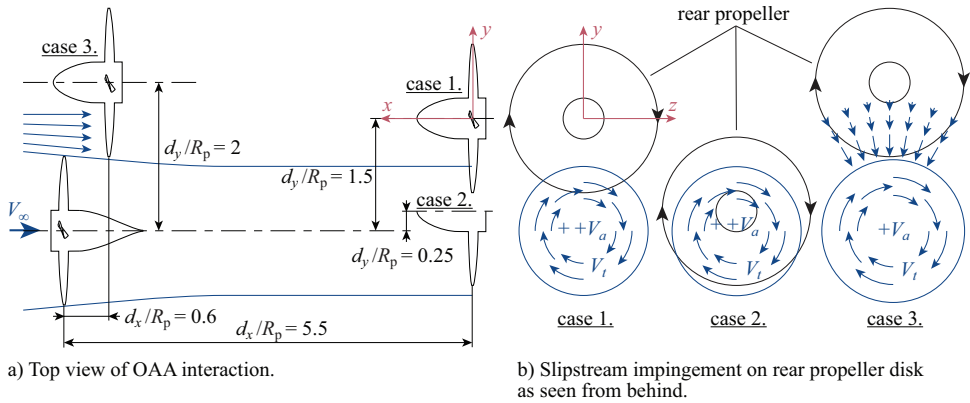


Figure 6.17: Sketch of interaction of rear propeller with slipstream of front propeller in OAA configuration. Three cases of different axial and lateral distance are distinguished.

The sketch in Fig. 6.17 illustrates this effect. A tangential velocity component in the local propeller reference frame increases blade sections angle of attack when it opposes the direction of propeller rotation and vice versa. This increases or decreases C_T and C_P respectively. The tangential velocity component in the front propeller reference frame needs to be transformed to the rear propeller reference frame, which introduces a dependency on d_y . When reducing the lateral distance from $d_y/R_p = 2$ to $d_y/R_p = 1$, for co-rotating propellers the rear propeller sees a relative increase in C_T and C_P by the tangential velocity component up to $d_y/R_p = 1$. Case 1 in Fig. 6.17 illustrates this opposing tangential velocity to the rotation direction for $d_y/R_p = 1.5$.

For $d_y/R_p < 1$ part of the propeller disk sees an increase and part of the disk a decrease of thrust and power by the tangential velocity component. When d_y becomes very small, for instance for $d_y/R_p = 0.25$ as shown in case 2 in Fig. 6.17, the tangential velocity is mainly in the direction of propeller rotation, reducing thrust and power. At $d_y/R_p = 0$ the effect of the tangential velocity is purely reducing C_T and C_P . This effect of the tangential velocity can be clearly recognized in the measurements for $d_x/R_p = 5.5$ by the sudden change in slope around $d_y/R_p \approx 0.75$. The BEM model prediction features this slope change too. The main deviation of the BEM model from the experimental result is found at $d_y/R_p = 0$. It is thought that, due to contraction of the slipstream, the area of the propeller disk affected by the slipstream does not increase anymore when reducing d_y at values slightly larger than $d_y/R_p = 0$. Therefore, a reduction in slope towards $d_y/R_p = 0$ would be expected and is also present in the experimental and BEM data. In the BEM data this is less so, possibly due to a difference in slipstream contraction. Note that surprisingly, the relative interaction effects for both advance ratios are the same.

The results for $d_x/R_p = 0.6$ are slightly different. At $d_y/R_p = 2$, there is a slightly increased C_P of 1.0% due to interaction compared to the isolated propeller. Whether this is accompanied by a similarly increased C_T cannot be concluded due to the large confidence interval for this performance parameter, however this is likely the case. At $d_y/R_p = 1.75$ still a 0.5% increased C_P is found compared to the isolated propeller. For

$d_y/R_p \leq 1.5$, C_T and C_P for the rear propeller decrease due to the interaction. The main difference for the close case compared to the far case, is that the slipstream is less contracted (See Fig. 4.11), meaning that the axial velocity at the rear propeller plane induced by the front propeller is lower for the close case, but spread over a wider area. This reduces the effect of slipstream impingement on the rear propeller performance as the effective advance ratio is less increased. However, this does not explain directly any increase in C_P or C_T . A possible explanation is that when a propeller operates in the region of contraction of another propeller, it experiences a local angle of attack, as sketched in case 3 for $d_y/R_p = 2$ in Fig. 6.17. From the results of Fig. 4.33 we know that operation at nonzero angle of attack increases C_T and C_P compared to the symmetric inflow case, thereby explaining the observation. At $d_y/R_p = 1.75$, when the front propeller slipstream already impinges on part of the rear propeller, the angle of attack effect apparently offsets the increased advance ratio effect. The BEM model does not capture this thrust increasing effect, because the induced velocity components outside of the slipstream tube are zero in this model.

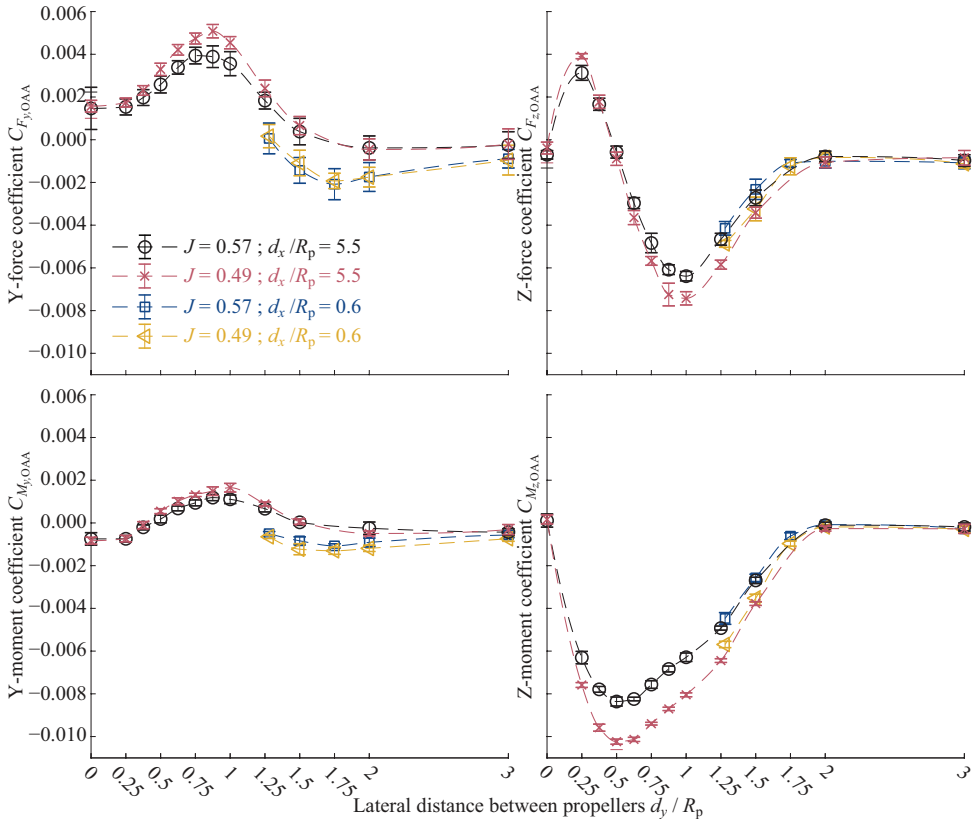


Figure 6.18: Rear propeller in-plane force coefficients and out-of-plane moment coefficients due to OAA interaction as function of d_y for $V_\infty = 20$ m/s, $\alpha_p = 0$ deg.

In Fig. 6.18 the corresponding in-plane force coefficients and out-of-plane moment coefficients of the rear propeller in OAA interaction are plotted. First consider the data for $d_x/R_p = 5.5$. At $d_y/R_p = 3$ no in-plane forces or out-of-plane moments are present since the propeller operates outside the front propeller slipstream and does not experience any non-uniformities in its inflow. This is maintained at $d_y/R_p = 2$.

Observe case 1 at $d_y/R_p = 1.5$ as sketched (in rear view) in Fig. 6.17. A decrease in thrust at the location of slipstream impingement results in a negative moment around the z-axis, which is indeed reflected in the results shown in Fig. 6.18. Furthermore, the corresponding local reduction in the tangential force on the affected blade sections cause a negative C_{F_z} . Similarly to what happens at nonzero angle of attack, reductions in thrust and tangential force likely experience a phase lag, resulting also in a positive C_{M_y} and C_{F_y} . The generation of positive y-moment and force is accentuated by the tangential velocity component, which relatively reduces thrust and tangential force more on the side of impingement with negative z-coordinates.

Around or slightly below $d_y/R_p = 1$, the effects for C_{F_z} , C_{M_y} and C_{F_y} experience extrema, since the slipstream impingement results in the most imbalance of effect between the positive and negative sides of the propeller disk in y-direction. For C_{M_z} this minimum is reached slightly later, probably since effects at small y-location do not weigh in as much as at larger y-location. The effects resulting in positive C_{M_y} and C_{F_y} and negative C_{M_z} are countered by effects on the positive side of the propeller disk in y-direction for $d_y/R_p < 1$, and therefore a decrease in magnitude towards $d_y/R_p = 0$ is seen for these components. For C_{F_z} a different trend is seen. This force component changes sign and experiences a small maximum around $d_y/R_p = 0.25$. This may be caused by a phase shift in thrust and tangential force reduction, although this is not entirely clear from the available data.

A surprising result is found for $d_y/R_p = 0$, where non-zero values of C_{M_y} and C_{F_y} were measured. In this axisymmetric condition in terms of inflow to the rear propeller, no in-plane forces and out-of-plane moments are expected. However, in Section 4.1.2 the effect of the fairing was discussed, and a local reduction in total pressure was found. A reduction in total pressure and thus a reduction in axial velocity locally results in a less decreased thrust of the rear propeller and may therefore have caused such an effect. As a result of the swirl, the exact location of this effect on the rear propeller is however not known and therefore this explanation cannot be confirmed.

The interaction effects for $d_x/R_p = 0.6$ are very similar to the described effects for $d_x/R_p = 5.5$. The main difference is found in the C_{F_y} and C_{M_y} components. Already for $d_y/R_p = 3$, the rear propeller experiences a negative C_{F_y} , and this becomes more negative with a minimum at $d_y/R_p = 1.75$. C_{M_y} follows a similar pattern. The earlier discussed angle of attack effect due to contraction of the slipstream, as sketched in case 3 in Fig. 6.17, would explain this difference in interaction compared to what was found for $d_x/R_p = 5.5$. The in-plane velocity components induced by the slipstream contraction, cause a reduction in thrust and tangential force on the negative side of the propeller disk in z-direction compared to the positive side.

The question can be raised if the described interaction effects on the force and moment components are significant for aircraft stability. Consider the layout of the Airbus

Vahana as sketched in Fig. 2.11. If the front propeller slipstreams impinge on the rear propellers when there is partial overlap, a pitch down moment will be generated by the negative moment around the z-axis and the positive force in y-direction. However, in terms of y-force, this may be dependent on the rotation direction of the propellers. Since the rear propeller is mounted relatively high, the reduced thrust of the rear propeller could result in a pitch up moment. The corresponding change of the rear propeller slipstream also impacts the loading on the horizontal and vertical tail planes. All in all, consideration of these interaction effects on aircraft stability seems important, non-trivial and very layout dependent.

PROPELLERS AT EQUAL THRUST

Also for the OAA configuration, the rear propeller rotational speed was varied to obtain the same T_C as without front propeller slipstream impingement. The result is given in Fig. 6.19 as the ratio of the power required for the rear propeller to the power of the isolated propeller to achieve the same T_C . Results are only shown for $d_x/R_p = 5.5$, since for $d_x/R_p = 0.6$ it cannot be assumed that the upstream effect on the front propeller thrust is negligible or small. Note that, since only the rear propeller power is considered and not the front propeller power, the found values should be divided by two if compared to results for SBS interaction in Fig. 6.15. Results for two different advance ratios of the front propeller are shown, with measurements in Fig. 6.19 a and BEM model predictions in Fig. 6.19 b. Very significant power increases are found when the propeller overlap is large, increasing to values larger than 30% for full overlap at $d_y/R_p = 0$. The trends are again very similar for both advance ratios. Prediction with a BEM model of this interaction effect is clearly sufficiently accurate, and such a method could thus successfully be used for initial design purposes.

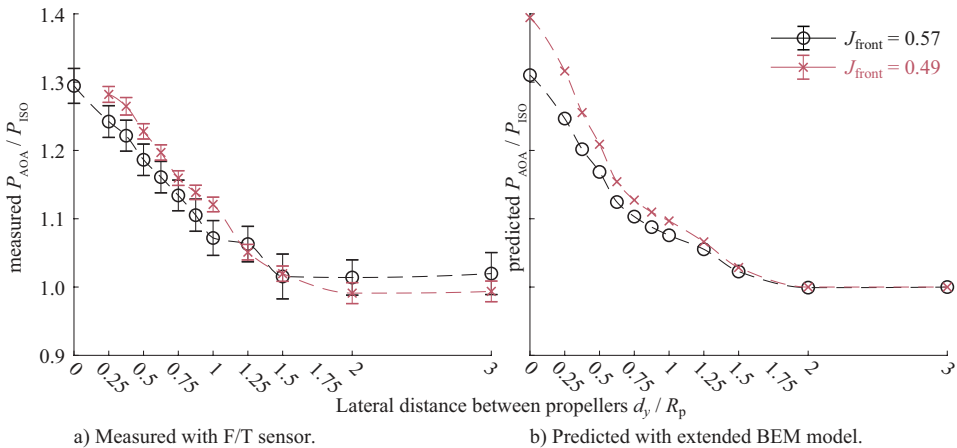


Figure 6.19: Change of rear propeller power to maintain thrust in OAA interaction as function of d_y for $V_\infty = 20$ m/s, $\alpha_p = 0$ deg.

6.3. CONCLUSIONS

In this chapter two different propeller interactions were studied, interaction with swirl-recovery vanes and interaction with another propeller. The conclusions are treated separately in the next two sections.

INTERACTION WITH SWIRL-RECOVERY-VANES

The aerodynamic interaction effects of a propeller combined with downstream swirl-recovery-vanes were investigated to answer research question **Q5**. These stator vanes remove part of the swirl in the slipstream, aiming to achieve a net force in thrust direction. In this way, for a given amount of shaft power to the propeller, the propulsive efficiency of the system can be enhanced.

It was shown that the tangential velocity in the propeller slipstream was reduced by the installation of SRVs. Acceptable agreement in the velocity field between the RANS CFD simulations and the validating experimental data was found, showing the same trends with installation of the SRVs. The main differences could be attributed to numerical diffusion near the slipstream edges and a possible upstream effect of the support structure in the experiment. As the design of these vanes was such that it underperformed in terms of thrust production compared to what is found in literature, and considering the scope of the dissertation, the focus of this study was on the (unsteady) interaction effects and not on the possible performance enhancement.

6

Two aerodynamic interaction mechanisms were found. The propeller experienced a small increase in thrust and torque of 1% due to an upstream pressure effect of the SRVs compared to the case of the isolated propeller. Furthermore, in both the computation and experiment the sectional blade normal-force at $r/R_p \approx 0.65$ was found to be fluctuating with 0.8% to 2.3% of the local time-averaged loading, relatively increasing with increasing J . Five periodic fluctuations were found in a full blade rotation, equal to the number of swirl-recovery-vanes.

As the swirl-recovery-vanes are located in the propeller slipstream, a much stronger downstream interaction was found. Apart from the changing time-averaged vane loading with propeller operating condition, impingement of the propeller blade wakes and tip vortices resulted in unsteady loading on the SRVs varying with the blade-passage frequency. Especially the effect of the tip-vortices was found to be strong, resulting in unsteady loading near the tip of the SRV which was one order of magnitude larger than on the rest of the vane. This was especially the case for the highest thrust condition ($J = 1.05$) due to the additional contraction in the slipstream at this J and thus smaller blade tip-vortex–SRV spacing and the increase in blade tip-vortex strength. Averaged over the span, the peak-to-peak amplitude of the unsteady SRV loading was equal to approximately 20% of the time-averaged result for all investigated advance ratios.

INTERACTION WITH PROPELLER

In the second part of this chapter, it was shown by means of experiment how propeller interaction in side-by-side and one-after-another configuration, as typically found on eVTOL vehicles, impacts propeller performance in terms of thrust, power, in-plane forces and out-of-plane moments. Dependency of these results on relative propeller distances

d_x and d_y was analysed too to answer research question Q6. For the one-after-another configuration an extended blade element momentum model was used to predict the performance effects, which seemed to capture most interaction effects with sufficient accuracy.

For the side-by-side interaction case, interaction effects depend strongly on propeller angle of attack α_p and vary from weak interaction at small angles to strong interaction at larger angles. A large drop in rear propeller thrust and power of up to 30% was found for $\alpha_p = 90$ deg, depending strongly on advance ratio and lateral distance between the propellers d_y . With increasing lateral distance, the interaction effects became less pronounced. The dependency on advance ratio was found to be different for the force and moment components. At large angle of attack, the rear propeller experiences a reduced effective angle of attack due to the downwash of the front propeller. The interaction effects for the front propeller were small to negligible and likely resulted from a small upwash from the rear propeller. These detrimental interaction results for the rear propeller may be indicative for eVTOL operation with such propeller configuration in the last stages of transition from vertical flight to forward flight. Compensation of the lost thrust in such situation by increasing rotational speed of either the rear propeller or both front and rear propeller resulted in power penalties of 5% to 13% for the two propellers combined, again depending on the lateral distance.

The effects of interaction for the rear propeller in one-after-another configuration were also studied. For large axial distance d_x , when the front propeller slipstream is fully contracted, a maximum loss in thrust and power of up to 80% was observed for the configuration with full overlap. A dependency of the interaction on the swirl and thus rotation direction of the propellers was found. This was deduced from sudden changes in slope of the rear propeller thrust versus lateral distance. At small d_x , in the region of the front propeller slipstream contraction, a small increase in thrust for the rear propeller arose outside of the slipstream, likely due to an induced angle of attack by the slipstream. This is the only thrust increasing interaction mechanism found in this research for any downstream located propeller. Compensation of the lost thrust through a rotational speed increase of the rear propeller led to significant power penalties of up to 30% for the rear propeller alone. If this type of interaction occurs on an eVTOL vehicle, for instance caused by a sudden change of angle of attack, the interaction effects experienced by the rear propeller influences aircraft stability. This is not only caused by the thrust reduction and its associated moments but also by the generation of in-plane forces and out-of-plane moments that were measured as a result of this interaction.

The found interaction effects are demonstrative of propeller interaction on a wide range of eVTOL vehicles and other vehicles, but a strong dependency on the precise geometric layout was found, as well as on the thrust level in case of the side-by-side configuration. Interaction of the propellers with static parts on such vehicles like wings may be of great importance too. Furthermore, the Reynolds number and Mach number may be significantly different as these results were measured at relatively low speed with scale propellers. The presented results can serve as a validated starting point for specific analyses with more realistic geometry.

7

COMBINED INTERACTION WITH MAIN ROTOR AND WINGTIP

Sometimes propellers are not interacting with a single object, but encounter interaction from multiple sources, experiencing momentum sinks and sources, potential effects resulting in angle of attack and dynamic pressure changes, rotational flowfields and vortices. A special case where this occurs is the compound helicopter, and specifically the layout of the Airbus RACER compound helicopter concept that was shown in Fig. 1.8, which is the investigated example in this chapter. The pusher-propellers on this helicopter experience the flowfield at the tip of a box-wing, unlike the interaction with planar wings as discussed in Chapter 5. This is complemented by the interaction with an overhead main rotor. This configuration is studied in cruise condition in Section 7.1, where research questions 7.1 and 7.2 are addressed:

Q7.1: *How does the box-wing affect the loading and efficiency of the propellers on the compound helicopter configuration in cruise, with varying flap deflection and varying angle of attack and sideslip, and how is the lift and drag of the box-wing altered?*

Q7.2: *What role does the main rotor play in the loading on the propellers of the compound helicopter configuration in cruise?*

The hover condition changes the flowfield by the propellers dramatically as no freestream flow is present and the velocity field is induced by the main rotor and propellers. This results in an almost perpendicular inflow to the propeller axis. In Section 7.2 the interaction effects for the propellers are investigated to answer research question 8:

Q8: *What is the influence of the main rotor and box-wing on the loading on the propellers of the compound helicopter configuration in hover?*

The contents of this chapter have been adapted from Refs. [69–71].

The situation in hover was simplified and investigated with an in-house experiment for validation and to answer the following research question 9, treated in Section 7.3:

Q9: *How does wing distance and flap deflection influence the loading on a wingtip-mounted pusher-propeller subject to flow perpendicular to the wing planform?*

7.1. WINGTIP-MOUNTED PUSHER-PROPELLERS ON A COMPOUND HELICOPTER IN CRUISE

In this section propellers are studied experiencing a rotational flowfield, momentum sink, potential effects and vortices from an upstream box-wing and angle of attack changes from an overhead main rotor. This occurs on the compound helicopter configuration in cruise. These effects were studied by means of RANS CFD simulations of the various configurations depicted in Fig. 7.1, at the design cruise speed of 220 kts (113.2 m/s) [221]. In this condition, the main rotor and propellers operate at an advance ratio (defined as $V_\infty/(\omega R)$ with ω in rad/s) above 0.5.

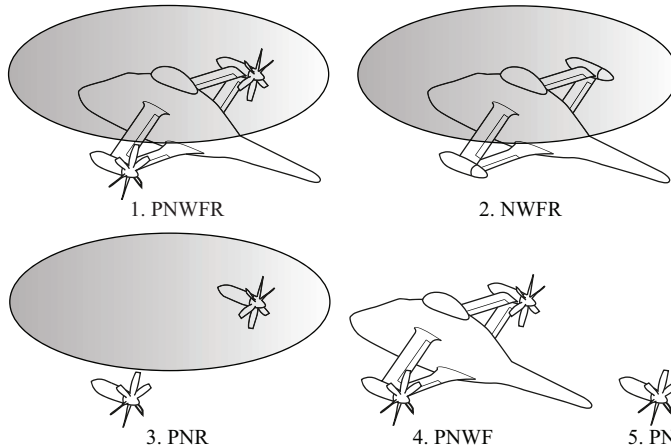


Figure 7.1: The five different simulated compound helicopter configurations including labels (P: propeller; N: nacelle; W: wing; F: fuselage; R: rotor), repeated from Fig. 3.23.

The model was simplified by removal of the tail unit and the time-averaged effect of the main rotor was introduced by an actuator-disk. Use of an actuator-disk for the main rotor reduces the computational cost significantly, which was the main reason for this choice as many conditions and configurations were studied in the project. Of course, one should consider that this setup neglects any of the transient effects that the main rotor blade tip vortices and wakes have on the propeller loading as described by Thiemeier et al. [137]. Furthermore, no interaction of the propeller on the main rotor loading is present as the actuator-disk loading is prescribed. A propeller close to the main rotor may affect the rotor flapping amplitude and bending moments due to its pressure field,

and as such the main rotor loading, as is known from the extensive experimental investigation of Bain and Landgrebe [139]. However, the actuator-disk loading includes the asymmetry occurring in the loading on the main rotor in forward flight between the advancing and retreating blade side and the radial non-uniformity present in the loading on rotors and as such represents the time-averaged effect of the main rotor on the flow-field accurately.

First, temporal and grid convergence results are presented in Section 7.1.1. Investigation of the aerodynamic interaction effects is split in Section 7.1.2 about the effects on propeller loading and flowfield and Section 7.1.3 about the effects on wing loading. At last, in Sections 7.1.4 and 7.1.5 the dependency of propeller loading on the wing flap deflection, and on angle of attack and sideslip are discussed respectively.

Note that a detailed interaction study by Frey et al. [222] has recently been published that takes the same approach as here by investigation of interaction effects through the removal of parts of the geometry. That study includes a simulated main rotor, active engine inlet and exhaust and nacelle cooling flow and uses an updated geometry of the Airbus RACER. Some comparisons are made in the next sections that are not included in the publications of this work (Refs. [69, 70]).

7.1.1. TEMPORAL AND GRID CONVERGENCE

Since only the time-averaged effect of the main rotor was modelled with the actuator disk, solutions of the aerodynamic loading were expected to be in general periodic with the propeller blade passage frequency. In order to obtain such periodic solutions for the cruise condition, first a steady solution was obtained on a coarse grid. This was then used as initial condition for time dependent simulations on the coarse, medium refined and at last the fine grid with a timestep equivalent to 1 deg of propeller rotation, using the solution from one grid level down as initial condition. The coarse and medium refined grids were obtained by structured grid coarsening, reducing the number of cells by a factor of 8.

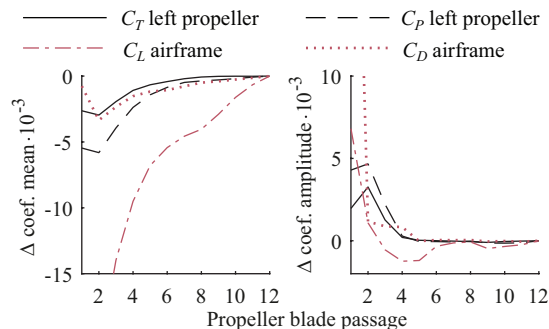


Figure 7.2: Convergence plots for the cruise condition obtained by calculating the mean and amplitude for each blade passage, and subtracting the last value.

Table 7.1: Grid convergence study results in the cruise condition based GCI and Richardson extrapolation. The airframe is composed of the fuselage, box-wings and nacelles.

	left propeller		right propeller		airframe	
	thrust	power	thrust	power	lift	drag
p	3.2	4.9	3.0	3.6	2.4	2.1
U_{ϕ_1} (%)	0.1	0.0	0.2	0.0	1.4	6.9
E_{ϕ_1} (%)	0.2	0.0	0.4	0.1	1.6	6.2

In Figure 7.2 convergence of the most important aerodynamic loading quantities on the fine grid is shown by taking the mean and amplitude of the quantities for each blade passage, subtracted by their values for the last blade passage. The selected quantities are the left propeller thrust coefficient C_T and power coefficient C_P (the right propeller convergence is very similar), and the airframe lift coefficient C_L and drag coefficient C_D (the complete body without the propeller blades is referred to as the *airframe*). For the cruise condition, sufficient convergence to a periodic solution was obtained after two propeller rotations or 12 blade passages on the fine grid. Especially the airframe lift and drag required some time to converge due to flow separation from the exhausts on the rear of the fuselage, since no active flow was simulated through the exhausts.

A summary of the grid-dependent uncertainties is given in Table 7.1 in terms of grid convergence index U_{ϕ_1} and Richardson extrapolation E_{ϕ_1} for the fine grid. The uncertainties estimated for the time-averaged propeller performance quantities are relatively small. For the airframe lift and drag, containing the fuselage, box-wings and nacelles, somewhat larger uncertainties are estimated. This is mainly due to earlier mentioned flow separation from the exhausts.

7

7.1.2. INTERACTION EFFECTS ON PROPELLER LOADING AND FLOWFIELD

In the cruise condition, the propellers experience the rotational flowfield at the wingtip and are close to the main rotor slipstream. In Fig. 2.13 this situation was sketched schematically and in Fig. 7.3 the flowfield through the left propeller is visualised by means of streamtraces with velocity contours. The respective influence of the wings and main rotor on the propeller performance is treated in this section, while the upstream influence of the propellers on the wings is discussed in the following section. Mainly results for the left propeller are given, since the results in this flight condition are qualitatively similar for both propellers. All results in this section are at zero angle of attack and sideslip with zero flap deflection, which results in positive lift on the box-wing.

In Table 7.2 the left propeller performance is given for the PNR and PNWFR configuration relative to the performance at zero angle of attack for the PN configuration. The different configurations were depicted in Fig. 7.1. For the PN configuration, the blade pitch was trimmed to a specific thrust target. For the PNR configuration, this blade pitch angle was maintained to see directly the effect of the main rotor slipstream on the propeller performance. However, for the PNWFR configuration the blade pitch angle was trimmed by a series of simulations at a reduced grid, in order to arrive at a thrust close to the initial target. The rotational speed and freestream velocity were maintained for both configurations. From the PNR configuration results, conclusions can be drawn on the ef-

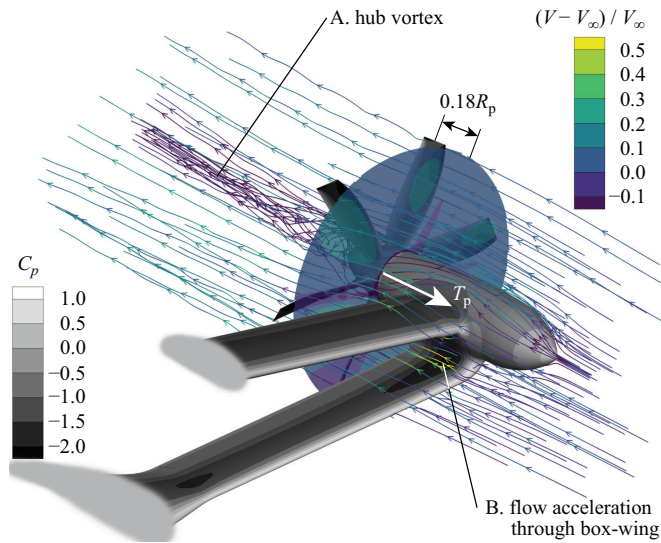


Figure 7.3: For the PNWFR configuration in cruise, the flowfield is visualised through the left propeller, with velocity contours on streamtraces and on a plane $0.18R_p$ upstream of the propeller. Only the left box-wing, nacelle and propeller are shown, marked with C_p contours.

fect of the main rotor on the propeller performance. In this configuration the propeller thrust T and shaft power P are increased as the propeller experiences a non-zero angle of attack from the potential effect of the main rotor and its slipstream. However, note that no main rotor slipstream impingement on the propeller disk occurs. The mechanism behind this thrust increase with angle of attack was explained in Section 4.2. The propulsive efficiency η_p is slightly increased as well by the same mechanism. This main rotor effect is less for the right propeller, since it experiences a reduced downwash on the retreating blade side of this clockwise turning main rotor, confirming the findings by Wentrup et al. [136].

From the comparison of PNR and PNWFR configuration results, conclusions can be drawn on the effect of the box-wing on the propeller performance. For the PNWFR configuration, a reduction in blade pitch angle was required to approximately maintain the thrust target. The propulsive efficiency is significantly increased by 7% as a result of installation. As it was shown that for the PNR configuration the propulsive efficiency was slightly increased as well, a part of this 7% increase is potentially a result of the angle

Table 7.2: Time-averaged left propeller performance for the PNR and PNWFR configurations relative to the PN configuration in cruise.

	PNR	PNWFR
ΔT	+2.9%	+0.7%
ΔP	+2.2%	-7.8%
$\Delta \eta_p$	+1.0%	+7.0%

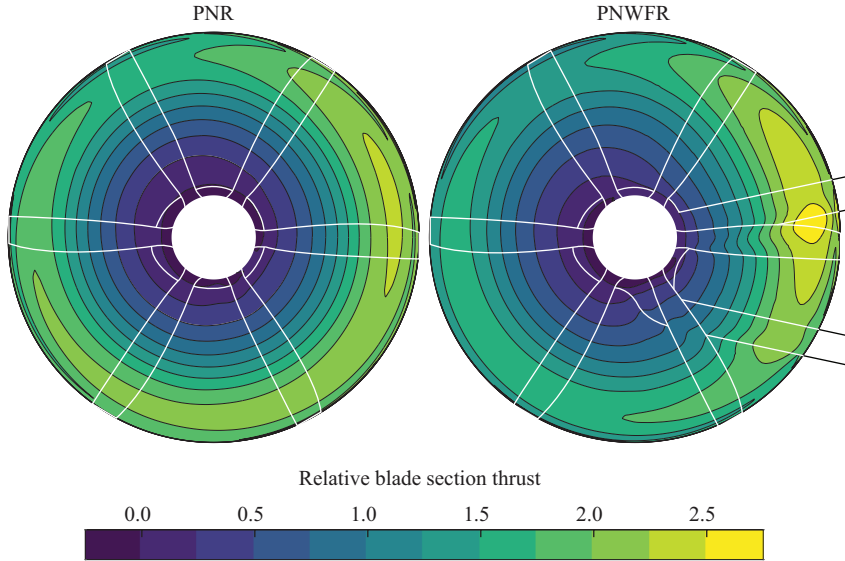


Figure 7.4: The blade section thrust relative to the time-averaged blade thrust is plotted for each circumferential position of the left propeller in cruise. The effect of the wings is shown by means of comparison of the PNR and PNWFR configuration.

7

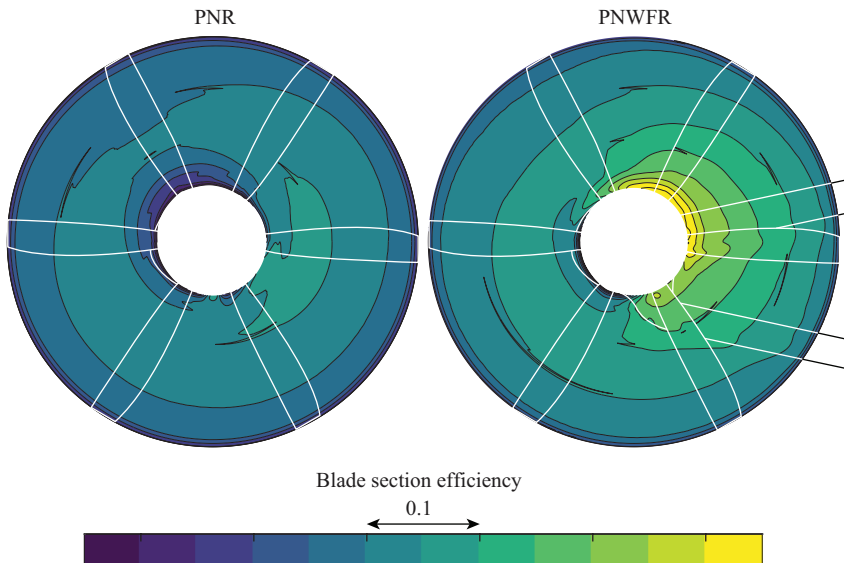


Figure 7.5: Blade section efficiency $T'V_{\infty}/P'$ corresponding to Fig. 7.4.

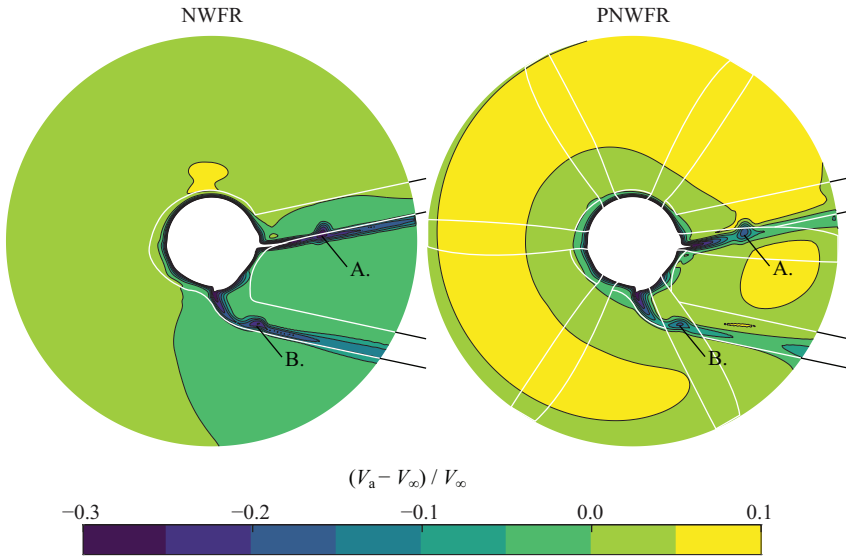


Figure 7.6: Time-averaged axial velocity component is plotted on the plane visualised in Fig. 7.3, upstream of the left propeller in cruise. The effect of the propeller is shown by means of comparison of the NWFR and PNWFR configuration. Annotation A. and B. indicate the effect of the upper and lower wing flap edge gap.

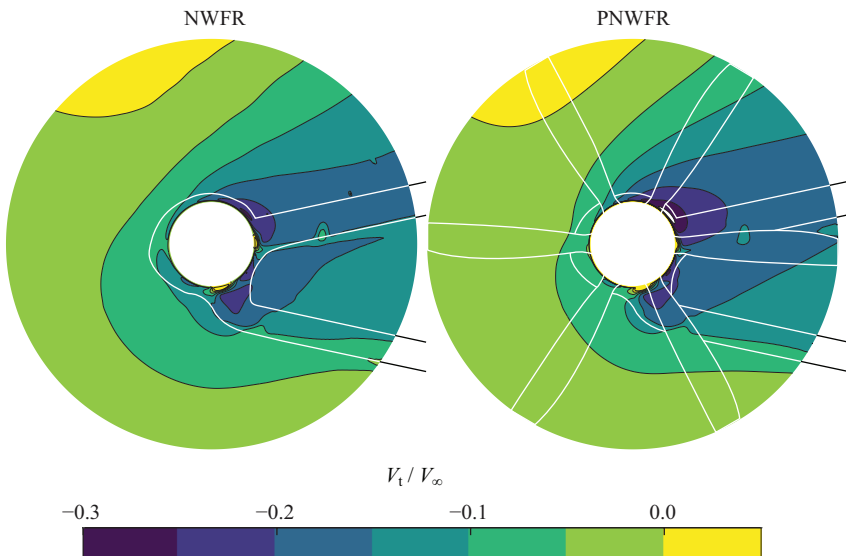


Figure 7.7: Time-averaged tangential velocity component is plotted corresponding to Fig. 7.6.

of attack induced by the main rotor, although as the main rotor downwash also influences the wing loading, these effects are not independent. This is further elaborated on in Section 7.1.4.

To investigate where the differences in propeller performance for the PNR and PNWFR configuration originate, in Fig. 7.4 contour plots of the blade section thrust are shown for the left propeller. The white outline of the upstream box-wing enables correlation of the thrust variation with the wing location. In the PNR configuration the propeller blades experience a sinusoidal thrust variation in time, which is typical for a propeller at angle of attack. The maximum blade thrust is experienced when the blade moves up, because then the angle of attack effect of the main rotor downwash results in the largest blade section angle of attack, as was shown before in Figs. 4.30 and 4.31 for the XPROP propeller. This confirms the observation by Wentrup et al. [136] for the same compound helicopter configuration. For the PNWFR configuration, additional non-uniformities are present. A maximum in blade section thrust is found around blade phase angle $\varphi = 180$ deg as defined in Fig. 7.11. This maximum can be correlated to the upper wing. A sudden increase in thrust is also noticeable in the proximity of the lower wing. Both effects are explained below.

The flowfield upstream of the propeller is plotted in Figs. 7.6 and 7.7 in terms of axial component V_a and tangential component V_t . The velocity components are defined in Fig. 2.12 with the tangential component positive in the direction of propeller rotation and they are plotted on the plane that was visualised in Fig. 7.3. Contour plots for the NWFR and PNWFR configuration are given, so without and with the propeller present. At the location of the wings in Fig. 7.4 (the peaks in thrust), a clear velocity deficit of the wake of the wings can be distinguished in the axial velocity field. Especially noticeable are the deficits at the location of the flap edge gaps indicated by annotation A. and B in Fig. 7.6. The axial velocity deficit results in a local advance ratio reduction and thus thrust increase. Comparing the contour plots for the NWFR and PNWFR configuration, the upstream acceleration of the flow induced by the propeller loading is clearly visible.

Pusher-propellers mounted at the tip of planar wings are associated with beneficial interaction effects in terms of propulsive efficiency, as is known from i.e. Refs. [15, 34–36] and from the results in Section 5.3. To show where the propulsive efficiency increase is coming from between the PNR and PNWFR configuration, in Fig. 7.5 a comparison of the blade section efficiency over the propeller disk is given. This is defined as the ratio of blade section contribution to thrust T' and blade section contribution to power P' , multiplied by the freestream velocity magnitude V_∞ . Although over the entire disk the blade section efficiency is raised for the PNWFR configuration compared to the PNR configuration, especially on the inboard side of the propeller disk and for blade sections at low radii a large increase can be noticed, as explained below.

The distribution of efficiency increase corresponds directly to the negative tangential velocity field shown in Fig. 7.7, which is resulting from the pressure differences between the pressure and suction sides of the wings. The negative tangential velocity component increases the propeller blade section angle of attack and tilts the section lift more in the direction of the thrust and less in the tangential direction, reducing the contribution to the torque or shaft power. Comparing the contour plots for the NWFR and PNWFR configuration, a small upstream effect of the propeller can be noticed by an increase of the

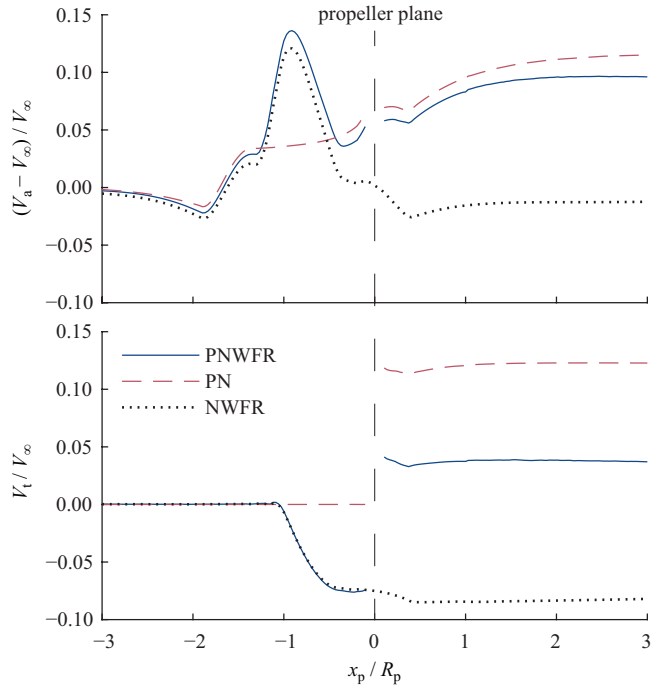


Figure 7.8: For three configurations, PNWFR, PN and NWFR, the radially and circumferentially averaged axial and tangential velocity distribution through the left propeller approximate streamtube is plotted in cruise. The streamtube was approximated by a cylinder of radius equal to the propeller radius from 3 radii upstream to 3 radii downstream of the propeller. Coordinate x_p is defined in Fig. 2.12.

7

negative tangential velocity. Since a propeller does not induce an upstream tangential velocity field, this change in tangential velocity is likely a result from a change in wing loading and its induced tangential velocity field.

To qualitatively show how the aerodynamic interactions change the flowfield through the propeller, in Fig. 7.8 velocity components through the approximated streamtube of the left propeller are plotted for the PNWFR, PN and NWFR configuration. The streamtube is approximated by a cylinder with a radius equal to the propeller radius and quantities are time- and space-averaged over disks from $3R_p$ upstream to $3R_p$ downstream of the propeller. For the PNWFR and NWFR configuration, a large peak in axial velocity can be noticed upstream of the propeller, which is a result of the acceleration of the flow around the wings, since the streamtube intersects part of the wings. This acceleration is also visible in the velocity contours on the streamtraces in Fig. 7.3 and in the reduced pressure coefficient on the wing and nacelle surface, especially in between the upper and lower wing as indicated with annotation A. The axial velocity increase is slightly higher for the PNWFR configuration because of the induced axial velocity by the propeller. Comparing the PNWFR and PN configuration, the axial velocity component just upstream of the propeller is lower on average for the installed case, likely due to the

wake of the wings and change in flow direction to more tangential flow. The difference in axial velocity upstream of the propeller impacts the slipstream of the propeller: The axial velocity component levels off to a slightly lower value for the PNWFR configuration compared to the PN configuration.

Looking at the tangential velocity plot in Fig. 7.8, a growth in negative tangential velocity component towards the propeller is present for the PNWFR and NWFR configuration, induced by the wing. Comparing the PNWFR and PN configuration results downstream of the propeller, the tangential velocity component is considerably lower for the installed case. Comparing the NWFR and PNWFR configuration results, the tangential velocity field around the wingtip has changed direction due to the propeller. As the tangential velocity magnitude is lower, the tangential kinetic energy in the slipstream has been reduced by the interaction.

7.1.3. INTERACTION EFFECTS ON WING LOADING

From Figs. 7.6 through 7.8 it is clear that part of the wing experiences a different flowfield as a result of the propellers, in particular in axial velocity. Therefore, it can be expected that the wing loading may also change. As there is a finite number of propeller blades and the propellers rotate, they also introduce time-dependent variations in wing loading. To identify changes in wing lift and drag by the propellers, in Fig. 7.9 the time-averaged spanwise wing loading is plotted for the left wing half. Note that the right wing half experiences higher wing lift due to the reduced main rotor downwash on that side [136], but the interaction phenomena are similar. The negative angle of attack induced by the main rotor and the asymmetry of this effect between the left and right box-wing is also clearly highlighted in the study of Frey et al. [222] by comparison of a simulation with and without main rotor.

In Fig. 7.9, results for the NWFR and PNWFR configurations are shown, including the time-dependent variation indicated by the shaded areas. The propellers introduce locally a slight reduction in upper wing lift and larger increase in lower wing lift. Wing drag is increased locally for the upper and lower wing, resulting in a net reduction of lift-over-drag ratio. At spanwise locations away from the region upstream of the propeller where it increases the axial velocity, the effect of the propeller reduces. It is shown by Frey et al. [222] that the increase in lower wing lift is a result of the suction of the propeller and the contracting streamtube in combination with the fuselage, inducing an increase in effective angle of attack for the lower wing.

In Fig. 7.10 the static pressure is plotted at an instance in time on a plane cutting through the wings and one of the propeller blades. The region of low pressure on the suction side of the propeller blade extends to the upstream wings and has a time-varying impact on the pressure distribution of the wings, dependent on the propeller orientation. While the blade rotates, its pressure field results in increased suction on the pressure side of the wing profiles, followed by increased suction at the suction side, especially near the trailing edge. This happens at different instances in the blade rotation for the upper and lower wings due to their vertical spacing.

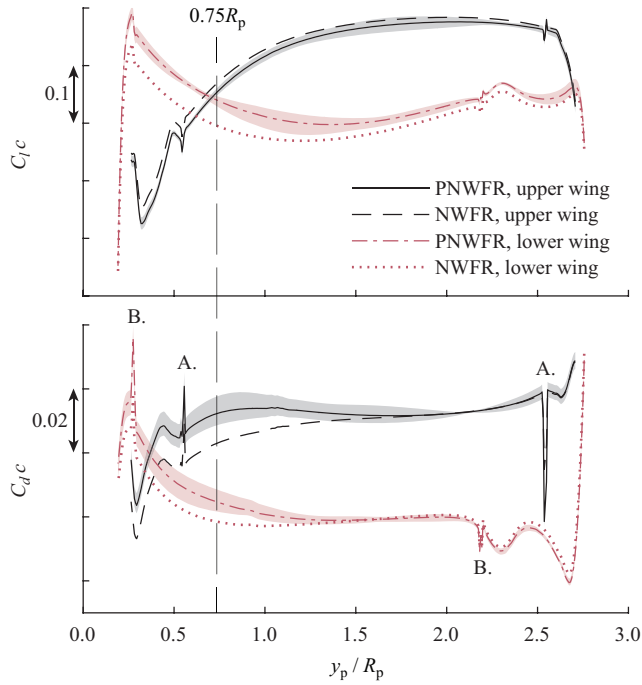


Figure 7.9: Time-averaged wing loading comparison between PNWFR and NWFR configuration for the left wing in cruise, with coordinate y_p as defined in Fig. 2.12. Shaded area indicates time-variation. Annotation A. and B. indicate the effect of the upper and lower wing flap edge gap.

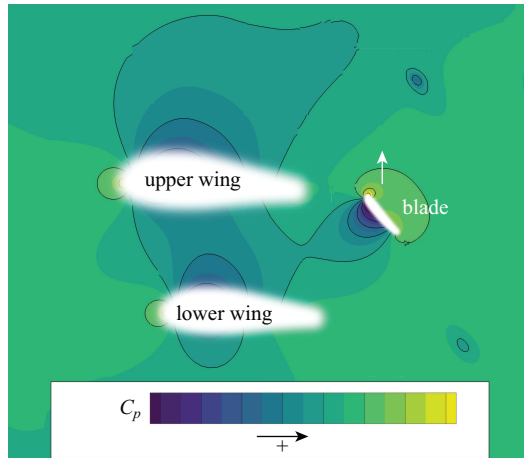


Figure 7.10: The upstream effect of the left propeller on the box-wing in cruise for the PNWFR configuration is highlighted by contours of instantaneous C_p on a plane cutting the wings and a propeller blade at $y_p = 0.75R_p$ as indicated in Fig. 7.9.

7.1.4. EFFECT OF WING LIFT ON PROPELLER LOADING

In this section the effect of wing lift on the propeller loading is investigated through flap deflection. All four wing-halves were equipped with trailing edge flaps. By increasing the flap deflection, the wing lift increases, which allows unloading of the main rotor. As the wing loading affects the propeller performance and also the main rotor loading through this unloading mechanism, the balance between the wing lift and main rotor lift is an important performance parameter in flight. Therefore, in this section the effect of flap deflection and thus wing lift on the propeller performance is investigated. In Fig. 7.12 the left propeller thrust and power are plotted over a blade passage starting from the orientation defined in Fig. 7.11 at $\varphi = 0$ deg. The thrust and power are plotted relative to the time-averaged thrust and power for $\delta_f = 0$ deg. For the three flap deflections the blade pitch was adjusted to achieve the same time-averaged thrust. A small peak-to-peak fluctuation of 1.5% to 2.5% in thrust is present. This fluctuation increases with increasing flap deflection. A clear effect of the wingtip vortex energy recovery can be noticed in the propeller power curves, as with increasing flap deflection the time-averaged power reduces. As flap deflection increases wing lift, the pressure difference between the upper side of the upper wing and lower side of the lower wing increases and thus the tangential velocity field that forms around the wingtip increases. Therefore, the required shaft power reduces with increasing flap deflection. Following the fluctuations in thrust, the fluctuations in power also increase with increasing flap deflection and are of similar magnitude.

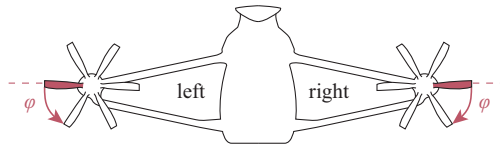


Figure 7.11: Rear view sketch of compound helicopter defining the blade phase angle φ .

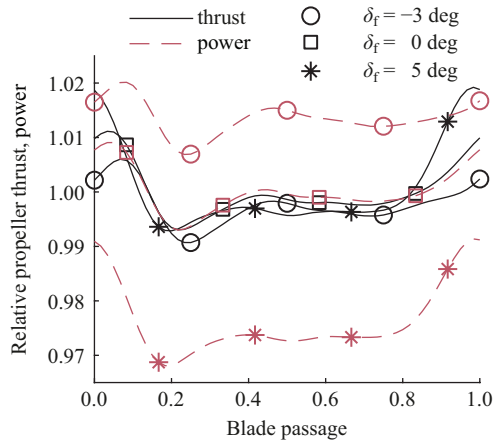


Figure 7.12: Left propeller performance relative to the time-averaged performance with $\delta_f = 0$ deg for the PNWFR configuration in cruise. The zero blade passage orientation is defined in Fig. 7.11 at $\varphi = 0$ deg.

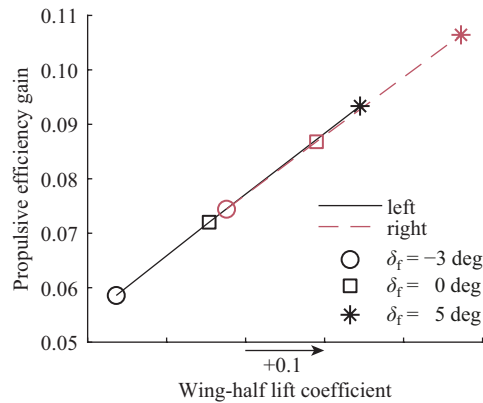


Figure 7.13: Propeller propulsive efficiency gain of propeller installation versus the wing-half lift for the PNWFR configuration in cruise.

Figure 7.13 highlights the wingtip vortex recovery effect, showing the gain in propeller propulsive efficiency with respect to the isolated propeller efficiency at equal thrust. This gain is plotted for the left and right propeller against the lift coefficient of the corresponding wing-half. The change in lift coefficient was achieved by flap deflection. Clearly, installation results in a considerable propulsive efficiency gain for both propellers, becoming larger with increasing wing lift or flap deflection. A similarly linear increase in propulsive efficiency or reduction in shaft power for constant thrust with wing lift was shown in Ref. [35] for a planar wing. Increasing the wing lift will allow further unloading of the main rotor and therefore the ratio of wing lift to main rotor lift has a large influence on the efficiency of the propellers.

The right propeller experiences a larger increase in propulsive efficiency than the left propeller, as the lift of the right box-wing is larger. As mentioned previously, the lift decreasing effect of the main rotor on the right box-wing was less than on the left side. As the main rotor has a lift decreasing influence on the wing and the wing lift has an efficiency increasing influence on the propeller, the net effect of the main rotor on the propeller is most likely efficiency decreasing, even though in Table 7.2 it was shown that the induced angle of attack by the main rotor for the propeller increased efficiency when the wing was absent. For constant blade pitch angle, Frey et al. [222] showed that the left and right propeller thrust indeed increased by removal of the main rotor by 4.6% and 1.5% respectively, and the power increased by a lesser amount of 4.0% and 1.3% respectively.

7.1.5. EFFECT OF ANGLE OF ATTACK AND SIDESLIP ON PROPELLER LOADING

Because of the strong aerodynamic interaction between the propellers and the box-wings, an investigation of the interaction for off-design conditions is essential to understand the flight performance and dynamics of this vehicle specific and of a wingtip-mounted pusher-propeller configuration in general. The effects of angle of attack and sideslip were studied with the PNWF and PN configurations, leaving the main rotor effect out of this study for simplification. In Fig. 7.14 the left propeller performance is plotted as function of angle of attack. Results are made relative with the performance at zero angle of attack for the PN configuration. For the PN configuration, the thrust and propulsive efficiency increase with angle of attack, symmetrically around zero angle of attack. For the PNWF configuration, the wing introduces an increase in thrust and efficiency at zero angle of attack due to the tangential velocity field and wing wakes. Since the strength of the tangential velocity field is correlated to wing lift and wing lift increases with angle of attack, an increase in angle of attack increases thrust and efficiency more than for the isolated propeller. The symmetry around zero angle of attack is therefore also lost as a result of the aerodynamic interaction with the wing.

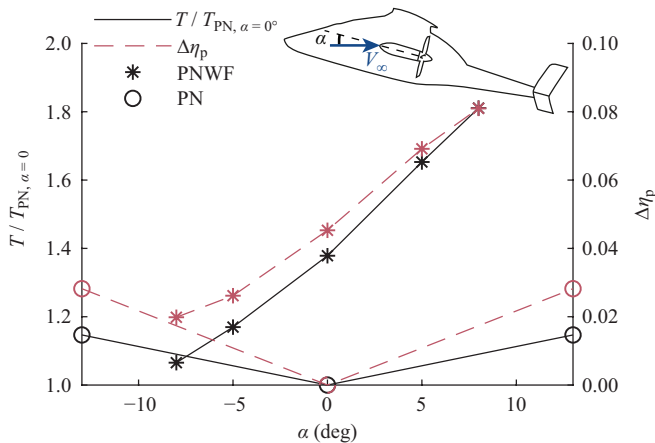


Figure 7.14: Left propeller thrust T and propulsive efficiency η_p are plotted against angle of attack α at constant blade pitch angle for $V_\infty = 220$ kt (113.2 m/s). A comparison is shown between the PNWF and PN configuration and quantities are with respect to PN configuration quantities at zero angle of attack.

To show the effects of sideslip, the right propeller was studied with a positive sideslip angle to avoid significant fuselage interaction. In Fig. 7.15 the right propeller performance as function of sideslip is plotted for a reduced manoeuvring cruise speed of $V_\infty = 140$ kt (72.0 m/s). Again at zero sideslip the thrust and efficiency are higher for the PNWF configuration due to the positive wing lift. This increased thrust and efficiency due to the wing is gradually reduced relative to the PN configuration due to reduction of wing lift with sideslip. Note that the propeller is operating at a different advance ratio, such that with increasing angle of attack the efficiency for the PN configuration reduces already for small angles, opposite to the results of Fig. 7.14.

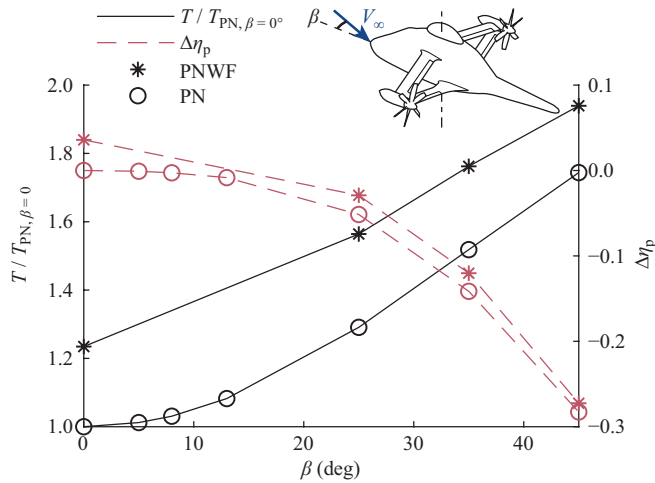


Figure 7.15: Right propeller thrust T and propulsive efficiency η_p are plotted against sideslip β at a reduced cruise speed for manoeuvring of $V_\infty = 140$ kt (72.0 m/s) at constant blade pitch angle. A comparison is shown between the PNWF and PN configuration and quantities are with respect to PN configuration quantities at zero sideslip.

7.2. WINGTIP-MOUNTED PUSHER-PROPELLERS ON A COMPOUND HELICOPTER IN HOVER

This part treats the hover condition for the compound helicopter CFD model of the previous section. In the hover condition, as no freestream flow is present, the flowfield is fully induced by the main rotor and propellers. This changes the inflow to the propellers considerably compared to the cruise condition of the previous section, as the propellers operate in the slipstream of the main rotor, resulting in a very skewed inflow. First again, temporal and grid convergence results are presented in Section 7.2.1. In the second Section 7.2.2 the aerodynamic interaction effects on propeller loading and flowfield are investigated.

7.2.1. TEMPORAL AND GRID CONVERGENCE

The hover condition required a different recipe to avoid divergence in the solver and to reach periodic behaviour with the blade passage frequency. A steady solution on the fine grid was obtained from steady solutions on the medium refined and coarse grid. This was used as initial condition for a time dependent simulation on the fine grid, advancing quickly in time with a timestep equivalent to 10 deg of propeller rotation. It was found that to reach periodic behaviour for this flight condition, many propeller rotations were required. At last, a simulation on the fine grid with a timestep equivalent to 1 deg of propeller rotation was used to obtain the final solution.

In Fig. 7.16 convergence of the most important aerodynamic loading quantities on the fine grid is shown, similar to Fig. 7.2 for the cruise condition. Only convergence of the part of the simulation with a timestep equivalent to 1 deg is shown. In the hover

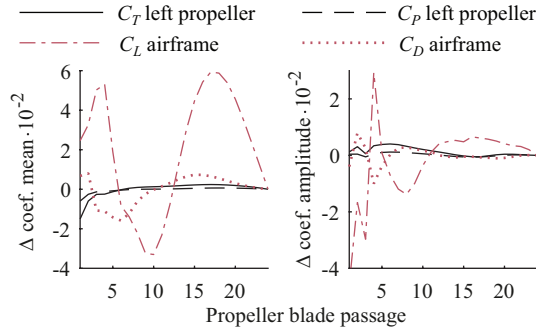


Figure 7.16: Convergence plots for the hover condition obtained by calculating mean and amplitude for each blade passage, and subtracting last value.

condition, the flowfield is almost entirely induced by the main rotor and the propellers, resulting in largely separated flow from the leading and trailing edges of the wings due to the very large inflow angle by the main rotor downwash. Note that for this condition, the lift and drag coefficient are defined with the theoretical downwash velocity V_d in the farfield of the main rotor based on momentum theory [204]:

$$V_d = \sqrt{\frac{2T_{mr}}{\rho_\infty \pi R_{mr}^2}} \quad (7.1)$$

7

In the convergence plots poor convergence with the blade passage frequency is observed for the mean of the airframe lift and to a lesser extent the drag. Instead, a fluctuation with a much lower frequency is observed, likely related to the time variation of the flow separation. However, the amplitude does show convergence. For the propeller coefficients better convergence is obtained.

A summary of the grid-dependent uncertainties for the hover condition is given in Table 7.3 in terms of grid convergence index U_{ϕ_1} and Richardson extrapolation E_{ϕ_1} for the fine grid. The uncertainties estimated for the time-averaged propeller performance quantities are again relatively small. The larger uncertainties for the airframe lift and drag are thought to be a result of the earlier mentioned flow separation. Note that the large GCI uncertainty for the airframe drag in the hover condition is a result of the very low apparent order of 1.0, which may be caused by the coarse grid being outside of the asymptotic range. The Richardson extrapolation uncertainty estimate E_ϕ is significantly lower for this quantity. Overall, as the focus of this study is on the propeller performance, the temporal and grid convergence of the simulations was deemed sufficient.

Table 7.3: Grid convergence study results in the hover condition based GCI and Richardson extrapolation. The airframe is composed of the fuselage, box-wings and nacelles.

	left propeller		right propeller		airframe	
	thrust	power	thrust	power	lift	drag
p	1.6	2.7	3.1	3.0	0.5	1.0
U_{ϕ_1} (%)	0.7	0.3	0.1	0.2	- [¶]	44.2 [§]
E_{ϕ_1} (%)	0.4	0.5	0.1	0.4	2.3	11.1

[¶]Oscillatory convergence observed

[§]Large GCI uncertainty due to very low apparent order p

7.2.2. INTERACTION EFFECTS ON PROPELLER LOADING AND FLOWFIELD

The main rotor plays only a minor role in the aerodynamic interactions experienced by the propellers in the cruise condition. However, the lack of shielding of the propellers allows for a significant main rotor interaction at low airspeed and particularly in the hover condition where the main rotor downwash impinges on the propellers, as was sketched in Fig. 2.14. The flowfield through the left and right propeller is visualised in Fig. 7.17 for the PNWFR configuration by streamtraces with velocity contours and this figure indicates the large angle of attack experienced by the propellers.

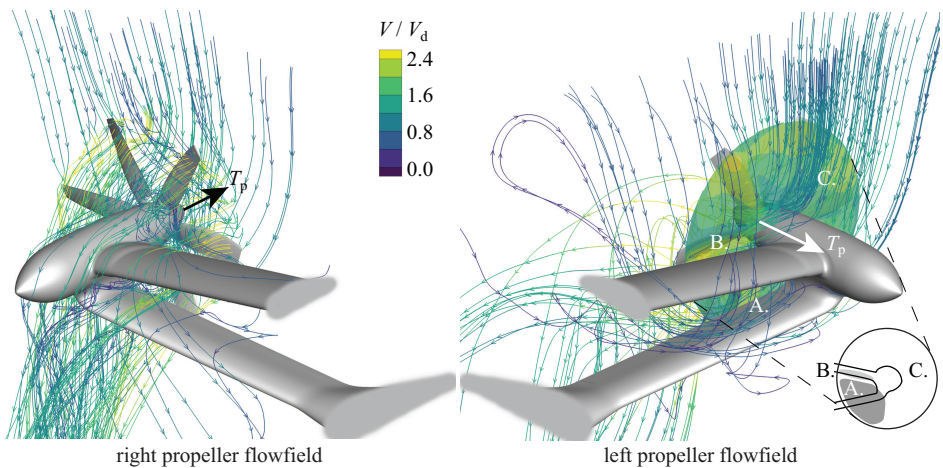


Figure 7.17: For the PNWFR configuration in hover, the flow through the propellers is visualised, with velocity contours on streamtraces and on a plane $0.18R_p$ upstream of the left propeller. The fuselage is not shown. Annotation A. indicates the wake of the wings and nacelle, B. main rotor downwash deflected by upper wing and C. the area undisturbed by the wings.

Note that, in order to counter the torque of the main rotor, the right propeller blade pitch angle is set to produce a reverse thrust in the hover condition. This is the investigated trimming strategy, although other strategies can be thought of where the right propeller produces zero or positive thrust and the main rotor thrust vector is tilted. An example of a different strategy is illustrated by layout of the Fairey Gyrodyne from Fig. 1.7, which features only one propeller for counter-torque purposes.

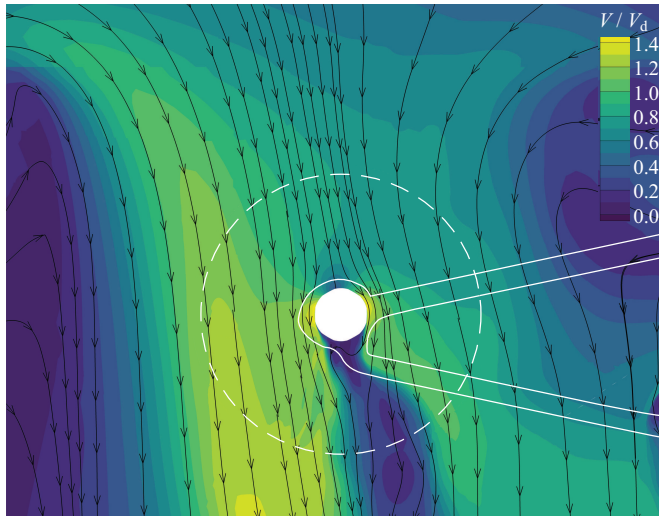


Figure 7.18: The velocity field in a plane through the left propeller in hover is shown for the NWFR configuration, so without propeller present.

Not only the propellers but also the wings experience the very large negative angle of attack due to the main rotor downwash, resulting in a net download, as was also shown by Lynn [140]. This resulted in the choice of a box-wing design for the Airbus RACER, in order to reduce the overall surface affected by the downwash. It can be seen that the wings introduce additional disturbances to the inflow of especially the left propeller with unknown impact on the propeller loading. Since the right propeller is producing reverse thrust, the wings are in its slipstream, and the effect of the wings on this propeller are likely different. Because of these unknowns, the impact of this complex interactional flow on the propeller performance and unsteady aerodynamic loading was investigated.

To further illustrate the flowfield experienced by the left propeller, in Fig. 7.18 the velocity magnitude is plotted with streamlines on a plane through the propeller for the NWFR configuration, so without propellers present. The propeller will experience a non-uniform distribution of downwash by the main rotor. Furthermore, an area of reduced velocity on the lower side of the nacelle can be distinguished. This wake is formed because the nacelle is shielding this area from the main rotor downwash. Considering that the wake is more pronounced on the inboard side of the nacelle, the shielding of the main rotor downwash by the wings likely also plays a role in the development of this wake. The flowfield in this plane at the location of the right propeller is very similar, since the main rotor loading is equal on both sides in the hover condition. The main difference is the out-of-plane swirl component introduced by the main rotor, which cannot be observed in this figure.

To establish a quantitative indication of the aerodynamic interaction effects, simulations were performed with the propeller-nacelle-main rotor configuration PNR and nacelle-wing-fuselage-main rotor configuration NWFR and were compared to results

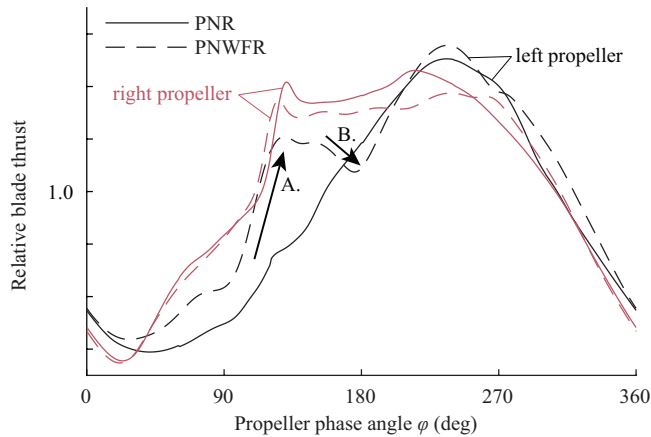


Figure 7.19: Blade thrust is plotted relative to the time-averaged blade thrust during a full rotation in hover for the PNR and PNWFR configuration. Phase angle φ is defined in Fig. 7.11 and the quantities are plotted divided through the PNWFR time-averaged value. Annotation A. indicates the effect of the wake of the wings and nacelle and B. the effect of the main rotor downwash deflected by the upper wing.

of the complete PNWFR configuration. Differences in integral propeller loading were found: Although the blade pitch angle and all other operating conditions were kept constant between the PNR and PNWFR configuration, for the left propeller the thrust in the PNWFR configuration was found to be 10.5% higher. This difference is therefore likely a result of the role the wings play in the interaction. The thrust-over-power ratio T/P for the left propeller in the PNWFR configuration was slightly reduced, although this could be directly a result of the increased thrust. Contrary, for the right propeller the thrust was 1.5% lower in the PNWFR configuration and the thrust-over-power ratio did not significantly change between the two configurations.

In order to investigate the differences between the propeller blade loading for the PNR and PNWFR configuration, in Fig. 7.19 the blade thrust evolution over a complete rotation is plotted for the left and right propeller, both relative to the time-averaged blade loading for the PNWFR configuration. For the left propeller the peak-to-peak variation is approximately equal to 60% of the maximum required thrust in hover for counter-torque (left propeller 100% thrust, right propeller 0% thrust), but note that this plotted case is not the maximum thrust requiring case. In general, the loading evolution is approximately sinusoidal for both propellers in both configurations. The phase and amplitude of the PNR and PNWFR result are very similar for both propellers. Note that although for the PNR configuration no wings and fuselage are present, the blade loading evolution is not perfectly sinusoidal for either propeller, which is normally expected for a propeller at angle of attack. This is likely related to the non-uniformity in the main rotor downwash that was illustrated in Fig. 7.18. When the wings are present, for the left propeller a significantly increased thrust is noticeable in between $\varphi = 90$ deg and 160 deg, indicated by annotation A., after which a relative reduction of thrust occurs indicated by annotation

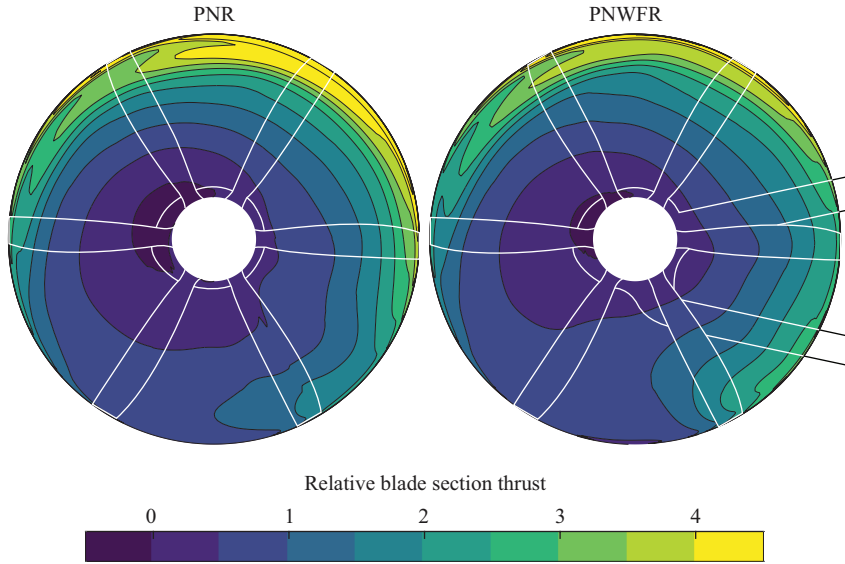


Figure 7.20: The blade section thrust relative to the time-averaged blade thrust is plotted for each circumferential position of the left propeller in hover. The effect of the wings is shown by means of comparison of the PNR and PNWFR configuration at equal blade pitch angle.

7

B. For the right propeller the differences between the PNR and PNWFR configuration results are very small. This is thought to be, because the wings are in the slipstream of the propeller and do not significantly disturb the inflow to the propeller.

For the left propeller the differences between the PNR and PNWFR configuration are larger than for the right propeller and therefore require further investigation. Figure 7.20 allows correlation of the thrust variation with the wing location for the left propeller through contour plots of the blade section thrust for the PNR and PNWFR configuration. This figure should be viewed alongside Figs. 7.21 and 7.22, which show a comparison of the axial and tangential velocity distribution for the NWFR and PNWFR configuration, so without and with propeller respectively. These contours are plotted on the plane visualised in Fig. 7.17 (right) just upstream of the left propeller, when seen from behind. Note that in this figure also a front view sketch is made of the propeller disk and a division is made in three zones annotated A., B. and C. An explanation of the propeller loading for each zone is given in the following paragraphs.

In zone A. the propeller in the PNWFR configuration draws air from the wake of the nacelle and wings that was made visible in Fig. 7.18. In Fig. 7.21 indeed an almost zero axial velocity component can be observed in this area when the propeller is not present in the NWFR configuration. The almost static inflow condition results in a large angle of attack for the propeller blade sections and thus high thrust, explaining the sudden thrust increase from $\phi = 90$ deg to 160 deg compared to the PNR configuration. In Fig. 7.21 a peak in axial velocity for the PNWFR configuration is visible in this area, induced by the

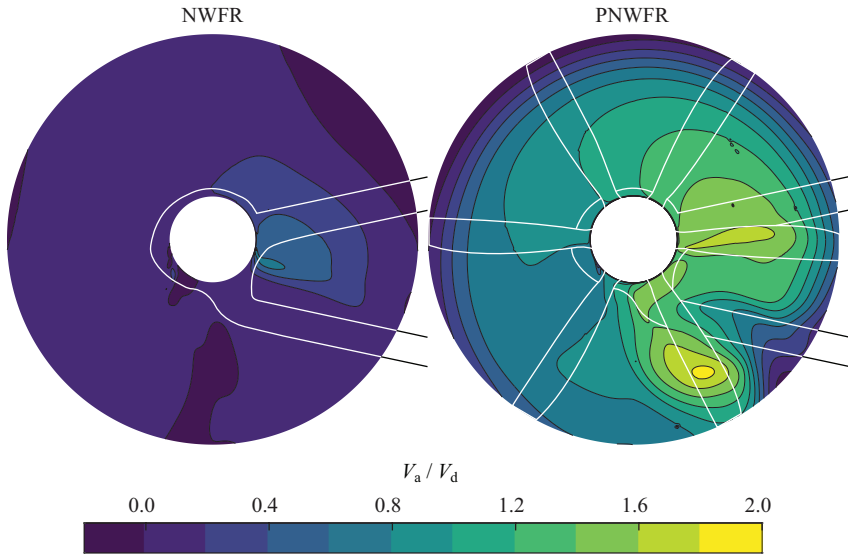


Figure 7.21: Time-averaged axial velocity component is plotted on the plane visualised in Fig. 7.17, upstream of the left propeller in hover. The effect of the propeller is shown by means of comparison of the NWFR and PNWFR configuration.

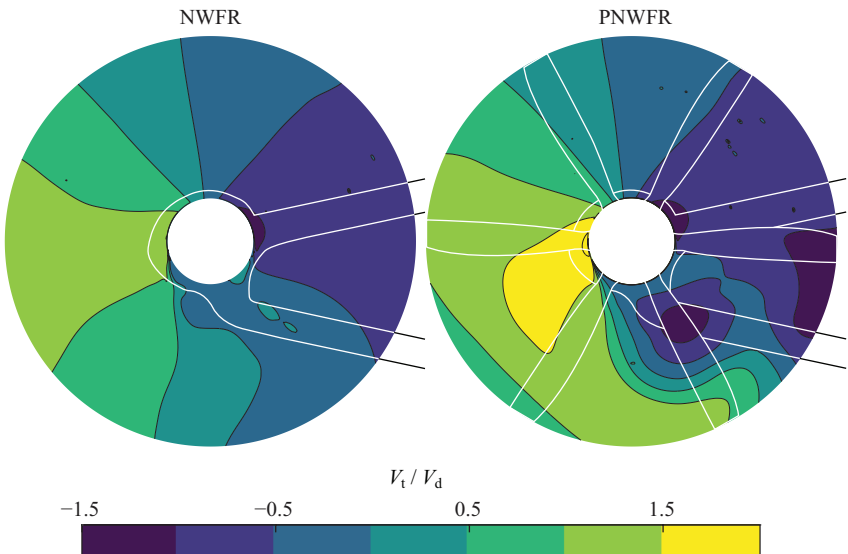


Figure 7.22: Time-averaged tangential velocity component is plotted corresponding to Fig. 7.21.

propeller as a result of the high thrust. Note that also a large negative tangential velocity component is induced by the propeller in this area, shown in Fig. 7.22. Typical of a propeller operating at static condition is that air is drawn to it from its wider surroundings and this is also clearly visible in Fig. 7.17, where a spanwise flow is visible in between the wings from inboard towards the propeller at its outboard location. The formation of the negative tangential velocity component upstream of the propeller may be a result of the lower wing guiding the propeller induced flow in that tangential direction.

In zone B. an area of positive axial velocity can be noticed in the NWFR result of Fig. 7.21, which is a result of the deflection of the main rotor downwash by the upper wing towards the propeller. This deflection can also be observed by the streamtraces in Fig. 7.17. This effect of the upper wing on the axial velocity is noticeable in the thrust distribution plot in Fig. 7.20 by a local reduction in thrust, as also previously identified in the blade loading evolution from $\phi = 160$ deg onwards. The axial velocity inflow reduces the angle of attack of the propeller blade sections and thus reduces thrust. Therefore, in the PNWFR result of Fig. 7.21, although an additional increase in axial velocity by the propeller is seen in this area, it is of lower magnitude than in zone A.

In zone C. no large differences between the PNWFR and PNR configuration in terms of propeller thrust are noticeable. The inflow to the propeller is free of objects for both configurations and operates in a way typical of a propeller at angle of attack. The increased integrated propeller thrust of 10.5% in the PNWFR configuration, which was mentioned earlier, should therefore be explained by the effects in zone A. and B. Apparently, the thrust increasing effect of the wake is stronger than the thrust decreasing effect by the deflection of the main rotor downwash by the upper wing, resulting in a net thrust increase due to the presence of the wings.

Also for this condition a detailed interaction study by Frey et al. [223] has recently been published that takes the same approach by investigation of interaction effects through the removal of parts of the geometry. In that work, the net effect of the wings on the left propeller thrust was found to be the opposite: A 14.9% decrease of left propeller thrust was found due to the addition of the wings compared to the 10.5% increase in this study. The thrust increasing and thrust decreasing mechanism in zone A. and B. were also found in the research of Frey et al. [223]. Furthermore, a reverse wingtip vortex effect was found due to the download on the wing, reducing the effective angle of attack over most of the propeller disk. That study included a simulated main rotor, active engine inlet and exhaust, nacelle cooling flow and used an updated geometry of the Airbus RACER. Furthermore, the propeller thrust was not the same, explaining possibly the different net interaction effect. It highlights at least the sensitivity of the interaction effects to the specific conditions.

7.3. PROPELLER-WINGTIP INTERACTION AT LARGE ANGLE OF ATTACK

In this part, experimental and CFD RANS results are shown for the XPROP propeller under the influence of a wing. This was done to replicate the interaction occurring for the left propeller on the compound helicopter in hover as described in the previous section, in order to validate the occurring interaction effects. Furthermore, the effects of wing distance from the propeller and flap deflection on the propeller performance were investigated, to see if the influence of the wing could be reduced.

An overview of the analysed test cases is given in Table 7.4. The isolated propeller performance without wing named PNP (Propeller-Nacelle-Pylon) was measured at $V_\infty = 0$ m/s, and with freestream airspeed for $0 \leq \alpha_p \leq 90$ deg. Up- and downsweeps of propeller rotational speed (3400 – 7600 rpm) were performed to vary helical tip Mach number M_{tip} in static condition and advance ratio when there was a freestream airspeed. This was done for a propeller blade pitch of $\beta_{0.7R_p} = 20$ deg and $\beta_{0.7R_p} = 30$ deg. These isolated propeller results were already shown in Sections 4.1.1 and 4.2.1. Based on these results, the results with wing named PNWP (Propeller-Nacelle-Wing-Pylon) were only measured for $\beta_{0.7R_p} = 20$ deg to prevent significant flow separation on the blades at large angle of attack. Furthermore, no measurements with wing at $V_\infty = 6$ m/s were performed because of the considerable angle of attack wall correction required for this airspeed as was shown in Fig. 4.27.

Table 7.4: Overview of analysed experimental test cases.

config.	$\beta_{0.7R_p}$ (deg)	V_∞ (m/s)	α_p (deg)	d_w	δ_f (deg)
PNP	20, 30	0	0	-	-
PNP	20, 30	6, 12, 18	0, 15, 30, 45, 60, 75, 90	-	-
PNWP	20	12, 18	90	0.4, 0.65, 0.9, 1.4	0
PNWP	20	12, 18	90	0.4	0, 10, 20

The situation in the experiment is sketched in Fig. 7.23. The wind-tunnel jet impinged at $\alpha_p = 90$ deg, normal to the wing planform. When the propeller was off, a stagnation line formed over the upper side of the wing and flow separation occurred around the leading and trailing edges and the wingtip. Approximated shearlines from tuft visualisation are presented in Fig. 7.24. These highlight the stagnation line at approximately two-thirds of the chord from the leading edge. The figure shows that the shearline pattern changes under the influence of the propeller as the propeller draws in air. On the outboard sections of the wing the stagnation line moves toward the leading edge.

As the propeller influences the flow around the wing, the opposite also occurs. The effect the wing has on the propeller performance is discussed in the next Section 7.3.1. The inflow to the propeller is affected, resulting in modified propeller performance. As indicated in Fig. 7.23, the distance of the wing to the propeller d_w was varied in the experiment, as well as the flap deflection δ_f . This was done to parametrically study the interaction effect of the wing. In Section 7.3.2, these experimentally obtained interaction effects on the propeller performance are discussed. While the goal of the exper-

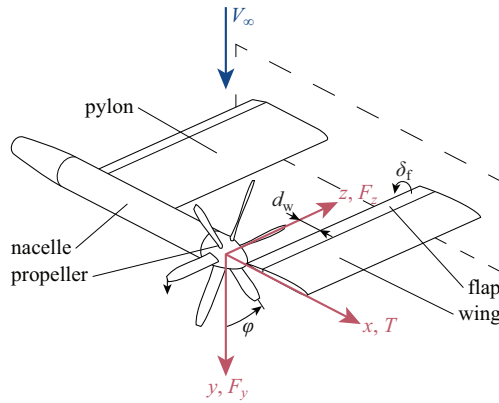


Figure 7.23: Sketch of propeller setup with wing, including definition of wing distance d_w , flap deflection δ_f , blade phase angle ϕ , and force components.

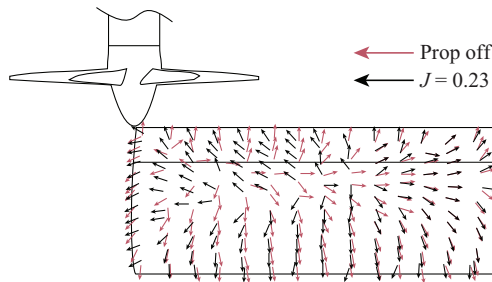


Figure 7.24: Flow visualisation on wing based on experimental measurement with tufts at $V_\infty = 12$ m/s; view along the direction of tunnel flow.

iment was to study the effect of the wing on the propeller performance, also possible unwanted interaction from the pylon was present. The effect of the pylon on the interaction results was studied with RANS CFD simulations and those results are presented in Section 7.3.3. Furthermore, as the experiment should represent interaction for a compound helicopter in hover, main rotor flow was approximated with an actuator-disk in the CFD simulations and compared to the situation with uniform freestream flow. Similar to the results of the previous section, the actuator-disk introduces the time-averaged effect of the main rotor on the flowfield, including the radial non-uniformity present in the hover condition. However, any of the transient effects that the main rotor blade tip vortices and wakes have on the propeller are not present, as well as any effect that the propeller has on the main rotor loading.

7.3.1. PROPELLER PERFORMANCE WITH WING

All results in this section were obtained for a fixed wing position and flap deflection of $d_w = 0.4$ and $\delta_f = 0$ deg, while in the next section these are varied. In Fig. 7.25 the main experimental performance results with wing are plotted versus advance ratio as 3rd or-

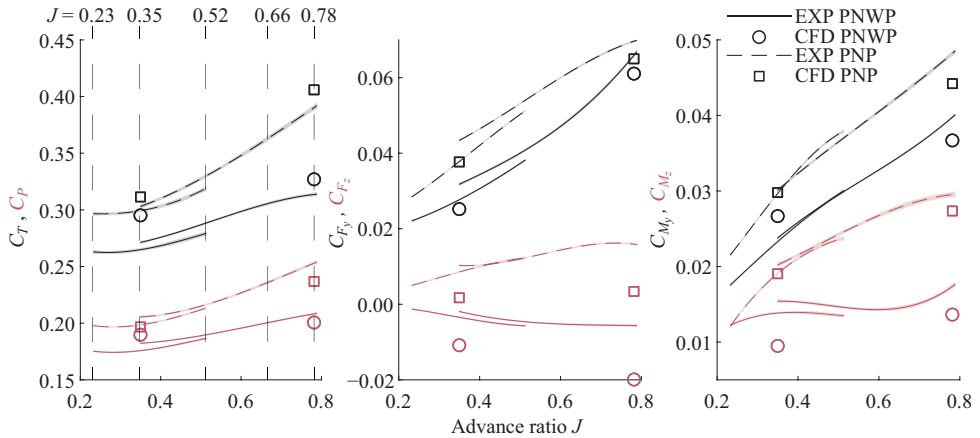


Figure 7.25: Propeller performance with and without wing effect for $\beta_{0.7R_p} = 20$ deg at $V_\infty = 12$ m/s and 18 m/s with $d_w = 0.4$ and $\delta_f = 0$ deg. CFD simulations obtained at 18 m/s.

der polynomial fits of the experimental data with 95% confidence bands. As a reference, also the performance without wing at $\alpha_p = 90$ deg is given and CFD results of the same configurations for $J = 0.35$ and $J = 0.78$ at 18 m/s are shown too. The wing causes a reduction of the thrust and power, the in-plane forces and the out-of-plane moments. The results with wing show some similarity to those without wing at reduced angle of attack ($\alpha_p \approx 60 - 75$ deg) from Fig. 4.26. The CFD simulations also predicted reductions in the performance quantities, although with considerable error compared to the experiment. This is partly due to a discrepancy in the prediction without wing at $\alpha_p = 90$ deg as discussed in relation to Fig. 4.29 and partly due to a discrepancy in the prediction of the effect of the wing. It is thought that, despite the differences, the mechanism of the aerodynamic interaction can be investigated with the CFD simulation results as the trends are the same in the CFD and experimental results.

A comparison of the blade thrust evolution with and without wing in Fig. 7.26 highlights where the differences arise. As visualised in Fig. 7.27, for $-30 < \varphi < 60$ deg (region A.), the propeller blade draws low momentum air from a wake formed below the wing. Flowfield analysis similar to that for Fig. 4.31 reveals the approximated blade section angle of attack in Fig. 7.26 b. As the propeller blade operates in a somewhat static condition in this area, the section angle of attack is larger than when no wing is present. As a result the thrust is larger too. When the blade reaches the vicinity of the trailing edge of the wing at $\varphi = 90$ deg, a decreased thrust due to the wing is found. The wing acts as a guiding vane, decreasing the large angle of attack of the freestream flow and locally increasing the axial velocity component in the propeller reference frame. As a result, the blade section angle of attack for $60 < \varphi < 180$ deg (region B.) is relatively small compared to the situation without wing and thus the corresponding thrust is reduced too. In the remainder of the blade evolution (region C.), the thrust is very similar and no large influence of the wing is found. The net result is a decrease of thrust.

A similar interaction with the wing was found for the left propeller on the compound

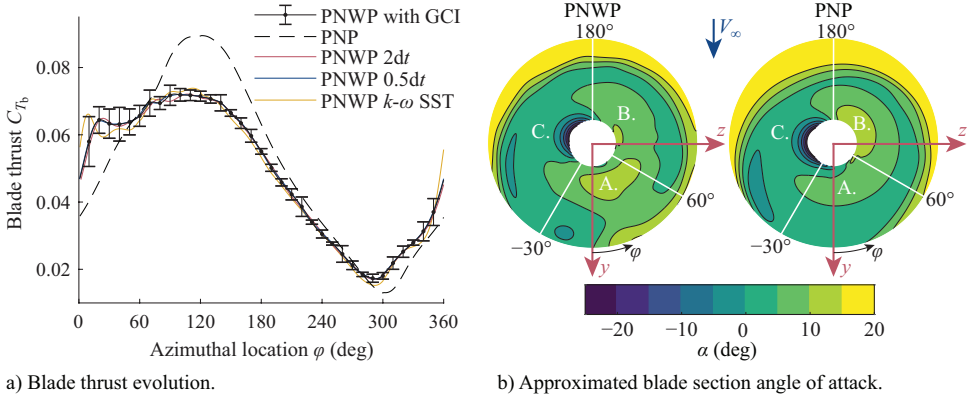


Figure 7.26: CFD results showing blade thrust evolution with grid convergence index (GCI) grid uncertainty, and section approximated angle of attack with and without wing effect for $J = 0.35$, $V_\infty = 18$ m/s and $\beta_{0.7R_p} = 20$ deg, including effect of timestep and turbulence model.

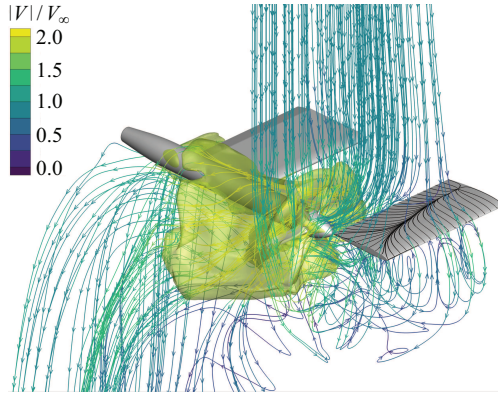


Figure 7.27: CFD PNWP result of wing interaction for $J = 0.35$, $V_\infty = 18$ m/s and $\beta_{0.7R_p} = 20$ deg; includes streamtraces with contour of velocity magnitude, isosurface for $|V|/V_\infty = 2$, and shearlines on wing (black).

helicopter in the previous Section 7.2. However, as the box wing (and nacelle) of that configuration is relatively larger and the propeller blades experience a wake for a larger portion of the rotation, the increase in thrust in region A. was found to be larger than the decrease of thrust in region B. and thus a net thrust increase as a result of the wing was found. Although the results of Frey et al. [223] show that also for this compound helicopter configuration the wing can cause a net decrease of thrust.

Figure 7.25 also shows a decrease of C_P as a result of the wing, following the same mechanism as described for C_T . Furthermore, the in-plane force coefficients decrease due to wing interaction. This is a result of changes to the in-plane tangential force on the propeller blade sections. As the thrust in region A. (See Fig. 7.26 b) is increased due to the wing, also an increase in the tangential force occurs. This results in a decrease in force in z-direction and thus C_{F_z} decreases. As the thrust in region B. is decreased due to the wing, the accompanying decrease in tangential force results in a decrease in force in

y-direction and thus C_{F_y} decreases. The out-of-plane moment coefficients follow similar trends due to the local changes in thrust.

The PNWP configuration is the most complex configuration in terms of aerodynamic interaction phenomena. Therefore, the chosen timestep and turbulence model were evaluated for this configuration. In Fig. 7.26 a the blade thrust evolution is shown for the PNWP configuration with a timestep equivalent to 0.5 deg and 2 deg of propeller rotation alongside the PNWP results with the default timestep equivalent to 1 deg of propeller rotation. Furthermore, results with the two-equation eddy viscosity $k-\omega$ SST turbulence model are shown with default timestep. In terms of timestep, only very small differences can be noticed, so the default timestep is considered sufficiently small. The result with $k-\omega$ SST turbulence model shows only small deviations from the default result with the Spalart-Allmaras turbulence model, despite the formation of the large wake behind the wing.

7.3.2. EFFECT OF WING POSITION AND FLAP DEFLECTION

The effect of the wing with varying wing position is presented in Fig. 7.28 as the ratio of thrust coefficient and thrust-over-power ratio with wing to the same quantities without wing. Results are shown for four advance ratios with $V_\infty = 12$ m/s and 18 m/s. For the closest distance of $d_w = 0.4$, the wing results in a clear thrust lapse as explained in the previous section. This is especially the case for the higher advance ratios as the propeller becomes relatively more sensitive to inflow changes when the rotational speed is lower, resulting in a maximum thrust reduction of 20% for $J = 0.78$. This dependency on J was already seen for the isolated propeller performance, where the effect of angle of attack in Fig. 4.26 was found to be larger for higher J . When the wing distance increases, the thrust increases, except for the higher advance ratios ($J = 0.78$ and to a lesser extent $J = 0.66$) where an intermediate reduction is found for $d_w = 0.9$. From the data available it is unclear what the cause is of this intermediate reduction in thrust, but it is most likely a physical effect as it is seen in repeated measurements for two different J and the effect gradually disappears with decreasing J . Note that, while the relative changes in

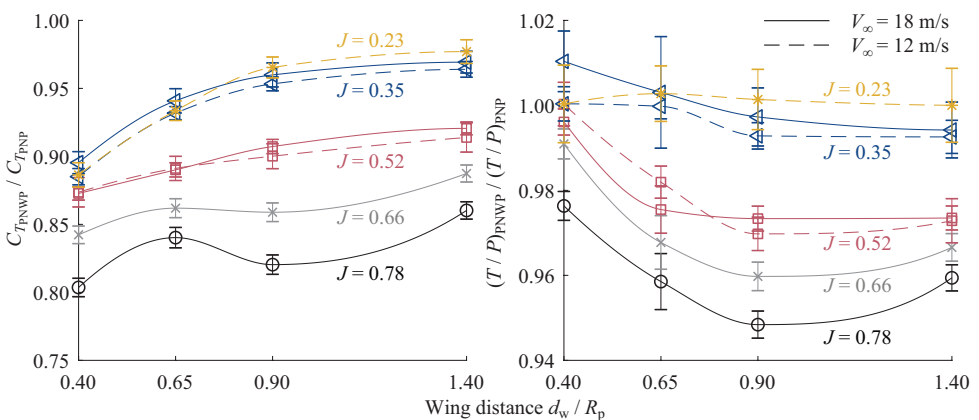


Figure 7.28: Experimental result showing change in propeller loading due to wing versus wing distance for $\beta_{0.7R_p} = 20$ deg at $V_\infty = 12$ m/s and 18 m/s.

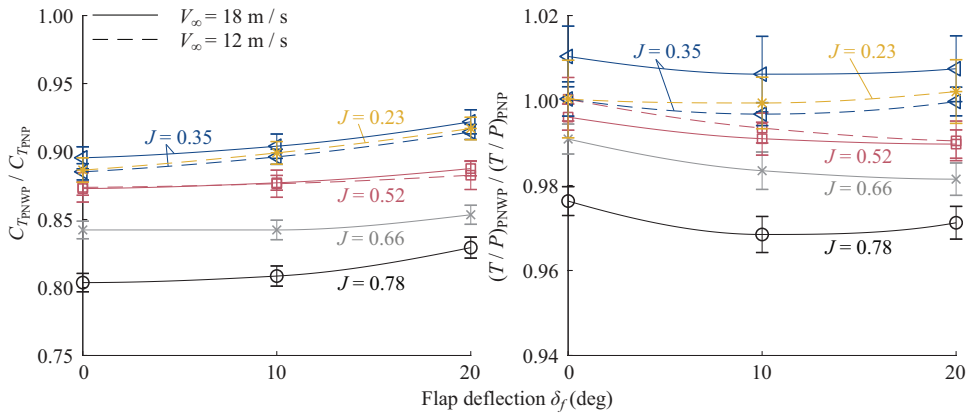


Figure 7.29: Experimental result showing change in propeller loading due to wing versus flap deflection for $\beta_{0.7R_p} = 20$ deg at $V_\infty = 12$ m/s and 18 m/s.

thrust are large for higher advance ratios, the absolute changes are small as the loading is relatively low for these operating conditions.

The thrust-over-power ratio T/P indicates the efficiency of the propeller operation. Depending on J , the wing either leads to a small increase or decrease of T/P . With increasing wing distance, T/P generally decreases. Apparently the disturbance of the inflow by the wing is for most tested operating conditions disadvantageous for the propeller performance. A similar conclusion was reached for the left propeller on the compound helicopter in Section 7.2.

The effects of flap deflection on the propeller performance are presented in Fig. 7.29. Compared to wing distance, only minor variations of the propeller performance quantities with flap deflection are found. If one would want to alleviate the effects of the wing on the propeller performance, increasing the distance seems more effective, although possibly larger flap deflections could be tried to see if the trend of reducing wing effect continues.

7.3.3. EFFECT OF PYLON AND MAIN ROTOR FLOW

In this section the presence of the pylon is investigated for the cases with wing by means of CFD simulations. Furthermore, the freestream flow is changed to a time-averaged approximation of main rotor flow by means of an actuator-disk (AD), to investigate how representative the experimental data is for the interaction on the compound helicopter. In Fig. 7.30 the blade thrust evolution is shown for all CFD configurations with wing. First consider the data with freestream flow. With the wing present, the effect of the pylon on the propeller thrust is not small, unlike for the case without wing where changes in thrust in the order of 1 % were found. The pylon reduces the time-averaged thrust by 11.5% according to the simulations.

In Fig. 7.31 the flowfield experienced by the propeller is presented for the case without pylon. In Fig. 7.31 a, a vortex pair can be observed from the streamtraces (checked with vorticity isosurfaces), which is formed in the wake of the wing. Apparently, the formation of these vortices is suppressed when the pylon is present, likely due to changes

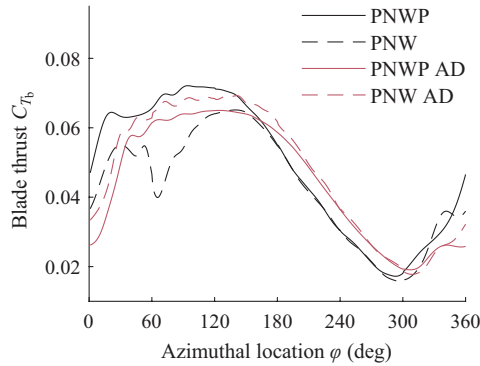


Figure 7.30: CFD blade thrust evolution showing effect of pylon and actuator-disk modelling for $J = 0.35$, $V_\infty = 18$ m/s and $\beta_{0.7R_p} = 20$ deg. Azimuthal location φ is defined in Fig. 7.23.

in the inflow direction to the wing induced by the pylon. This vortex pair is ingested by the propeller and has a significant effect on the propeller loading. In Fig. 7.31 b the consequence of the vortex pair on the flowfield experienced by the propeller is shown. In the tangential velocity field, the effect of the vortices is seen by two areas of increased and decreased V_t . This has a pronounced effect on the section angle of attack. Vortex 1, located around $\varphi = 0$ deg, results in increased α near the root of the blade and decreased α near the tip. As the loading on the propeller blade generally increases towards the tip with maxima outboard of $r/R_p = 0.8$ (see Fig. 4.3), the impact of the reduction in α is larger and a thrust reduction is found around $\varphi = 0$ deg in Fig. 7.30. As vortex 2 is of opposite sign to vortex 1 and is located radially more outboard, also this vortex results in a pronounced reduction of thrust, visible in Fig. 7.30 by the local minimum around $\varphi = 60$ deg. For the remainder of the blade evolution, no significant differences in blade thrust are found due to the pylon. As a vortex pair of such strength is only present for the PNW configuration and not for the other CFD configurations with wing (PNWP, PNWP AD and PNW AD), it is unclear whether this would occur in the experiment if the pylon was removed.

Figure 7.30 also includes results where the freestream flow was replaced by flow induced by an actuator-disk representing the time-averaged effect of a main rotor. For the case with pylon, qualitatively a similar thrust distribution is found, but a phase shift is present. The mean thrust is decreased by 7.0% as a result of the simulated main rotor downwash. When the actuator-disk is present, the effect of the pylon on the thrust distribution is less pronounced. In Fig. 7.32 a the actuator-disk flowfield is visualised while in Fig. 7.32 b the assumed main rotor radial thrust distribution is shown. Considering the large radial non-uniformity of the oncoming flow as a result of the non-uniformity in main rotor thrust distribution, the effects this has on the propeller thrust distribution are surprisingly small. Because of this similarity in thrust evolution, it is thought that the conclusions as drawn in the previous two sections based on the experimental results with freestream flow, are representative for the interaction occurring on the compound helicopter. However, the aspect missing in this interaction are the unsteady effects of the main rotor flow on the propeller performance.

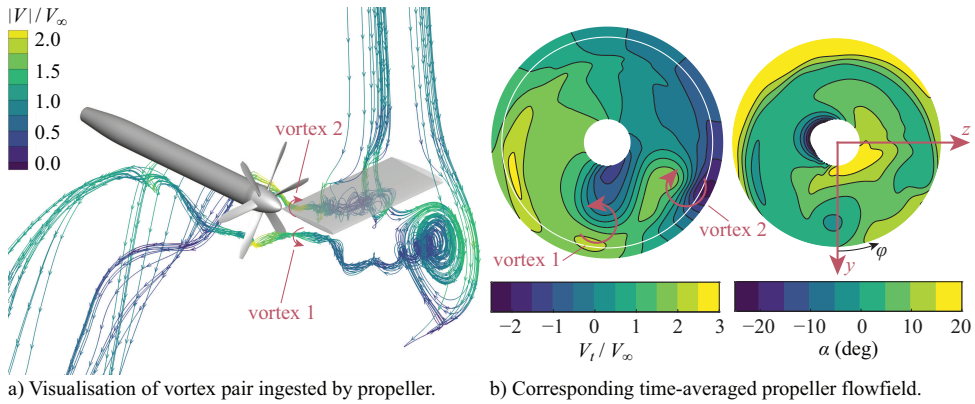


Figure 7.31: CFD visualisation of vortex pair and contours of propeller flowfield for PNW configuration for $J = 0.35$, $V_\infty = 18$ m/s and $\beta_{0.7R_p} = 20$ deg.

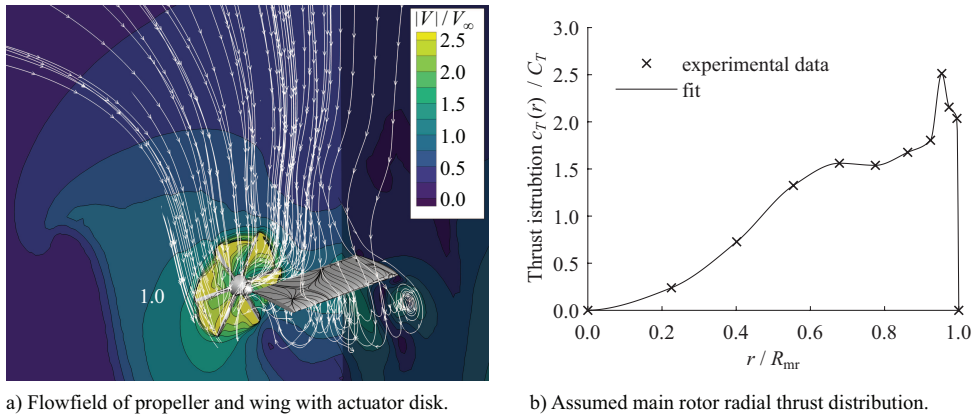


Figure 7.32: CFD visualisation of flowfield with main rotor modelling and corresponding thrust distribution for $J = 0.35$, $V_\infty = 18$ m/s and $\beta_{0.7R_p} = 20$ deg. Includes streamtraces (white) and shearlines on wing (black).

7.4. CONCLUSIONS

In this chapter, the aerodynamic interactions occurring on the compound helicopter configuration were investigated in a cruise and hover condition. A breakdown was presented of the aerodynamic interactions between the propellers, the box-wings and the main rotor, focussing mainly at the effects on the propeller loading. Furthermore, for an angle of attack of 90 deg the interaction of the XPROP propeller with an upstream wing was studied, to replicate the interaction occurring on the the compound helicopter in hover in a simplified manner. The conclusions for the compound helicopter simulations are drawn first, answering research questions **Q7.1**, **Q7.2** and **Q8**, after which the conclusions for the XPROP propeller study with wing are given to answer **Q9**.

COMPOUND HELICOPTER CONFIGURATION

Since the propellers of this compound helicopter are situated below the main rotor and the main rotor slipstream passes over propellers in the cruise condition, the effect which the main rotor has on the propellers is limited to an angle of attack effect. A small negative angle of attack is induced to the inflow of the propellers (and the wings), resulting in a sinusoidally varying propeller blade loading. Contrary, in the hover condition the direct impingement of the main rotor downwash on the propellers results in a very significant sinusoidally varying blade loading due to the inflow at almost perpendicular angle to the propeller axis. Any such compound helicopter layout where a propeller is situated below the main rotor would experience a similar interaction, if no other aerodynamic surfaces would be shielding it.

Since the propellers of this compound helicopter are located behind the wing at the wingtip, they ingest the rotational velocity field formed by the pressure difference between the upper and lower wing surfaces. Considering that the rotation direction of the propellers is against the rotation of the flow around the wingtip, an increase in thrust occurs. Furthermore, the low axial velocity of the wing wake is ingested, also resulting in a local propeller thrust increase. Comparison with the isolated propeller performance has led to the conclusion that installation increases propeller propulsive efficiency by 7% if the blade pitch is reduced to maintain equal thrust. The majority of this gain can likely be ascribed to the rotational flowfield. Due to the close proximity of the propeller to the wing, an upstream effect on the wing was found. For this helicopter, the propellers increase wing lift, through a lift increase of the lower wing and a smaller lift decrease of the upper wings. The propellers increase drag of the upper and lower wings, thereby decreasing the wing lift-over-drag ratio.

The effect of wing lift on the propeller loading was investigated through flap deflection. A strong positive correlation was found between wing lift obtained through flap deflection and propeller efficiency, resulting in a maximum efficiency gain from installation of the propeller of 11% at $\delta_f = 5$ deg. This close coupling of propeller and wing loading has also consequences for off-design conditions. The effects of angle of attack and sideslip angle on the propeller performance changed drastically compared to those of an isolated propeller as the wing loading and thus the inflow to the propellers varied.

Since in the hover condition the propellers on the compound helicopter are used to counter the torque of the main rotor, an asymmetry arises between the left and right propeller. For the left propeller, the wing introduces disturbances to the inflow. This causes local changes in the sinusoidal propeller blade loading induced by the main rotor. The left upper wing deflects the main rotor downwash towards the left propeller, resulting in an axial velocity component which decreases locally the thrust. The wake formed by the nacelle and wings in the main rotor downwash causes the left propeller to locally operate in static condition, increasing the thrust. Overall, the wings increase the left propeller thrust by 10.5% with slightly reduced thrust-over-power ratio for equal blade pitch. For the right propeller, the wings are in its slipstream. They lead to a decrease of right propeller reverse thrust by 1.5% with constant thrust-over-power ratio for equal blade pitch.

In general very significant aerodynamic interaction effects can be expected when a main rotor, propellers and wing are in proximity to each other. A breakdown of aero-

dynamic interaction effects by leaving away parts of the geometry, as presented here, can provide the necessary insight into these effects. Although results were shown for a specific compound helicopter configuration representing the Airbus RACER, the drawn conclusions may be more widely applicable to wingtip-mounted pusher-propeller configurations and propeller-rotor interaction cases.

XPROP PROPELLER CONFIGURATION WITH WING

At an angle of attack of 90 deg, the interaction of the propeller with an upstream wing was studied. The wing was found to reduce all propeller performance quantities on average. In terms of thrust, a thrust increasing and thrust decreasing mechanism were found numerically, leading to a net thrust decrease. A local blade thrust increase of up to 35% of the time average arose as the propeller drew air from the low momentum wake formed on one side of the wing. A local thrust decrease of up to 35% of the time average occurred because the wing acted as a turning vane for the freestream flow, locally decreasing the angle of attack and increasing the axial velocity component in the inflow to the propeller. Wing distance and flap deflection were varied in the experiment. For the closest distance to the propeller, a maximum thrust decrease of 20% was found for the highest tested advance ratio. For most tested operating conditions, the wing resulted in a small decrease of propeller thrust-over-power ratio in the order of 1%. With decreasing advance ratio and increasing wing distance, the effect of the wing on thrust and power generally decreased. For the tested range from 0 deg to 20 deg, flap deflection had only a minor influence on the propeller performance, decreasing the effect of the wing slightly.

From the numerical investigation of the effect of the pylon on the propeller performance it was found that it may have been significant (11.5% thrust reduction) as the inflow to the wing was influenced. A pair of strong vortices in the wing wake were found to be the source of the performance change. It is unknown whether in the experiment a similar phenomenon would have occurred without pylon. As wing interaction was studied to represent the interaction occurring for the left propeller on the compound helicopter in hover, the freestream flow in the CFD simulation was also replaced with the time-averaged effect of a main rotor through an actuator-disk. Despite the non-uniform velocity distribution in the main rotor slipstream, no major changes in blade thrust evolution were found compared to the situation with freestream flow. With the actuator-disk no strong vortex pair was formed in the wing wake when the pylon was removed, suggesting that this phenomenon is very particular to the exact configuration and operating condition.

In general, the results in this study are qualitatively representative for the aerodynamic interaction occurring on the compound helicopter in hover. However, while for the compound helicopter the left propeller thrust was increased with 10.5% by the wings, in this case a decrease in thrust was found from the interaction. It is thought that since the box wing (and nacelle) of the compound helicopter is relatively larger and the propeller blades experience a wake for a larger portion of the rotation, the thrust increasing mechanism was more significant than the thrust decreasing mechanism. Therefore a net thrust increase as a result of the wing was found. It is recommended for future work to integrate the propeller and motor into a nacelle at the wingtip, to remove any unwanted influence of the pylon on the results.

8

CONCLUSIONS AND RECOMMENDATIONS

8.1. CONCLUSIONS

The objective of the research discussed in this dissertation is to get a fundamental understanding of the role of aerodynamic interaction on the loading and performance of primarily the propeller and secondarily the interacting object(s) in typical configurations where interaction dominates the flowfield. These insights may lead to improved aerodynamic design, specifically related to propeller propulsion integration. Furthermore, the experimental results may provide a validated starting point for follow-up research on related configurations. Five different configurations were studied by a combined numerical and experimental approach:

- A wingtip-mounted propeller in tractor configuration,
- a small-scale wingtip-mounted propeller in pusher configuration typical of a distributed propulsion setup,
- propeller interaction with downstream swirl-recovery-vanes (SRVs),
- interaction between two propellers in configurations applicable to eVTOL vehicles, and
- pusher-propellers mounted on the tip of a box-wing from a compound helicopter.

The wingtip-mounted propeller in tractor configuration was used to study the accuracy of different propeller modelling methods in RANS simulations in Section 5.1. Experimental data of the same configuration provided data for validation and comparison. The effects of windmilling on the wing loading were investigated in Section 5.2 for the same configuration. With the wingtip-mounted propeller in pusher configuration, the consequences of propeller design, size and thrust target were investigated numerically in Section 5.3.

Propeller-SRV interaction was studied by RANS simulations with validating experimental results in Section 6.1. In the same chapter, experimental results from the interaction between two propellers were discussed in Section 6.2.

The compound helicopter configuration was studied by RANS simulations in a cruise and hover condition in Sections 7.1 and 7.2 respectively. In Section 7.3 the situation in hover was simplified and investigated with an experiment consisting of a propeller and upstream planar wing. The effects of wing distance and flap deflection were studied with this setup.

The aerodynamic interaction effects on the propeller in these configurations were generated by a variety of flow phenomena. After a conclusion on the propeller modelling methods, conclusions are drawn on the effects of the identified flow phenomena on the propeller loading and transient behaviour. Finally, a conclusion is presented on the changes in loading for the objects in interaction with the propeller.

8.1.1. PROPELLER MODELLING METHODS

Three levels of propeller modelling fidelity have been addressed. Two levels of RANS CFD simulations were performed: Resolving the propeller blades, and modelling the effect of the propeller in terms of momentum and energy by means of an actuator-disk and actuator-line representation. The latter two models were investigated as a means to reduce the computational cost of the simulations.

Furthermore, lower order propeller methods were used for quick analysis and design: a blade element momentum and lifting line method. Design optimisation with the lifting line method was performed to study whether the favourable wingtip-mounted pusher-propeller interaction could be enhanced by propeller design for the non-uniform flow-field. Propeller analysis with the extended blade element momentum method was performed to show to what extent it can be used to predict interaction between propellers.

RESOLVING PROPELLERS IN RANS SIMULATIONS

In general, reasonable agreement was found in terms of isolated propeller performance and slipstream between resolving propellers in RANS simulations and experimental data from wind-tunnel tests. The analysis was done 2nd accurate for a one-equation Spalart–Allmaras (SA) and two-equation $k - \omega$ SST turbulence model. It was found that prediction of flow separation on propeller blades at high blade loading, for instance when the propeller operates in static condition without freestream flow, comes with an error in propeller performance (approximately 15% in thrust and 6% in power) due to modelling and due to discretization. These errors reduce significantly (approximately 2% in thrust and 3% in power) when reducing blade pitch and thus blade loading to a regime where flow separation on the blades is less present.

The numerically modelled slipstream flowfields agreed well with experimental data except for in the tip vortex regions. There, a significant error due to discretization was present due to numerical diffusion. Unfortunately, the numerical methods found in typical 2nd order CFD solvers require extremely dense grids to avoid numerical diffusion and to preserve the tip-vortex strength. This error also resulted in reduced contraction of the slipstream. The SA turbulence model only showed differences from the $k - \omega$ SST model in the downstream part of the slipstream (more than two blade radii downstream of the propeller), where numerical diffusion in the vortex cores was less for the SA model.

Propeller performance was also predicted at angles of attack up to 90 deg. Reasonably good agreement with experimental data was found for all force and moment components (on average approximately 3% difference in thrust and power and 8% difference in the primary in-plane force and the out-of-plane moments over the angle sweep), although loading on the spinner may have introduced deviations from the experimental data, especially in terms of secondary in-plane force (on average approximately 60% difference over the angle sweep, partly due to the very small values). Loading on the spinner is an important factor to consider for the in-plane forces.

Two experimental datasets allowed detailed validation of loading and flowfield in interaction. For the wingtip-mounted tractor-propeller configuration, agreement of the time-averaged pressure distribution on the part of the wing in the slipstream was obtained, matching the good agreement obtained for the integrated lift coefficient (maximum difference of 0.8%). The slipstream and wake behind the wing agreed well in a time-averaged and time-accurate sense. Most of the differences were already present in the simulations of the isolated propeller and wing, and were mainly a result of numerical diffusion in the vortex cores. As long as the uncertainty due to numerical diffusion is accounted for by a grid dependency study or reduced by local grid refinement, RANS simulations with an SA turbulence model are able to model this interaction.

The other validation case investigated propeller interaction with downstream swirl-recovery-vanes. Acceptable agreement in the velocity field between the simulations and the experimental data was found, showing the same trends with installation of the SRVs. Again the main differences could be attributed to numerical diffusion near the slipstream edges and a possible upstream effect of the support structure in the experiment.

ACTUATOR-DISK AND ACTUATOR-LINE MODELLING IN RANS SIMULATIONS

Instead of resolving the propeller, its effect can be modelled in a simulation by sources of momentum and energy. In the actuator-line model, the propeller blades are replaced with distributions of momentum and energy sources along lines representing the blades. Instead of representing the blades by lines, in the actuator-disk model their averaged effect on the propeller disk is modelled, taking into account radial and azimuthal variations in loading. While the actuator-line model is inherently time-dependent, a simulation with the actuator-disk model can be solved as a steady problem. These models were developed as part of this research as a means to reduce the computational cost of the simulations.

A study was performed on the accuracy of actuator-disk and actuator-line modelling for the wingtip-mounted tractor-propeller configuration. A 17% reduction in computational cost was estimated for the actuator-line simulation compared to resolving the propeller blades. The actuator-disk model provided the ability to further reduce the cost of the simulation with 85% by removing time dependency. This excludes the time required to predict and provide these models with the propeller blade loading data, as this was not part of the study. Instead, they were tested in their most accurate form, by providing the extracted blade loading from the blade resolving simulations.

For the reference isolated propeller simulations the actuator-disk and actuator-line models of the propeller provided an accurate time-averaged slipstream, only deviating

from the blade resolving simulation results close to the nacelle. That deviation was likely caused by a difference in modelling the close interaction of the blade root and nacelle by neglecting the blade thickness, and due to the lack of time dependence in the flow separation from the blade root in both models. The actuator-line model agreed almost one-to-one with the blade resolving simulation in a time-accurate sense.

Also in interaction with the downstream wingtip, the actuator-line simulation agreed well with the blade resolving simulation in terms of time-averaged and time-accurate pressure distributions on the wing. The actuator-disk result showed a slightly lower pressure on the suction side, likely due to a difference in slipstream-wing interaction as a result of the inherently time-averaged slipstream in this model. This resulted in a 3.9% increase in integrated lift, with no increase in drag. The slipstream and wake agreed well in a time-averaged and time-accurate sense for all the propeller modelling methods.

In a scenario where the blade loading data for the actuator models is provided by means of a lower order propeller model, the time required to run the lower order model and the uncertainty involved should be accounted for as well. This was not part of the current study.

BLADE ELEMENT MOMENTUM AND LIFTING LINE METHODS

A blade element momentum and lifting line propeller method were used to predict propeller performance at reduced cost. First, both models were validated against experimental data of an isolated propeller. They were both found adequate for isolated propeller performance prediction.

The extended blade element momentum model was used to predict interaction between propellers in one-after-another configuration, where one propeller was placed in the slipstream of the other propeller at varying lateral spacing with equal rotation direction. This model captured most interaction effects on the thrust and power of the downstream propeller with sufficient accuracy.

The lifting line propeller method was used to perform aerodynamic design optimization for the wingtip-mounted pusher-propeller configuration. The propeller inflow field was extracted from an isolated wing simulation, which was circumferentially averaged before providing it to the lifting line propeller tool. For a reference propeller, the resulting performance in interaction from the tool was in line with the time-averaged propeller loading of fully resolved propeller-wing RANS CFD simulations, providing confidence in the validity of the approach. This was despite the large fluctuation found in the transient propeller blade loading due to circumferential non-uniformities in the inflow field, which were inherently lacking in the lifting line results.

8.1.2. EFFECTS OF INTERACTION ON PROPELLER LOADING

The discussion of aerodynamic interaction effects on the propeller loading is subdivided by the flow phenomena in the inflow to the propeller that cause the effects. These flow phenomena were identified in Chapter 2.

DECREASED TOTAL PRESSURE FROM MOMENTUM SINKS

Two wingtip-mounted pusher-propeller configurations were studied with blade resolving RANS simulations: With a planar wing and a small-scale propeller, and with a box-

wing on a compound helicopter. On both configurations, the propeller blades experienced local increases in thrust when they passed the low momentum wakes trailing from the wing in a cruise condition. For the planar wing, a local peak in thrust of about 10% of the time-averaged blade loading was present. As the wake locally reduces the axial velocity in the inflow to the propeller, the blade sections angle of attack increases, resulting in increased thrust. This can also be viewed as a local advance ratio reduction. For the compound helicopter, the propeller blades experienced the wake of the box-wing twice in a full rotation, increasing locally the thrust as well. A lesser increase in power was found, locally improving the propeller propulsive efficiency.

An example of a large effect of a momentum sink on the propeller loading was found on the compound helicopter configuration in hover condition. The propellers are used to counter the torque of the main rotor in hover, resulting in an asymmetry between the left and right propeller as the left propeller is set to produce forward thrust and the right propeller reverse thrust. For the left propeller, the wing introduced disturbances to the inflow. As the main rotor downwash impinged on the wing and propeller approximately normal to the wing planform, a large wake formed below the wing and nacelle. For the part of the rotation where the propeller draws air from this low momentum wake, the propeller loading is similar to that in static condition (no freestream flow) or at very low advance ratio, considerably increasing the thrust temporarily.

The interaction of a propeller with an upstream planar wing was studied in a 3/4 open jet wind-tunnel, to replicate the interaction occurring for the left propeller on the compound helicopter in hover. As the propeller and wing were placed at 90 deg to the flow, also for this configuration a wake formed downstream of the wing. In the corresponding blade resolving RANS simulations a local blade thrust increase of up to 35% of the time average arose compared to the situation without wing, as the propeller drew air from the low momentum wake.

INCREASED TOTAL PRESSURE FROM MOMENTUM SOURCES

The main rotor on the compound helicopter can be viewed as a momentum source. As the main rotor slipstream impinged on the propellers in hover, they experienced a very large effective angle of attack, resulting in sinusoidal blade loading with a period equal to a full blade rotation. The left upper wing deflected the main rotor downwash towards the left propeller, resulting in an increased axial velocity in the inflow to this propeller. This resulted locally in a decrease of the thrust through a decrease of the blade sections angle of attack. However overall, the wing increased the left propeller thrust by 10.5% with slightly reduced thrust-over-power ratio. For the right propeller, the disturbance of the wing to the main rotor slipstream had a smaller effect on the propeller loading, leading to a decrease of reverse thrust by 1.5% with constant thrust-over-power ratio.

In the replicating experiment, an overall thrust decrease due to the wing was found for all tested conditions. The RANS simulations showed that as a result of the wing a local thrust decrease of up to 35% of the time average was present as the wing deflected the wind-tunnel jet towards the propeller. Replacing the freestream flow with the time-averaged effect of a main rotor through an actuator-disk did not result in major changes in the interaction. These results contradict the results found for the compound helicopter configuration as there an overall thrust increase was found. It is thought that

since the box-wing and nacelle of the compound helicopter are relatively larger and the propeller blades experience a wake for a larger portion of the rotation, the increase in thrust was larger than the decrease in thrust and therefore a net thrust increase as a result of the wing was found for that configuration and not for the experiment.

In the experiment, also the effects of propeller-wing spacing and flap deflection on the propeller loading were investigated to see if the interaction effects of the wing could be reduced. For the closest distance to the propeller, a maximum thrust decrease of 20% was found for the highest tested advance ratio. For most tested operating conditions, the wing resulted in a small decrease of propeller thrust-over-power ratio in the order of 1%. With decreasing advance ratio and increasing wing distance, the effect of the wing generally reduced. For the tested range from 0 deg to 20 deg, flap deflection had only a minor influence on the propeller performance, decreasing the effect of the wing on the propeller loading only slightly.

The effects of a momentum source on propeller loading were also highlighted by the experimentally studied interaction between two co-rotating propellers applicable to eVTOL vehicles. For the one-after-another (OAA) configuration, the effects of interaction for the rear propeller were investigated for varying lateral and axial distance between the propellers. The rear propeller experienced an increased axial velocity when it operated in the slipstream of the front propeller, reducing thrust. A maximum loss in thrust of up to 80% was observed for this configuration with full overlap, and furthermore, the interaction resulted in in-plane forces and out-of-plane moments. Compensation of the lost thrust through a rotational speed increase of the rear propeller led to significant power penalties of up to 30% for the rear propeller alone. If this type of interaction occurs on an eVTOL vehicle, for instance caused by a sudden change of angle of attack, the interaction effects experienced by the rear propeller influence aircraft stability. This is not only caused by the thrust reduction and its associated moments but also by the generated in-plane forces and out-of-plane moments as a result of this interaction.

8

CHANGED DYNAMIC PRESSURE OR ANGLE OF ATTACK FROM POTENTIAL EFFECTS

It was found that operating a propeller in the vicinity of a slipstream of another rotor can have significant effects on the propeller loading, even though no direct impingement of the slipstream on the propeller disk is present. The principle behind this is the change of effective angle of attack as the flowfield around the slipstream is deflected with the slipstream. For the compound helicopter configuration in a cruise condition, the propellers (and also the wings) experienced a small negative angle of attack from the overhead slipstream of the main rotor, resulting in sinusoidal blade loading typical of a propeller at angle of attack.

In the experiment investigating the interaction between two propellers, this type of interaction was mainly present for the side-by-side (SBS) configuration. Especially when the configuration was placed at larger angles of attack, the rear propeller experienced a drop in thrust from the interaction with the front propeller slipstream. For $\alpha_p = 90$ deg, a maximum drop in thrust of 30% was measured, depending strongly on the advance ratio and lateral distance between the propellers. This drop occurred since the rear propeller

experienced a decreased effective angle of attack due to the downwash of the front propeller. The interaction effects for the front propeller were small to negligible and likely resulted from a small upwash from the rear propeller and its slipstream. These detrimental interaction results for the rear propeller may be indicative for eVTOL operation with such propeller configuration in the last stages of transition from vertical flight to forward flight. Compensation of the lost thrust in such situation by increasing rotational speed of either the rear propeller or both front and rear propeller resulted in power penalties of 5% to 13% for the two propellers combined, again depending on the lateral distance.

Also for the OAA configuration, an effective angle of attack change was likely present for the rear propeller in the vicinity of the front propeller slipstream: For small axial distance, in the region of the front propeller slipstream contraction, a small increase in thrust for the rear propeller was present when it was placed just outside of the slipstream. This is likely due to an induced angle of attack by the slipstream. This is the only thrust increasing interaction mechanism found in the experiment for any downstream located propeller.

The last observed potential effect that affected propeller loading was found for the interaction with the downstream swirl-recovery-vanes. In the blade resolving RANS simulations, the propeller experienced a small increase in thrust and torque of 1% due to an upstream pressure effect of the SRVs compared to the case of the isolated propeller. Furthermore, a fluctuation was present in the blade loading: In both the computation and experiment the sectional blade normal-force at $r/R_p \approx 0.65$ was found to be fluctuating with 0.8% to 2.3% of the local time-averaged loading, relatively increasing with increasing advance ratio. Five periodic fluctuations were found in a full blade rotation, equal to the number of swirl-recovery-vanes.

ROTATIONAL FLOWFIELDS

Rotational flowfields were the dominant source of interaction for the investigated wingtip-mounted pusher-propellers. As a pressure difference is present on a wing with lift between the lower and upper side, a rotational flowfield is induced around the wingtip towards the upper side. For both the small-scale propeller on a planar wing and the propellers on the compound helicopter, the tangential velocity in the rotational flowfield opposed the direction of propeller rotation, increasing the blade sections angle of attack. For the compound helicopter configuration, a comparison with the isolated propeller has led to the conclusion that installation increases propeller propulsive efficiency by 7% if the blade pitch is reduced to maintain equal thrust. This was mainly a result of the rotational flowfield. Furthermore, by varying the wing lift through flap deflection, it was found that there was a strong positive correlation between wing lift and propeller propulsive efficiency, resulting in a maximum propulsive efficiency gain from installation of the propeller of 11% at a 5 deg flap deflection. This latter value also includes the small incidence angle effect of the main rotor. This close coupling of propeller and wing loading has also consequences for manoeuvring. The effects of angle of attack and sideslip angle on the propeller performance changed drastically compared to those of an isolated propeller as the wing loading and thus the inflow to the propellers varied.

For the propeller on a planar wing, a design study was performed. The possible propulsive efficiency gains for the propeller due to installation were significant: Up to

16% increase in efficiency was achieved at the lowest investigated thrust level of 5% of the wing drag, decreasing with a reducing slope to approximately 7.5% for the highest investigated thrust level of 100% of the wing drag. The propulsive efficiency gain was only significantly dependent on the propeller radius for low thrust levels of less than 30% of the wing drag. It was found that effectively the propeller geometry is optimized for the required thrust level and to a lesser degree for the non-uniformity in the flowfield. Propeller blade optimisation and installation resulted in higher profile efficiency in the blade root sections and a more inboard thrust distribution over the blade.

For both wingtip-mounted pusher-propeller configurations, circumferential variation in the tangential velocity field from the wingtip were present. These variations caused fluctuating blade loads as the blade sections angle of attack varied.

The swirl in a slipstream can also be seen as a rotational flowfield. For the interaction between propellers in OAA configuration, the decrease in thrust for the rear propeller was likely dependent on the swirl in the slipstream of the front propeller. Depending on the overlap of the propellers, the swirl resulted locally in increases and decreases of blade sections angle of attack. This was deduced from sudden changes in slope of the rear propeller thrust versus lateral distance between the propeller axes. The effects were however small compared to the effect of the axial velocity component in the impinging slipstream.

IMPINGING VORTICES

For the wingtip-mounted pusher-propellers, the wingtip vortex impinged on the propeller disk. This was especially clear for the planar wing, where the crossing of a propeller blade through the wingtip vortex caused a variation in the radial distribution of loading on the blade. However, the time-averaged effect of this interaction on the propeller loading was found to be small. As the vortex was approximately aligned with the propeller axis and impinged off-center from the axis, the propeller blade experienced locally a decrease and increase of blade section angle of attack, depending on the radial location. Due to the propeller rotation direction, the decrease occurred on the inboard side of the propeller blade.

A second case of vortex impingement occurred for the interaction between propellers in OAA configuration. As a propeller slipstream consists of tip- and root-vortices, the rear propeller must have experienced variations in the inflow from these vortices. Since the experimental campaign only investigated time-averaged effects, the individual effects of these vortices were not measured and no conclusions can be drawn.

8.1.3. EFFECTS ON STUDIED OBJECTS IN INTERACTION WITH A PROPELLER

The objects for which interaction with the propeller were studied consist of the wingtip and swirl-recovery-vanes. The effects which these aerodynamic surfaces experience are discussed separately in the next two sections.

WINGTIP

Interaction effects for the wingtip were most pronounced for the wingtip-mounted tractor-propeller. The configuration was for a large part used to study propeller modelling meth-

ods in RANS simulations and the results were focussed on comparison with the experimental data rather than on the occurring phenomena. Flap deflection was used to camber the wing and generate lift. All results from the different CFD models and the experimental data showed a clear reduction in tangential velocity or swirl in the slipstream behind the wing for the case with the propeller rotating against the rotation of the wingtip vortex compared to the case with rotation with the wingtip vortex. With a change of flap deflection from -10 deg to $+10$ deg (or in other words from outboard-up to inboard-up rotation), for all CFD models and the experiment the ratio of rotational to total kinetic energy decreased from about 0.05 to about 0.01. This highlights the increase in performance as less rotational kinetic energy is left in the flow downstream of the wing.

For inboard-up propeller rotation, an increase in wing lift was found and also the lift-to-drag ratio increased about 25% compared to the propeller-off case. Note that this number is very specific to the configuration. This is a combined effect of the increased dynamic pressure and the swirl in the slipstream. While the increased dynamic pressure increased the wing lift and drag locally, the swirl resulted in a forward tilt of the resultant force vector on the wing in thrust direction, opposing drag.

With this validated model for positive thrust, the consequences of windmilling were investigated as a concept to harvest energy in-flight, for instance during descent. The aerodynamic interaction phenomena changed drastically compared to the case at positive thrust setting. With inboard-up rotation, the lift and lift-to-drag ratio worsened with increasingly negative propeller thrust. This is due to the reduced dynamic pressure in the propeller slipstream compared to the freestream, and the reversal of the swirl compared to the conventional case with positive thrust. In energy-harvesting mode a reduction of lift-to-drag ratio of about 25% was observed. The decrease in lift-to-drag ratio was reflected in the slipstream by an increase in average swirl from upstream of the wing to downstream. For outboard-up propeller rotation, the interaction phenomena were reversed compared to the inboard-up rotation case. Improved wing performance was achieved at negative thrust conditions as a maximum increase in wing lift-to-drag ratio of near 50% was obtained compared to the propeller-off case. This is however not at constant lift coefficient.

For the pusher-propeller mounted on a planar wing, the upstream effect of the propeller on the wing performance was investigated with an actuator-disk representation of the propeller in multiple wing simulations and was found to be very limited for the tested thrust levels. This was a requirement for the taken approach as the propellers were designed using the flowfield from the isolated propeller simulation. However, a trend of increasing wing lift coefficient and decreasing lift-to-drag ratio was observed with increasing propeller thrust, which may become significant for higher thrust levels than currently investigated.

A stronger upstream effect was found for the compound helicopter, as the propellers were relatively larger and produced relatively higher thrust. The propellers increased lift on the box-wing, through a lift increase of the lower wing and a smaller lift decrease of the upper wing. The propellers increased drag of the upper and lower wings, thereby decreasing the wing lift-to-drag ratio. This is likely a result of the increased axial velocity upstream of the propeller.

SWIRL-RECOVERY-VANES

It was shown that the tangential velocity in the propeller slipstream was reduced by the installation of the swirl-recovery-vanes. As the design of these vanes was such that it underperformed in terms of thrust production compared to what is found in literature, and considering the scope of the dissertation, the focus of this study was on the (unsteady) interaction effects and not on the possible performance enhancement. As the SRVs are located in the propeller slipstream, a much stronger downstream interaction was found than the the upstream effect of the SRVs on the propeller.

Apart from the changing time-averaged vane loading with propeller operating condition, impingement of the propeller blade wakes and tip vortices resulted in unsteady loading on the SRVs varying with the blade-passage frequency. Especially the effect of the tip-vortices was found to be strong, resulting in unsteady loading near the tip of the SRV which was one order of magnitude larger than on the rest of the vane. This was especially the case for the highest investigated thrust condition due to the additional contraction in the slipstream and thus smaller blade tip-vortex–SRV spacing and the increase in blade tip-vortex strength. Averaged over the span, the peak-to-peak amplitude of the unsteady SRV loading was equal to approximately 20% of the time-averaged result for all investigated advance ratios.

8.2. RECOMMENDATIONS

The following recommendations were made throughout the dissertation, split in recommendations related to interaction effects analysis, design and propeller modelling.

INTERACTION EFFECTS ANALYSIS

The interaction between two propellers was studied experimentally in configurations similar to what is found on eVTOL vehicle concepts. However, in these concepts, often wings and other aerodynamic surfaces are present as well. It is recommended to use the presented data as a validated starting point for specific analyses with more realistic geometry, as the influence of the other object can be significant.

The propeller interaction study focussed on the time-averaged effects of interaction on the propeller loading quantities and theories were established on the occurring interaction effects. In order to prove these theories, more detailed flowfield visualisation from an experiment or simulation and temporal analysis of the propeller blade loading are recommended.

For the compound helicopter configuration only the time-averaged effect of the main rotor was modelled with an actuator-disk. The effect of the main rotor was especially noticeable on the propeller performance in the hover condition. It is recommended to investigate the time-dependent effect of the main rotor in this interaction, possibly with an actuator-line simulation to maintain reduced computational cost over resolving the blades of the main rotor.

DESIGN

It is still an open question whether the wingtip-mounted pusher or tractor variant offers the highest integration benefit in terms of propeller and wing aerodynamic performance

improvement. Not only blade optimisation but also wing shape optimisation for each case separately would be required for a fair comparison.

For the wingtip-mounted propeller in tractor configuration, the study of the effects of windmilling were performed with a propeller not designed specifically for power extraction. A propeller could be optimised to deliver thrust efficiently in one condition and extract power efficiently in a different condition. It is recommended to study the effects of propeller design changes on the downstream wingtip loading.

Similar to the open question on the efficiency benefit of wingtip-mounted propellers in tractor versus pusher configuration, the effects of windmilling could be investigated in such a comparative study. As the pusher propeller experiences a beneficial rotational inflow, and Ref. [224] has shown that this could be used for power extraction with a turbine, the requirement of power extraction could possibly be the deciding factor in the question whether to use a pusher or tractor propeller for aerodynamic performance improvement.

Other research on SRVs has shown the possible propulsive efficiency benefits attainable with SRVs with improved designs compared to the SRVs used in this work. However, still lacking is a design study with variable pitch SRVs. Considering the range of swirl angle SRVs experience with changing operating condition of the propeller, a variable pitch design would possibly be worthwhile, in order to align the vanes optimally with the oncoming slipstream and prevent flow separation.

PROPELLER MODELLING

The actuator-disk and actuator-line model were tested in their most accurate form, by extracting the propeller blade loading from blade-resolving RANS simulations. Of course, this did not result in a reduction of computational cost as the blade-resolving simulations were still required. For a future application, the most promising approach to use actuator models is by predicting the loading on the propeller and applying that to the actuator model as a response to the inflow occurring in the CFD simulation. This requires sectional data corrected for the three-dimensional flow effects occurring on the propeller blade. The difficulty lies in the extraction of the flowfield variables, since the local effect of the source terms on the inflow needs to be corrected for.

The presented results in this dissertation provide insight in the possible effects of aerodynamic interaction on the propeller loading through study of five different configurations. However, it is also shown that every specific layout comes with its own peculiarities which may change the balance of performance increasing and decreasing effects that occur in a rotation. It is recommended to perform detailed study of propeller interaction for a concept vehicle, as aerodynamic interaction may have large effects on propeller power demand and may also introduce in-plane forces and out-of-plane moments that affect vehicle stability. This work provides a starting point for such analyses in terms of available methods, experimental datasets for validation and magnitude of possible interaction effects.

REFERENCES

- [1] Knaack, M. S., *Encyclopedia of US Air Force aircraft and missile systems*, Vol. 2, Office of Air Force History, Washington, D.C., 1978.
- [2] Anon, "Lear Fan Collapses," *Flight international*, 1985, p. 30.
- [3] Betz, A., *Introduction to the Theory of Flow Machines*, first english edition ed., Pergamon Press, 1966.
- [4] McLemore, H. C., "Wind-Tunnel Tests of a 1/20-Scale Airship Model with Stern Propellers," Technical Note D-1026, NASA, Langley Field, Virginia, Jan. 1962.
- [5] Goldschmied, F. R., and Goldschmied, P. E., "Aerodynamic Design of Low-Speed Aircraft with a NASA Fuselage/Wake-Propeller Configuration," *AIAA/AHS/ASSEE Aircraft Systems, Design and Technology Meeting*, AIAA Paper 1986-2693, Dayton, Ohio, 1986. doi:10.2514/6.1986-2693.
- [6] Anon, "The Wing," *Flight*, 1947, pp. a–b, 241.
- [7] Anderson, E., *Northrop: An Aeronautical History*, Northrop Corporation, Los Angeles, 1976.
- [8] Strack, W. C., Knip, G., Weisbrich, A. L., Godston, J., and Bradley, E., "Technology and Benefits of Aircraft Counter Rotation Propellers," Technical Memorandum 82983, NASA, Cleveland, Ohio, Oct. 1982.
- [9] Gazzaniga, J., and Rose, G., "Wind Tunnel Performance Results of Swirl Recovery Vanes as Tested with an Advanced High Speed Propeller," *28th Joint Propulsion Conference and Exhibit*, AIAA Paper 1992-3770, Nashville, Tennessee, 1992. doi: 10.2514/6.1992-3770.
- [10] Garrison, P., "Little Bighorn With Wings," *Aviation History*, 2019.
- [11] Anon, "Beech Buys Rutan Technology," *Flight international*, 1985, p. 15.
- [12] Yin, J., Stuermer, A., and Aversano, M., "Aerodynamic and Aeroacoustic Analysis of Installed Pusher-Propeller Aircraft Configurations," *Journal of Aircraft*, Vol. 49, No. 5, 2012, pp. 1423–1433. doi:10.2514/1.C031704.
- [13] Wright, T., "Why There Will Never Be Another Flying Pancake." *Air & Space Magazine*, 2013.
- [14] Loth, J. L., and Loth, F., "Induced Drag Reduction with Wing Tip Mounted Propellers," *2nd Applied Aerodynamics Conference*, AIAA Paper 1984-2149, Seattle, Washington, 1984. doi:10.2514/6.1984-2149.

- [15] Miranda, L. R., and Brennan, J. E., "Aerodynamic Effects of Wingtip-Mounted Propellers and Turbines," *4th Applied Aerodynamics Conference*, AIAA Paper 1986-1802, San Diego, California, 1986. doi:10.2514/6.1986-1802.
- [16] Sinnige, T., van Arnhem, N., Stokkermans, T. C. A., Eitelberg, G., and Veldhuis, L. L. M., "Wingtip-Mounted Propellers: Aerodynamic Analysis of Interaction Effects and Comparison with Conventional Layout," *Journal of Aircraft*, Vol. 56, No. 1, 2018, pp. 295–312. doi:10.2514/1.C034978.
- [17] Deere, K. A., Viken, J. K., Viken, S., Carter, M. B., Wiese, M., and Farr, N., "Computational Analysis of a Wing Designed for the X-57 Distributed Electric Propulsion Aircraft," *35th AIAA Applied Aerodynamics Conference*, AIAA Paper 2017-3923, Denver, Colorado, 2017. doi:10.2514/6.2017-3923.
- [18] Steiner, H.-J., Seitz, A., Wieczorek, K., Plötner, K., Isikveren, A. T., and Hornung, M., "Multi-Disciplinary Design and Feasibility Study of Distributed Propulsion Systems," *28th International Congress of the Aeronautical Sciences*, Brisbane, Australia, 2012, pp. 23–28.
- [19] Stoll, A. M., and Veble Mikić, G., "Design Studies of Thin-Haul Commuter Aircraft with Distributed Electric Propulsion," *16th AIAA Aviation Technology, Integration, and Operations Conference*, AIAA Paper 2016-3765, Washington, D.C., 2016. doi:10.2514/6.2016-3765.
- [20] Jansen, R., Bowman, C., Jankovsky, A., Dyson, R., and Felder, J., "Overview of NASA Electrified Aircraft Propulsion (EAP) Research for Large Subsonic Transports," *53rd AIAA/SAE/ASEE Joint Propulsion Conference*, AIAA Paper 2017-4701, Atlanta, Georgia, 2017. doi:10.2514/6.2017-4701.
- [21] de Vries, R., Hoogreef, M., and Vos, R., "Preliminary Sizing of a Hybrid-Electric Passenger Aircraft Featuring Over-the-Wing Distributed-Propulsion," *AIAA Scitech 2019 Forum*, AIAA Paper 2019-1811, San Diego, California, 2019. doi:10.2514/6.2019-1811.
- [22] de Vries, R., Brown, M., and Vos, R., "Preliminary Sizing Method for Hybrid-Electric Distributed-Propulsion Aircraft," *Journal of Aircraft*, Vol. 56, No. 6, 2019, pp. 2172–2188. doi:10.2514/1.C035388.
- [23] Schmollgruber, P., Atinault, O., Cafarelli, I., Döll, C., François, C., Hermetz, J., Liboeruf, R., Paluch, B., and Ridel, M., "Multidisciplinary Exploration of DRAGON: An ONERA Hybrid Electric Distributed Propulsion Concept," *AIAA Scitech 2019 Forum*, AIAA Paper 2019-1585, San Diego, California, 2019. doi:10.2514/6.2019-1585.
- [24] Anon, "Fairy Gyrodyne," *Flight*, 1949, pp. 453–459.
- [25] "The Fairy FB-1 Gyrodyne," *Jane's All The World's Aircraft 1948*, edited by L. Bridgman, Sampson Low, Marston & Company, Ltd., London, 1948.

- [26] Houston, S. S., "The Gyrodyne—A Forgotten High Performer?" *Journal of the American Helicopter Society*, Vol. 52, No. 4, 2007, pp. 382–391. doi:10.4050/JAHS.52.382.
- [27] Ormiston, R. A., "Revitalizing Advanced Rotorcraft Research—And the Compound Helicopter: 35th AHS Alexander A. Nikolsky Honorary Lecture," *Journal of the American Helicopter Society*, Vol. 61, No. 1, 2016, pp. 1–23. doi:10.4050/JAHS.61.011001.
- [28] Yeo, H., and Johnson, W., "Optimum Design of a Compound Helicopter," *Journal of Aircraft*, Vol. 46, No. 4, 2009, pp. 1210–1221. doi:10.2514/1.40101.
- [29] Enconniere, J., Ortiz-Carretero, J., and Pachidis, V., "Mission Performance Analysis of a Conceptual Coaxial Rotorcraft for Air Taxi Applications," *Aerospace Science and Technology*, Vol. 69, 2017, pp. 1–14. doi:10.1016/j.ast.2017.06.015.
- [30] Yeo, H., "Design and Aeromechanics Investigation of Compound Helicopters," *Aerospace Science and Technology*, Vol. 88, 2019, pp. 158–173. doi:10.1016/j.ast.2019.03.010.
- [31] Airbus, "Airbus Helicopters Reveals Racer High-Speed Demonstrator Configuration," <https://www.airbus.com/newsroom/press-releases/en/2017/06/Airbus-Helicopters-reveals-Racer-high-speed-demonstrator-configuration.html>, Jun. 2017.
- [32] Lienard, C., Salah el Din, I., Renaud, T., and Fukari, R., "RACER High-Speed Demonstrator: Rotor and Rotor-Head Wake Interactions with Tail Unit," *AHS International 74th Annual Forum & Technology Display*, Phoenix, Arizona, 2018.
- [33] Andrews, S. A., and Perez, R. E., "Comparison of Box-Wing and Conventional Aircraft Mission Performance Using Multidisciplinary Analysis and Optimization," *Aerospace Science and Technology*, Vol. 79, 2018, pp. 336–351. doi:10.1016/j.ast.2018.05.060.
- [34] Patterson Jr, J. C., and Bartlett, G. R., "Effect of a Wing-Tip Mounted Pusher Turboprop on the Aerodynamic Characteristics of a Semi-Span Wing," *AIAA/SAE/ASME/ASEE 21st Joint Propulsion Conference*, AIAA Paper 1985-1286, Monterey, California, 1985. doi:10.2514/6.1985-1286.
- [35] Patterson Jr, J. C., and Bartlett, G. R., "Evaluation of Installed Performance of a Wing-Tip-Mounted Pusher Turboprop on a Semispan Wing," Technical Paper 2739, NASA, Hampton, Virginia, Aug. 1987.
- [36] Janus, J. M., Chatterjee, A., and Cave, C., "Computational Analysis of a Wingtip-Mounted Pusher Turboprop," *Journal of Aircraft*, Vol. 33, No. 2, 1996, pp. 441–444. doi:10.2514/3.46959.
- [37] Perry, D., "X3 Breaks Helicopter Speed Record," <https://www.flightglobal.com/news/articles/x3-breaks-helicopter-speed-record-386956/>, Jun. 2013.

- [38] Brelje, B. J., and Martins, J. R. R. A., “Electric, Hybrid, and Turboprop Fixed-Wing Aircraft: A Review of Concepts, Models, and Design Approaches,” *Progress in Aerospace Sciences*, Vol. 104, 2019, pp. 1–19. doi:10.1016/j.paerosci.2018.06.004.
- [39] Anon, “Aircraft Electrical Propulsion – The Next Chapter of Aviation?” Tech. rep., Roland Berger, Sep. 2017.
- [40] Anon, “Flying Cars: Investment Implications of Autonomous Urban Air Mobility,” Tech. rep., Morgan Stanley Research, 2018.
- [41] Anon, “Fast-Forwarding to a Future of On-Demand Urban Air Transportation,” Whitepaper, Uber, Oct. 2016.
- [42] Johnson, W., Silva, C., and Solis, E., “Concept Vehicles for VTOL Air Taxi Operations,” *AHS Technical Conference on Aeromechanics Design for Transformative Vertical Flight*, San Francisco, California, 2018.
- [43] Kim, H. D., Perry, A. T., and Ansell, P. J., “A Review of Distributed Electric Propulsion Concepts for Air Vehicle Technology,” *2018 AIAA/IEEE Electric Aircraft Technologies Symposium*, AIAA Paper 2018-4998, Cincinnati, Ohio, 2018. doi:10.2514/6.2018-4998.
- [44] Kraenzler, M., Schmitt, M., and Stumpf, E., “Conceptual Design Study on Electrical Vertical Take Off and Landing Aircraft for Urban Air Mobility Applications,” *AIAA Aviation 2019 Forum*, AIAA Paper 2019-3124, Dallas, Texas, 2019. doi:10.2514/6.2019-3124.
- [45] Kasliwal, A., Furbush, N. J., Gawron, J. H., McBride, J. R., Wallington, T. J., Kleine, R. D. D., Kim, H. C., and Keoleian, G. A., “Role of Flying Cars in Sustainable Mobility,” *Nature Communications*, Vol. 10, No. 1, 2019, pp. 1–9. doi:10.1038/s41467-019-09426-0.
- [46] Anon, “Cora Fact Sheet,” <https://cora.aero/press/>, Sep. 2019.
- [47] Droandi, G., Syal, M., and Geoffrey, B., “Tiltwing Multi-Rotor Aerodynamic Modeling in Hover, Transition and Cruise Flight Conditions,” *AHS International 74th Annual Forum & Technology Display*, Phoenix, Arizona, 2018.
- [48] Silva, C., Johnson, W. R., Solis, E., Patterson, M. D., and Antcliff, K. R., “VTOL Urban Air Mobility Concept Vehicles for Technology Development,” *2018 Aviation Technology, Integration, and Operations Conference*, AIAA Paper 2018-3847, Atlanta, Georgia, 2018. doi:10.2514/6.2018-3847.
- [49] Veldhuis, L. L. M., “Propeller Wing Aerodynamic Interference,” Dissertation, Delft University of Technology, Delft, The Netherlands, Jun. 2005.
- [50] Stuermer, A., and Yin, J., “Pylon Trailing Edge Blowing for the Control of CROR Unsteady Blade Loads,” *New Results in Numerical and Experimental Fluid Mechanics VIII: Contributions to the 17th STAB/DGLR Symposium Berlin, Germany 2010*, edited by A. Dillmann, G. Heller, H.-P. Kreplin, W. Nitsche, and I. Peltzer, Notes on

- Numerical Fluid Mechanics and Multidisciplinary Design, Springer Berlin Heidelberg, Berlin, Heidelberg, 2013, pp. 715–722. doi:10.1007/978-3-642-35680-3_85.
- [51] Glauert, H., “Airplane Propellers,” *Aerodynamic Theory: A General Review of Progress*, Vol. 4, edited by W. F. Durand, Julius Springer, Berlin, 1935, pp. 169–360.
- [52] Droandi, G., Gibertini, G., Grassi, D., Campanardi, G., and Liprino, C., “Propropeller–Wing Aerodynamic Interaction in the First Stages of Conversion from Helicopter to Aeroplane Mode,” *Aerospace Science and Technology*, Vol. 58, 2016, pp. 116–133. doi:10.1016/j.ast.2016.08.013.
- [53] Godston, J., and Reynolds, C., “Future Prop-Fans – Tractor or Pusher,” *21st Joint Propulsion Conference*, AIAA Paper 1985-1189, Monterey, California, 1985. doi: 10.2514/6.1985-1189.
- [54] Propeller, *Merriam-Webster*, 2019.
- [55] Propeller, *Lexico*, 2019.
- [56] Rotor, *Merriam-Webster*, 2019.
- [57] Rotor, *Lexico*, 2019.
- [58] Airscrew, *Merriam-Webster*, 2019.
- [59] Airscrew, *Lexico*, 2019.
- [60] Fan, *Lexico*, 2019.
- [61] Fan, *Merriam-Webster*, 2019.
- [62] Propfan, *Lexico*, 2019.
- [63] Stokkermans, T. C. A., Van Arnhem, N., and Veldhuis, L. L. M., “Mitigation of Propeller Kinetic Energy Losses with Boundary Layer Ingestion and Swirl Recovery Vanes,” *Proceedings of the 2016 Applied Aerodynamics Research Conference*, Royal Aeronautical Soc. London, Bristol, United Kingdom, 2016, pp. 56–69.
- [64] Stokkermans, T. C. A., van Arnhem, N., Sinnige, T., and Veldhuis, L. L. M., “Validation and Comparison of RANS Propeller Modeling Methods for Tip-Mounted Applications,” *AIAA Journal*, Vol. 57, No. 2, 2018, pp. 566–580. doi:10.2514/1.J057398.
- [65] Stokkermans, T. C. A., Nootbos, S., and Veldhuis, L. L. M., “Analysis and Design of a Small-Scale Wingtip-Mounted Pusher Propeller,” *AIAA Aviation 2019 Forum*, AIAA Paper 2019-3693, Dallas, Texas, 2019. doi:10.2514/6.2019-3693.
- [66] Sinnige, T., Stokkermans, T. C. A., van Arnhem, N., and Veldhuis, L. L. M., “Aerodynamic Performance of a Wingtip-Mounted Tractor Propeller Configuration in Windmilling and Energy-Harvesting Conditions,” *AIAA Aviation 2019 Forum*, AIAA Paper 2019-3033, Dallas, Texas, 2019. doi:10.2514/6.2019-3033.

- [67] Stokkermans, T. C. A., Usai, D., Sinnige, T., and Veldhuis, L. L. M., "Aerodynamic Interaction Effects between Propellers in Typical eVTOL Vehicle Configurations," (under review).
- [68] Sinnige, T., Stokkermans, T. C. A., Ragni, D., Eitelberg, G., and Veldhuis, L. L. M., "Aerodynamic and Aeroacoustic Performance of a Propeller Propulsion System with Swirl-Recovery Vanes," *Journal of Propulsion and Power*, Vol. 34, No. 6, 2018, pp. 1376–1390. doi:10.2514/1.B36877.
- [69] Stokkermans, T. C. A., Voskuil, M., Veldhuis, L. L. M., Soemarwoto, B., Fukari, R., and Eglin, P., "Aerodynamic Installation Effects of Lateral Rotors on a Novel Compound Helicopter Configuration," *AHS International 74th Annual Forum & Technology Display*, Phoenix, Arizona, 2018.
- [70] Stokkermans, T., Veldhuis, L., Soemarwoto, B., Fukari, R., and Eglin, P., "Breakdown of Aerodynamic Interactions for the Lateral Rotors on a Compound Helicopter," *Aerospace Science and Technology*, Vol. 101, 2020, p. 105845. doi:10.1016/j.ast.2020.105845.
- [71] Stokkermans, T. C. A., and Veldhuis, L. L. M., "Propeller Performance at Large Angle of Attack Applicable to Compound Helicopters," (under review).
- [72] Ortun, B., Boisard, R., and Gonzalez-Martino, I., "In-Plane Airloads of a Propeller with Inflow Angle: Prediction vs. Experiment," *30th AIAA Applied Aerodynamics Conference*, AIAA Paper 2012-2778, New Orleans, Louisiana, 2012. doi:10.2514/6.2012-2778.
- [73] McLemore, H. C., and Cannon, M. D., "Aerodynamic Investigation of a Four-Blade Propeller Operating Through an Angle-of-Attack Range from 0 Deg to 180 Deg," Technical Note 3228, NACA, Langley Field, Virginia, Jun. 1954.
- [74] Smith, H. R., "Engineering Models of Aircraft Propellers at Incidence," Dissertation, University of Glasgow, Glasgow, United Kingdom, 2015.
- [75] Samuelsson, I., "Experimental Investigation of Low Speed Model Propeller Slipstream Aerodynamic Characteristics Including Flow Field Surveys and Nacelle/Wing Static Pressure Measurements," *17th Congress of the International Council of the Aeronautical Sciences*, Stockholm, Sweden, 1990, pp. 71–84.
- [76] Smith, L. H., "Wake Ingestion Propulsion Benefit," *Journal of Propulsion and Power*, Vol. 9, No. 1, 1993, pp. 74–82. doi:10.2514/3.11487.
- [77] Drela, M., "Power Balance in Aerodynamic Flows," *AIAA journal*, Vol. 47, No. 7, 2009, pp. 1761–1771. doi:10.2514/1.42409.
- [78] Kim, H. D., and Felder, J. L., "Control Volume Analysis of Boundary Layer Ingesting Propulsion Systems with or without Shock Wave Ahead of the Inlet," *49th AIAA Aerospace Sciences Meeting*, AIAA Paper 2011-222, Orlando, Florida, 2011. doi:10.2514/6.2011-222.

- [79] Arntz, A., Atinault, O., Destarac, D., and Merlen, A., "Exergy-Based Aircraft Aero-propulsive Performance Assessment: CFD Application to Boundary Layer Ingestion," *32nd AIAA Applied Aerodynamics Conference*, AIAA Paper 2014-2573, Atlanta, Georgia, 2014. doi:10.2514/6.2014-2573.
- [80] Seitz, A., Peter, F., Bijewitz, J., Habermann, A., Goraj, Z., Kowalski, M., Castillo Pardo, A., Hall, C., Meller, F., Merkler, R., Petit, O., Samuelsson, S., Della Corte, B., van Sluis, M., Wortmann, G., and Dietz, M., "Concept Validation Study for Fuselage Wake-Filling Propulsion Integration," *31st Congress of the International Council of the Aeronautical Sciences*, Belo Horizonte, Brazil, 2018.
- [81] Van Manen, J. D., "Invloed van de ongelijkmatigheid van het snelheidsveld op het ontwerp van scheepsschroeven," Dissertation, Delft University of Technology, Delft, The Netherlands, Jul. 1951.
- [82] Hirner, A., Dorn, F., Lutz, T., and Krämer, E., "Improvement of Propulsive Efficiency by Dedicated Stern Thruster Design," *7th AIAA Aviation Technology, Integration and Operations Conference*, AIAA Paper 2007-7702, Belfast, Northern Ireland, 2007. doi:10.2514/6.2007-7702.
- [83] Lv, P., and Rao, A. G., "Conceptual Analysis of Boundary Layer Ingestion towards Aircraft Propulsion Integration," *The XXI International Symposium of Air Breathing Engines*, Busan, Korea, 2013.
- [84] Atinault, O., Carrier, G., Grenon, R., Verbecke, C., and Viscat, P., "Numerical and Experimental Aerodynamic Investigations of Boundary Layer Ingestion for Improving Propulsion Efficiency of Future Air Transport," *31st AIAA Applied Aerodynamics Conference*, AIAA Paper 2013-2406, San Diego, California, 2013. doi:10.2514/6.2013-2406.
- [85] Bousquet, J. M., and Gardarein, P., "Improvements on Computations of High Speed Propeller Unsteady Aerodynamics," *Aerospace Science and Technology*, Vol. 7, No. 6, 2003, pp. 465–472. doi:10.1016/S1270-9638(03)00046-4.
- [86] Roosenboom, E. W. M., Stürmer, A., and Schröder, A., "Advanced Experimental and Numerical Validation and Analysis of Propeller Slipstream Flows," *Journal of Aircraft*, Vol. 47, No. 1, 2010, pp. 284–291. doi:10.2514/1.45961.
- [87] Moore, M. D., and Fredericks, B., "Misconceptions of Electric Propulsion Aircraft and Their Emergent Aviation Markets," *52nd Aerospace Sciences Meeting*, AIAA Paper 2014-0535, National Harbor, Maryland, 2014. doi:10.2514/6.2014-0535.
- [88] Borer, N. K., Patterson, M. D., Viken, J. K., Moore, M. D., Clarke, S., Redifer, M. E., Christie, R. J., Stoll, A. M., Dubois, A., Bevirt, J., Gibson, A. R., Foster, T. J., and Osterkamp, P. G., "Design and Performance of the NASA SCEPTOR Distributed Electric Propulsion Flight Demonstrator," *16th AIAA Aviation Technology, Integration, and Operations Conference*, AIAA Paper 2016-3920, Washington, D.C., 2016. doi:10.2514/6.2016-3920.

- [89] Sinnige, T., Ragni, D., Eitelberg, G., and Veldhuis, L. L. M., "Mitigation of Pusher-Propeller Installation Effects by Pylon Trailing-Edge Blowing," *Journal of Aircraft*, Vol. 54, No. 1, 2016, pp. 292–300. doi:10.2514/1.C034000.
- [90] Goldsmith, I. M., "A Study to Define the Research and Technology Requirements for Advanced Turbo/Propfan Transport Aircraft," NASA Contractor Report 166138, McDonnell Douglas Corporation, Douglas Aircraft Company, Long Beach, California, Feb. 1981.
- [91] van Arnhem, N., de Vries, R., Vos, R., and Veldhuis, L. L. M., "Aerodynamic Performance of an Aircraft Equipped with Horizontal Tail Mounted Propellers," *AIAA Aviation 2019 Forum*, AIAA Paper 2019-3036, Dallas, Texas, 2019. doi:10.2514/6.2019-3036.
- [92] Kim, S.-E., and Rhee, S. H., "Efficient Engineering Prediction of Turbulent Wing Tip Vortex Flows," *Computer Modeling in Engineering & Sciences (CMES)*, Vol. 62, No. 3, 2010, pp. 291–309. doi:10.3970/cmcs.2010.062.291.
- [93] Gomariz-Sancha, A., Maina, M., and Peace, A. J., "Analysis of Propeller-Airframe Interaction Effects through a Combined Numerical Simulation and Wind-Tunnel Testing Approach," *53rd AIAA Aerospace Sciences Meeting*, AIAA Paper 2015-1026, Kissimmee, Florida, 2015. doi:10.2514/6.2015-1026.
- [94] Moens, F., and Gardarein, P., "Numerical Simulation of the Propeller/Wing Interactions for Transport Aircraft," *19th AIAA Applied Aerodynamics Conference*, AIAA Paper 2001-2404, Anaheim, California, 2001. doi:10.2514/6.2001-2404.
- [95] Troldborg, N., Sørensen, J. N., and Mikkelsen, R., "Actuator Line Simulation of Wake of Wind Turbine Operating in Turbulent Inflow," *Journal of Physics: Conference Series*, Vol. 75, No. 1, 2007, p. 012063. doi:10.1088/1742-6596/75/1/012063.
- [96] Troldborg, N., "Actuator Line Modeling of Wind Turbine Wakes," Dissertation, Technical University of Denmark, Copenhagen, Denmark, 2009.
- [97] Chirico, G., Szubert, D., Vigevano, L., and Barakos, G., "Numerical Modelling of the Aerodynamic Interference between Helicopter and Ground Obstacles," *CEAS Aeronautical Journal*, Vol. 8, No. 4, 2017, pp. 589–611. doi:10.1007/s13272-017-0259-y.
- [98] MacCready, P., "Regenerative Battery-Augmented Soaring," *Technical Soaring*, Vol. 23, No. 1, 1999, pp. 28–32.
- [99] Barnes, J. P., "Flight Without Fuel – Regenerative Soaring Feasibility Study," *General Aviation Technology Conference & Exhibition*, SAE Technical Paper 2006-01-2422, Wichita, Kansas, 2006. doi:10.4271/2006-01-2422.
- [100] Galvao, F., "A Note on Glider Electric Propulsion," *Technical Soaring*, Vol. 36, No. 4, 2012, pp. 94–101.

- [101] Erzen, D., Andrejasic, M., and Kosel, T., "An Optimal Propeller Design for In-Flight Power Recuperation on an Electric Aircraft," *2018 Aviation Technology, Integration, and Operations Conference*, AIAA Paper 2018-3206, Atlanta, Georgia, 2018. doi:10.2514/6.2018-3206.
- [102] Miller, C. J., "Euler Analysis of a Swirl Recovery Vane Design for Use with an Advanced Single-Rotation Propfan," *24th Joint Propulsion Conference*, AIAA Paper 1988-3152, Boston, Massachusetts, 1988. doi:10.2514/6.1988-3152.
- [103] Yamamoto, O., "Numerical Calculations of Propfan/Swirl Recovery Vane Flow Field," *28th Joint Propulsion Conference and Exhibit*, AIAA Paper 1992-3771, Nashville, Tennessee, 1992. doi:10.2514/6.1992-3771.
- [104] Dittmar, J. H., and Hall, D. G., "Cruise Noise of an Advanced Propeller with Swirl Recovery Vanes," *Journal of aircraft*, Vol. 30, No. 2, 1993, pp. 221–226. doi:10.2514/3.56885.
- [105] Wang, Y., Li, Q., Eitelberg, G., Veldhuis, L. L. M., and Kotsonis, M., "Design and Numerical Investigation of Swirl Recovery Vanes for the Fokker 29 Propeller," *Chinese Journal of Aeronautics*, Vol. 27, No. 5, 2014, pp. 1128–1136. doi:10.1016/j.cja.2014.03.009.
- [106] Sinnige, T., van Kuijk, J. J., Lynch, K. P., Ragni, D., Eitelberg, G., and Veldhuis, L. L. M., "The Effects of Swirl Recovery Vanes on Single-Rotation Propeller Aerodynamics and Aeroacoustics," *21st AIAA/CEAS Aeroacoustics Conference*, AIAA Paper 2015-2358, Dallas, Texas, 2015. doi:10.2514/6.2015-2358.
- [107] Stokkermans, T. C. A., "Design and Analysis of Swirl Recovery Vanes for an Isolated and a Wing Mounted Tractor Propeller," Master's Thesis, Delft University of Technology, Delft, The Netherlands, Aug. 2015.
- [108] Li, Q., "Towards Optimum Swirl Recovery for Propeller Propulsion Systems," Dissertation, Delft University of Technology, Delft, The Netherlands, 2019.
- [109] Weinig, F., *Aerodynamik der Luftschraube*, Julius Springer, Berlin, 1940.
- [110] Çelik, F., and Güner, M., "Energy Saving Device of Stator for Marine Propellers," *Ocean Engineering*, Vol. 34, No. 5, 2007, pp. 850–855. doi:10.1016/j.oceaneng.2006.03.016.
- [111] Lummer, M., Akkermans, R. A., Richter, C., Präber, C., and Delfs, J., "Validation of a Model for Open Rotor Noise Predictions and Calculation of Shielding Effects Using a Fast BEM," *19th AIAA/CEAS Aeroacoustics Conference*, AIAA Paper 2013-2096, Berlin, Germany, 2013. doi:10.2514/6.2013-2096.
- [112] Kennedy, J., Eret, P., and Bennett, G., "A Parametric Study of Installed Counter Rotating Open Rotors," *19th AIAA/CEAS Aeroacoustics Conference*, AIAA Paper 2013-2094, Berlin, Germany, 2013. doi:10.2514/6.2013-2094.

- [113] Stuermer, A. W., "Validation of uRANS-Simulations of Contra-Rotating Open Rotor-Powered Aircraft at Take-Off Conditions," *2018 AIAA Aerospace Sciences Meeting*, AIAA Paper 2018-1265, Kissimmee, Florida, 2018. doi:10.2514/6.2018-1265.
- [114] Yin, J. P., and Ahmed, S. R., "Helicopter Main-Rotor/Tail-Rotor Interaction," *Journal of the American helicopter society*, Vol. 45, No. 4, 2000, pp. 293–302. doi:10.4050/JAHS.45.293.
- [115] Coleman, C. P., "A Survey of Theoretical and Experimental Coaxial Rotor Aerodynamic Research," NASA Technical Paper 3675, NASA, Moffett Field, California, 1997.
- [116] Heyson, H. H., "Preliminary Results From Flow-Field Measurements Around Single and Tandem Rotors in the Langley Full-Scale Tunnel," Technical Note 3242, NACA, Langley Field, Virginia, Nov. 1954.
- [117] Dingeldein, R. C., "Wind-Tunnel Studies of the Performance of Multirotor Configurations," Technical Note 3236, NACA, Langley Field, Virginia, Aug. 1954.
- [118] Stepniewski, W. Z., and Keys, C. N., *Rotary-Wing Aerodynamics*, Dover Publications, New York, 1984.
- [119] Lee, J.-W., Oh, S.-J., Yee, K.-J., and Kim, D.-K., "Numerical Investigation on Overlap Effects of Tandem Rotors in Forward Flight," *International Journal of Aeronautical and Space Sciences*, Vol. 10, No. 2, 2009, pp. 63–76.
- [120] Anon, "PAV – eVTOL Passenger Air Vehicle," <https://www.aurora.aero/pav-evtol-passenger-air-vehicle/>, 2019.
- [121] Ventura Diaz, P., Johnson, W., Ahmad, J., and Yoon, S., "The Side-by-Side Urban Air Taxi Concept," *AIAA Aviation 2019 Forum*, AIAA Paper 2019-2828, Dallas, Texas, 2019. doi:10.2514/6.2019-2828.
- [122] Stoll, A. M., Bevirt, J., Pei, P. P., and Stilson, E. V., "Conceptual Design of the Joby S2 Electric VTOL PAV," *14th AIAA Aviation Technology, Integration, and Operations Conference*, AIAA Paper 2014-2407, Atlanta, Georgia, 2014. doi:10.2514/6.2014-2407.
- [123] Sweet, G. E., "Hovering Measurements for Twin-Rotor Configurations with and without Overlap," Technical Note D-534, NASA, Langley Field, Virginia, 1960.
- [124] Harris, F. D., "Technical Note: Twin Rotor Hover Performance," *Journal of the American Helicopter Society*, Vol. 44, No. 1, 1999, pp. 34–37. doi:10.4050/JAHS.44.34.
- [125] Ramasamy, M., "Measurements Comparing Hover Performance of Single, Coaxial, Tandem, and Tilt-Rotor Configurations," *AHS International Forum 69*, Phoenix, Arizona, 2013.

- [126] Ramasamy, M., "Hover Performance Measurements toward Understanding Aerodynamic Interference in Coaxial, Tandem, and Tilt Rotors," *Journal of the American Helicopter Society*, Vol. 60, No. 3, 2015, pp. 1–17. doi:10.4050/JAHS.60.032005.
- [127] Yoon, S., Lee, H. C., and Pulliam, T. H., "Computational Analysis of Multi-Rotor Flows," *54th AIAA Aerospace Sciences Meeting*, AIAA Paper 2016-0812, San Diego, California, 2016. doi:10.2514/6.2016-0812.
- [128] Sheng, C., and Narramore, J. C., "Computational Simulation and Analysis of Bell Boeing Quad Tiltrotor Aero Interaction," *Journal of the American Helicopter Society*, Vol. 54, No. 4, 2009. doi:10.4050/JAHS.54.042002.
- [129] Otsuka, H., and Nagatani, K., "Thrust Loss Saving Design of Overlapping Rotor Arrangement on Small Multirotor Unmanned Aerial Vehicles," *2016 IEEE International Conference on Robotics and Automation (ICRA)*, Stockholm, Sweden, 2016, pp. 3242–3248. doi:10.1109/ICRA.2016.7487494.
- [130] Theys, B., Dimitriadis, G., Hendrick, P., and Schutter, J. D., "Influence of Propeller Configuration on Propulsion System Efficiency of Multi-Rotor Unmanned Aerial Vehicles," *2016 International Conference on Unmanned Aircraft Systems (ICUAS)*, Arlington, Virginia, 2016, pp. 195–201. doi:10.1109/ICUAS.2016.7502520.
- [131] Brazinskas, M., Prior, S. D., and Scanlan, J. P., "An Empirical Study of Overlapping Rotor Interference for a Small Unmanned Aircraft Propulsion System," *Aerospace*, Vol. 3, No. 4, 2016. doi:10.3390/aerospace3040032.
- [132] Nandakumar, G., Srinivasan, A., and Thondiyath, A., "Theoretical and Experimental Investigations on the Effect of Overlap and Offset on the Design of a Novel Quadrotor Configuration, VOOPS," *Journal of Intelligent & Robotic Systems*, Vol. 92, No. 3-4, 2018, pp. 615–628. doi:10.1007/s10846-017-0707-2.
- [133] Zhou, W., Ning, Z., Li, H., and Hu, H., "An Experimental Investigation on Rotor-to-Rotor Interactions of Small UAV Propellers," *35th AIAA Applied Aerodynamics Conference*, AIAA Paper 2017-3744, Denver, Colorado, 2017. doi:10.2514/6.2017-3744.
- [134] Alvarez, E. J., and Ning, A., "Modeling Multirotor Aerodynamic Interactions Through the Vortex Particle Method," *AIAA Aviation 2019 Forum*, AIAA Paper 2019-2827, Dallas, Texas, 2019. doi:10.2514/6.2019-2827.
- [135] Ventura Diaz, P., and Yoon, S., "High-Fidelity Computational Aerodynamics of Multi-Rotor Unmanned Aerial Vehicles," *2018 AIAA Aerospace Sciences Meeting*, AIAA Paper 2018-1266, Kissimmee, Florida, 2018. doi:10.2514/6.2018-1266.
- [136] Wentrup, M., Yin, J., Kunze, P., Streit, T., Wendisch, J.-H., Schwarz, T., Pinacho, J.-P., Kicker, K., and Fukari, R., "An Overview of DLR Compound Rotorcraft Aerodynamics and Aeroacoustics Activities within the CleanSky2 NACOR Project," *AHS International 74th Annual Forum & Technology Display*, Phoenix, Arizona, 2018.

- [137] Thiemeier, J., Öhrle, C., Frey, F., Keßler, M., and Krämer, E., “Aerodynamics and Flight Mechanics Analysis of Airbus Helicopters’ Compound Helicopter RACER in Hover under Crosswind Conditions,” *CEAS Aeronautical Journal*, Vol. 11, 2020, pp. 49–66. doi:10.1007/s13272-019-00392-3.
- [138] Orchard, M., and Newman, S., “The Fundamental Configuration and Design of the Compound Helicopter,” *Proceedings of the Institution of Mechanical Engineers, Part G: Journal of Aerospace Engineering*, Vol. 217, No. 6, 2003, pp. 297–315. doi:10.1243/095441003772538570.
- [139] Bain, L. J., and Landgrebe, A. J., “Investigation of Compound Helicopter Aerodynamic Interference Effects,” Tech. Rep. SER-50474, United Aircraft Corporation, Sikorsky Aircraft Division, Stratford, Connecticut, Nov. 1967.
- [140] Lynn, R. R., “Wing-Rotor Interactions,” *Journal of Aircraft*, Vol. 3, No. 4, 1966, pp. 326–332. doi:10.2514/3.43742.
- [141] Frota, J., and Maury, E., “Analysis of APIAN High Speed Isolated Test Results - Acoustics and Aerodynamics,” *Air & Space Europe*, Vol. 3, No. 3, 2001, pp. 87–92. doi:10.1016/S1290-0958(01)90064-4.
- [142] Sinnige, T., “Aerodynamic and Aeroacoustic Interaction Effects for Tip-Mounted Propellers: An Experimental Study,” Dissertation, Delft University of Technology, Delft, The Netherlands, 2018.
- [143] Li, Q., Öztürk, K., Sinnige, T., Ragni, D., Eitelberg, G., Veldhuis, L., and Wang, Y., “Design and Experimental Validation of Swirl-Recovery Vanes for Propeller Propulsion Systems,” *AIAA Journal*, Vol. 56, No. 12, 2018, pp. 4719–4729. doi:10.2514/1.J057113.
- [144] Li, Q., Liu, X., Eitelberg, G., and Veldhuis, L., “Numerical Investigation of Configurations with Optimum Swirl Recovery for Propeller Propulsion Systems,” *AIAA Journal*, Vol. 57, No. 4, 2019, pp. 1502–1513. doi:10.2514/1.J057704.
- [145] Veldhuis, L. L., Kotsonis, M., and van Berkel, E., “Non-Uniform Inflow Effects on Propeller Performance,” *31st AIAA Applied Aerodynamics Conference*, AIAA Paper 2013-2801, San Diego, California, 2013. doi:10.2514/6.2013-2801.
- [146] Sinnige, T., and Veldhuis, L. L. M., “Pylon Trailing Edge Blowing Effects on the Performance and Noise Production of a Pusher Propeller,” *52nd Aerospace Sciences Meeting*, AIAA Paper 2014-0566, National Harbor, Maryland, 2014. doi:10.2514/6.2014-0566.
- [147] Yang, Y., Sciacchitano, A., Veldhuis, L. L. M., and Eitelberg, G., “Analysis of Propeller-Induced Ground Vortices by Particle Image Velocimetry,” *Journal of Visualization*, Vol. 21, No. 1, 2018, pp. 39–55. doi:10.1007/s12650-017-0439-1.
- [148] Drela, M., and Youngren, H., “XROTOR 7.55 (Computer Software),” MIT, Software, 2011.

- [149] Nahuis, R., and Sinnige, T., “Design, Manufacture and Commissioning of a New NLR Six-Component Rotating Shaft Balance for Delft University of Technology,” *10th International Symposium on Strain-Gauge Balances*, Mianyang, China: China Aerodynamics Research and Development Center, 2016.
- [150] Sayers, A. T., and Ball, D. R., “Blockage Corrections for Rectangular Flat Plates Mounted in an Open Jet Wind Tunnel,” *Proceedings of the Institution of Mechanical Engineers, Part C: Journal of Mechanical Engineering Science*, Vol. 197, No. 4, 1983, pp. 259–263. doi:10.1243/PIME_PROC_1983_197_107_02.
- [151] Hackett, J. E., Ashill, P. R., and Mokry, M., “Wall Correction Methods for Powered Models of Conventional Take Off and Landing Aircraft,” AGARDograph 336, Advisory Group for Aerospace Research and Development, Neuilly-Sur-Seine, France, Oct. 1998.
- [152] Eitelberg, G., “Rotor Corrections,” Personal communication, Delft University of Technology, Delft, The Netherlands, Nov. 2018.
- [153] Langer, H.-J., Peterson, R. L., and Maier, T. H., “An Experimental Evaluation of Wind Tunnel Wall Correction Methods for Helicopter Performance,” *AHS International Forum 52*, Washington, D.C., 1996.
- [154] Barlow, J. B., Rae, W. H., and Pope, A., *Low-Speed Wind Tunnel Testing*, 3rd ed., Wiley-Interscience, New York, 1999.
- [155] Yeo, D., Atkins, E. M., Bernal, L. P., and Shyy, W., “Experimental Validation of an Aerodynamic Sensing Scheme for Post-Stall Aerodynamic Moment Characterization,” *AIAA Atmospheric Flight Mechanics (AFM) Conference*, AIAA Paper 2013-4979, Boston, Massachusetts, 2013. doi:10.2514/6.2013-4979.
- [156] Gunasekaran, S., Altman, A., and Ol, M. V., “Errors in Off-Axis Loading of Off-the-Shelf 6-Component Force Transducers: A Cautionary Tale,” *53rd AIAA Aerospace Sciences Meeting*, AIAA Paper 2015-1562, Kissimmee, Florida, 2015. doi:10.2514/6.2015-1562.
- [157] Verstraete, D., and MacNeill, R., “The Effects of Blockage on the Performance of Small Propellers,” *20th Australasian Fluid Mechanics Conference*, Perth, Australia, 2016.
- [158] Han, H., Xiang, C., Xu, B., and Yu, Y., “Experimental and Computational Analysis of Microscale Shrouded Coaxial Rotor in Hover,” *2017 International Conference on Unmanned Aircraft Systems (ICUAS)*, Miami, Florida, 2017, pp. 1092–1100. doi:10.1109/ICUAS.2017.7991413.
- [159] Heinzen, S. B., “Flight Testing of the Free-to-Pitch Variable Pitch Propeller,” *2018 AIAA Aerospace Sciences Meeting*, AIAA Paper 2018-0762, Kissimmee, Florida, 2018. doi:10.2514/6.2018-0762.

- [160] Serrano, D., Ren, M., Qureshi, A. J., and Ghaemi, S., "Effect of Disk Angle-of-Attack on Aerodynamic Performance of Small Propellers," *Aerospace Science and Technology*, Vol. 92, 2019, pp. 901–914. doi:10.1016/j.ast.2019.07.022.
- [161] Scarano, F., and Riethmuller, M. L., "Iterative Multigrid Approach in PIV Image Processing with Discrete Window Offset," *Experiments in Fluids*, Vol. 26, No. 6, 1999, pp. 513–523. doi:10.1007/s003480050318.
- [162] Wieneke, B., "PIV Uncertainty Quantification from Correlation Statistics," *Measurement Science and Technology*, Vol. 26, No. 7, 2015, p. 074002. doi:10.1088/0957-0233/26/7/074002.
- [163] Sinnige, T., de Vries, R., Della Corte, B., Avallone, F., Ragni, D., Eitelberg, G., and Veldhuis, L. L. M., "Unsteady Pylon Loading Caused by Propeller-Slipstream Impingement for Tip-Mounted Propellers," *Journal of Aircraft*, Vol. 55, No. 4, 2018, pp. 1605–1618. doi:10.2514/1.C034696.
- [164] Steijl, R., and Barakos, G., "Sliding Mesh Algorithm for CFD Analysis of Helicopter Rotor–Fuselage Aerodynamics," *International Journal for Numerical Methods in Fluids*, Vol. 58, No. 5, 2008, pp. 527–549. doi:10.1002/flid.1757.
- [165] Laban, M., Kok, J. C., and Prananta, B. B., "Numerical Tools for Contra-Rotating Open-Rotor Performance, Noise and Vibration Assessment," *27th International Congress of the Aeronautical Sciences*, Nice, France, 2010, pp. 19–24.
- [166] Francois, B., Costes, M., and Dufour, G., "Comparison of Chimera and Sliding Mesh Techniques for Unsteady Simulations of Counter Rotating Open-Rotors," *20th ISABE Conference*, ISABE-2011-1231, Gothenburg, Sweden, 2011.
- [167] Morgado, J., Abdollahzadeh, M., Silvestre, M. A. R., and Páscoa, J. C., "High Altitude Propeller Design and Analysis," *Aerospace Science and Technology*, Vol. 45, 2015, pp. 398–407. doi:10.1016/j.ast.2015.06.011.
- [168] Capitaio Patrao, A., Grönstedt, T., Avellán, R., and Lundbladh, A., "Wake Energy Analysis Method Applied to the Boxprop Propeller Concept," *Aerospace Science and Technology*, Vol. 79, 2018, pp. 689–700. doi:10.1016/j.ast.2018.06.018.
- [169] Sørensen, J. N., Shen, W. Z., and Munduate, X., "Analysis of Wake States by a Full-Field Actuator Disc Model," *Wind Energy*, Vol. 1, No. 2, 1998, pp. 73–88. doi:10.1002/(SICI)1099-1824(199812)1:2<73::AID-WE12>3.0.CO;2-L.
- [170] Snel, H., Houwink, R., and Bosschers, J., "Sectional Prediction of Lift Coefficients on Rotating Wind Turbine Blades in Stall," Tech. Rep. ECN-C-93-052, Netherlands Energy Research Foundation, Petten, Netherlands, Dec. 1994.
- [171] Márquez Gutiérrez, C., Stuermer, A., Clemen, C., and Grimminger, A., "Validation of Actuator Disk Simulations of CROR Propulsion Systems at Low-Speed Flight Conditions," *30th AIAA Applied Aerodynamics Conference*, AIAA Paper 2012-2787, New Orleans, Louisiana, 2012. doi:10.2514/6.2012-2787.

- [172] Schollenberger, M., Lutz, T., and Krämer, E., "Boundary Condition Based Actuator Line Model to Simulate the Aerodynamic Interactions at Wingtip Mounted Propellers," *New Results in Numerical and Experimental Fluid Mechanics XII*, edited by A. Dillmann, G. Heller, E. Krämer, C. Wagner, C. Tropea, and S. Jakirlić, Springer International Publishing, 2020, pp. 608–618.
- [173] Kim, T., Oh, S., and Yee, K., "Improved Actuator Surface Method for Wind Turbine Application," *Renewable Energy*, Vol. 76, 2015, pp. 16–26. doi:10.1016/j.renene.2014.11.002.
- [174] Churchfield, M. J., Schreck, S. J., Martinez, L. A., Meneveau, C., and Spalart, P. R., "An Advanced Actuator Line Method for Wind Energy Applications and Beyond," *35th Wind Energy Symposium*, AIAA Paper 2017-1998, Grapevine, Texas, 2017. doi:10.2514/6.2017-1998.
- [175] Linton, D., Barakos, G., Widjaja, R., and Thornbern, B., "A New Actuator Surface Model with Improved Wake Model for CFD Simulations of Rotorcraft," *AHS International 73th Annual Forum & Technology Display*, Fort Worth, Texas, 2017.
- [176] Shen, W. Z., Hansen, M. O. L., and Sørensen, J. N., "Determination of the Angle of Attack on Rotor Blades," *Wind Energy*, Vol. 12, No. 1, 2008, pp. 91–98. doi:10.1002/we.277.
- [177] Sinnige, T., "The Effects of Pylon Blowing on Pusher Propeller Performance and Noise Emissions," Master's Thesis, Delft University of Technology, Delft, The Netherlands, 2013.
- [178] Borer, N. K., and Moore, M. D., "Integrated Propeller-Wing Design Exploration for Distributed Propulsion Concepts," *53rd AIAA Aerospace Sciences Meeting*, AIAA Paper 2015-1672, Kissimmee, Florida, 2015. doi:10.2514/6.2015-1672.
- [179] Humpert, B., Gaeta, R., and Jacob, J. D., "Optimal Propeller Design for Quiet Aircraft Using Numerical Analysis," *21st AIAA/CEAS Aeroacoustics Conference*, AIAA Paper 2015-2360, Dallas, Texas, 2015. doi:10.2514/6.2015-2360.
- [180] Nootebos, B., "Aerodynamic Analysis and Optimisation of Wingtip-Mounted Pusher Propellers: An Investigation into the Propulsive Gains and Optimal Geometry of Small-Scale Propellers," Master's Thesis, Delft University of Technology, Delft, The Netherlands, 2018.
- [181] Drela, M., "XFOIL: An Analysis and Design System for Low Reynolds Number Airfoils," *Low Reynolds Number Aerodynamics*, Lecture Notes in Engineering, Vol. 54, edited by T. J. Mueller, Springer, Berlin, Heidelberg, 1989, pp. 1–12. doi:10.1007/978-3-642-84010-4_1.
- [182] Anon, "Matlab R2017b Documentation, Fmincon," The MathWorks, Inc., 2017.
- [183] Usai, D., "Aerodynamic Interaction Between Overlapping Propellers: A Numerical And Experimental Study," Master's Thesis, Politecnico di Torino, Turin, Italy, Jul. 2019.

- [184] Sears, W. R., "A Systematic Presentation of the Theory of Thin Airfoils in Non-Uniform Motion," Dissertation, California Institute of Technology, Pasadena, California, 1938. doi:10.7907/EM5X-CZ66.
- [185] Sears, W. R., "Some Aspects of Non-Stationary Airfoil Theory and Its Practical Application," *Journal of the Aeronautical Sciences*, Vol. 8, No. 3, 1941, pp. 104–108.
- [186] Chandrasekaran, B., "Method for the Prediction of the Installation Aerodynamics of a Propfan at Subsonic Speeds," NASA Contractor Report 3887, Vigyan Research Associates, Hampton, Virginia, 1985.
- [187] Anon, "Help System ANSYS® Academic Research Release 16.0, CFX," ANSYS, Inc., Software, 2015.
- [188] Anon, "Help System ANSYS® Academic Research Release 16.0, Fluent," ANSYS, Inc., Software, 2015.
- [189] Anon, "Help System ANSYS® Academic Research Release 18.1, Fluent," ANSYS, Inc., Software, 2017.
- [190] Boerstael, J. W., Kassies, A., Kok, J. C., and Spekreijse, S. P., "ENFLOW, a Full-Functionality System of CFD Codes for Industrial Euler/Navier-Stokes Flow Computations," Technical Publication 96286 U, NLR, 1996.
- [191] Boelens, O. J., Ven, H., Kok, J. C., and Prananta, B. B., "Rotorcraft Simulations Using a Sliding-Grid Approach," Technical Publication 2008-779, NLR, Amsterdam, The Netherlands, 2008.
- [192] Antoniadis, A. F., Drikakis, D., Zhong, B., Barakos, G., Steijl, R., Biava, M., Vigevano, L., Brocklehurst, A., Boelens, O., Dietz, M., Embacher, M., and Khier, W., "Assessment of CFD Methods against Experimental Flow Measurements for Helicopter Flows," *Aerospace Science and Technology*, Vol. 19, No. 1, 2012, pp. 86–100. doi: 10.1016/j.ast.2011.09.003.
- [193] Anon, "U.S. Standard Atmosphere, 1976," Tech. Rep. NOAA-S/T 76-1562, NOAA, NASA, US Air Force, Washington, D.C., Oct. 1976.
- [194] Barth, T., and Jespersen, D., "The Design and Application of Upwind Schemes on Unstructured Meshes," *27th Aerospace Sciences Meeting*, AIAA Paper 1989-366, Reno, Nevada, 1989. doi:10.2514/6.1989-366.
- [195] Menter, F. R., "Two-Equation Eddy-Viscosity Turbulence Models for Engineering Applications," *AIAA Journal*, Vol. 32, No. 8, 1994, pp. 1598–1605. doi:10.2514/3.12149.
- [196] Ruiz-Calavera, L. P., and Perdonés-Díaz, D., "CFD Computation of In-Plane Propeller Shaft Loads," *49th AIAA/ASME/SAE/ASEE Joint Propulsion Conference*, AIAA Paper 2013-3798, San Jose, California, 2013. doi:10.2514/6.2013-3798.

- [197] Meheut, M., "Thrust and Torque Far-Field Analysis of Propeller and Counter Rotating Open Rotor Configurations," *31st AIAA Applied Aerodynamics Conference*, AIAA Paper 2013-2803, San Diego, California, 2013. doi:10.2514/6.2013-2803.
- [198] Falissard, F., Boisard, R., and Delattre, G., "Aeroacoustic Computation of a Contra Rotating Open Rotor Model with Test Rig Installation Effects," *18th AIAA/CEAS Aeroacoustics Conference*, AIAA Paper 2012-2218, Colorado Springs, Colorado, 2012. doi:10.2514/6.2012-2218.
- [199] Spalart, P. R., and Allmaras, S. R., "A One-Equation Turbulence Model for Aerodynamic Flows," *30th Aerospace Sciences Meeting and Exhibit*, AIAA Paper 1992-0439, Reno, Nevada, 1992. doi:10.2514/6.1992-439.
- [200] Dacles-Mariani, J., Zilliac, G. G., Chow, J. S., and Bradshaw, P., "Numerical/Experimental Study of a Wingtip Vortex in the near Field," *AIAA Journal*, Vol. 33, No. 9, 1995, pp. 1561–1568. doi:10.2514/3.12826.
- [201] Spalart, P. R., and Rumsey, C. L., "Effective Inflow Conditions for Turbulence Models in Aerodynamic Calculations," *AIAA Journal*, Vol. 45, No. 10, 2007, pp. 2544–2553. doi:10.2514/1.29373.
- [202] Wallin, S., and Johansson, A. V., "An Explicit Algebraic Reynolds Stress Model for Incompressible and Compressible Turbulent Flows," *Journal of Fluid Mechanics*, Vol. 403, 2000, pp. 89–132. doi:10.1017/S0022112099007004.
- [203] Srinivasan, G. R., Raghavan, V., Duque, E. P. N., and McCroskey, W. J., "Flowfield Analysis of Modern Helicopter Rotors in Hover by Navier-Stokes Method," *Journal of the American Helicopter Society*, Vol. 38, No. 3, 1993, pp. 3–13. doi:10.4050/JAHS.38.3.3.
- [204] Johnson, W., *Helicopter Theory*, Courier Corporation, 1994.
- [205] Potsdam, M. A., and Strawn, R. C., "CFD Simulations of Tiltrotor Configurations in Hover," *Journal of the American Helicopter Society*, Vol. 50, No. 1, 2005, pp. 82–94. doi:10.4050/1.3092845.
- [206] Strawn, R. C., and Djomehri, M. J., "Computational Modeling of Hovering Rotor and Wake Aerodynamics," *Journal of Aircraft*, Vol. 39, No. 5, 2002, pp. 786–793. doi:10.2514/2.3024.
- [207] Anon, "P2012 Traveller," <https://www.tecnam.com/aircraft/p2012-traveller/>, Oct. 2018.
- [208] Alba, C., "A Surrogate-Based Multi-Disciplinary Design Optimization Framework Exploiting Wing-Propeller Interaction," Master's Thesis, Delft University of Technology, Delft, The Netherlands, 2017.
- [209] Batrakov, A., Kusyumov, A., Mikhailov, S., and Barakos, G., "Aerodynamic Optimization of Helicopter Rear Fuselage," *Aerospace Science and Technology*, Vol. 77, 2018, pp. 704–712. doi:10.1016/j.ast.2018.03.046.

- [210] Salah el Din, I., Lienard, C., Huot, R., and Fukari, R., "RACER High-Speed Demonstrator: Tail Unit Vertical Fin Aerodynamic Design," *AHS International 74th Annual Forum & Technology Display*, Phoenix, Arizona, 2018.
- [211] Öhrle, C., Schäferlein, U., Keßler, M., and Krämer, E., "Higher-Order Simulations of a Compound Helicopter Using Adaptive Mesh Refinement," *AHS International 74th Annual Forum & Technology Display*, Phoenix, Arizona, 2018.
- [212] Roache, P. J., "Quantification of Uncertainty in Computational Fluid Dynamics," *Annual Review of Fluid Mechanics*, Vol. 29, No. 1, 1997, pp. 123–160. doi:10.1146/annurev.fluid.29.1.123.
- [213] Eça, L., and Hoekstra, M., "Discretization Uncertainty Estimation Based on a Least Squares Version of the Grid Convergence Index," *Proceedings of the Second Workshop on CFD Uncertainty Analysis*, Instituto Superior Tecnico, Lisbon, Portugal, 2006.
- [214] Ekaterinaris, J. A., "High-Order Accurate, Low Numerical Diffusion Methods for Aerodynamics," *Progress in Aerospace Sciences*, Vol. 41, No. 3, 2005, pp. 192–300. doi:10.1016/j.paerosci.2005.03.003.
- [215] Binder, N., Courty-Audren, S.-K., Duplaa, S., Dufour, G., and Carbonneau, X., "Theoretical Analysis of the Aerodynamics of Low-Speed Fans in Free and Load-Controlled Windmilling Operation," *Journal of Turbomachinery*, Vol. 137, No. 10, 2015. doi:10.1115/1.4030308.
- [216] Wood, D., "Small Wind Turbines," *Advances in Wind Energy Conversion Technology*, edited by M. Sathyajith and G. S. Philip, Environmental Science and Engineering, Springer, Berlin, Heidelberg, 2011, pp. 195–211. doi:10.1007/978-3-540-88258-9_8.
- [217] Nallasamy, N., Yamamoto, O., Warsi, S., and Bober, L. J., "Large-Scale Advanced Propeller Blade Pressure Distributions - Prediction and Data," *Journal of Propulsion and Power*, Vol. 7, No. 3, 1991, pp. 452–461. doi:10.2514/3.23347.
- [218] Klein, C., Henne, U., Sachs, W. E., Hock, S., Falk, N., Ondrus, V., Beifuss, U., and Schaber, S., "Pressure Measurement on Rotating Propeller Blades by Means of the Pressure-Sensitive Paint Lifetime Method," *New Results in Numerical and Experimental Fluid Mechanics IX: Contributions to the 18th STAB/DGLR Symposium, Stuttgart, Germany, 2012*, edited by A. Dillmann, G. Heller, E. Krämer, H.-P. Kreplin, W. Nitsche, and U. Rist, Notes on Numerical Fluid Mechanics and Multi-disciplinary Design, Springer International Publishing, Cham, 2014, pp. 535–544. doi:10.1007/978-3-319-03158-3_54.
- [219] van Arnhem, N., Sinnige, T., Stokkermans, T. C. A., Eitelberg, G., and Veldhuis, L. L. M., "Aerodynamic Interaction Effects of Tip-Mounted Propellers Installed on the Horizontal Tailplane," *2018 AIAA Aerospace Sciences Meeting*, AIAA Paper 2018-2052, Kissimmee, Florida, 2018. doi:10.2514/6.2018-2052.

- [220] Thom, A., and Duraisamy, K., “Computational Investigation of Unsteadiness in Propeller Wake–Wing Interactions,” *Journal of Aircraft*, Vol. 50, No. 3, 2013, pp. 985–988. doi:10.2514/1.C031866.
- [221] Hirschberg, M., “Clean Sky 2 Update, Part 1: The Airbus Racer,” *Vertiflite*, Vol. 63, No. 5, September/October 2017, pp. 26–28.
- [222] Frey, F., Thiemeier, J., Öhrle, C., Keßler, M., and Krämer, E., “Aerodynamic Interactions on Airbus Helicopters’ Compound Helicopter RACER in Cruise Flight,” *Journal of the American Helicopter Society*, Vol. 65, No. 4, 2020, pp. 1–14. doi: 10.4050/JAHS.65.042001.
- [223] Frey, F., Öhrle, C., Thiemeier, J., Keßler, M., and Krämer, E., “Aerodynamic Interactions on Airbus Helicopters’ Compound Helicopter RACER in Hover,” *VFS International 76th Annual Forum & Technology Display*, Virginia Beach, Virginia, 2020.
- [224] Patterson Jr, J. C., and Flechner, S. G., “Exploratory Wind-Tunnel Investigation of a Wingtip-Mounted Vortex Turbine for Vortex Energy Recovery,” Technical Paper 2468, NASA, Hampton, Virginia, Jun. 1985.
- [225] Liepmann, H. W., and Roshko, A., *Elements of Gas Dynamics*, Dover Publications, Mineola, New York, 2001.

A

SIMPLE WAKE INGESTION MODEL

In this appendix, equations for the thrust and power of a wake propeller behind a fuselage body are derived. These derivations support statements on wake ingestion in Section 2.2. In Section A.1 the governing equations are described, assuming frictionless flow in the control volumes. In Sections A.2 and A.3 control volumes around respectively a fuselage body and a wake propeller are analysed. Some observations are made in the last Section A.4 from the derived equations of the previous sections and the power required by a wake propeller is compared to the power required by a propeller in the freestream.

A.1. GOVERNING EQUATIONS

Following Liepmann and Roshko [225] the continuity, momentum and energy equations for frictionless non-stationary flow can be written in integral form with tensor notation as:

$$\iiint_V \frac{\partial \rho}{\partial t} dV = - \oint_A \rho u_j n_j dA \quad (\text{A.1})$$

$$\iiint_V \frac{\partial}{\partial t} (\rho u_i) dV + \oint_A (\rho u_i) u_j n_j dA = - \oint_A p n_i dA + \iiint_V \rho f_i dV \quad (\text{A.2})$$

$$\begin{aligned} & \iiint_V \rho q dV + \iiint_V \rho f_i u_i dV - \oint_A p n_i u_i dA = \\ & \iiint_V \frac{\partial}{\partial t} \left(\rho e + \frac{1}{2} \rho u^2 \right) dV + \oint_A \left(\rho e + \frac{1}{2} \rho u^2 \right) u_j n_j dA \end{aligned} \quad (\text{A.3})$$

These equations apply to a control volume V enclosed by a simple closed control surface A , where n_i is a unit vector, normal to the element of surface area dA , positive when directed outward. In these equations ρ is the density, u_i the velocity vector, p the static

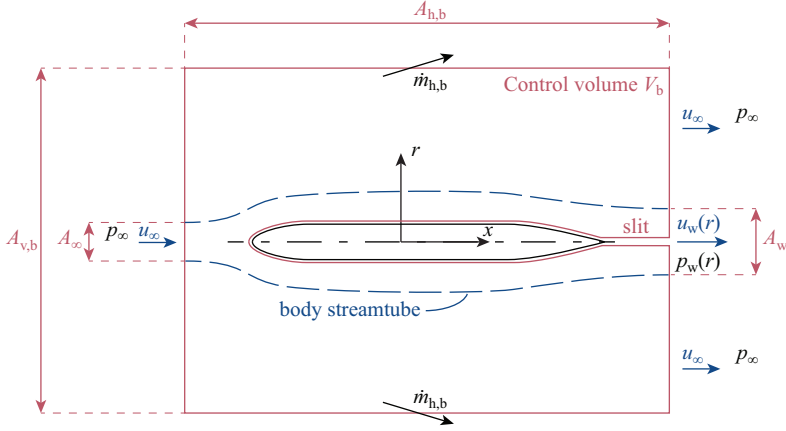


Figure A.1: Control volume definition around fuselage body with body at rest.

pressure, f_i a body force vector per unit mass (e.g. inertial forces, gravity forces and electromagnetic forces), q the rate of heat addition per unit mass and e the internal energy of the fluid per unit mass.

In the following sections, a reference frame is chosen with the fuselage body and wake propeller at rest, resulting in a steady flow and thus zero partial derivatives with respect to time. Furthermore, it is assumed that there are no body forces or any heat addition, and changes in the energy of the fluid only occur through changes in kinetic energy. Then the previous equations are simplified to:

$$\oiint_A \rho u_j n_j dA = 0 \quad (\text{A.4})$$

$$\oiint_A (\rho u_i) u_j n_j dA = - \oiint_A p n_i dA \quad (\text{A.5})$$

$$- \oiint_A p n_i u_i dA = \oiint_A \left(\frac{1}{2} \rho u^2 \right) u_j n_j dA \quad (\text{A.6})$$

A.2. CONTROL VOLUME ANALYSIS AROUND BODY

For a fuselage body, in Fig. A.1 a control volume V_b is defined enclosed by a simple closed control surface A_b . Through a slit, part of the control surface consists of the body wall. A streamtube is drawn starting upstream from freestream conditions, enclosing exactly the total pressure deficit downstream of the body, i.e. the wake. The body is assumed at rest, making this a steady problem. Thus only the convective part of the continuity

equation needs to be analysed as given in Eq. (A.4). For control volume V_b this results in:

$$\oint_{A_b} \rho u_j n_j dA = \rho_\infty u_\infty (-A_\infty - (A_{v,b} - A_\infty) + (A_{v,b} - A_w)) + \dot{m}_{h,b} + \iint_{A_w} \rho_w u_w dA = 0 \quad (\text{A.7})$$

$$-\rho_\infty u_\infty A_w + \dot{m}_{h,b} + \iint_{A_w} \rho_w u_w dA = 0 \quad (\text{A.8})$$

where $\dot{m}_{h,b}$ is the mass flow of freestream fluid leaving the horizontal sides of the control volume. Evaluating the continuity equation through the body streamtube only gives:

$$\iint_{A_w} \rho_w u_w dA = \rho_\infty u_\infty A_\infty \quad (\text{A.9})$$

Combining the previous two equations gives an expression for $\dot{m}_{h,b}$:

$$\dot{m}_{h,b} = \rho_\infty u_\infty (A_w - A_\infty) \quad (\text{A.10})$$

The next step is to evaluate the momentum equation as shown in Eq. A.5. First the left hand side is evaluated in x-direction:

$$\oint_{A_b} (\rho u_1) u_j n_j dA = \quad (\text{A.11})$$

$$\rho_\infty u_\infty^2 (-A_\infty - (A_{v,b} - A_\infty) + (A_{v,b} - A_w)) + \dot{m}_{h,b} u_\infty + \iint_{A_w} \rho_w u_w^2 dA = \quad (\text{A.12})$$

$$-\rho_\infty u_\infty^2 A_w + \dot{m}_{h,b} u_\infty + \iint_{A_w} \rho_w u_w^2 dA \quad (\text{A.13})$$

This can be simplified with the result from Eq. (A.10):

$$\oint_{A_b} (\rho u_1) u_j n_j dA = -\rho_\infty u_\infty^2 A_\infty + \iint_{A_w} \rho_w u_w^2 dA \quad (\text{A.14})$$

Inserting Eq. A.9 into this result gives:

$$\oint_{A_b} (\rho u_1) u_j n_j dA = -u_\infty \iint_{A_w} \rho_w u_w dA + \iint_{A_w} \rho_w u_w^2 dA \quad (\text{A.15})$$

$$= \iint_{A_w} \rho_w u_w (u_w - u_\infty) dA \quad (\text{A.16})$$

Next the right hand side of the momentum equation is evaluated in x-direction, realising that the (pressure) drag D on the body exerts a similar force in negative x-direction on

the fluid:

$$-\iint_{A_b} p n_1 dA = p_\infty (A_\infty + (A_{v,b} - A_\infty) - (A_{v,b} - A_w)) - \iint_{A_w} p_w dA - D \quad (\text{A.17})$$

$$= p_\infty A_w - \iint_{A_w} p_w dA - D \quad (\text{A.18})$$

$$= \iint_{A_w} (p_\infty - p_w) dA - D \quad (\text{A.19})$$

Combining the left and right hand side of the momentum equation in x-direction gives:

$$\iint_{A_w} \rho_w u_w (u_w - u_\infty) dA = \iint_{A_w} (p_\infty - p_w) dA - D \quad (\text{A.20})$$

This can be rewritten for the body drag as:

$$D = \iint_{A_w} \rho_w u_w (u_\infty - u_w) dA + \iint_{A_w} (p_\infty - p_w) dA \quad (\text{A.21})$$

A.3. CONTROL VOLUME ANALYSIS AROUND WAKE PROPELLER

For a wake propeller behind the fuselage body, in Fig. A.2 a control volume V_p is defined enclosed by a simple closed control surface A_p . Through a slit, the propeller (actuator disk) is outside of the control volume, surrounded by the control surface. A streamtube is drawn starting upstream from the streamtube of Fig. A.1, enclosing exactly the propeller and its slipstream. The propeller is assumed at rest, making this a steady problem. So again only the convective part of the continuity equation needs to be evaluated as given in Eq. (A.4). For control volume V_p this results in:

$$\iint_{A_p} \rho u_j n_j dA = \quad (\text{A.22})$$

$$- \iint_{A_w} \rho_w u_w dA + \rho_\infty u_\infty (- (A_{v,p} - A_w) + (A_{v,p} - A_s)) - \dot{m}_{h,p} + \iint_{A_s} \rho_s u_s dA = 0 \quad (\text{A.23})$$

$$- \iint_{A_w} \rho_w u_w dA + \rho_\infty u_\infty (A_w - A_s) - \dot{m}_{h,p} + \iint_{A_s} \rho_s u_s dA = 0 \quad (\text{A.24})$$

where $\dot{m}_{h,p}$ is the mass flow of freestream fluid entering the horizontal sides of the control volume. Evaluating the continuity equation through the propeller streamtube gives:

$$\iint_{A_w} \rho_w u_w dA = \iint_{A_s} \rho_s u_s dA \quad (\text{A.25})$$

Combining the previous two equations gives an expression for $\dot{m}_{h,p}$:

$$\dot{m}_{h,p} = \rho_\infty u_\infty (A_w - A_s) \quad (\text{A.26})$$

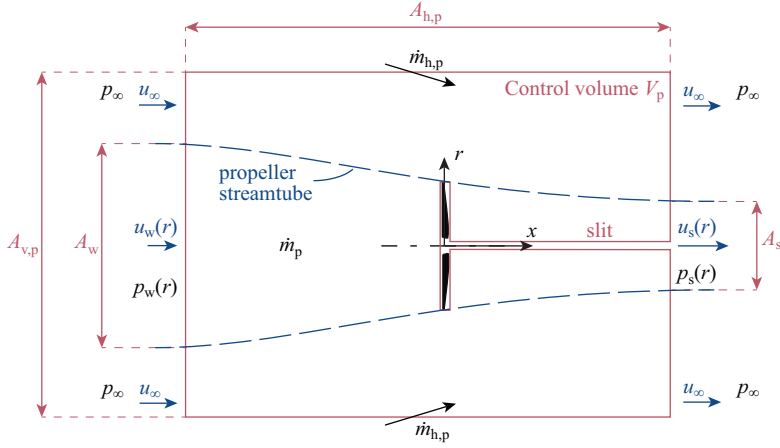


Figure A.2: Control volume definition around wake propeller with propeller at rest.

Next the momentum equation is evaluated as shown in Eq. A.5, starting with the left hand side in x-direction:

$$\oint_{A_p} (\rho u_1) u_j n_j dA = \quad (\text{A.27})$$

$$- \iint_{A_w} \rho_w u_w^2 dA + \rho_\infty u_\infty^2 (- (A_{v,p} - A_w) + (A_{v,p} - A_s)) - \dot{m}_{h,p} u_\infty + \iint_{A_s} \rho_s u_s^2 dA = \quad (\text{A.28})$$

$$- \iint_{A_w} \rho_w u_w^2 dA + \rho_\infty u_\infty^2 (A_w - A_s) - \dot{m}_{h,p} u_\infty + \iint_{A_s} \rho_s u_s^2 dA \quad (\text{A.29})$$

This can be simplified with the result from Eq. (A.26):

$$\oint_{A_p} (\rho u_1) u_j n_j dA = \iint_{A_s} \rho_s u_s^2 dA - \iint_{A_w} \rho_w u_w^2 dA \quad (\text{A.30})$$

Next the right hand side of the momentum equation is evaluated in x-direction, realising that the (pressure) thrust T on the propeller exerts a similar force in positive x-direction on the fluid:

$$- \oint_{A_p} p n_1 dA = \iint_{A_w} p_w dA + p_\infty ((A_{v,p} - A_w) - (A_{v,p} - A_s)) - \iint_{A_s} p_s dA + T \quad (\text{A.31})$$

$$= \iint_{A_w} p_w dA + p_\infty (A_s - A_w) - \iint_{A_s} p_s dA + T \quad (\text{A.32})$$

$$= \iint_{A_s} (p_\infty - p_s) dA - \iint_{A_w} (p_\infty - p_w) dA + T \quad (\text{A.33})$$

A

Combining the left and right hand side of the momentum equation in x-direction gives:

$$\iint_{A_s} \rho_s u_s^2 dA - \iint_{A_w} \rho_w u_w^2 dA = \iint_{A_s} (p_\infty - p_s) dA - \iint_{A_w} (p_\infty - p_w) dA + T \quad (\text{A.34})$$

This can be rewritten for the propeller thrust as:

$$T = \iint_{A_s} \rho_s u_s^2 dA - \iint_{A_w} \rho_w u_w^2 dA + \iint_{A_w} (p_\infty - p_w) dA - \iint_{A_s} (p_\infty - p_s) dA \quad (\text{A.35})$$

At last the energy equation is evaluated as shown in Eq. A.6, starting with the left hand side, which is the rate of work on the fluid by pressure. Here one should realise that the propeller is exerting work on the fluid in the control volume with a rate of \dot{W}_p increasing the energy of the fluid. Furthermore, one should realise that the mass flow $\dot{m}_{h,p}$ results in pressure work done by the outside fluid on the fluid in the control volume:

$$-\oint_{A_p} p n_i u_i dA = \quad (\text{A.36})$$

$$\iint_{A_w} p_w u_w dA + p_\infty u_\infty ((A_{v,p} - A_w) - (A_{v,p} - A_s)) + \frac{\dot{m}_{h,p}}{\rho_\infty} p_\infty - \iint_{A_s} p_s u_s dA + \dot{W}_p = \quad (\text{A.37})$$

$$\iint_{A_w} p_w u_w dA + p_\infty u_\infty (A_s - A_w) + \frac{\dot{m}_{h,p}}{\rho_\infty} p_\infty - \iint_{A_s} p_s u_s dA + \dot{W}_p \quad (\text{A.38})$$

This can be simplified with the result from Eq. (A.26):

$$-\oint_{A_p} p n_i u_i dA = \iint_{A_w} p_w u_w dA - \iint_{A_s} p_s u_s dA + \dot{W}_p \quad (\text{A.39})$$

Now evaluate the right hand side of the energy equation:

$$\oint_{A_p} \left(\frac{1}{2} \rho u^2 \right) u_j n_j dA = \quad (\text{A.40})$$

$$-\iint_{A_w} \frac{1}{2} \rho_w u_w^3 dA + \frac{1}{2} \rho_\infty u_\infty^3 (- (A_{v,p} - A_w) + (A_{v,p} - A_s)) - \frac{1}{2} u_\infty^2 \dot{m}_{h,p} + \iint_{A_s} \frac{1}{2} \rho_s u_s^3 dA = \quad (\text{A.41})$$

$$-\iint_{A_w} \frac{1}{2} \rho_w u_w^3 dA + \frac{1}{2} \rho_\infty u_\infty^3 (A_w - A_s) - \frac{1}{2} u_\infty^2 \dot{m}_{h,p} + \iint_{A_s} \frac{1}{2} \rho_s u_s^3 dA \quad (\text{A.42})$$

This can be simplified with the result from Eq. (A.26):

$$\oint_{A_p} \left(\frac{1}{2} \rho u^2 \right) u_j n_j dA = \iint_{A_s} \frac{1}{2} \rho_s u_s^3 dA - \iint_{A_w} \frac{1}{2} \rho_w u_w^3 dA \quad (\text{A.43})$$

Combining the left and right hand side of the energy equation gives:

$$\iint_{A_w} p_w u_w dA - \iint_{A_s} p_s u_s dA + \dot{W}_p = \iint_{A_s} \frac{1}{2} \rho_s u_s^3 dA - \iint_{A_w} \frac{1}{2} \rho_w u_w^3 dA \quad (\text{A.44})$$

And thus rate of work done by the propeller on the fluid in the control volume is:

$$\dot{W}_p = \iint_{A_s} \frac{1}{2} \rho_s u_s^3 dA - \iint_{A_w} \frac{1}{2} \rho_w u_w^3 dA + \iint_{A_s} p_s u_s dA - \iint_{A_w} p_w u_w dA \quad (\text{A.45})$$

A.4. OBSERVATIONS

In this section a number of observations are made with the derived Eqs. (A.21) and (A.35) for the fuselage body drag and wake propeller thrust respectively and Eq. (A.45) for the work done on the fluid by the wake propeller.

A.4.1. CONSTANT PROPERTIES OVER STREAMTUBE CROSS SECTIONS

The integrals in the derived equations can be simplified by assuming constant properties over the cross sections of the fuselage body and propeller streamtube. This results in the following equations:

$$D = \rho_w u_w (u_\infty - u_w) A_w + (p_\infty - p_w) A_w \quad (\text{A.46})$$

$$= \dot{m}_p (u_\infty - u_w) + (p_\infty - p_w) A_w \quad (\text{A.47})$$

$$T = \rho_s u_s^2 A_s - \rho_w u_w^2 A_w + (p_\infty - p_w) A_w - (p_\infty - p_s) A_s \quad (\text{A.48})$$

$$= \dot{m}_p (u_s - u_w) + (p_\infty - p_w) A_w - (p_\infty - p_s) A_s \quad (\text{A.49})$$

$$\dot{W}_p = \frac{1}{2} \rho_s u_s^3 A_s - \frac{1}{2} \rho_w u_w^3 A_w + p_s u_s A_s - p_w u_w A_w \quad (\text{A.50})$$

$$= \frac{1}{2} \dot{m}_p (u_s^2 - u_w^2) + \dot{m}_p \left(\frac{p_s}{\rho_s} - \frac{p_w}{\rho_w} \right) \quad (\text{A.51})$$

A.4.2. THRUST-DRAG BALANCE

If the assumption is made that $T = D$ and a large enough control volume V_p is drawn around the propeller such that $p_s = p_\infty$, i.e. the slipstream pressure recovers to freestream condition, then equating Eq. (A.35) to (A.21) gives:

$$\iint_{A_s} \rho_s u_s^2 dA - \iint_{A_w} \rho_w u_w^2 dA + \iint_{A_w} (p_\infty - p_w) dA = \iint_{A_w} \rho_w u_w (u_\infty - u_w) dA + \iint_{A_w} (p_\infty - p_w) dA \quad (\text{A.52})$$

$$\iint_{A_s} \rho_s u_s^2 dA = \iint_{A_w} \rho_w u_w u_\infty dA \quad (\text{A.53})$$

Inserting Eq. A.25 into this result gives:

$$\iint_{A_s} \rho_s u_s^2 dA = \iint_{A_s} \rho_s u_s u_\infty dA \quad (\text{A.54})$$

$$\iint_{A_s} \rho_s u_s (u_s - u_\infty) dA = 0 \quad (\text{A.55})$$

It is observed that one of the solutions is $u_s = u_\infty$. In case of constant properties over the streamtube cross sections $u_s = u_\infty$ is the only solution. In such case, $\rho_s = \rho_\infty$ and $A_s = A_\infty$. Of course, this conclusion is only valid within the assumption of zero heat addition and with a propeller imparting only axial momentum on the fluid and no angular momentum resulting in swirl.

A.4.3. PROPELLER POWER EVALUATION

Consider that the power required by the propeller is equal to the work done by the propeller on the fluid per unit time, i.e. $P = \dot{W}_p$. From the thrust–drag balance it was found that $u_s = u_\infty$ for $p_s = p_\infty$ for the case of constant properties over the streamtube cross sections. Applying this result to Eqs. A.49 and A.51 gives:

$$T = \dot{m}_p (u_\infty - u_w) + (p_\infty - p_w) A_w \quad (\text{A.56})$$

$$\dot{W}_p = \frac{1}{2} \dot{m}_p (u_\infty^2 - u_w^2) + \dot{m}_p \left(\frac{p_\infty}{\rho_\infty} - \frac{p_w}{\rho_w} \right) \quad (\text{A.57})$$

Although unrealistic, if an incompressible flow is assumed and the control volume and wake propeller are positioned such that $p_w = p_\infty$, i.e. the propeller is located far downstream of the fuselage and the control volume extends far upstream of the propeller, then we get:

$$T = \dot{m}_p (u_\infty - u_w) \quad (\text{A.58})$$

$$\dot{W}_p = \frac{1}{2} \dot{m}_p (u_\infty^2 - u_w^2) = \frac{1}{2} T (u_\infty + u_w) \quad (\text{A.59})$$

In comparison, the power required by a propeller located in the freestream is:

$$\dot{W}_p = \frac{1}{2} \dot{m}_p (u_s^2 - u_\infty^2) = \frac{1}{2} T (u_s + u_\infty) \quad (\text{A.60})$$

Since the slipstream velocity u_s for a propeller in the freestream is larger than the freestream u_∞ or wake velocity u_w , the power required for a propeller in the freestream in Eq. (A.60) is higher than for a propeller in the wake of the fuselage body in Eq. (A.59). However, in realistic applications the static pressure in the wake is larger than the freestream static pressure, and then the benefit of wake ingestion reduces.

ACKNOWLEDGEMENTS

I would not have completed this research without the help of others. First of all, I would like to thank Leo for convincing me to do a PhD in the first place, with a very appealing project on the Airbus RACER. The supervision of Mark and Leo during my PhD has substantially improved the quality of the research and I am greatly indebted to them.

Most of the research in this dissertation has been done in collaboration. I would like to thank Tomas in particular for our fruitful collaborations. I have learned a great deal from him about setting up and executing successful wind tunnel campaigns. The many discussions on propeller related topics were very helpful to progress my research. Equally much have I benefited from the collaboration with and help of Nando. Together we have discovered the best practices for RANS propeller simulations. We had many discussions on our work which helped me steer my work in the right direction. Also, his excellent technical support before and during experiments was vital.

I also had the pleasure to (co-)supervise a number of MSc thesis projects during my PhD. I would like to especially mention Bas and Daniele for their pleasant collaboration and very nice contribution to this work. Furthermore, thanks to Peter and Ed from DEMO for their patience, excellent manufacturing of the propeller interaction test setup and quick problem solving during the wind-tunnel campaign.

The successful completion of the PROPTER project on the lateral rotors of the Airbus RACER is a result of a good collaboration between NLR, Airbus Helicopters and my supervisors and me. I would like to thank Bambang for his technical input and support, as well as for the management of the project. Furthermore, thanks to Michel for his efforts in the preparation of the computational grids. During the course of the project we had excellent input and feedback from Raphaël and Paul, for which I would like to thank them.

Throughout my PhD we had many fruitful discussions during our propeller research group meetings. I would like to especially thank Georg for his very useful and knowledgeable input, but also all the other participants. I learned a lot from the presentations and discussions of all the related research. Also, the PhD would not have been so much fun without the colleagues in the Flight Performance and Propulsion section, from the people in the office, to all the other FPPs during coffee breaks, (friday) afternoon drinks and FPP trips. Thank you for this very pleasant chapter in my life.

Of course, I am very grateful for the support of my parents during this long trajectory of learning all the way to the completion of this dissertation. And finally, I would like to thank Vicky for her love and support and for hosting me in Cape Town, Beijing and Ilkley during the last year of remote work. That experience gave me the inspiration to finish the book that is in front of you.

CURRICULUM VITAE

Tom Caton Arnaud STOKKERMANS

27-11-1989 Born in Heerlen, the Netherlands.

RESEARCH

2015–2020 **PhD in Aerospace Engineering**
Delft University of Technology, Delft, the Netherlands
Dissertation: Aerodynamics of Propellers in Interaction Dominated Flowfields: An Application to Novel Aerospace Vehicles
Promotor: Prof. dr. ir. L.L.M. Veldhuis
Copromotor: Prof. dr. ir. M. Voskuijl

EDUCATION

2015–2019 **Doctoral Education Program**
Delft University of Technology, Delft, the Netherlands

2012–2015 **MSc in Aerospace Engineering (with distinction)**
Delft University of Technology, Delft, the Netherlands
Thesis: Design and Analysis of Swirl Recovery Vanes for an Isolated and a Wing Mounted Tractor Propeller
Supervisors: Prof. dr. ir. L.L.M. Veldhuis
Prof. Dr.-Ing. G. Eitelberg

2011–2012 **MSc in Aeronautics**
California Institute of Technology, Pasadena, USA

2008–2011 **BSc in Aerospace Engineering (with distinction)**
Delft University of Technology, Delft, the Netherlands
Minor: Sustainable Energy Technology

2002–2008 **Pre-University Education (with distinction)**
Bernardinus College, Heerlen, the Netherlands

LIST OF PUBLICATIONS

JOURNAL PAPERS

6. Stokkermans, T. C. A., and Veldhuis, L. L. M., "Propeller Performance at Large Angle of Attack Applicable to Compound Helicopters," (Under review).
5. Stokkermans, T. C. A., Usai, D., Sinnige, T., and Veldhuis, L. L. M., "Aerodynamic Interaction Effects between Propellers in Typical eVTOL Vehicle Configurations," (Under review).
4. Stokkermans, T. C. A., Veldhuis, L. L. M., Soemarwoto, B., Fukari, R., and Eglin, P., "Break-down of Aerodynamic Interactions for the Lateral Rotors on a Compound Helicopter," *Aerospace Science and Technology*, Vol. 101, (2020), pp. 105845. doi: 10.1016/j.ast.2020.105845
3. Stokkermans, T. C. A., van Arnhem, N., Sinnige, T., Eitelberg, G., and Veldhuis, L. L. M., "Validation and Comparison of RANS Propeller Modeling Methods for Tip-Mounted Applications," *AIAA Journal*, Vol. 57, No. 2 (2019), pp. 566-580. doi: 10.2514/1.J057398
2. Sinnige, T., van Arnhem, N., Stokkermans, T. C. A., Eitelberg, G., and Veldhuis, L. L. M., "Wingtip-Mounted Propellers: Aerodynamic Analysis of Interaction Effects and Comparison with Conventional Layout," *Journal of Aircraft*, Vol. 56, No. 1 (2019), pp. 295-312. doi: 10.2514/1.C034978
1. Sinnige, T., Stokkermans, T. C. A., Ragni, D., Eitelberg, G., and Veldhuis, L. L. M., "Aerodynamic and Aeroacoustic Performance of a Propeller Propulsion System with Swirl-Recovery Vanes," *Journal of Propulsion and Power*, Vol. 34, No. 6 (2018), pp. 1376-1390. doi: 10.2514/1.B36877

CONFERENCE PAPERS

7. Stokkermans, T. C. A., Nootebos, S., Veldhuis, L. L. M., "Analysis and Design of a Small-Scale Wingtip-Mounted Pusher Propeller," *AIAA Aviation 2019 Forum*, AIAA Paper 2019-3693, June 2019. doi: 10.2514/6.2019-3693
6. Sinnige, T., Stokkermans, T. C. A., van Arnhem, N., Veldhuis, L. L. M., "Aerodynamic Performance of a Wingtip-Mounted Tractor Propeller Configuration in Windmilling and Energy-Harvesting Conditions," *AIAA Aviation 2019 Forum*, AIAA Paper 2019-3033, June 2019. doi: 10.2514/6.2019-3033
5. Stokkermans, T., Voskuijl, M., Veldhuis, L., Soemarwoto, B., Fukari, R., and Eglin, P., "Aerodynamic Installation Effects of Lateral Rotors on a Novel Compound Helicopter Configuration," *AHS International 74th Annual Forum & Technology Display*, May 2018.
4. Stokkermans, T. C. A., van Arnhem, N., Sinnige, T., and Veldhuis, L. L. M., "Validation and Comparison of RANS Propeller Modeling for Tip-Mounted Applications," *2018 AIAA Aerospace Sciences Meeting*, AIAA Paper 2018-0542, June 2018. doi: 10.2514/6.2018-0542

3. van Arnhem, N., Sinnige, T., Stokkermans, T. C. A., Eitelberg, G., and Veldhuis, L. L. M., "Aerodynamic Interaction Effects of Tip-Mounted Propellers Installed on the Horizontal Tailplane," *2018 AIAA Aerospace Sciences Meeting*, AIAA Paper 2018-2052, June 2018. doi: 10.2514/6.2018-0778
2. Veldhuis, L. L. M., Stokkermans, T. C. A., Sinnige, T., and Eitelberg, G., "Analysis of Swirl Recovery Vanes for Increased Propulsive Efficiency in Tractor Propeller Aircraft," *30th Congress of the International Council of the Aeronautical Sciences*, ICAS Paper 2016-0060, Sept. 2016.
1. Stokkermans, T. C. A., van Arnhem, N., and Veldhuis, L. L. M., "Mitigation of Propeller Kinetic Energy Losses with Boundary Layer Ingestion and Swirl Recovery Vanes," *Proceedings of the 2016 Applied Aerodynamics Research Conference*, 2016, pp. 56–69.